

UNIVERSIDAD NACIONAL AUTONOMA
DE MEXICO

FACULTAD DE CIENCIAS

DIVISION DE ESTUDIOS DE POSGRADO

PROPIEDADES FISICAS Y ESTADISTICAS DE LAS NUBES
SIMULACIONES NUMERICAS DEL MEDIO INTERESTELAR

T E S I S

QUE PARA OBTENER EL GRADO ACADEMICO DE
DOCTOR EN CIENCIAS (ASTRONOMIA)

P R E S E N T A

JAVIER BALLESTEROS PAREDES

DIRECTOR DE TESIS: DR. ENRIQUE VAZQUEZ SEMADENI

1999



UNAM – Dirección General de Bibliotecas

Tesis Digitales
Restricciones de uso

DERECHOS RESERVADOS ©
PROHIBIDA SU REPRODUCCIÓN TOTAL O PARCIAL

Todo el material contenido en esta tesis está protegido por la Ley Federal del Derecho de Autor (LFDA) de los Estados Unidos Mexicanos (Méjico).

El uso de imágenes, fragmentos de videos, y demás material que sea objeto de protección de los derechos de autor, será exclusivamente para fines educativos e informativos y deberá citar la fuente donde la obtuvo mencionando el autor o autores. Cualquier uso distinto como el lucro, reproducción, edición o modificación, será perseguido y sancionado por el respectivo titular de los Derechos de Autor.

Agradecimientos

Primero que nada quiero agradecer a mi asesor, Enrique Vázquez Semadeni, la infinita paciencia y la ayuda constante que durante más de 4 años me ha brindado, en los cuales ha dirigido mi trabajo de investigación, de quien he aprendido mucho en esas exquisitas e interminables discusiones todo lo que está plasmado en este trabajo, quien incluso a larga distancia, vía correo electrónico, estuvo al pendiente de mi desarrollo académico, y quien además me ha enseñado algunas mañas en el squash.

Así mismo, quiero agradecer a quienes aceptaron ser sinodales de este trabajo, aún cuando no quedaron en la lista final: Jorge Cantó, con su gran capacidad analítica y su apoyo solidario en todo momento tanto a Paola como a mí; Jesús González, siempre dispuesto a posponer lo propio para ayudar a los demás; John Scalo, que me apoyó para conseguir el posdoc en NY, pero sobre todo por esos maravillosos, largos e intrincados correos electrónicos repletos de referencias a citas inimaginables, los cuales han sido el mejor libro de texto que he tenido a mi alcance; y Alyssa Goodman, que me brindó todo su apoyo durante mi estancia en Boston y con quien espero poder concretar el trabajo iniciado ahí.

A los sinodales, quienes leyeron cuidadosamente este trabajo e hicieron muy buenos comentarios: Lee Hartmann, por haberme invitado a colaborar con él, y que aunque me enseñó que "the best is the enemy of the good", tan sólo he logrado que me diga "its no so bad". Thierry Passot, con quien trabajé intensivamente en Niza, quien me enseñó la terrible frase de "don't think, do it!", y quien, a la inversa de John, me ha enseñado mucho con pocas palabras. Marco Martos, por compartir la pasión por la astronomía, la mística de los cotejos futboleros y uno que otro raquetazo en la cabeza. Susana Lizano, Alex Raga, Luis Felipe Rodríguez, con quienes además tomé clases durante la maestría y el doctorado y de quienes he aprendido mucho.

Quiero también agradecer a todos los amigos de Boston: a todo el personal del Center for Astrophysics, y en particular, a Alyssa Goodman (mencionada previamente); Phill Myers, por habernos dado la oportunidad de trabajar en el CfA, invitarnos a las reuniones de su grupo y escucharnos atentamente cuando hablábamos con nuestro pésimo inglés; Tom Mullen, a quien le debo un mezcal con gusano porque el que le lleve no tenía. Soy un abestia. Nancy Poole, con quien se chismeaba muy a gusto aunque a veces demasiado tiempo. Nuria Calvet, que en aras de nuestro bien aplicaba una especie de terrorismo científico para hacernos trabajar y avanzar, y que junto con Lee estuvo siempre al pendiente de nosotros, invitándonos maravillosas comidas en los calurosos días de verano, y deliciosas Ales y Stouts en la John Harvard Brewery; a Héctor Arce, puertorriqueño independentista, amigo I

profesional entrañable, me ha enseñado lo poco que se de observar, y nunca me contesta los e-mails porque siempre tiene cosas más importantes que hacer, ifyunoguaraimín. A Maite Beltrán, por esas idas a tomar aire fresco; a Joao Alves y Nurita Huélamo, quienes en poco tiempo se hicieron querer intensivamente; a Erik Gullbring y su familia (en particular a Markus, con quien compartí la ilusión de ir “up to the moon, again and again and again”). Muy especialmente a César Briceño, con quien compartimos un año de astronomía, un mundial de futbol, algunos Belmont, y un casero, debo agradecerle infinitamente la revisión cuidadosa y meticulosa de la introducción sobre el problema post-T Tauri del presente trabajo; a Ray Jayawardana; a James Muzerolle (Mr. Correlation) fanático como nosotros de Star Trek Next Generation y su “comander data”; y a Lori Allen, por ser tan dulce y por ilustrarnos con auténticas fotografías del HST cómo es en realidad el medio interestelar. A Youngung y a Chiang Won, por el placer de comer comida koreana.

Cómo no agradecer también a Remi Avila y Adriana Gazol, quienes me rescataban del “obsergvatug” las frías noches de noviembre en Niza, quienes intentaron enseñarme a comer quesos fuertes, aunque no aprendí mucho, por su apoyo solidario después que sufrió mi primer robo en el extranjero.

Al Instituto de Astronomía de la UNAM, por el apoyo brindado a lo largo de todos estos años a sus estudiantes; al personal que labora en él y en particular a aquellos que tienen que lidiar con nuestras eternas quejas computacionales: Alf, sin cuya valiosa colaboración la impresión de esta tesis hubiera salido muy chafa, Caramelito, Liliana y Gil, porque han sabido mantener la red en perfectas condiciones y a al usuario a raya. A todos los estudiantes e investigadores con quienes he compartido las clases, los seminarios y los coloquios. En particular, a Sangrita, excelente amiga, maravillosa tía de Sebastián, que espero siga dando las pláticas tan buenas como siempre. A Mayra Lebrón y Mayra Osorio, que lástima que se hayan ido a Morelia, porque acá la pasabamos muy bien. A Stan, Will, Jane, Lorenzo, Maru, Mau, Iqui, Eva, Anabel, Luis, Gerardo, Barbikius. A Carlos Román, mi exconcubulino; a Vale, que sigue siendo mi surrugatta preferida; a los Betos (Alberto, Vero, Alonso y Rodrigo), fieles e inseparables amigos. A Salvador Curiel, que de manera incondicional me invitó por vez primera a Boston. A Silvia Torres, Manuel Peimbert, Deborah Dultzin, Irene C-G. A Miriam Peña, por su incansable labor en la conducción de este posgrado, y a Bertha Vázquez, quien lleva los papeles de este posgrado de manera eficiente y agradable; Rafa Costero, quien de la manera más fina y elegante lo alburca a uno y aún así uno queda feliz; a Leti, que ha estado siempre muy al pendiente de Sebastián y quien debería patentar una marca de ropa y accesorios para bebés “Carigi”; a Pepe Franco, por sus chistes malos; y a Juanito y Marcelo, por esos maravillosos taquitos los fines de semana. A Juanita y Dieguito, Pedro el Vicentito e Irene V., Garcí-Garcí (juanmanuel), Doña Maru y Doña Lupita, y a todos los que se me están olvidando...

Al Armans, Deborah O., Carlos (sapito o charales) e Isa, con quienes he compartido una gran amistad, llantos de despecho, terapiadas con cerveza y sobre todo mucha risa. Y dentro del terreno de las terapiadas, cómo no, a Hector Socorro, que me ayudó a entenderme a mí mismo.

A mi familia Venezolana: Hebe (Almaviajera) y Santiago (Dr. Palermo), quienes nos han apoyado en todo, y quienes a pesar de estar lejos los llevo siempre muy cerca. A Diegucho, por esas maravillosas historias de aventuras en la selva amazónica rodeado de animales salvajes, cumbres borrascosas, ríos con pirañas, cascadas gigantescas, viajes en parapente y mujeres a sus pies (¿vahajoderalmaguevón?); a Mada, Ricardo, Cauchos Berna y familia, quienes saben que tienen reservado en exclusiva el penjaus de Coyoacán; a Bibi, Javier y Camilita, quienes nos deben una visita.

Por supuesto a mis hermanos: Güicho, fanático de rollos interminables pero noble y tierno (aunque él lo dude); Pepino, a quien extraño si pasa más de dos días sin hablarle; Silvia y Eduardón, que con su amor infinito a Sebastián nos han ido engañando poco a poco, haciéndonos creer que tenemos una necesidad compulsiva de llevarlo pa' su casa; Patricia y José Antonio, por su rica relación y para que se acuerden de hablarnos más seguido. A mi mamá y a mi papá, quienes con su tezón, cuidado, trabajo y cariño nos han hecho crecer, quererlos, y ser solidarios. Los quiero mucho.

A Paola, por el placer y la delicia de vivir contigo y de tener a Sebastián, y a Sebastián mismo, el chiquito más bonito, hablador, consentido, gordito, y maravilloso de este planeta. Gracias a los dos por hacerme tan feliz. Los adoro.

Índice General

| | |
|---|----|
| Agradecimientos | i |
| 1 Abstract | 1 |
| 2 Resumen | 3 |
| I Conceptos Introductorios | 5 |
| 3 Introducción | 7 |
| 3.1 Propiedades del Medio Interestelar | 7 |
| 3.2 Modelos del Medio Interestelar | 9 |
| 3.2.1 Formación de Nubes | 13 |
| 3.3 Objetivo y Plan de la Tesis | 17 |
| 4 Hidrodinámica y Teorema Virial Lagrangiano | 19 |
| 4.1 Conceptos de la Hidrodinámica | 19 |
| 4.1.1 Descripciones Lagrangiana y Euleriana | 19 |
| 4.1.2 Derivada material | 19 |
| 4.1.3 Ecuaciones de la MHD | 20 |
| 4.2 Teorema Virial | 21 |
| 4.2.1 Teorema Virial Lagrangiano | 22 |
| 4.3 Estabilidad y Flujo Magnético | 24 |
| 5 El Modelo y el Código Numérico | 31 |
| 5.1 Características | 31 |
| 5.2 Definición de las nubes en las simulaciones y cálculo de sus propiedades físicas y estadísticas | 33 |
| II Teorema Virial, Balance Energético y Relaciones de Escala | 35 |
| 6 Teorema Virial y Balance Energético | 37 |
| 6.1 Introducción | 37 |
| 6.2 Teorema Virial Euleriano | 37 |

| | | |
|------------|---|-----------|
| 6.3 | Consideraciones sobre el Análisis de McKee y Zweibel (1992) | 39 |
| 6.4 | El papel de los términos de superficie | 42 |
| 6.5 | Equilibrio Virial y Balance Energético | 45 |
| 6.6 | Trabajos Publicados al Respecto | 45 |
| 7 | Artículo 1 | 47 |
| | <i>Cloud Statistics in Numerical Simulations of the ISM</i> | 47 |
| 7.1 | Introduction | 48 |
| 7.2 | The Method | 48 |
| 7.3 | Results | 50 |
| 7.4 | Conclusions | 51 |
| 7.5 | Fé de Erratas: | 51 |
| 8 | Artículo2 | 53 |
| | <i>Virial Balance in Turbulent MHD Two Dimensional Numerical Simulations of the ISM</i> | 53 |
| 8.1 | Introduction | 54 |
| 8.2 | Virial Theorem in 2D | 54 |
| 8.3 | Preliminary Statistics | 55 |
| 8.4 | Final Remarks | 55 |
| 9 | Las Relaciones de Larson | 59 |
| 9.1 | Las Relaciones de Larson y Algunas de sus Implicaciones. | 59 |
| 9.2 | Trabajo Publicado al Respecto | 63 |
| 10 | Artículo 3 | 65 |
| | <i>A Search for Larson-Type Relations in Numerical Simulations of the ISM. Evidence for Non-Constant Column Densities</i> | 65 |
| 10.1 | Introduction | 66 |
| 10.2 | Numerical Method | 68 |
| 10.3 | Statistical Cloud Properties | 70 |
| 10.4 | Discussion | 74 |
| 10.4.1 | Applicability and limitations of the results | 74 |
| 10.4.2 | Implications of the results | 78 |
| 10.4.3 | Comparison with observations | 82 |
| 10.5 | Summary and Conclusions | 86 |
| 10.6 | Appendix | 88 |
| 11 | Dimensión Fractal y Autosimilaridad de las Nubes Interestelares | 93 |
| III | Formación de Nubes | 97 |
| 12 | Presentación | 99 |

| | |
|--|------------|
| 13 Artículo 4 | 101 |
| <i>Clouds as turbulent density fluctuations. Implications for pressure confinement and spectral line data interpretation</i> | |
| 13.1 Introduction | 103 |
| 13.2 Kinetic Terms in the Eulerian Virial Theorem | 105 |
| 13.3 Numerical Simulations | 106 |
| 13.4 Results and Discussion | 108 |
| 13.4.1 Density and velocity field topology | 108 |
| 13.4.2 Virial surface terms and pressure confinement | 114 |
| 13.4.3 Super- and sub-Alfvénic motions and magnetic field topology | 116 |
| 13.5 Comparison with observations. | 117 |
| 13.5.1 Comparison between observed spectral-line maps and mass-weighted velocity histograms | 117 |
| 13.5.2 Magnetic Field: alignment, advection and field reversals | 120 |
| 13.5.3 Lifetimes of turbulent clouds | 120 |
| 13.6 Discussion | 121 |
| 13.6.1 Applicability to molecular gas and the role of γ_{eff} | 121 |
| 13.6.2 Can hydrostatic structures form within turbulent clouds? | 122 |
| 13.6.3 Do molecular clouds have sharp boundaries? | 125 |
| 13.6.4 Effect of dimensionality | 126 |
| 13.7 Summary and conclusions | 127 |
| 13.8 Appendix A | 129 |
| 14 Introducción al Problema Post-T Tauri | 131 |
| 15 Artículo 5 | 137 |
| <i>Turbulent Flow-Driven Molecular Cloud Formation: A Solution to the Post-T Tauri Problem?</i> | |
| 15.1 Introduction | 138 |
| 15.2 Historical Context: The post-T Tauri problem | 140 |
| 15.3 Atomic and molecular gas: Maps and velocity-position diagrams | 143 |
| 15.4 Numerical Simulations | 151 |
| 15.4.1 The Model | 151 |
| 15.4.2 Results | 152 |
| 15.4.3 Comparison with Observations | 155 |
| 15.5 Discussion | 156 |
| 15.5.1 Evidence for Turbulent Compressions | 156 |
| 15.5.2 Limitations of the Model | 158 |
| 15.6 Summary | 159 |
| 16 Conclusiones | 161 |
| 17 Conclusions | 165 |

| | |
|---|------------|
| A Término Gravitacional en el Teorema Virial | 169 |
| B Teorema Virial en 2D | 171 |
| B.1 Término de Presión Térmica | 171 |
| B.2 Término Magnético | 172 |
| Bibliografía | 175 |

Capítulo 1

Abstract

The present work focuses on determining and understanding the physical and statistical properties of interstellar clouds, primarily employing numerical simulations of the turbulent ISM by Vázquez-Semadeni, Passot, & Pouquet (1995a, 1996); Passot, Vázquez-Semadeni y Pouquet (1995), and comparing the properties of the clouds arising in those simulations with observational data. The most important results are:

1. The clouds in the numerical simulations have comparable kinetic, magnetic and gravitational energies (Ballesteros-Paredes & Vázquez-Semadeni 1995) in spite of not being in equilibrium. Thus, energy equipartition does not necessarily imply virial equilibrium.
2. The clouds in the numerical simulations are not “virialized” (i.e., are not in virial equilibrium) (Ballesteros-Paredes & Vázquez-Semadeni 1997), but have in general non-zero values of the second time-derivative of their moment of inertia. In the simulations, the clouds are dynamical entities, changing their shapes and exchanging mass, energy and momentum with their surrounding medium.
3. The clouds in the numerical simulations reproduce the velocity dispersion-size relationship observed in real clouds (Larson 1981), but do not follow the mean density-size relationship. This result supports the suggestion that the former relationship may originate directly as a consequence of the energy spectrum of the turbulence, while the observational density-size relationship may be an artifact of sensitivity limitations of observational surveys (Vázquez-Semadeni, Ballesteros-Paredes & Rodríguez 1997).
4. The clouds in the numerical simulations also seem to reproduce the mass spectrum of the clouds (Vázquez-Semadeni, Ballesteros-Paredes & Rodríguez 1997).
5. Both super-Alfvénic and sub-Alfvénic velocities are found in the clouds in the numerical simulations (Ballesteros-Paredes, Vázquez-Semadeni & Scalo 1999), contrary to the standard assumption that motions within molecular clouds are sub-Alfvénic.

6. The clouds in the simulations do not have sharp boundaries. Instead, the density field is continuous and the velocity field does not show shocks at the edges of the clouds (Ballesteros-Paredes, Vázquez-Semadeni & Scalo 1999).
 7. The clouds in the simulations are turbulent density fluctuations, i.e., the density peaks are due to the advection of mass produced by the velocity field (Ballesteros-Paredes, Vázquez-Semadeni & Scalo 1999). It is also suggested that the apparently sharp boundaries of the interstellar clouds are due to a phase transition between the atomic and molecular regimes, as has been suggested by other authors (e.g., Blitz 1991).
 8. It is also predicted that the magnetic field must have reversals within clouds as a consequence of the advection of the magnetic field (Ballesteros-Paredes, Vázquez-Semadeni & Scalo 1999).
 9. For an effectively polytropic gas, gravitational collapse triggered by the external turbulence cannot be stopped unless the effective polytropic index γ_{eff} changes during the process. This may not occur until proto-stellar densities are reached (Ballesteros-Paredes, Vázquez-Semadeni & Scalo 1999).
 10. Cloud formation by larger-scale stream collisions may cause simultaneous compression along elongated regions, which, based only on their internal velocity dispersion, might appear to be causally disconnected. This process has been invoked as a possible solution of the so-called Post-T-Tauri problem in Ballesteros-Paredes, Hartmann & Vázquez-Semadeni (1999).
-

Capítulo 2

Resumen

El presente trabajo se ha enfocado a determinar y entender las propiedades físicas y estadísticas de las nubes interestelares, empleando fundamentalmente simulaciones numéricas del Medio Interestelar (ISM) utilizando el código de Vázquez-Semadeni, Passot & Pouquet (1995a, 1996); Passot, Vázquez-Semadeni y Pouquet (1995), y comparando las propiedades de las nubes de las simulaciones con datos observacionales. Los resultados más importantes pueden resumirse así:

1. Las nubes en las simulaciones numéricas tienen energía cinética, magnética y gravitacional similares (Ballesteros-Paredes & Vázquez-Semadeni 1995), aunque no estén en equilibrio. Entonces, la equipartición de la energía no necesariamente implica equilibrio virial.
2. Las nubes en las simulaciones numéricas no esán “virializadas” (es decir, no están en equilibrio virial) (Ballesteros-Paredes & Vázquez-Semadeni 1997). Por el contrario, tienen valores no nulos de la segunda derivada del momento de inercia. En las simulaciones, las nubes son entidades dinámicas, cambiando su forma e intercambiando masa, energía y momento con el medio que las rodea.
3. Las nubes en las simulaciones numéricas reproducen la relación dispersión de velocidades-tamaño observada para nubes reales (Larson 1981), pero no siguen la relación densidad media-tamaño. Este resultado confirma la sugerencia de que la primera relación puede ser consecuencia del espectro de energías de la turbulencia, mientras que la relación observacional densidad media-tamaño puede ser una consecuencia de las limitaciones en sensitividad de los censos observacionales (Vázquez-Semadeni, Ballesteros-Paredes & Rodríguez 1997).
4. Las nubes en las simulaciones numéricas reproducen el espectro de masas de las nubes observadas (Vázquez-Semadeni, Ballesteros-Paredes & Rodríguez 1997).
5. Las nubes en las simulaciones numéricas presentan tanto velocidades super- como sub-alfvénicas (Ballesteros-Paredes, Vázquez-Semadeni & Scalo 1999), contrario a la suposición estándar de que los movimientos dentro de las nubes moleculares son sub-alfvénicos.

6. Las nubes en las simulaciones no presentan fronteras abruptas. Por el contrario, el campo de densidad es continuo y el campo de velocidad no presenta choques en las orillas de las nubes (Ballesteros-Paredes, Vázquez-Semadeni & Scalo 1999).
7. Las nubes en las simulaciones son fluctuaciones del campo turbulento de densidad, es decir, son producto de la advección de masa por el campo de velocidad (Ballesteros-Paredes, Vázquez-Semadeni & Scalo 1999). Se sugiere también que, observationalmente, las fronteras abruptas de las nubes interestelares se deben a una transición de fase entre los regímenes atómico y molecular, como ha sido sugerido previamente por otros autores (Blitz 1991). Se predice también que el campo magnético debe presentar inversiones (*reversals*) dentro de las nubes, como consecuencia de la advección del campo magnético por el campo de velocidades.
8. Para un gas efectivamente politrópico, el colapso gravitacional desatado por la turbulencia externa no puede ser detenido a menos que el índice politrópico γ_{eff} cambie durante el proceso. Sin embargo, esto no ocurre hasta que no se alcanzan densidades protoestelares (Ballesteros-Paredes, Vázquez-Semadeni & Scalo 1999).
9. La formación de nubes mediante colisiones puede causar compresión simultánea a lo largo de regiones elongadas, las cuales, basándose únicamente en su dispersión de velocidades interna, pueden aparecer causalmente desconectadas. Este proceso ha sido invocado como una posible solución al denominado problema Post-T Tauri (Ballesteros-Paredes, Hartmann & Vázquez-Semadeni 1999).

Parte I

Conceptos Introductorios

FALTA PAGINA

No. 6

Capítulo 3

Introducción

La presente tesis es un estudio de las propiedades físicas y estadísticas de las nubes en el medio interestelar (MI o ISM, por sus siglas en inglés), de manera que es conveniente hacer un breve resumen de sus características observacionales, de las propiedades inferidas a partir de las observaciones, de los mecanismos de inyección y disipación de energía, así como de los modelos propuestos para explicar la estructura y el comportamiento del MI.

3.1 Propiedades del Medio Interestelar

La información que tenemos acerca del MI se basa principalmente en la absorción, emisión o dispersión de radiación por átomos, moléculas y/o granos de polvo. A través de esta información se detecta al gas en el medio interestelar en alguna de las siguientes formas: gas ionizado “caliente” ($T \gtrsim 10^6$ K), gas ionizado “tibio” ($T \sim 8 \times 10^3$ K), gas neutro “tibio” ($T \sim 6 \times 10^3$ K), gas neutro frío ($T \sim 10^2$ K) y nubes moleculares ($T \sim 10$ K), aunque en realidad es probable que exista un continuo de densidades y temperaturas.

La existencia de gas con temperaturas de $\geq 10^6$ K y densidades $\leq 0.01\text{cm}^{-3}$ fue predicha por Spitzer (1956) y ha sido confirmada alrededor de remanentes de supernovas. Ha sido propuesto que esta componente domina en volumen al medio interestelar (McKee & Ostriker 1977), aunque este hecho ha sido cuestionado recientemente por Cox (1995) y por Slavin y Cox (1993, ver §3.2). Por su parte, las regiones fotoionizadas se encuentran frecuentemente en las vecindades de las estrellas OB (regiones H II), y en las vecindades de estrellas viejas (nebulosas planetarias) donde la intensidad de la radiación ultravioleta, capaz de ionizar el hidrógeno, es importante. Adicionalmente, lejos de las estrellas O y B, existe una radiación difusa ultravioleta capaz de ionizar al medio menos denso. Las densidades de este medio son del orden de 0.03 cm^{-3} , y las temperaturas determinadas a partir de cocientes de líneas varían entre 7.000 y 10.000 K. A esta componente se le conoce como el medio ionizado tibio.

Por su parte, el medio neutro tibio, con temperaturas de $T \sim 6,000$ K, y densidades alrededor de 0.1 cm^{-3} , ha sido detectado mediante líneas de absorción ultravioleta y de H I (ver por ej., Spitzer 1978 y referencias ahí citadas).

El gas neutro frío, por su parte, ha sido detectado principalmente mediante la radiación

de 21 centímetros de los átomos de hidrógeno. Como se ve en la Tabla 3.1, la densidad característica para este gas es de 1 cm^{-3} en la vecindad solar, y la escala de altura del disco galáctico en H I es de aproximadamente 250 pc (Spitzer 1978). Las temperaturas características oscilan alrededor de 80 K.

Finalmente, las nubes moleculares poseen densidades altas ($\geq 10^2 \text{ cm}^{-3}$) y temperaturas bajas ($\sim 10 \text{ K}$). Se observan principalmente a través del ^{12}CO , ya que la molécula más abundante, la de H_2 , tiene momento dipolar nulo, lo que dificulta mucho su detección en aquellas regiones que no son calentadas por choques o por radiación UV, que harían que el H_2 emita en transiciones vibrarotacionales. Por su parte, las regiones más densas de las nubes moleculares (núcleos o *cores*) se detectan en NH_3 , CS e isótopos de CO menos abundantes, como el ^{13}CO y el C^{18}O . El principal mecanismo de calentamiento de esta componente son los rayos cósmicos, capaces de penetrar las altas extinciones que hay hacia el interior de las nubes moleculares. En general, se considera que estas regiones tienen temperatura aproximadamente constante, aunque existe evidencia de que en la vecindad de regiones de formación estelar hay importantes desviaciones producidas por el calentamiento de las estrellas (Torrelles et al. 1983, Solomon et al. 1985, Alves et al. 1999).

Propiedades generales del MI

| Componente | $\langle n \rangle [\text{cm}^{-3}]$ | $\langle T \rangle [\text{K}]$ | $\langle P/k \rangle [\text{din cm}^{-2}]$ | Tamaño típico |
|-----------------------------|--------------------------------------|--------------------------------|--|-----------------------|
| Gas Coronal | ~ 0.01 | $\geq 10^5$ | $\sim 10^3$ | ? |
| Regiones HII | ≥ 1 | 8000 | $\geq 7 \times 10^5$ | $\sim 1 \text{ pc}$ |
| Medio Internube Ionizado | ~ 0.1 | 8000 | $\sim 10^3$ | $> \text{decenas pc}$ |
| Nubes Difusas Neutras (H I) | 1-20 | 80 | $\sim 10^3$ | varias decenas de pc |
| Nubes Moleculares Gigantes | $10 - 10^2$ | 10 - 50 | $\sim 10^5 10^4$ | decenas de pc |
| Nubes Moleculares | $10^3 - 10^4$ | 10 - 50 | $\sim 10^{-5} 10^{-4}$ | 1-20 pc |
| Núcleos Densos | $10^4 - 10^6$ | 10 | | $< 1 \text{ pc}$ |

TABLA 3.1: Detalles sobre el origen de estas propiedades puede verse en Spitzer 1978; Blitz 1994; Plume et al. 1997; y referencias ahí citadas.

Adicionalmente, el medio interestelar está permeado por el campo magnético y por rayos cósmicos. Los valores del campo magnético oscilan desde unos cuantos μGauss hasta varios mG, y además de ejercer un efecto dinámico a través de la fuerza de Lorenz, permite la alineación de granos de polvo interestelar, lo cual da lugar a la polarización de la luz. Los rayos cósmicos, por su parte, son partículas energéticas, principalmente protones a velocidades relativistas que parecen permear de manera uniforme el medio interestelar.

Usando la medida de emisión $\text{EM} \equiv \int_0^L n_e dl$, junto con la medida de dispersión, $\text{DM} \equiv \int_0^L n_e dl$ y la medida de rotación, $\text{RM} \propto \int n_e B_{||} dl$, ha sido posible encontrar que el medio interestelar presenta importantes fluctuaciones tanto en la densidad electrónica como en el campo magnético del medio ionizado (Tufte et al. 1999; Cordes 1999 y referencias ahí citadas). Por otra parte, mediciones de los anchos de las líneas H α y H I han mostrado que los movimientos en el medio interestelar son supersónicos en general. McCray & Snow (1979), resumen una serie de trabajos observacionales en todas las frecuencias, mostrando que el medio interestelar es altamente dinámico, con componentes que presentan velocida-

des que van desde varios cientos o miles de km s^{-1} en regiones cercanas a estrellas masivas o supernovas, hasta el H I que si bien presenta una dispersión de velocidades característica de $\sim 8 \text{ km s}^{-1}$, posee también componentes con velocidades de varias decenas de km s^{-1} , evidenciando la presencia de procesos altamente energéticos y de choques intensos.

3.2 Modelos del Medio Interestelar

Una de las hipótesis subyacentes en los primeros modelos del MI queda plasmada en la frase de Spitzer (1978, §11.3) “las ecuaciones de la hidrodinámica tienden hacia el equilibrio de presión” (térmica). Un importante modelo del medio interestelar fue presentado por Field, Goldsmith y Habing (1969), y es conocido como el “modelo de dos fases”. Este se basaba en el cálculo detallado del calentamiento del MI mediante rayos cósmicos de baja energía. Field et al. (1969) encontraron la existencia de dos fases en equilibrio de presión. Una “caliente”, a $T \sim 10,000 \text{ K}$, y una “fría” ($T \leq 300 \text{ K}$). Adicionalmente, predijeron la existencia de una tercera fase, con temperaturas de $T \sim 5000 \text{ K}$, térmicamente inestable, que no puede existir por más de $\sim 10^6$ años. En su modelo, Field et al. (1969) encontraron que la fase fría debía contener aproximadamente el 75% de la masa del gas, y estar distribuida alrededor del plano central del disco, ocupando pequeñas fracciones del volumen total. Sin embargo, el modelo de Field et al. (1969) tenía problemas para predecir algunas líneas de absorción en el ultravioleta (McCray & Snow 1979), y tampoco predecía la existencia de una fase mucho más caliente, con temperaturas del orden de 10^5 K (McKee & Ostriker 1977).

Cox y Smith (1974) consideraron la emisión de rayos X suaves en el plano galáctico, y propusieron que el MI consiste en una serie de agujeros y túneles interconectando estos agujeros, como producto de la explosión de supernovas. Estos espacios deberían tener temperaturas de $\geq 10^5 \text{ K}$, y sería ahí donde se produciría la absorción de O VI observada. Sin embargo, Shapiro & Field (1976) mostraron que esta interpretación requería una presión interestelar poco realista, y propusieron que la absorción de O VI debía provenir solamente de las paredes de dichos túneles.

Posteriormente, McKee & Ostriker (1977) plantearon que el modelo de dos fases no podía ser mantenido dada la tasa observada de supernovas en el MI. Ellos postularon un medio dominado por explosiones de supernovas, encontrando que éste desarrolla tres fases en equilibrio de presión: La fase caliente o coronal, con temperaturas $\geq 10^5 \text{ K}$ y densidades de 10^{-2} cm^{-3} , ocupa la mayor parte del volumen (70% - 80%), y es moderadamente inhomogénea; el medio tibio, con temperaturas del orden de los 8.000 K, y que contiene a su vez dos regímenes: el neutro y el ionizado, ocupa aproximadamente el 20% del volumen total. Finalmente, el medio frío, denso, con densidades de 10^{-3} cm^{-3} , temperaturas de 80 K y factores de llenado de unos cuantos por cientos. Evidencia al respecto fueron las observaciones de O VI en el ultravioleta, y observaciones de emisión en rayos X, indicando la existencia de la fase coronal. Adicionalmente, McKee & Ostriker (1977) plantean un ciclo estacionario de flujo de masa entre las fases, donde las nubes se evaporan por la radiación, y el gas coronal, a su vez, se condensa gracias a la acción de barrido de la onda de choque de las supernovas.

Recientemente el modelo de las tres fases ha recibido serios cuestionamientos. Ob-

servaciones en UV recientes han revelado la presencia de gradientes de presión (térmica) importantes en el medio interestelar local (Bowyer et al. 1995; Cox 1995), y simulaciones numéricas han estudiado la evolución de burbujas remanentes de supernova en simulaciones numéricas, encontrando que la fase de gas caliente a temperaturas de 10^5 K no necesariamente tiene factores de llenado grandes (Slavin & Cox 1993), como plantearon originalmente McKee y Ostriker (1977).

Por su parte, desde hace ya medio siglo se ha sugerido que el MI es altamente turbulento (e.g., von Weizsäcker 1951), y que posee estructuras complejas que no deben modelarse como esferoides discretos en equilibrio hidrostático (Chandrasekhar & Münch 1952; Nakano 1998, Ballesteros-Paredes et al. 1999a). Por “turbulencia” entendemos el estado de un flujo caracterizado por grandes fluctuaciones desordenadas en la velocidad, frecuentemente estructuradas de manera anidada o jerárquica. Existen actualmente varias evidencias de que el MI puede considerarse turbulento, como señala Scalo (1987): i) la fuerte no-linealidad de las ecuaciones de la magnetohidrodinámica con las que representamos el ISM; ii) el acoplamiento no-lineal de los procesos físicos relevantes; iii) la existencia de fluctuaciones de densidad, velocidad, y presión, cubriendo un amplio intervalo de escalas; iv) la estructura jerárquica de las nubes (Scalo 1985), v) la existencia de relaciones de escala con forma de leyes de potencia, por ejemplo, entre la dispersión de velocidades y el tamaño, en un rango de escalas de varios órdenes de magnitud (Larson 1981, Torrelles et al. 1983; Myers 1983, Dame et al. 1986, Scalo 1990, Falgarone et al. 1991); vi) la existencia de movimientos supersónicos en el MI (McCray & Snow 1979; Larson 1981, Blitz 1993); vii) el ancho no-térmico de los perfiles de línea observados en las nubes interestelares, explicados en términos de turbulencia a pequeña escala por Zukerman & Evans (1974); viii) La existencia de nubes con evidencia de vorticidad (ver, por ejemplo, Arquilla & Goldsmith 1985; Miville-Deschéne et al. 1998); ix) el espectro de masas en ley de potencia para las nubes moleculares (Larson 1981, Dame et al. 1986, Williams et al. 1995) x) la existencia de mecanismos de alimentación de energía en todas las escalas (Scalo 1987; Norman & Ferrara 1996); xi) la apariencia fractal de las nubes interestelares (Scalo 1990; Falgarone et al. 1991, entre otros).

Adicionalmente, existe un parámetro adimensional, llamado el Número de Reynolds

$$\mathcal{R} \equiv \frac{ul}{\nu} \quad (3.1)$$

(donde ν es la viscosidad cinemática, en unidades de $\text{cm}^{-2} \text{ seg}^{-1}$, y u es la velocidad característica de la escala l), el cual mide el cociente entre los términos advecutivo y viscoso en la ecuación de momento (4.7), cuantificando qué tan turbulento es un flujo dado. Esta transición se da cuando \mathcal{R} excede cierto valor crítico. En fluidos terrestres, la turbulencia (incompresible) se da para números de Reynolds del orden de algunas veces 10^3 . Sin embargo, en el medio interestelar, Scalo (1987) estima

$$\mathcal{R} \sim 3 \times 10^7 \left(\frac{u}{\text{km s}^{-1}} \right) \left(\frac{l}{\text{pc}} \right) \left(\frac{n}{10^3 \text{cm}^{-3}} \right) \quad (3.2)$$

mientras que Combes (1999) da valores de $\sim 10^9$. De cualquier manera, es claro que, para valores típicos del MI, los números de Reynolds son varios órdenes de magnitud mayores

que los correspondientes a los números de Reynolds de fluidos terrestres, y por ende, es de esperar que el medio interestelar sea turbulento.

Como se ha mencionado previamente, el MI es altamente compresible: presenta grandes fluctuaciones de densidad a todas las escalas, y los números de Mach correspondientes a las fluctuaciones de velocidad son supersónicas (Scalo 1987). Incluso, recientes trabajos teóricos proponen que dichas fluctuaciones son incluso superalfvénicas (Ballesteros-Paredes et al. 1999a; Padoan & Nordlund 1999). Entonces, es de esperar que ocurran ondas de choque en todas las escalas (por ejemplo, jets y vientos estelares, expansión de regiones H II, explosiones de supernovas, ondas de densidad espiral, etc.).

Mientras que en la teoría de Kolmogorov (1941) para turbulencia incompresible se supone que la energía es inyectada en las escalas grandes y de ahí se transfiere a escalas más pequeñas mediante una cascada de energía para ser disipada, en el MI la energía es probablemente inyectada a todas las escalas (ver, e.g., Scalo 1987, Norman & Ferrara 1996). Por ejemplo, la rotación diferencial Galáctica, las superburbujas y la onda de densidad espiral pueden inyectar energía al MI en escalas del orden de 1 kpc (Fleck 1981), aunque se cree que la primera es una fuente muy ineficiente (Shu et al. 1987); otras fuentes operan a escalas intermedias (del orden de 100 pc), tales como regiones H II en expansión y explosiones de supernova; y otras más a pequeña escala (de entre unas pocas décimas de parsec, hasta unos cuantos parsecs), como vientos estelares y flujos bipolares. Estos mecanismos son fuentes importantes de energía cinética.

Toda esta evidencia sugiere entonces que el medio interestelar es muy dinámico y turbulento, con un fuerte acoplamiento dinámico entre las diferentes escalas, de manera que para desarrollar un modelo del MI realista es necesario realizar simulaciones numéricas capaces de incluir los principales agentes físicos que operan en el MI, donde se resuelvan las ecuaciones de la magnetohidrodinámica de manera no-lineal, incorporando el transporte radiativo, la química, el grado de ionización, etc. Dado el enorme costo computacional, sin embargo, en la actualidad un nivel descriptivo intermedio incluye la magneto-hidrodinámica (MHD) y términos modelo para las fuentes y sumideros. Uno de los trabajos pioneros es el de Bania & Lyon (1980), quienes estudiaron los efectos de estrellas OB en el MI usando simulaciones numéricas 2D que incluían el balance térmico entre el calentamiento de rayos cósmicos y de rayos X de baja energía, y el enfriamiento¹, tomado de Dalgarno & McCray (1972). En su modelo, Bania & Lyon (1980) localizaban las estrellas de manera aleatoria en un espacio que representaba 180^2 pc con resoluciones de 40^2 pixeles. Con las limitaciones computacionales de la época, Bania & Lyon (1980) encontraron importantes conclusiones: primeramente, que el medio es altamente dinámico, ya que las regiones H II producidas por las estrellas OB, en su expansión sobre el medio circundante, pueden aglomerar el gas, encontrando que hasta el 70% de la masa total puede ser aglomerada en estas nubes, las cuales, a su vez, podrían colapsar gravitacionalmente. Adicionalmente, encontraron que son precisamente los efectos dinámicos de las estrellas las que producen las nubes, y no los encuentros entre nubes menores, sugiriendo que la confluencia de corrientes de material podría ser un mecanismo más eficiente para formar nubes que la aglomeración, mecanismo

¹Es importante recalcar que los autores le llaman a este modelo "transporte radiativo implícito", aunque, estrictamente hablando, no resuelven el transporte radiativo.

de formación de nubes que en los años 80's era favorecido. Sin embargo, estas simulaciones carecían de campos magnéticos y gravedad, y eran de baja resolución, lo cual dificulta el estudio de los efectos de un campo turbulento sobre un intervalo considerable de escalas.

Por su parte, Passot, Pouquet y Woodward (1988), Léorat, Passot y Pouquet (1990) y Pouquet, Passot & Léorat (1991) presentaron simulaciones numéricas hidrodinámicas y magnetohidrodinámicas en 2 dimensiones con resoluciones de hasta 512^2 , compresibles y con autogravedad, las cuales les permitieron estudiar el comportamiento turbulento del medio interestelar y la influencia de la turbulencia en el soporte en contra del colapso. Las escalas de interés en dichas simulaciones eran menores a 10 pc. A diferencia del trabajo de Bania y Lyon (1980), dichas simulaciones no incluían calentamiento estelar, ni el enfriamiento radiativo. En el primer trabajo, Passot et al. (1988) encontraron que en sus simulaciones, con números de Mach del orden de la unidad, se desarrollan espectros del tipo k^{-2} , sugiriendo que las relaciones de escala (en particular, Δv vs l) tienen un origen turbulento, como en el caso de un espectro de Kolmogorov para turbulencia incompresible, y que el campo de densidad desarrollaba estructuras filamentarias compatibles con las observaciones de nubes moleculares. Adicionalmente, Léorat et al. (1990) encontraron que tanto a grandes como a pequeñas escalas la autogravedad juega un papel importante para determinar la coherencia de las estructuras, mientras que en escalas intermedias, la hidrodinámica parece ser suficiente para describir la evolución del medio en escalas de tiempo más cortas que los tiempos de caída libre de las estructuras. Asimismo, Léorat et al. (1990) encuentran que la componente compresiva del campo de velocidades puede modificar el criterio de Jeans, ya que esta componente es capaz de jugar el papel de las ondas acústicas e inhibir el colapso gravitacional, sugiriendo que éste puede ser un mecanismo para dar soporte a las nubes, y explicando entonces el hecho de que las nubes moleculares tienen tiempos de vida mucho mayores que su tiempo de caída libre.

Motivados por entender el comportamiento no-lineal de las estructuras y los mecanismos de formación de nubes, y el estudio de la turbulencia compresible en presencia de parámetros con valores típicos del MI, Vázquez-Semadeni, Passot & Pouquet (1995a, 1996), y Passot, Vázquez-Semadeni & Pouquet (1995) ampliaron el código de Léorat et al. (1991) a fin de incluir el calentamiento estelar, la autogravedad, el campo magnético, la rotación galáctica, y una parametrización para la rotación diferencial, así como para la formación y el efecto de las estrellas, bajo un régimen completamente no lineal, compresible, y con escalas características entre 1 y 1000 pc.

Estas simulaciones reproducen algunas propiedades observadas o predichas para el medio interestelar. Por ejemplo, reproducen el comportamiento predicho por la teoría lineal para la formación de nubes (Elmegreen 1991), la tasa de formación estelar para estrellas masivas, la densidad promedio de complejos gigantes de nubes, la intensidad del campo magnético oscilando entre casi 0 y algunas decenas de μG y la dispersión de velocidades del MI a escalas de ~ 1 kpc.

Actualmente existen otros estudios numéricos que intentan estudiar el comportamiento general del MI: Ostriker, Gammie & Stone (1999), Mac Low et al. (1999), Padoan & Nordlund (1999), Balsara et al. (1999), que, a diferencia de las simulaciones de Vázquez-Semadeni et. al, se han enfocado al comportamiento de las nubes moleculares, es decir, a

medios con temperaturas bajas (10 K), y densidades altas ($\sim 10^3 \text{ cm}^{-3}$) bajo un régimen isotérmico y con forzamiento aleatorio. Estos trabajos se han dirigido a determinar las tasas de disipación de la turbulencia, encontrando que en ausencia de inyección de energía, la turbulencia puede disiparse en escalas de tiempo comparables con el tiempo de caída libre de las nubes. Estos resultados, entonces, dejan abierta la incógnita de las escalas de tiempo de vida de las nubes, ya que si la turbulencia se disipa rápidamente, entonces es difícil concebir que los tiempos de vida de éstas sean del orden de varias veces 10^7 años, como sugieren, e.g., Blitz & Shu (1980).

Sin embargo, para los propósitos del presente trabajo, son preferibles las simulaciones del MI “multifase” por las siguientes razones: por un lado, se modelan regiones mayores, permitiendo estudiar el papel de las escalas grandes ($\geq 100 \text{ pc}$) de la turbulencia para formar y deformar las estructuras más pequeñas (nubes). Por el otro, dado que la energía es inyectada puntualmente en las regiones donde la densidad alcanza un valor crítico, permite estudiar la evolución de un medio donde la energía se inyecta de manera más realista.

El presente trabajo ha sido enfocado al estudio de las propiedades físicas y estadísticas de las nubes en las simulaciones de Vázquez-Semadeni et al. (1995). Por un lado, hemos estudiado el comportamiento de las energías en cada una de las nubes. Por otro lado, hemos calculado el balance virial detallado para éstas, así como la variación de cantidades como la dispersión de velocidades, la densidad promedio como función de la escala característica de las nubes, la dimensión fractal de éstas, y el espectro de masas. Para esto fue necesario desarrollar un algoritmo sencillo que permitiera la identificación de nubes en estas simulaciones.

Por otra parte, como consecuencia de estos estudios se hizo evidente que la turbulencia a gran escala jugaba un papel importante en la formación y deformación de las estructuras de densidad y en la inducción/prevención del colapso gravitacional. Hacemos entonces un breve resumen sobre el estatus de las teorías de formación de nubes.

3.2.1 Formación de Nubes

Un problema fundamental en la comprensión del MI y de la formación estelar es el de la formación de nubes, proceso que probablemente involucra varios mecanismos (Elmegreen 1987; Elmegreen 1994), incluyendo el paso de ondas de densidad espiral y las inestabilidades a gran escala (Elmegreen 1993a; Gammie 1996; Martos & Cox 1998) operando preferentemente en la formación de estructuras grandes, así como en la producción de condensaciones más pequeñas y densas en las regiones de interacción de flujos convergentes (Elmegreen & Elmegreen 1978; Vishniac 1983; Hunter et al. 1986; Vázquez-Semadeni et al. 1995a; Vázquez-Semadeni et al. 1995b; Ballesteros-Paredes et al. 1999b; Martos et al. 1999). Estos últimos procesos pueden ser ocasionados por el efecto de un evento específico, como es el caso de una SN o una región H II, en cuyo caso la morfología de la región puede sugerir cuál ha sido el origen de dichos movimientos (por ejemplo, el anillo de λ Ori), o simplemente por la turbulencia interestelar global (§15).

Los principales procesos de formación de nubes considerados a la fecha son: acumu-

lación de material en filamentos mediante choques, coagulación de nubes más pequeñas para formar estructuras mayores, inestabilidades y turbulencia. A continuación describimos brevemente los principales modelos y escenarios correspondientes a cada uno de estos procesos.

Acumulación de material en filamentos mediante choques.- La evidencia observacional que sugiere la existencia de este proceso son las estructuras filamentarias observadas en el medio interestelar, el aparente alineamiento del campo magnético con las estructuras filamentarias, y el incremento de la intensidad de estos campos magnéticos (Troland & Heiles 1982). Ejemplos de las primeras son las muchas estructuras filamentarias que pueden verse en los mapas de H I (ver Fig. 3.1). En particular, el North Polar Loop ($l \sim 135^\circ$, $b \sim 40^\circ$, $-10 \text{ km s}^{-1} \leq v \leq +10 \text{ km s}^{-1}$), que consiste en un gran arco de H I, el cual contiene a su vez varias condensaciones de gas molecular. La explicación convencional para estos mecanismos son explosiones de supernova (ver, por ejemplo, Pound & Goodman 1997), o la presencia de asociaciones OB cercanas, aunque estructuras similares han sido explicadas como la colisión de gas de alta velocidad con el disco galáctico (Santillán 1999 y referencias ahí citadas).

Coagulación.- Oort (1954) propuso que los grandes complejos de nubes interestelares se formaban mediante la colisión y coagulación de nubes pequeñas interactuando gravitacionalmente. La importancia de estos modelos aumentó a raíz de la observación de una alta fracción molecular en los 5 kpc internos del disco Galáctico (Scoville & Solomon 1975; Burton et al. 1975), pues implicaba que una proporción importante del gas debía estar en forma de nubes moleculares, las cuales se consideraban fuertemente autogravitantes. Algunos de los puntos fuertes de este modelo (ver, e.g., Elmegreen 1987) consisten en que la tasa de formación de nubes aumenta en regiones donde el gas converge, como es el caso de los brazos espirales, explicando los tamaños relativamente grandes de las nubes en los brazos espirales, comparadas con el tamaño de las nubes que no se encuentran en los brazos. Sin embargo, el medio interestelar consiste en un fluido continuo (y más aún si se considera el efecto dinámico del campo magnético), en el que el movimiento de las parcelas no puede considerarse como balístico, y la densidad no necesariamente presenta saltos abruptos entre la región interna y la externa a la nube, como es el caso en los modelos de coagulación. Otro problema importante con este modelo es que la generación de complejos grandes, con masas de entre 10^5 y $10^6 M_\odot$ requiere de tiempos extremadamente largos, del orden de algunas veces 10^8 años (ver, e.g., Kwan 1979).

Inestabilidades.- Varias inestabilidades han sido sugeridas como mecanismos de formación de nubes. Las más comunes son la gravitacional, la térmica y la de Parker. La inestabilidad gravitacional (Jeans 1902), proviene del balance de fuerzas entre el gradiente de presión y la autogravedad de la nube. Dado un medio infinito de densidad uniforme ρ_0 sometido a una perturbación de tamaño λ , existe una longitud L_J tal que si $\lambda > L_J$ la perturbación comienza a colapsarse, pues el valor absoluto de su energía gravitacional supera al de su energía interna al menos inicialmente. La formación de nubes mediante la inestabilidad gravitacional fue considerada factible cuando se descubrieron los grandes complejos de nubes en otras galaxias, con masas ($M \sim 10^5 M_\odot$) y tamaños similares ($L \sim 300 \text{ pc}$) a los de Jeans (Wright et al. 1972).

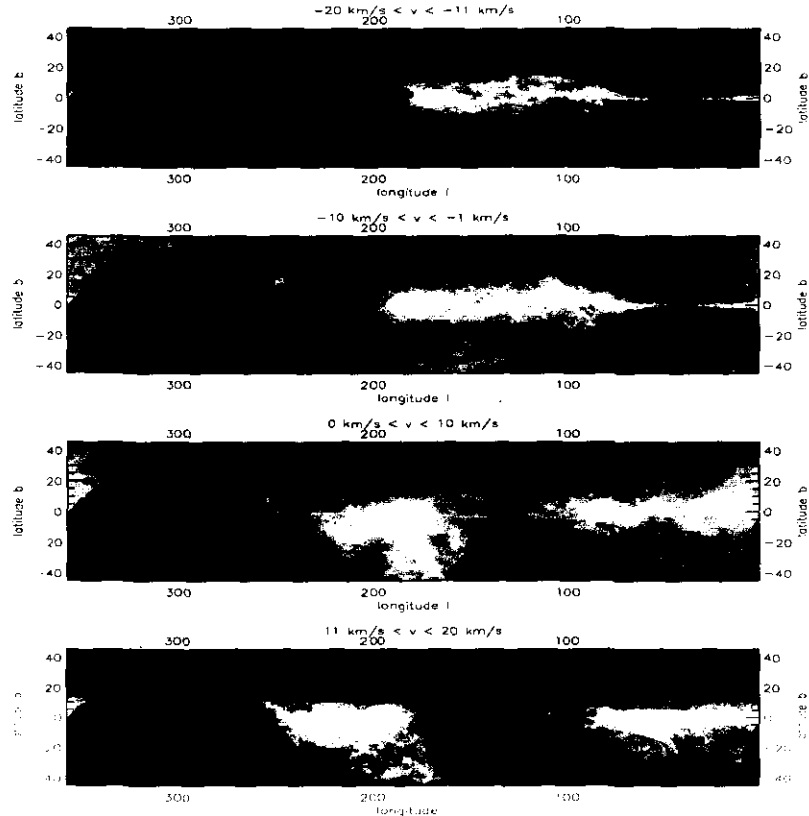


FIGURA 3.1: Mapa de la Galaxia en H I (21 cm). Datos del Atlas de Hidrógeno Neutro de la Galaxia (Hartmann & Burton 1997). Nótese la alta filamentariedad de las estructuras en H I. En particular, se cree que la estructura en ($l \sim 135^\circ$, $b \sim 40^\circ$, $-10 \text{ km s}^{-1} \leq v \leq +10 \text{ km s}^{-1}$) es el resultado de una explosión de supernova (Pound & Goodman (1997).

La inestabilidad térmica fue usada para explicar la existencia de dos o tres fases en el MI (Field et al. 1969; McKee & Ostriker 1977), pues dichas fases en equilibrio de presión a temperaturas muy diferentes son estables, separadas por un intervalo inestable de temperaturas. Por su parte, el estudio de la inestabilidad de Parker (1966) en dos dimensiones ha permitido explicar la existencia de grandes complejos moleculares en el plano medio del disco Galáctico, separados a distancias del orden de 1 kpc, como consecuencia de que, frente a alguna perturbación, las líneas de campo magnético originalmente paralelas al plano del disco galáctico, se inclinan, permitiendo al material del disco caer hacia el plano medio. Sin embargo, el estudio de la inestabilidad de Parker en tres dimensiones parece indicar que en realidad éste podría no ser un buen mecanismo para explicar la existencia de grandes complejos en el plano medio (Asseo et al. 1978, 1980; véase también Shu 1992, §23).

Turbulencia.- Recientemente se ha reconocido a la turbulencia como un agente capaz de formar nubes, aunque tradicionalmente se le había considerado únicamente como un mecanismo de soporte. En un trabajo pionero, Sasaki (1973) estudió la turbulencia homogénea, compresible e isotrópica, encontrando que si la mayor parte de la energía turbulenta se encuentra en los modos de escalas mayores a la longitud de Jeans, la turbulencia es capaz de generar fluctuaciones de densidad que contribuyen al colapso gravitacional. Por su parte, Elmegreen (1993b) encuentra que la turbulencia supersónica en nubes autogravitantes y difusas es capaz de producir estructuras de densidad autosimilares con líneas anchas en un intervalo amplio de escalas, y plantea que si la región comprimida está dentro de una región densa, ésta puede colapsar, mientras que si la región está dentro de una nube difusa, la turbulencia es capaz de dispersarla.

La capacidad para colapsar de una región que ha sufrido el efecto de una compresión turbulenta depende de las energías gravitacional, magnética, interna, etc., disponibles en el material, así como de la tasa de cambio de éstas durante la compresión y posterior colapso. Considerando únicamente el soporte térmico, es posible calcular si la energía interna es capaz de soportar a la nube contra su propia gravedad. Como fue demostrado por Chandrasekhar (1961), una región esférica puede ser soportada por presión si $\gamma_{\text{eff}} > 4/3$, donde γ_{eff} es el índice barotrópico, i.e., $P \propto \rho^{\gamma_{\text{eff}}}$. El número de Mach necesario para inducir el colapso gravitacional como función de γ_{eff} fue calculado por Tohline et al. (1987). En el caso en que la compresión sea a lo largo de varias direcciones simultáneamente, $\gamma_{\text{eff}} > 2(1 - 1/n)$ (con n el número de direcciones a lo largo de las cuales se efectúa la compresión², $1 \leq n \leq 3$) es la condición para el exponente politrópico para el cual la región no colapsará (McKee et al. 1993; Vázquez-Semadeni et al. 1996). Entonces, es plausible el colapso de regiones que han sido comprimidas mediante flujos convergentes de gas, a menos de que γ_{eff} aumente en el proceso (Ballesteros-Paredes et al. 1999a).

Tradicionalmente, el estudio del colapso gravitacional hacia la formación estelar se ha hecho mediante el Teorema Virial, postulando que las estructuras están en equilibrio hidrostático entre la autogravidad y la presión hidromagnética, y que “resbalan” quasi-estáticamente por difusión ambipolar (ver por ej., Shu 1992; Hartmann 1998). De dicho teorema se ha derivado el valor de la masa crítica que puede ser sostenida por la energía interna en contra del colapso gravitacional. Además, dado que el teorema virial permite relacionar de manera particular los valores de las diferentes energías involucradas en los procesos físicos, así como relacionar valores observables como la dispersión de velocidades en una línea particular, con la masa de la región emisora, es frecuente encontrar en la literatura referencias al teorema virial y al estado de virialización de las nubes. Sin embargo, para estudiarlo es necesario primero escribir las ecuaciones de la magneto-hidrodinámica (MHD), pues es de la ecuación de momento de donde sale este teorema. Entonces, la discusión sobre la masa crítica, el problema del flujo magnético en el colapso gravitacional, y resultados clásicos que se obtienen del teorema virial será diferida a la sección 4.2.

²Por ejemplo, un choque plano tiene $n = 1$

3.3 Objetivo y Plan de la Tesis

El objetivo de la presente tesis consiste en hacer un análisis detallado del comportamiento físico y estadístico de las nubes en las simulaciones numéricas de Passot et al. (1995) y Vázquez-Semadeni et al. (1996), con el fin de compararlas con datos observacionales de las nubes interestelares, y de interpretar estas últimas físicamente. Se estudia también el papel que juega la turbulencia en el balance energético y la generación de estructuras de densidad. La tesis se encuentra dividida en tres partes. Como continuación de esta primera parte, discutiremos los conceptos generales de la magneto-hidrodinámica, así como el Teorema Virial (§4) y el código numérico utilizado (§5). En la parte II estudiamos el balance energético, el balance virial, y las relaciones de escala que presentan las nubes en nuestras simulaciones. Esta parte a su vez se divide en: una discusión sobre la versión euleriana del Teorema Virial y resultados encontrados previamente por McKee y Zweibel (1992) (§6); dos artículos presentados en memorias de congresos donde se discute el balance energético (§7) y el balance virial euleriano de las nubes (§8); una introducción a las relaciones de escala o de Larson (§9), y un artículo donde se estudian estas relaciones en el contexto de las simulaciones (§10). Finalmente, la parte II concluye con una breve discusión sobre la dimensión fractal de las nubes en las simulaciones (§11). La parte III, también está relacionada con los mecanismos de formación de nubes. En ella se discute cómo la turbulencia puede ser capaz de generar estructuras de densidad y posiblemente desatar colapso, así como la importancia de los perfiles de línea asimétricos y multicomponentes como evidencia de turbulencia a gran escala (§13). Por último, se discute cómo, si la turbulencia es capaz de generar estructuras de densidad en tiempos cortos, el problema de la falta de estrellas post-T Tauri en la región de Tauro (§14) pudiera ser debido a que ésta se ha formado recientemente, de tal manera que sólo en los últimos 1-3 millones de años ha producido estrellas (§15). De esta forma, daremos una visión global de cómo un modelo magneto-hidrodinámico, con turbulencia homogénea y con los agentes físicos principales del MI, tales como la inyección de energía de estrellas masivas, la autogravedad, la rotación galáctica, el calentamiento y el enfriamiento difusos, la fuerza de Coriolis, etc., es capaz de reproducir una serie de características observacionales del MI, presentando a la turbulencia como agente formador y deformador de estructuras. Finalmente, en la sección 16 se discuten, de manera global, las conclusiones del presente trabajo, y se dan las pautas para el trabajo a realizar en el futuro próximo.

Capítulo 4

Hidrodinámica y Teorema Virial Lagrangiano

4.1 Conceptos de la Hidrodinámica

4.1.1 Descripciones Lagrangiana y Euleriana

Como se mencionó anteriormente, un nivel intermedio de descripción del MI está dado por las ecuaciones de la magnetohidrodinámica en presencia de fuentes de calentamiento, enfriamiento, campo gravitatorio, y otros términos fuente. Estas ecuaciones pueden estudiarse con una descripción euleriana o lagrangiana. En la primera se emplea un marco de referencia fijo, de tal manera que la posición x_i (usando notación tensorial) y el tiempo t son las variables independientes de las cuales dependen todas las variables que caracterizan al flujo (densidad, temperatura, velocidad, campo magnético, potencial gravitacional, etc.). En la segunda, por el contrario, se emplea un sistema de referencia que se mueve con el fluido, de manera que todas las variables, incluida la posición x_i , dependen del tiempo t .

4.1.2 Derivada material

Sea α una variable del campo (e.g., la densidad), y considérese entonces un sistema lagrangiano. Durante un intervalo de tiempo corto δt , el cambio en la variable α puede escribirse como:

$$\delta\alpha = \frac{\partial\alpha}{\partial t}\delta t + \frac{\partial\alpha}{\partial x}\delta x + \frac{\partial\alpha}{\partial y}\delta y + \frac{\partial\alpha}{\partial z}\delta z \quad (4.1)$$

de manera que

$$\frac{\delta\alpha}{\delta t} = \frac{\partial\alpha}{\partial t} + \frac{\partial\alpha}{\partial x}\frac{\delta x}{\delta t} + \frac{\partial\alpha}{\partial y}\frac{\delta y}{\delta t} + \frac{\partial\alpha}{\partial z}\frac{\delta z}{\delta t} \quad (4.2)$$

El lado izquierdo de esta ecuación representa el cambio total en el intervalo de tiempo δt de la variable α en dicho sistema. Entonces, si hacemos tender $\delta t \rightarrow 0$, este lado izquierdo se convierte en la derivada temporal de α en un sistema lagrangiano. Por su parte, las

cantidades $\delta x_i / \delta t$ se vuelven la componente en la dirección i de la velocidad, u_i . Entonces, si $\delta t \rightarrow 0$, tenemos

$$\frac{d\alpha}{dt} = \frac{\partial \alpha}{\partial t} + u_i \frac{\partial \alpha}{\partial x_i} \quad (4.3)$$

En esta ecuación, como a lo largo del presente texto, se usa la convención de Einstein para la suma, donde índices repetidos se suman. A la cantidad $d\alpha/dt$ se le llama "derivada total, "material", o "derivada lagrangiana", y a veces se le representa también como $D\alpha/Dt$.

4.1.3 Ecuaciones de la MHD

Sean ρ , u_i , ϕ , P , B_i y e la densidad, velocidad en dirección i , potencial gravitacional, presión térmica, componente i del campo magnético, y la energía interna, respectivamente, y sea

$$T_{ij} = \frac{1}{4\pi} \left(B_i B_j - \frac{1}{2} B^2 \delta_{ij} \right) \quad (4.4)$$

el tensor de esfuerzos electromagnéticos de Maxwell. Las ecuaciones de la magneto-hidrodinámica se escriben entonces como (ver, por ej., Shu 1992):

1. *Ecuación de Conservación de Masa:*

$$\frac{\partial \rho}{\partial t} + \frac{\partial(\rho u_i)}{\partial x_i} = 0. \quad (4.5)$$

Esta ecuación puede reescribirse, utilizando la derivada total o lagrangiana (4.3), como

$$\frac{d\rho}{dt} + \rho \frac{\partial u_i}{\partial x_i} = 0. \quad (4.6)$$

2. *Ecuación de Conservación de Momento:*

$$\frac{\partial(\rho u_i)}{\partial t} + \frac{\partial(\rho u_i u_j)}{\partial x_j} = -\frac{\partial P}{\partial x_i} + \rho \frac{\partial \phi}{\partial x_i} + \frac{\partial T_{ij}}{\partial x_j} + \rho \nu_i \left(\frac{\partial}{\partial x_j} \frac{\partial u_i}{\partial x_j} + \frac{\partial}{\partial x_i} \frac{\partial u_j}{\partial x_j} \right) \quad (4.7)$$

donde los primeros tres términos del lado derecho son la fuerza del gradiente de presión, la fuerza gravitacional y la fuerza de Lorentz, respectivamente, mientras que los últimos dos términos corresponden a términos de disipación (viscosidad). Usando la ecuación de masa (4.5), la ecuación de momento se puede reescribir como

$$\rho \frac{du_i}{dt} = -\frac{\partial P}{\partial x_i} + \rho \frac{\partial \phi}{\partial x_i} + \frac{\partial T_{ij}}{\partial x_j} + \rho \nu_i \left(\frac{\partial}{\partial x_j} \frac{\partial u_i}{\partial x_j} + \frac{\partial}{\partial x_i} \frac{\partial u_j}{\partial x_j} \right) \quad (4.8)$$

3. Ecuación de Conservación de Energía Interna:

$$\frac{\partial(\rho e)}{\partial t} + \frac{\partial(\rho eu_j)}{\partial x_j} = \frac{\partial}{\partial x_j}(u_i\Pi_{ij}) + u_i\rho f_i - \frac{\partial q_j}{x_j} \quad (4.9)$$

donde $\rho u_j f_j$ es el trabajo hecho por la fuerza por unidad de masa f_j sobre el fluido, q_j es el flujo conductivo de calor, y donde Π_{ij} es el tensor de esfuerzos cortantes, relacionado con la presión mediante la relación

$$P_i = \Pi_{ij}n_j \quad (4.10)$$

donde n_j es un vector unitario en la dirección j .

4. Ecuación de campo magnético

La ecuación que gobierna la evolución del campo magnético se lee:

$$\frac{\partial \mathbf{B}}{\partial t} = \nabla \times (\mathbf{u} \times \mathbf{B}) + \eta \nabla^2 \mathbf{B} \quad (4.11)$$

5. Ecuación de Poisson

Finalmente, la autogravedad del fluido se describe a través de la ecuación de Poisson:

$$\nabla^2 \phi = -4\pi G \rho \quad (4.12)$$

Estas ecuaciones pueden describir el comportamiento del MI bajo la aproximación de un solo fluido con tensor de presión isotrópico, si los procesos físicos relevantes en el medio interestelar son modelados de la manera adecuada como fuentes y sumideros en las ecuaciones de momento y de energía. En esta tesis consideraremos soluciones numéricas de estas ecuaciones en el régimen completamente turbulento, el cual es altamente no lineal. Por supuesto, dependiendo de los procesos físicos considerados, los términos del lado derecho de estas ecuaciones pueden sufrir modificaciones. Además, en ciertos casos es necesaria la inclusión de términos artificiales que modelen fenómenos físicos complejos, como son el calentamiento estelar o el enfriamiento y calentamiento radiativos.

4.2 Teorema Virial

El Teorema Virial (TV) es una expresión matemática obtenida a partir de la ecuación de momento, que permite estudiar de manera global el balance energético de las nubes interestelares, aunque sin suplir las soluciones exactas de la magnetohidrodinámica. En los trabajos pioneros (y frecuentemente en estudios observacionales), el TV ha sido estudiado despreciando el efecto de los llamados términos de superficie (Mestel & Spitzer 1956; Larson 1981; Myers & Goodman 1988a; Solomon et al. 1987). Otros estudios, preferentemente teóricos, han considerado la importancia de estos términos (Parker 1957; Strittmatter 1966; Mouschovias & Spitzer 1976; Zweibel 1990; McKee & Zweibel 1992; Ballesteros-Paredes et al. 1999a), aunque en general, ha sido utilizado para relacionar valores observables de

las nubes interestelares como son la dispersión de velocidades, o el valor de los campos magnéticos, con propiedades como su masa, o su habilidad para auto-soportarse en contra del colapso gravitacional (Larson 1981; Myers & Goodman 1988a; Myers & Goodman 1988b). Sin embargo, antes de discutir las situaciones físicas en donde ha sido invocado el TV, y cuáles son las simplificaciones más comúnmente adoptadas, derivamos el TV en su forma lagrangiana, de manera que la masa de una nube es constante mientras que su volumen va deformándose, siguiendo a la masa. La forma euleriana, en la cual el volumen se considera fijo, será derivada como materia de investigación, más adelante (§6.2).

4.2.1 Teorema Virial Lagrangiano

Esta es la forma más comúnmente usada del TV, y se deduce a partir del producto escalar del vector de posición x_i con la ecuación de momento en su forma lagrangiana (ec. [4.8]), e integrando sobre el volumen de interés (ver, por ej., Chandrasekhar & Fermi 1953; Spitzer 1979; Parker 1979; Shu 1992; Hartmann 1998, aunque el Teorema Virial se conoce en mecánica clásica desde principios de siglo):

$$\int x_i \rho \frac{du_i}{dt} dV = - \int x_i \frac{\partial P}{\partial x_i} dV + \int x_i \frac{\partial T_{ij}}{x_j} dV - \int \rho x_i \frac{\partial \phi}{x_i} dV \quad (4.13)$$

El término del lado izquierdo puede desarrollarse de la siguiente manera:

$$\begin{aligned} \int x_i \rho \frac{du_i}{dt} dV &= \int x_i \frac{du_i}{dt} dm = \int x_i \frac{d^2 x_i}{dt^2} dm = \\ &= \int \frac{d}{dt} \left(x_i \frac{dx_i}{dt} \right) dm - \int \left(\frac{dx_i}{dt} \right)^2 dm \end{aligned} \quad (4.14)$$

De esta última expresión, el segundo término es el doble de la energía cinética. El primer término por su parte puede reescribirse como

$$\begin{aligned} \frac{1}{2} \frac{d}{dt} \int 2x_i \frac{dx_i}{dt} dm &= \frac{1}{2} \frac{d}{dt} \int \frac{dx_i^2}{dt} dm = \\ &= \frac{1}{2} \frac{d^2}{dt^2} \int x_i^2 dm \equiv \frac{1}{2} \ddot{\mathcal{I}}_L, \end{aligned} \quad (4.15)$$

donde $\mathcal{I}_L \equiv \int x^2 dm$ es el momento de inercia, y donde nos hemos permitido extraer de la integral las derivadas temporales. Esto es válido ya que en la descripción lagrangiana el elemento de masa dm es constante y no depende del tiempo. Considérense ahora los términos de la derecha de la ecuación (4.13). El primero se reescribe como:

$$\int x_i \frac{\partial P}{\partial x_i} dV = \int \frac{\partial(x_i P)}{\partial x_i} dV - 3 \int P dV = \oint (x_i P) \hat{n}_i dS - 2\mathcal{E}_{\text{th}} \quad (4.16)$$

donde se ha usado el hecho de que $\partial x_i / \partial x_i = 3$. De manera similar, el término magnético puede reescribirse de la manera siguiente:

$$\begin{aligned}
\mathcal{M} &\equiv \int x_i \frac{\partial T_{ij}}{\partial x_j} dV = \int \frac{\partial}{\partial x_j} (x_i T_{ij}) dV - \int T_{ij} \frac{\partial x_i}{\partial x_j} dV = \\
&= \oint (x_i T_{ij}) \hat{n}_j dS - \int T_{ii} dV = \\
&= \oint (x_i T_{ij}) \hat{n}_j dS - \frac{1}{8\pi} \int B_i^2 dV
\end{aligned} \tag{4.17}$$

donde ahora ha sido usado el hecho de que $\partial x_i / \partial x_j = \delta_{ij}$, siendo δ_{ij} la delta de Kroenecker. En la última igualdad de (4.17), el segundo término del lado derecho es la energía magnética \mathcal{E}_{mag} . Por último, el término gravitacional se puede reescribir como:

$$\begin{aligned}
\mathcal{W} &\equiv - \int \rho x_i \frac{\partial \phi}{\partial x_i} dV = - \int \frac{\partial(\rho x_i \phi)}{\partial x_i} dV + \int \phi \frac{\partial(\rho x_i)}{\partial x_i} dV = \\
&= - \oint (\rho x_i \phi) \hat{n}_i dS + \int \phi x_i \frac{\partial \rho}{\partial x_i} dV + 3 \int \phi \rho dV = \\
&= - \oint (\rho \phi x_i) \hat{n}_i dS + \int \phi x_i \frac{\partial \rho}{\partial x_i} dV - 6\mathcal{E}_g
\end{aligned} \tag{4.18}$$

donde $\mathcal{E}_g = -1/2 \int_V \rho \phi dV$ es la energía gravitacional de la nube. De esta ecuación puede verse que el término gravitacional involucra, por un lado, la energía gravitacional. Sin embargo, existe un término de presión gravitacional evaluado en la superficie de la nube, así como un término que depende de la estructura de densidad en el interior de la nube. Es importante aclarar, además, que ϕ es el potencial gravitacional debido a toda la masa considerada, y no exclusivamente a la masa dentro del volumen de integración V . Adicionalmente, es posible demostrar que en el caso de una nube aislada, el término gravitacional \mathcal{W} se convierte en \mathcal{E}_g (ver apéndice A).

Recopilando los términos de las ecuaciones (4.14), (4.15), (4.16), (4.17), y (4.18), para sustituirlos en la ecuación (4.13), el teorema virial lagrangiano queda expresado de la forma:

$$\frac{1}{2} \frac{d^2 \mathcal{I}_L}{dt^2} = 2\mathcal{E}_{\text{kin}} + 2\mathcal{E}_{\text{th}} + \mathcal{E}_{\text{mag}} + \mathcal{W} - 2\mathcal{T}_{\text{th}} + \mathcal{T}_{\text{mag}}, \tag{4.19}$$

donde

$$\mathcal{T}_{\text{th}} \equiv \frac{1}{2} \oint (x_i P) \hat{n}_i dS \tag{4.20}$$

y

$$\mathcal{T}_{\text{mag}} \equiv \oint (x_i T_{ij}) \hat{n}_j dS \tag{4.21}$$

son los términos de superficie térmico y magnético.

4.3 Estabilidad y Flujo Magnético

El teorema virial ha sido ampliamente usado en la literatura en el caso de equilibrio virial ($\ddot{I} = 0$), e incluso, más estrictamente, en el caso hidrostático (i.e., $\rho du_i/dt = 0$, implicando $\ddot{I} = 2\mathcal{E}_{\text{kin}} = 0$), a fin de estudiar la estabilidad de configuraciones de equilibrio para colapsar bajo la acción de su campo gravitacional, considerando las diferentes fuerzas involucradas (gradiente de presión, campo magnético, etc.). Este análisis es relevante porque es el punto de partida de muchos trabajos teóricos que consideran la formación estelar como consecuencia del colapso de núcleos densos en dichas configuraciones de equilibrio.

Sin embargo, como se sugiere a lo largo del presente trabajo (ver §6.5, §8, y §13) la apariencia altamente dinámica de las simulaciones sugiere que las nubes están lejos del equilibrio. A continuación mostraremos algunos de los resultados más frecuentemente mencionados en la literatura astronómica que se obtienen de postular equilibrio hidrostático; los desarrollos pueden también encontrarse en varios libros de texto, como son el de Spitzer (1978), el de Shu (1992), o el de Hartmann (1998). Adicionalmente, discutimos el problema del flujo magnético y algunas evidencias que conducen a pensar que la formación estelar se da en escalas de tiempo más cortas ($\sim 1-3$ millones de años) que las de la difusión ambipolar (del orden de 10^7 años).

Supóngase que la nube en consideración es esférica, con radio R_N , en balance de fuerzas, y que se encuentra rodeada de un medio mucho más tenue, de densidad y temperatura constantes. Por simplicidad, supondremos que el campo magnético en el interior de la nube es constante, con valor B_N , mientras que en el exterior varía como $B = B_N(r/R_N)^{-3}$, lo cual reproduce el comportamiento de un dipolo magnético a grandes distancias. Entonces, consideremos el Teorema Virial Lagrangiano para un volumen esférico, de radio R_b , suficientemente grande de manera tal que los efectos de superficie del campo magnético sean despreciables (i.e., $\mathcal{T}_{\text{mag}} = 0$) en R_b , y que el término gravitacional de todo el volumen de radio R_b pueda aproximarse como la energía gravitacional de la nube de radio R_N ¹. Con estas suposiciones, el término gravitacional puede escribirse de la forma:

$$\mathcal{W} = \mathcal{E}_g = -\frac{3}{5} \frac{GM_N^2}{R_N}, \quad (4.22)$$

donde $M_N = \int_V \rho dV$ es la masa de la nube. Por su parte, la energía magnética vale

$$\mathcal{E}_{\text{mag}} = \frac{1}{3} R_N^3 B_N^2, \quad (4.23)$$

donde la mitad proviene del interior de la nube, y la otra mitad del volumen entre R_N y R_b . Supóngase además que el gas es ideal e isotérmico, de manera que $P = c^2\rho$ y por lo tanto

$$\mathcal{E}_{\text{th}} = \frac{3}{2} \int_V P dV = \frac{3}{2} c^2 M_N, \quad (4.24)$$

Finalmente consideremos el término superficial de presión:

¹Como se mostrará en la §6, si se está estudiando el balance virial del medio difuso, despreciar el término gravitacional de éste puede ser erróneo.

$$\oint_S (Px_i)\hat{n}_i dS = P_{\text{ext}} \oint_S x_i \hat{n}_i dS = 4\pi R_N^3 P_{\text{ext}} \quad (4.25)$$

donde P_{ext} es la presión externa a la nube, la cual es constante. Sustituyendo estos términos en el teorema virial lagrangiano (4.19), y suponiendo equilibrio (cuasi) hidrostático, se obtiene

$$-\frac{3}{5} \frac{GM_N^2}{R_N} + \frac{1}{3} B_N^2 R_N^3 + 3c^2 M_N - 4\pi R_N^3 P_{\text{EE}} = 0. \quad (4.26)$$

donde hemos dejado explícito que la presión P_{EE} es la presión externa a la región para una configuración de equilibrio. De esta ecuación es posible sacar varias conclusiones (ver, e.g., Shu 1992; Hartmann 1998):

a) Primeramente, despreciando los términos magnético y gravitacional, se obtiene la ley de Boyle para un gas ideal a temperatura constante:

$$P_{\text{EE}} V_N = cte. \quad (4.27)$$

donde V_N es el volumen de la nube en una configuración de equilibrio, n es la densidad numérica de partículas, T es la temperatura, y k es la constante de Boltzmann.

b) Considérense ahora despreciables los efectos del campo magnético y de la presión externa (es decir, si $B, P \rightarrow 0$). Bajo estas condiciones:

$$R_N = \frac{1}{5} \frac{GM_N}{c^2} \sim \frac{15}{4\pi} \left(\frac{c^2}{G\rho} \right)^{1/2} \sim \left(\frac{\pi c^2}{G\rho} \right)^{1/2}. \quad (4.28)$$

De ésta última expresión puede verse que el radio de equilibrio es del orden de magnitud de la longitud de Jeans. Sin embargo, ésta es una configuración de equilibrio inestable, como veremos en el siguiente inciso.

c) Considérese ahora el efecto de la presión externa. Despreciando todavía el campo magnético, y analizando el cambio de la presión externa requerido para el equilibrio como función del radio de la nube R_N a partir de la ec. (4.26):

$$\frac{dP_{\text{EE}}}{dR_N} = \frac{1}{4\pi} \left(-\frac{9c^2 M_N}{R_N^4} + \frac{12}{5} \frac{GM_N^2}{R_N^5} \right). \quad (4.29)$$

De aquí puede verse que si $R_N \rightarrow \infty$ entonces $dP_{\text{EE}}/dR_N < 0$, mientras que si $R_N \rightarrow 0$ entonces $dP_{\text{EE}}/dR_N > 0$. Finalmente, $dP_{\text{EE}}/dR_N = 0$ si

$$R_N = R_{\text{crit}} = \frac{4}{15} \frac{GM_N}{c^2}. \quad (4.30)$$

El primer caso, $R_N > R_{\text{crit}}$, es una configuración de equilibrio estable, ya que en esta configuración, si el radio de la nube aumenta repentinamente, existe un exceso de presión externa sobre la configuración de equilibrio, induciendo a que la región regrese a su configuración original; y si el radio de la nube disminuye, existe un defecto de presión externa respecto a la configuración de equilibrio, permitiendo que la nube se re-expanda. Sin embargo, para radios menores que R_{crit} , la situación es de equilibrio inestable, pues un decremento en el tamaño de la región causaría que la presión externa fuese mayor que

la presión de equilibrio, provocando que el sistema se contraiga aún más. Finalmente, la presión externa de equilibrio tiene un valor máximo dado por (ver ec. [4.26]):

$$P_{\text{crit}} \simeq \frac{3c^8}{G^3 M^2}; \quad (4.31)$$

de manera que si la presión externa supera este valor la nube se colapsará. La variación de P_{EE} como función del radio R_N para una configuración de equilibrio puede verse en la Fig. 4.1,

Nótese que existen dos configuraciones que admiten $P_{\text{EE}} = 0$. La primera, de tamaño infinito, que cae en el intervalo estable. La segunda, de tamaño dado por la ec. (4.28), que cae en el intervalo de equilibrio inestable. Esto es razonable, pues, por definición, la longitud de Jeans es la mínima escala para la cual existe equilibrio inestable.

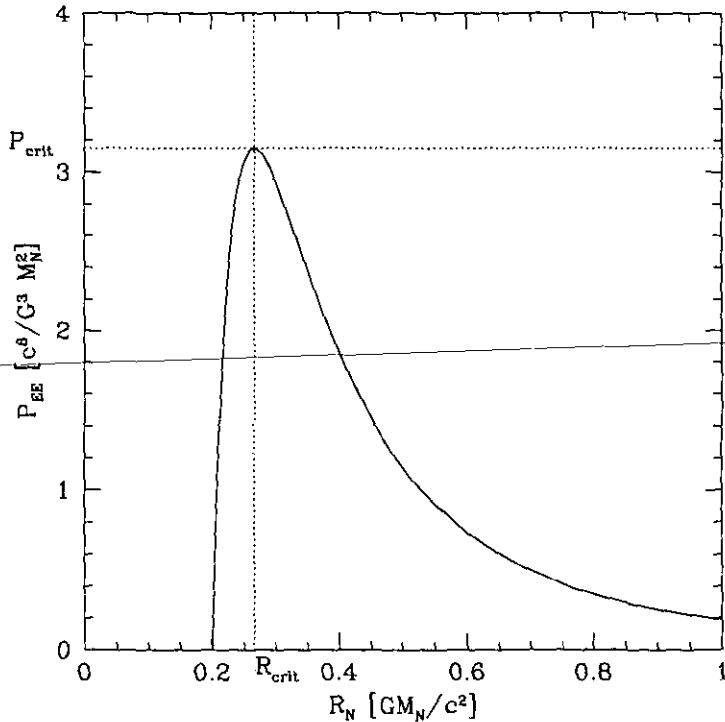


FIGURA 4.1: Presión externa de equilibrio P_{EE} como función del radio de una nube R_N , suponiendo una nube esférica, sin campo magnético y en equilibrio hidrostático. Varias situaciones pueden verse en esta gráfica: primero, que para presiones mayores que P_{crit} no existe solución de equilibrio posible. Segundo, que para tamaños mayores a R_{crit} , el sistema tiene configuraciones de equilibrio estable, mientras que para tamaños menores a R_{crit} , las configuraciones de equilibrio son inestables. Por último, nótese que existen dos soluciones de equilibrio con presión externa nula: una dada por la ecuación (4.28), y la otra con tamaño infinito. La primera es una configuración inestable, y para tamaños menores que el dado por (4.28) no existe solución de equilibrio posible y la región necesariamente se colapsa. La segunda, de tamaño infinito, es una configuración estable (ver texto).

d) Por último, considérese el caso magnético. En este caso, la presión externa que satisface el equilibrio está dada por:

$$P_{EE} = \frac{1}{4\pi} \left(\frac{3}{5} \frac{G}{R_N^4} (M_\Phi^2 - M_N^2) + \frac{3}{2} \frac{c^2 M_N}{R_N^3} \right). \quad (4.32)$$

donde se ha definido la masa crítica como:

$$M_\Phi = \left(\frac{1}{10\pi} \right)^2 G^{-1/2} \Phi_m \quad (4.33)$$

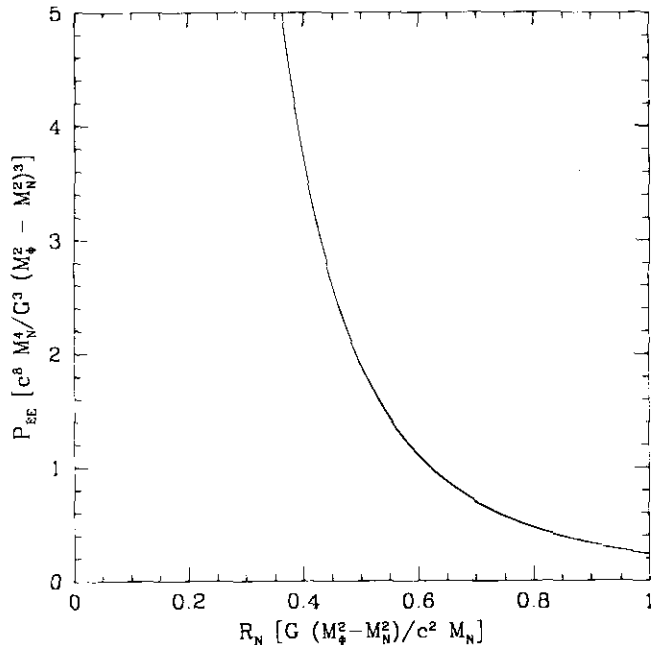
y el flujo magnético que atraviesa la sección recta de la nube como $\Phi = \pi R_N^2 B_N$. De esta ecuación podemos considerar dos casos: si $M_N < M_\Phi$ (ver Fig. 4.2a), un análisis similar al análisis de estabilidad previo nos hace concluir que, independientemente del valor de la presión externa, la situación es de equilibrio estable, es decir, que la energía magnética es capaz de soportar a la nube si la masa de la nube M_N es menor que la masa crítica M_Φ . Por el contrario, si $M_N > M_\Phi$ (Fig. 4.2b), la nube no puede ser soportada contra su propia gravedad si el radio es menor que cierto valor crítico, dado por

$$R_{crit} = -\frac{4}{15} \frac{G(M_\Phi^2 - M_N^2)}{c^2 M} \quad (4.34)$$

para el cual la presión máxima de equilibrio vale

$$P_{EE} = \frac{1}{4\pi} \left(3 \frac{c^2 M_N}{R^3} + \frac{3}{5} \frac{G(M_\Phi^2 - M_N^2)}{R^4} \right) \quad (4.35)$$

Además, si la presión externa es mayor a este valor, la nube se colapsará forzosamente. En el primer caso se dice que la nube es subcrítica, mientras que en el segundo se dice que la nube es supercrítica.



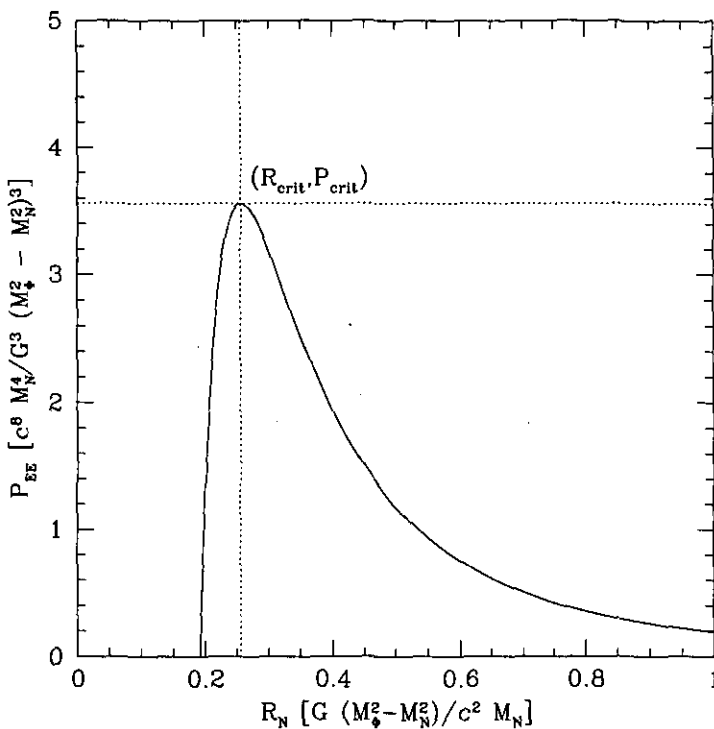


FIGURA 4.2: Presión externa de equilibrio vs. radio de la nube para una configuración esférica en equilibrio (cuasi) hidrostático. a) Caso magnéticamente subcrítico. b) Caso magnéticamente supercrítico.

Es importante aquí hacer mención de un comentario dado por Hartmann (1998): estos resultados tienen como hipótesis la suposición de que una nube de cierta masa no cambie su temperatura durante su evolución. Esta hipótesis es razonable si consideramos que, para densidades características de las nubes moleculares ($\sim 10^3 \text{ cm}^{-3}$), el calentamiento está dado principalmente por los rayos cósmicos, mientras que el enfriamiento está dado por la emisión del ^{12}CO , siempre y cuando la región sea ópticamente delgada. Con estas características, el balance entre enfriamiento y calentamiento nos lleva a concluir que la temperatura es más o menos independiente de la densidad, y tiene valores de aproximadamente 10 K. Estas temperaturas han sido corroboradas observacionalmente por muchos autores (ver por ej., Cernicharo 1991).

Shu et al. (1987) sugirieron que debía haber dos modos de formación estelar: uno para estrellas de alta masa y otro para estrellas de baja masa. Las primeras deberían formarse en regiones supercríticas, mientras que las segundas deberían formarse en regiones subcríticas. Ahora bien, suponiendo que toda la masa está en forma de hidrógeno molecular, a una densidad de 10^4 cm^{-3} , y que el campo magnético tiene intensidades de $100 \mu\text{G}$, la masa crítica es del orden de $100 M_\odot$. Si además el campo magnético está anclado en el fluido, y si los mecanismos de disipación (reconexión o difusión magnéticas) no son suficientemente eficientes, entonces el número de líneas de campo magnético que permean a un elemento de masa es constante, sugiriendo que es difícil hacer estrellas con masas similares a las del Sol. Este problema es lo que se conoce como el problema del flujo magnético.

La solución estándar a este problema consiste en considerar que, dado que el campo magnético actúa únicamente sobre las partículas cargadas, las partículas neutras no están sujetas a la acción del campo magnético excepto por colisiones con las partículas cargadas. En principio, este proceso (denominado difusión ambipolar) permite al gas neutro “resbalar” a las regiones internas para formar los núcleos (*cores*) densos (Mestel & Spitzer 1956). Un cálculo sencillo permite demostrar que esta escala de tiempo está dada por

$$t_{\text{a.d.}} \sim 5 \times 10^{13} \left(\frac{n_i}{n_{H_2}} \right) \text{yr} \quad (4.36)$$

(véase, p.ej., Mouschovias 1987; Hartmann 1998), donde n_i es la densidad numérica de iones, y n_{H_2} es la densidad numérica de moléculas de hidrógeno. Para condiciones típicas en los núcleos densos, $n_i/n_{H_2} \leq 10^{-7}$, de manera que la difusión ambipolar puede remover suficiente flujo magnético en escalas de tiempo del orden de 10^7 años. Este resultado es importante porque permite que los núcleos densos formen estrellas de baja masa mediante este proceso de difusión de campo magnético (Shu et al. 1987). Esta idea es atractiva porque establece que todo núcleo denso puede, dado el tiempo suficiente, formar estrellas de masa baja, aún cuando inicialmente su masa sea menor que la masa crítica.

Sin embargo, existen algunos problemas asociados con este esquema. El primero es la validez de las hipótesis. Por un lado hemos supuesto una nube esférica, densa, fría, con temperatura, densidad y campo magnético constantes, embebida en un medio mucho más tenue, de densidad y temperatura constantes, pero con una dependencia particular del campo magnético con la distancia. Asimismo, hemos despreciado la contribución del medio externo a la nube al potencial gravitacional, pero hemos considerado importante la contribución de su presión a la dinámica de la región. Estas condiciones parecen poco probables en un MI realista, que contiene fluctuaciones importantes de la densidad, campo magnético y velocidad. Por el contrario, pareciera que las condiciones descritas en este ejemplo son mas bien condiciones *ad hoc* tales que nos permiten despreciar una serie de términos y considerar otros.

Además, existe otra serie de problemas, como menciona Hartmann (1998): el primero y más evidente es que toda la presente discusión ha sido basada en el equilibrio virial, suposición que no necesariamente se cumple en las nubes moleculares o en sus núcleos como se verá en capítulos posteriores. Adicionalmente, las fracciones de ionización en regiones de formación estelar pueden ser considerablemente altas, en particular en regiones de formación estelar masiva (Myers & Khersonsky 1995), alargando el tiempo de difusión ambipolar. Así mismo, existe evidencia observacional de que la formación estelar se da más rápidamente que lo predicho por la ec. (4.36), tanto en regiones de baja densidad (Hartmann et al. 1991), como en regiones de densidad alta (Herbig & Terndrup 1986). Así, algunas observaciones recientes sugieren que el grueso de la formación estelar en la nebulosa de Orión ha sucedido en períodos de 1 millón de años (Hillenbrand 1997), mientras que observaciones de núcleos densos sugieren que la mayoría de éstos se encuentran en colapso y sus escalas de tiempo estimadas no exceden 2 millones de años (Lee & Myers 1999). Por otra parte, como discute Hartmann (1998, §2.7) se sabe que las regiones de formación estelar masiva también forman muchas estrellas de baja masa, sugiriendo que estas

estrellas pueden ser formadas en regiones magnéticamente supercríticas sin necesidad de un proceso de difusión ambipolar. Basado en argumentos de plausibilidad, Hartmann (1998) sugiere que si todas las estrellas (tanto de baja como de alta masa) se formasen en regiones magnéticamente supercríticas, entonces la baja eficiencia de formación estelar observada en la Galaxia debería reflejar que el número de regiones magnéticamente supercríticas es considerablemente menor que el número de regiones magnéticamente subcríticas.

Independientemente de si existen o no dos escenarios de formación estelar, la sugerencia de Hartmann (1998), junto con las observaciones de bajas escalas de tiempo para formar estrellas indican que los modelos de formación estelar deben ser revisados. En particular, como se mencionó previamente, el problema de que las edades de estrellas en regiones de formación estelar sea de alrededor de unos pocos millones de años sugiere que la formación estelar es un fenómeno que probablemente se da en escalas de tiempo mucho más cortas que lo que se ha considerado hasta la fecha. Un posible mecanismo, como se mencionó en la sección 3.2.1, es que un medio interestelar compresible, bajo el efecto de flujos turbulentos convergentes puede sufrir un colapso gravitatorio rápido. Estos temas se tratan en los capítulos 13 y 15.

Capítulo 5

El Modelo y el Código Numérico

5.1 Características

El modelo numérico presentado por Vázquez-Semadeni et al. (1995a, 1996) y Passot, et al. (1995) representa el medio interestelar a escalas de ~ 1 kpc. Si bien el código permite la realización de simulaciones tridimensionales (3D), en el presente trabajo se hace uso de simulaciones en dos dimensiones (2D), con el fin de maximizar la resolución espacial y permitir el análisis en detalle de las estructuras de densidad que surjan en las simulaciones. El código modela el medio bajo la aproximación magnetohidrodinámica, y se consideran como fuentes de momento la acción de la gravedad, el gradiente de presión, la fuerza de Lorentz, y la fuerza de Coriolis.

Respecto a la ecuación de energía, se incluyen términos (fuentes y sumideros de energía interna) que modelan el calentamiento estelar (fuentes puntuales), el calentamiento difuso o de fondo y el enfriamiento radiativo. Las ecuaciones que resuelve el código son:

$$\frac{\partial \rho}{\partial t} + \nabla \cdot (\rho \mathbf{u}) = \mu \nabla^2 \rho, \quad (5.1)$$

$$\frac{\partial \mathbf{u}}{\partial t} + \mathbf{u} \cdot \nabla \mathbf{u} = -\frac{\nabla P}{\rho} - \nu_8 \nabla^8 \mathbf{u} - \left(\frac{J}{M_a}\right)^2 \nabla \phi + \frac{1}{\rho} (\nabla \times \mathbf{B}) \times \mathbf{B} - 2\Omega \times \mathbf{u}, \quad (5.2)$$

$$\frac{\partial e}{\partial t} + \mathbf{u} \cdot \nabla e = -(\gamma - 1)e \nabla \cdot \mathbf{u} + \kappa_T \frac{\nabla^2 e}{\rho} + \Gamma_d + \Gamma_s - \rho \Lambda, \quad (5.3)$$

$$\frac{\partial \mathbf{B}}{\partial t} = \nabla \times (\mathbf{u} \times \mathbf{B}) - \nu_8 \nabla^8 \mathbf{B}, \quad (5.4)$$

y

$$\nabla^2 \phi = \rho - 1. \quad (5.5)$$

El código es pseudoespectral y utiliza una base discreta de modos de Fourier, implicando que las condiciones a la frontera son periódicas. El avance temporal, la evaluación de los términos lineales y las derivadas espaciales se realizan en el espacio de Fourier, mientras que los términos no-lineales se calculan en el espacio real. En todas las ecuaciones se incluyen términos difusivos de segundo orden en ∇ . En las ecuaciones de momento y

de flujo magnético se incluye además un término “hiperdisipativo” ∇^8 , que permite usar coeficientes mucho más pequeños para los términos de orden ∇^2 , aunque algo de disipación de segundo orden sigue siendo necesaria para eliminar oscilaciones locales producidas por los términos de hiperdisipación (Passot & Pouquet 1988). El uso de la hiperdisipación confina los efectos disipativos a las escalas más pequeñas, maximizando el intervalo dinámico. En la ecuación de energía interna, el término difusivo corresponde a la conducción térmica, pero en la ecuación de continuidad carece de significado físico y se incluye sólo por razones de estabilidad numérica. La elección de los valores de los parámetros se describe en Passot et al. (1995) y Vázquez-Semadeni et al. (1996). Aquí se describen brevemente los términos del modelo físico.

1. El calentamiento difuso Γ_d se modela como

$$\Gamma_d = \Gamma_0 \left(\frac{\rho}{\rho_{ic}} \right)^{-1/2}, \quad (5.6)$$

donde $\Gamma_0 = 0.034 \text{ ergs seg}^{-1} \text{ gr}^{-1}$, $\rho_{ic} = 0.2 \text{ m}_H \text{ gr cm}^{-3}$ es la densidad característica del medio difuso, y $m_H = 1.64 \times 10^{-24} \text{ g}$ es la masa del átomo de hidrógeno. Esta expresión permite simular un efecto de auto-escudamiento (*self-shielding*), de manera que las regiones más densas son calentadas con menor eficiencia, como sucede en el caso del calentamiento del MIE por radiación UV difusa, toda vez que la opacidad aumenta hacia las regiones más internas de las nubes.

2. El calentamiento estelar Γ_s se modela por medio de fuentes de energía locales que representan estrellas masivas, las cuales se colocan en aquellos lugares donde la densidad excede cierto valor crítico ρ_{sf} y simultáneamente los movimientos son convergentes ($\nabla \cdot \mathbf{u} < 0$). El valor característico de estas fuentes de energía es el debido a estrellas masivas ($0.85 \text{ ergs s}^{-1} \text{ gr}^{-1}$), las cuales se mantienen encendidas durante 6 millones de años (1/2 unidad temporal del código).
3. El enfriamiento es parametrizado como funciones de leyes de potencia de la temperatura, tal como los utilizan Rosen et al. (1993) y Rosen & Bregman (1995) a partir de las funciones de enfriamiento de Dalgarno y McCray (1972) y Raymond et al. (1976). Estas funciones de enfriamiento se escriben entonces como:

$$\Lambda = \begin{cases} 0 & 0 \leq T < 100 \text{ K} \\ \Lambda_1 T^2 & 100 \text{ K} \leq T < 2000 \text{ K} \\ \Lambda_2 T^{1.5} & 2000 \text{ K} \leq T < 8000 \text{ K} \\ \Lambda_3 T^{2.867} & 8000 \text{ K} \leq T < 10^5 \text{ K} \\ \Lambda_4 T^{-0.65} & 10^5 \text{ K} \leq T < 4 \times 10^7 \text{ K} \end{cases}.$$

Los valores de estas Λ_i están dados en la Tabla 5.1.

4. Para la rotación Galáctica se supone que la región modelada rota alrededor del centro Galáctico con velocidad angular constante, de valor $\Omega_0 = \pi/10^8 \text{ años}^{-1}$, correspondientes a la velocidad de rotación a la distancia galactocéntrica solar, de manera que

las coordenadas x y y corresponden a las direcciones azimutal y radial, respectivamente. Entonces, la fuerza de Coriolis en la ecuación de momento (5.2), se escribe $-2\Omega_0 \times \mathbf{u}$. Además, como la fuerza centrífuga y la fuerza gravitacional radial se balancean para cada radio, entonces únicamente es necesario modelar la rotación diferencial. Dada la restricción de condiciones a la frontera periódicas, la rotación diferencial se modela como una función sinusoidal de la forma

$$u_x(y) = A_0 \sin \frac{2\pi y}{L_0} \quad (5.7)$$

donde L_0 es la longitud de la caja, y donde la constante $A_0 = 4.4 \text{ km s}^{-1}$ está dada por la constante A de Oort, ya que este valor de la amplitud nos permite generar un gradiente de velocidad de 8.8 km s^{-1} a lo largo de la mitad de la caja de integración, que es equivalente a 500 pc.

Como se menciona en Vázquez-Semadeni et al. (1996), como consecuencia de la dependencia funcional en ρ y T de las funciones de calentamiento y enfriamiento, y de que las escalas de tiempo dinámicas son mucho más largas que las escalas de tiempo en las que se establece el equilibrio térmico fuera de las regiones de calentamiento estelar, el gas tiene un comportamiento barotrópico de acuerdo al régimen de temperaturas (y por ende, régimen de enfriamiento), es decir, la presión obedece la relación $P \propto \rho^{\gamma_{\text{eff}}}$. En términos de los parámetros del código:

$$P = \left(\frac{\Gamma_0 \rho_{\text{ic}}^\alpha}{\Lambda_i} \right)^{1/\beta_i} \left(\frac{\rho^{\gamma_{\text{eff}}}}{\gamma M_a^2} \right) . \quad (5.8)$$

donde

$$\gamma_{\text{eff}} = \begin{cases} 0.25 & 1.57 < \rho \ (100 < T < 2000) \\ 0. & 0.39 < \rho \leq 1.57 \ (2000 \leq T < 8000) \\ 0.48 & 3.15 \times 10^{-3} < \rho \leq 0.39 \ (8000 \leq T < 10^5) \end{cases} \quad (5.9)$$

5.2 Definición de las nubes en las simulaciones y cálculo de sus propiedades físicas y estadísticas

En el presente trabajo, frecuentemente se calculan las propiedades físicas (e.g., energías, dispersión de velocidades, densidad promedio, etc.) de las nubes en las simulaciones numéricas. Para esto, es necesario definir operacionalmente a las nubes. Una nube en las simulaciones es un conjunto conexo de puntos en el espacio x , y , cuya densidad excede un cierto valor umbral ρ_{th} . El valor de ρ_{th} se escoge de acuerdo al tipo de nube que se desee. Por ejemplo, los complejos más grandes resultan de tomar un valor pequeño de ρ_{th} ¹, mientras que si uno desea estudiar las estructuras más pequeñas, entonces se deben tomar típicamente valores grandes de ρ_{th} . El considerar diferentes valores de ρ_{th} es análogo a observar las nubes con diferentes trazadores, de manera que el intervalo de densidades observado depende del trazador utilizado.

¹Aunque como se menciona en §10, también se encuentran nubes pequeñas al usar umbrales bajos.

Los valores característicos de los diferentes parámetros adoptados para las simulaciones se presentan en la Tabla 1 de Passot et al. (1995). Por completez, en la Tabla 5.1 reproducimos los valores físicos más importantes.

Parámetros usados en las simulaciones numéricas

| Cantidad física | Símbolo | Valor |
|---|--------------------|--|
| Unidad de longitud | L_0 | 1 kpc |
| Unidad de velocidad | u_0 | 11.7 km s ⁻¹ |
| Unidad de tiempo | t_0 | 8.1×10^7 años |
| Unidad de densidad de masa | ρ_0 | 1.67×10^{-24} gr cm ⁻³ |
| Unidad de densidad de partículas | n_0 | 1 cm ⁻³ |
| Unidad de energía interna | e_0 | u_0^2 |
| Unidad de temperatura | T_0 | 10^4 K |
| Unidad de intensidad de campo magnético | B_1 | 5 μ G |
| Componente uniforme del campo magnético | B_0 | 1.6 μ G |
| Componente fluctuante del campo magnético | B_{rms} | 5 μ G |
| Velocidad angular de rotación Galáctica | Ω_0 | $\pi/10^8$ años ⁻¹ |
| Longitud de Jeans | L_J | 2 kpc |
| Tasa de calentamiento difuso a 0.2 ρ_0 | Γ_d | 0.034 ergs s ⁻¹ gr ⁻¹ |
| Tasa de calentamiento estelar | Γ_s | 0.85 ergs s ⁻¹ gr ⁻¹ |
| Densidad crítica de formación estelar | ρ_{th} | 30 cm ⁻³ a una resolución de 512^2 y 800^2 |
| Amplitud del deslizamiento | A_0 | 4.4 km s ⁻¹ |
| Coeficientes de la función de enfriamiento | Λ_1 | 1.14×10^{15} erg s ⁻¹ gr ⁻² cm ³ |
| | Λ_2 | 5.08×10^{16} erg s ⁻¹ gr ⁻² cm ³ |
| | Λ_3 | 2.35×10^{11} erg s ⁻¹ gr ⁻² cm ³ |
| | Λ_4 | 9.03×10^{28} erg s ⁻¹ gr ⁻² cm ³ |

TABLA 5.1: Valores característicos de los parámetros utilizados en las simulaciones (tomado de Passot et al. 1995).

Parte II

Teorema Virial, Balance Energético y Relaciones de Escala

Capítulo 6

Teorema Virial y Balance Energético

6.1 Introducción

Al derivar el Teorema Virial en la sección 4.2 lo hicimos mediante el uso de la forma lagrangiana de la ecuación de momento. Sin embargo, se obtiene una forma diferente si se usa la ecuación de momento en su forma euleriana, ec. (4.7). La diferencia entre ambas formas consiste en considerar la evolución temporal de un elemento de masa (forma lagrangiana) o de un elemento de volumen fijo en el espacio (forma euleriana).

Dado que nuestro interés es estudiar el posible balance virial y energético de las nubes en simulaciones numéricas, y dado que dichas simulaciones han sido realizadas utilizando un esquema euleriano, es conveniente estudiar el TV en su forma euleriana.

En la presente sección derivaremos el Teorema Virial Euleriano (TVE) de primeros principios (§6.2) y discutiremos algunos de los resultados obtenidos por McKee & Zweibel (1992) (§6.3), así como el papel de los términos de superficie en el TVE (§6.4), y el posible balance virial (§6.5).

6.2 Teorema Virial Euleriano

Parker (1979) derivó el TVE para un flujo MHD despreciando los términos superficiales. Por su parte, McKee & Zweibel (1992) lo derivan sin despreciar ningún término, a partir de la definición de momento de inercia en un sistema euleriano. A continuación derivamos el TVE a partir de la ecuación de momento en su forma euleriana. Para ésto, considérese el producto escalar de la ecuación de momento en su forma euleriana (4.7) por el vector x_i e intégrese en volumen:

$$\begin{aligned} \int_V \frac{\partial(\rho u_i)}{\partial t} x_i dV = & - \int x_i \frac{\partial P}{\partial x_i} dV - \int x_i \rho \frac{\partial \phi}{\partial x_i} dV + \\ & + \int x_i \frac{\partial T_{ij}}{\partial x_i} dV - \int x_i \frac{\partial(\rho u_i u_j)}{\partial x_j} dV \end{aligned} \quad (6.1)$$

donde hemos considerado despreciables los términos disipativos de la ec. (4.7). Dado que ni el vector x_i ni el volumen V dependen del tiempo, las derivadas parciales respecto al

tiempo dentro de las integrales de volumen pueden escribirse como derivadas totales afuera de éstas. Por lo tanto, el lado izquierdo de la ecuación (6.1) puede escribirse como:

$$\begin{aligned}
 \int_V x_i \frac{\partial(\rho u_i)}{\partial t} dV &= \frac{d}{dt} \int_V x_i \rho u_i dV = \\
 &= \frac{1}{2} \frac{d}{dt} \left[\int_V \frac{\partial(\rho u_i x^2)}{\partial x_i} dV - \int_V \frac{\partial(\rho u_i)}{\partial x_i} x^2 dV \right] = \\
 &= \frac{1}{2} \frac{d}{dt} \oint_S (\rho x^2 u_i) \hat{n}_i dS + \frac{1}{2} \frac{d}{dt} \int_V \frac{\partial \rho}{\partial t} x^2 dV = \\
 &= \frac{1}{2} \frac{d}{dt} \oint_S (\rho x^2 u_i) \hat{n}_i dS + \frac{1}{2} \frac{d^2}{dt^2} \int_V \rho x^2 dV = \\
 &= \frac{1}{2} \frac{d\Phi}{dt} + \frac{1}{2} \ddot{I}_E
 \end{aligned} \tag{6.2}$$

donde se ha utilizado la ecuación de masa (4.5) para pasar del segundo al tercer renglón, $\Phi \equiv \oint_S (\rho x^2 u_i) \hat{n}_i dS$ es el flujo de densidad de momento de inercia ρx^2 a través de la superficie de la nube, e $I_E \equiv \int_V \rho x^2 dV$ es el momento de inercia. Considerando ahora el lado derecho de la ecuación (6.1), notamos que todos los términos escritos ya han aparecido en el TVL excepto el último, el cual puede reescribirse como:

$$\begin{aligned}
 \int x_i \frac{\partial(\rho u_i u_j)}{\partial x_j} dV &= \int \frac{\partial(x_i \rho u_i u_j)}{\partial x_j} dV - \int \rho u_i u_j \frac{\partial x_i}{\partial x_j} dV \\
 &= 2(\mathcal{T}_{\text{kin}} - \mathcal{E}_{\text{kin}})
 \end{aligned} \tag{6.3}$$

donde $\mathcal{E}_{\text{kin}} \equiv 1/2 \int \rho u^2 dV$ es la energía cinética contenida en el volumen V , y $\mathcal{T}_{\text{kin}} \equiv 1/2 \oint_S (x_i \rho u_i u_j) \hat{n}_j dS$. En particular, en el caso incompresible, \mathcal{T}_{kin} es la cuarta parte del flujo a través de la superficie de la nube de la tasa de cambio del momento de inercia $2x_i \rho u_i$ (en el caso compresible, la interpretación de este término no es tan clara). Igualando entonces las ecuaciones (6.1) y (6.2) y utilizando la ecuación (6.3), queda escrito el Teorema Virial en su forma euleriana:

$$\frac{1}{2} \ddot{I}_E = 2 \left(\mathcal{E}_{\text{kin}} + \mathcal{E}_{\text{th}} - \mathcal{T}_{\text{kin}} - \mathcal{T}_{\text{th}} \right) - \frac{1}{2} \frac{d\Phi}{dt} + \mathcal{W} + \mathcal{E}_{\text{mag}} + \mathcal{T}_{\text{mag}} \tag{6.4}$$

Si al tiempo t la masa considerada en el caso lagrangiano coincide espacialmente con el volumen euleriano, entonces $\mathcal{I}_E = \mathcal{I}_L$. Sin embargo, sus segundas derivadas son diferentes:

$$\ddot{I}_L - \ddot{I}_E = 4\mathcal{T}_{\text{kin}} + \frac{d\Phi}{dt} \tag{6.5}$$

como consecuencia del flujo de masa a través de la superficie del volumen euleriano.

6.3 Consideraciones sobre el Análisis de McKee y Zweibel (1992)

Una idea fundamental subyacente en todo el presente trabajo es que la turbulencia es un fenómeno multiescala, es decir, el campo de velocidades es caótico en todas las escalas. Sin embargo, es frecuente encontrar en la literatura, de manera automática y sin justificación, la idea de microturbulencia, es decir, que las escalas asociadas a los movimientos turbulentos son pequeñas comparadas con las escalas de la región en consideración. Un ejemplo de ésto es el trabajo realizado por McKee y Zweibel (1992), donde se estudia el comportamiento de una nube aislada, densa y fría, rodeada por un medio mucho menos denso y más caliente, donde las cantidades varían lenta y suavemente y donde se trata a la turbulencia como si contuviera sólo modos en escalas mucho menores que las escalas de la nube¹. Dado que algunos de los resultados de dicho trabajo están en aparente contradicción con algunos de la presente tesis, a continuación presentamos una discusión al respecto.

En la primer parte de dicho trabajo se escribe la versión lagrangiana del Teorema Virial, y se deduce de primeros principios la versión euleriana, escrita previamente por Parker (1979), pero sin despreciar los términos de superficie. Sin embargo, en la segunda parte algunos resultados parecen erróneos. Estos resultados son, primero: McKee & Zweibel (1992) encuentran que los términos que contienen derivadas temporales en el TVE (ec. [6.4]) son despreciables frente al resto de los términos cuando se les promedia en escalas de tiempo mucho mayores que las escalas de tiempo dinámicas; segundo, encuentran que la componente de la velocidad del medio internube perpendicular a la frontera de la nube decrece cerca de la frontera de ésta (ver §4.1 y §4.2 de McKee & Zweibel 1992), de manera que la presión hidrodinámica del medio internube, evaluada en la frontera de la nube, es mucho menor que la presión térmica. Tercero, que el medio internube es *force-free*, es decir, que la fuerza neta en el medio internube es idénticamente cero. Cuarto, que conforme el gas del medio internube fluye cerca de la nube, la presión térmica del medio internube evaluada en la frontera debe decrecer. Físicamente, esta disminución “está asociada con la disminución de la presión conforme el gas internube fluye alrededor de la nube (efecto Venturi)” (sic). A continuación discutimos por qué estos resultados nos parecen erróneos.

1. El primer problema en el tratamiento de McKee & Zweibel (1992) consiste en confundir dos escalas de tiempo muy diferentes: la primera, la escala de tiempo dinámica del medio internube, la cual es del orden de:

$$t_{\text{din}} \sim \frac{R_{\text{ic}}}{c_{\text{ic}}} \quad (6.6)$$

donde R_{ic} es el tamaño característico de la región completa (nube y medio internube), y c_{ic} es la velocidad del sonido del medio internube², la cual permite estimar el tiempo

¹ McKee y Zweibel (1992) discuten brevemente el caso de “modos grandes” de la turbulencia, pero sólo como ondas de choque alcanzando a la nube, sin considerar la continuidad del campo de velocidad en la frontera de la nube.

² Estrictamente hablando, en el caso magnético la velocidad sónica efectiva está dada por $(v_a^2 + c_{\text{ic}}^2)^{1/2}$, donde v_a es la velocidad de Alfvén.

característico de las variaciones de las propiedades del sistema. La segunda, una escala de tiempo mucho mayor t_{av} tal que

$$t_{av} \gg t_{din}, \quad (6.7)$$

que es utilizada para promediar los términos del TVE. El problema se da en el momento en que consideran que en una escala de tiempo t_{av} es válida la relación

$$\Delta\alpha \sim \alpha, \quad (6.8)$$

donde α es una variable arbitraria del sistema. Esto es cierto si el intervalo de tiempo es del orden de la escala de tiempo dinámica, que se define precisamente como el tiempo después del cual la ecuación (6.8) se satisface. Sin embargo, para tiempos $t_{av} \gg t_{din}$, y regímenes altamente no lineales, $\Delta\alpha$ deja de ser comparable con α (es decir, el sistema “ pierde memoria” de las condiciones iniciales).

2. El siguiente problema consiste en considerar que el término gravitacional del medio internube es despreciable por el hecho de que su energía gravitacional es despreciable (§4.1 de McKee y Zweibel 1992). Como se mencionó en la sección 4.2.1, el término gravitacional de una región arbitraria es igual a la energía gravitacional sólo si la única contribución al potencial gravitacional de dicha región es la de la masa contenida en la región de interés. Sin embargo, para el caso del medio internube esta condición no se cumple. Por el contrario, la presencia de la nube masiva en la región hace que el término gravitacional del medio internube no pueda escribirse como su energía gravitacional, sino que será esencialmente la energía gravitacional debida al peso del medio internube en el potencial de la nube. Esta contribución no es despreciable a priori, y McKee & Zweibel (1992) no demuestran que lo sea³.
3. Un tercer problema (véase la discusión posterior a la ecuación [4.7] de McKee & Zweibel 1992) consiste en considerar que, para un volumen V con una superficie S justo afuera de la nube, la ecuación

$$I_L = I_E = I_{cl} \quad (6.9)$$

implica que

$$\ddot{I}_L = \ddot{I}_E = \ddot{I}_{cl}, \quad (6.10)$$

donde I_L es el momento de inercia en un marco lagrangiano, I_E es el momento de inercia en un marco euleriano, e I_{cl} es el momento de inercia de la nube. Como se ve de la ecuación (6.5), aún cuando al tiempo t los volúmenes lagrangiano y euleriano coincidan, y aún cuando la igualdad (6.9) sea válida, la ecuación (6.10) no es válida si existe un flujo de masa a través de la superficie de la nube.

³Para poder despreciar el peso gravitacional del medio internube en el potencial de la nube se debe valer la relación $c_{ic} > v_{esc}$, donde v_{esc} es la velocidad de escape de una partícula desde la superficie de la nube.

Estos tres resultados infundados conducen a McKee y Zweibel (1992), como se muestra a continuación, a cuatro conclusiones que, por lo tanto, son también infundadas. Además, están en contradicción con los resultados de la presente tesis:

- Primeramente, el resultado 1 conduce a que los términos que contienen derivadas temporales en el TVE (ec. [6.4]) sean despreciables. Sin embargo, como se verá en la §8, son estos términos los que dominan en el TVE.
- Los resultados 1 y 2 conducen a McKee y Zweibel (1992) a postular que el medio internube es *force-free* (véase su ec. [4.5]), puesto que el hecho de que los términos que contienen derivadas temporales en el TVE y el término gravitacional sean despreciables (inciso anterior y punto 2 arriba) implica que en la ecuación de momento:

$$\frac{\partial T_{ij}}{\partial x_j} + \frac{\partial P}{\partial x_i} + \frac{\partial(\rho u_i u_j)}{\partial x_j} = 0. \quad (6.11)$$

Adicionalmente, “ignorando la posibilidad de que la condición *force-free* se obtenga del balance entre la presión del gas y las fuerzas magnéticas”, McKee & Zweibel (1992) obtienen que

$$\frac{\partial T_{ij}}{\partial x_j} \sim \frac{\partial}{\partial x_j}(P\delta_{ij} + \rho u_i u_j) \sim 0. \quad (6.12)$$

Todas estas conclusiones quedan invalidadas debido a la invalidez de los puntos 1 y 2 dados arriba.

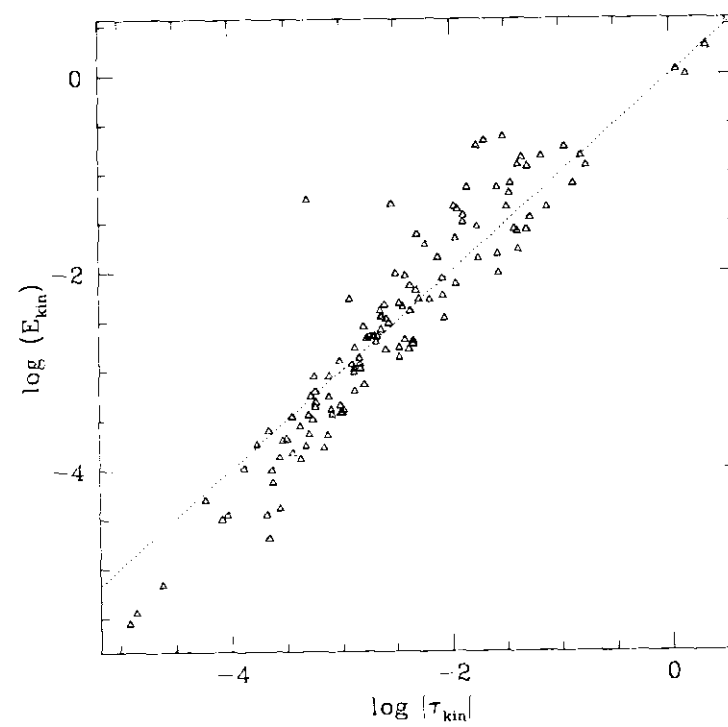
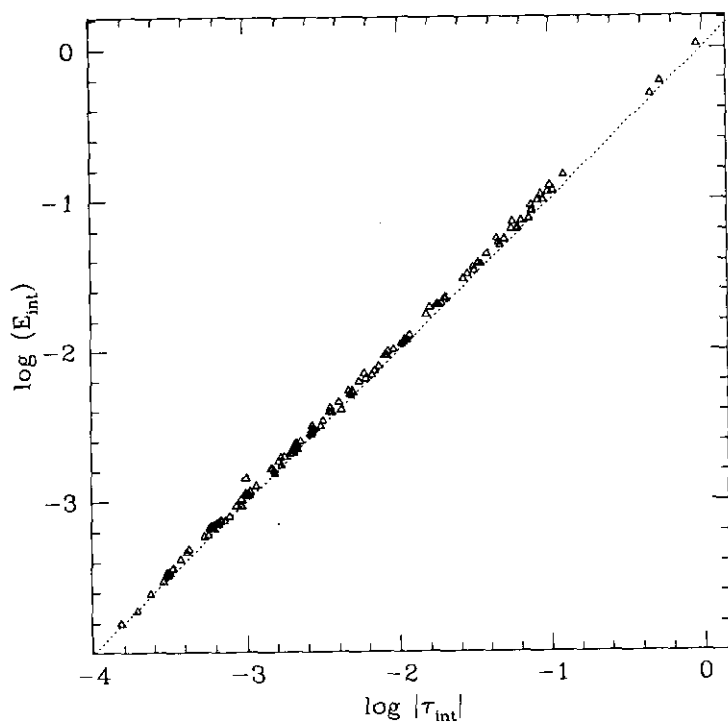
- El resultado 3 (ec. [6.10]) conduce a los autores a considerar que la componente perpendicular de la velocidad turbulenta del medio internube decrece cerca de la superficie de la nube (ver discusión posterior a la ec. [4.7] de McKee & Zweibel 1992). En efecto, de la ec. (6.10), la definición de \mathcal{T}_{kin} , y de despreciar de las derivadas temporales, seguiría que $\mathcal{T}_{\text{kin}} \sim 0$ (ec. [6.5]). Pero \mathcal{T}_{kin} involucra la componente de la velocidad perpendicular a la superficie de la nube. De nuevo, este resultado queda invalidado por la invalidez de la ecuación (6.10). Además, este efecto, hasta donde hemos evaluado en las simulaciones, no se da. Por el contrario, los campos de velocidad y de densidad son en general continuos a lo largo de las estructuras de densidad, independientemente del criterio usado para determinar la localización de la frontera (arbitraria) de la nube (ver §13).
- Como consecuencia de los dos incisos anteriores (*force-free* y disminución de la presión turbulenta en la superficie de la nube), los autores concluyen que, conforme el medio internube fluye alrededor de la nube, éste experimenta una caída de presión, como es el caso del efecto Venturi. Este efecto, además de no haber sido observado en las simulaciones, no es de esperarse en el altamente compresible medio interestelar, ya que dicho efecto se manifiesta principalmente en medios incompresibles, y disminuye según aumenta la compresibilidad del flujo.

Finalmente, es importante mencionar que, en general, el medio (nube e internube) en las simulaciones no está lejos del equilibrio de presión térmica, con un contraste entre la presión máxima y la mínima ≤ 5 , excepto en regiones de formación estelar, donde la presión térmica llega a ser hasta 60 veces mayor. Cabe notar además que a los argumentos cuestionables presentados por McKee & Zweibel (1992) se suman hipótesis de trabajo que parecen poco realistas: un medio turbulento en escalas pequeñas comparadas con las escalas de la nube, donde las cantidades varían poco; una nube esférica, de densidad constante, embebida en un medio homogéneo de densidad mucho menor, donde la energía gravitacional del medio externo es despreciable. Tales condiciones parecen más válidas para protoestrellas que para nubes interestelares, en las que el campo de densidad es un continuo, y donde la turbulencia es un fenómeno multiescala y las formas de las nubes son extremadamente irregulares, con fronteras fractales (§11). Así pues, consideramos que las discrepancias entre nuestros resultados y los de McKee y Zweibel (1992) no son motivo de preocupación, pues dicho trabajo parece altamente cuestionable. En los artículos reproducidos en los siguientes capítulos se describen varios de nuestros resultados, aunque en ellos hemos preferido evitar hacer mención directa de la discrepancia de resultados con McKee y Zweibel (1992).

A continuación describiremos resultados adicionales no incluidos en los artículos, concernientes al balance entre los términos volumétricos y de superficie del TVE.

6.4 El papel de los términos de superficie

En la Fig. 6.1a mostramos la energía interna \mathcal{E}_{th} , vs. el término de presión térmica en la frontera de la nube T_{th} , para un conjunto de nubes en las simulaciones numéricas a un tiempo dado. De esta gráfica puede verse que ambas son comparables, sugiriendo que existe balance de presión térmica entre las nubes y sus alrededores. Por otra parte, en la Fig. 6.1b graficamos la energía cinética, \mathcal{E}_{kin} , vs. el término de presión turbulenta en la superficie de las nubes, T_{kin} . Nótese que, aunque existe balance entre la presión interna y externa (Fig. 6.1a), la existencia de movimientos turbulentos podría distorsionar las nubes, ya que éstos no están claramente balanceados por la energía cinética interna de la nube (Fig. 6.1b). Finalmente, en la Fig. 6.1c mostramos la energía magnética, \mathcal{E}_{mag} , vs. el término magnético evaluado en la superficie de las nubes, mostrando que en este otro caso, tampoco hay un balance exacto entre estos términos. Estas son manifestaciones directas de la naturaleza turbulenta del flujo, y contribuyen al estado de no-equilibrio virial de las nubes.



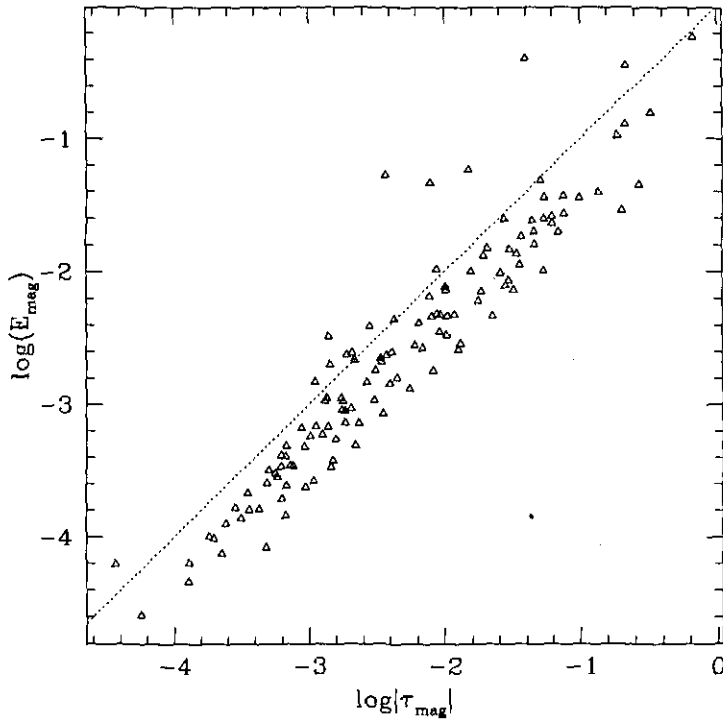


FIGURA 6.1: Términos volumétricos vs. términos de superficie que intervienen en el TVE. a) \mathcal{E}_{th} vs. \mathcal{T}_{th} ; b) \mathcal{E}_{kin} vs. \mathcal{T}_{kin} ; c) \mathcal{E}_{mag} vs. \mathcal{T}_{mag} . Nótese que en todos los casos, las integrales de superficie tienen valores comparables con las integrales de volumen, aunque no necesariamente se cancelan idénticamente. Sin embargo, nótese que en el caso de la presión térmica, el término volumétrico y superficial no tienen tantas fluctuaciones, indicando que las nubes están aproximadamente en balance de presión térmica. Entonces, los movimientos deben ser producidos por el gradiente de presión hidrodinámica (cinética) y magnética.

Es frecuente encontrar en la literatura – y en particular en la literatura observational – referencias al teorema virial en las que se desprecian los términos de superficie. El origen de esta práctica probablemente se debe a que observationalmente es imposible evaluar la presión térmica, el tensor de Maxwell o la presión hidrodinámica en la frontera de las nubes, tanto porque no existe una definición observational precisa de las nubes (ver Scalo 1990), como porque las observaciones sólo permiten determinar de manera directa cantidades integradas a lo largo de la línea de visión, y no las cantidades en un lugar preciso en el espacio. Sin embargo, en el presente trabajo se muestra cómo en un medio turbulento existe un flujo de masa a través de la frontera del volumen considerado (§8, §13). Desde el punto de vista lagrangiano, las fronteras de la nube (que delimitan la masa) se deben estar deformando constantemente como consecuencia de la presión (anisotrópica) hidrodinámica. En particular, hemos evaluado la importancia de los términos de superficie en el TVE para las simulaciones numéricas analizadas, encontrando que éstos son tan importantes como los respectivos términos volumétricos. Como se mostró en las Figs. 6.1a, b, y c, los términos \mathcal{E}_{th} vs. \mathcal{T}_{th} , \mathcal{E}_{kin} vs. \mathcal{T}_{kin} y \mathcal{E}_{mag} vs. \mathcal{T}_{mag} , respectivamente, los términos de superficie son comparables a los términos volumétricos correspondientes, aunque en el caso de los términos cinéticos y magnéticos, no existe un balance detallado entre cada par

de términos.

6.5 Equilibrio Virial y Balance Energético

Una de las suposiciones más frecuentes en la literatura es que las nubes y sus núcleos densos están en equilibrio virial (ver, e.g., Shu et al. 1987; Myers & Goodman 1988), es decir, que se satisface

$$\ddot{\mathcal{I}}_E = 0. \quad (6.13)$$

Sin embargo, las simulaciones numéricas nos han permitido determinar que en general ésto no se cumple (§8). Por otro lado, un resultado interesante es que las nubes sí se encuentran cerca de la equipartición de la energía (§7).

Una consecuencia importante de que exista equipartición entre las energías gravitacional y cinética es que es posible derivar, suponiendo una cierta geometría para la nube observada, la masa de una nube a partir de observaciones de líneas (véase, por ej., Estalella & Anglada, 1996). En muchos casos las estimaciones de las masas de las nubes moleculares usando este método coinciden razonablemente bien con las derivaciones de las masas usando otros métodos (e.g., intensidad de la línea de ^{12}CO). Sin embargo, recalcamos, esto es consecuencia de la equipartición entre la energía gravitacional y la energía cinética (turbulenta) de la nube, mas no del equilibrio virial.

6.6 Trabajos Publicados al Respecto

En los siguientes dos capítulos se estudia el balance energético (§7) y el teorema virial euleriano (§8) para las nubes en las simulaciones numéricas realizadas. A diferencia de estudios previos, los resultados aquí presentados constituyen el primer intento de hacer un balance exacto y detallado del TV, a fin de evaluar la importancia relativa de cada uno de los términos que intervienen en éste, en situaciones razonablemente realistas y no en situaciones idealizadas. Como se ha mencionado y como se verá en estos capítulos, se encuentra que si bien las nubes están aproximadamente en un balance energético, la situación de equilibrio virial no se cumple, indicando entonces que el medio interestelar se encuentra en un estado altamente dinámico.

Capítulo 7

Artículo 1

Cloud Statistics in Numerical Simulations of the ISM

Javier Ballesteros-Paredes and Enrique Vázquez-Semadeni

Publicado en

Revista Mexicana de Astronomía y Astrofísica, Serie de Conferencias, Vol 3, 105.
1995.

"Fifth Mex-Tex Meeting in Astrophysics. Gaseous Nebulae and Star Formation"

Resumen

Presentamos resultados preliminares de simulaciones numéricas bidimensionales sobre el balance energético de las nubes del medio interestelar. Mediante el uso de un algoritmo de identificación de nubes, calculamos las energías gravitacional, interna, cinética y magnética de las mismas. Encontramos que, con una dispersión de aproximadamente un orden de magnitud, la energía gravitacional en las nubes está balanceada por las energías restantes. Adicionalmente, y con dispersiones comparables, parece haber equipartición entre las energías cinética y magnética.

Abstract

We present preliminary results on the energy budgets of clouds in two-dimensional numerical simulations of the interstellar medium. Using an automated cloud-identification algorithm, we calculate the gravitational, internal, kinetic and magnetic energies of the

clouds. We find that, within a dispersion of roughly one order of magnitude, the gravitational energy in the clouds is balanced by the remaining energies. Furthermore, within the same dispersion, there appears to be equipartition between the kinetic and magnetic energies.

7.1 Introduction

Interstellar clouds appear to be close to virial equilibrium between the gravitational and other forms of energy (Larson 1981; Myers & Goodman 1988 a,b), even though the assumption that they are in a static equilibrium is highly questionable, as both the clouds and their embedding medium are highly turbulent (e.g., Larson 1981; Hunter & Fleck 1982; Henriksen & Turner 1984; Dickman 1985; Scalo 1987; Falgarone 1989; Fleck 1992). Recently, Vázquez-Semadeni, Passot & Pouquet (1995a, Paper I) have suggested that the apparent virialization may be due to nearly-virialized clouds having longer lifetimes, although the flow may not necessarily have a tendency towards forming virialized clouds. In order to test this conjecture, we have initiated a program to produce “surveys” of the clouds that form in numerical simulations of the interstellar medium (ISM) including magnetic fields (Passot, Vázquez-Semadeni & Pouquet, 1995, hereafter Paper II), and to evaluate the various energies and terms in the virial theorem for each cloud.

In this paper we present preliminary results of this work. In §7.2 we briefly describe the numerical algorithm and define the relevant quantities. In §7.3 we present measurements of the various energies and comparisons that indicate rough equipartition between them. Finally, in §7.4 we summarize and discuss the results.

7.2 The Method

The two-dimensional numerical simulation from which the data are taken represents a square region of 1 kpc on a side in the Galactic plane, at roughly the Solar circle. Details on the numerical method can be found in Papers I and II. The simulation gives the time evolution over 1.3×10^8 yr for all relevant physical quantities including the density, velocity, temperature and magnetic field, respectively measured in units of $\rho_0 = 1 \text{ cm}^{-3}$, $u_0 = 11.7 \text{ km s}^{-1}$, $T_0 = 10^4 \text{ K}$ and $B_0 = 5 \mu\text{G}$. The gravitational, kinetic, internal and magnetic energies (respectively \mathcal{E}_g , \mathcal{E}_{kin} , \mathcal{E}_{th} and \mathcal{E}_{mag}) are defined as¹

$$\begin{aligned}\mathcal{E}_g &\equiv -\frac{1}{2} \int \rho \phi dV, \\ \mathcal{E}_{\text{kin}} &\equiv \frac{1}{2} \int \rho u^2 dV, \\ \mathcal{E}_{\text{th}} &\equiv \frac{3}{2} \int P dV,\end{aligned}$$

¹Nota del Autor: Nótese que la energía magnética está definida con un factor de 1/2 en lugar del factor 1/8π. La razón de esto es que hay un factor de 1/4π ya incluido en la adimensionalización de las ecuaciones del código.

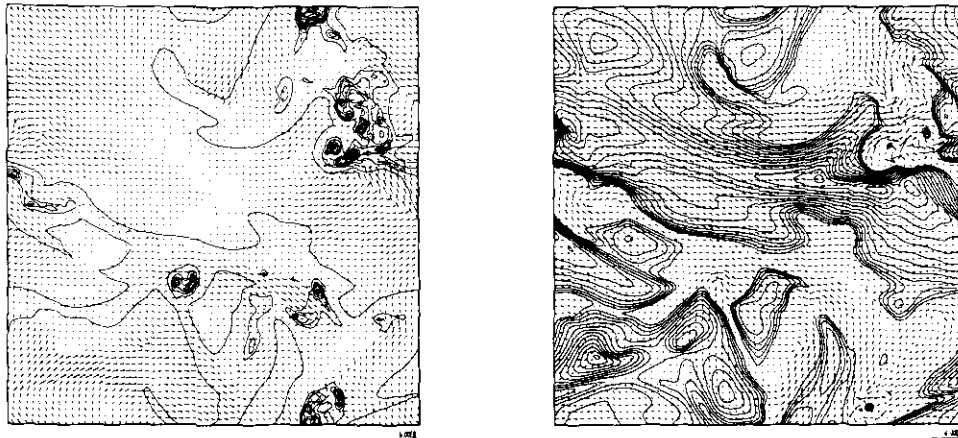


FIGURA 7.1: (Left) Density (contours) and velocity (arrows) fields of the numerical simulation at $t = 6.6 \times 10^7$ yr into the evolution. (Right) Same for the temperature (contours) and magnetic field (arrows). This is a two-dimensional simulation with a resolution of 512 grid points per dimension.

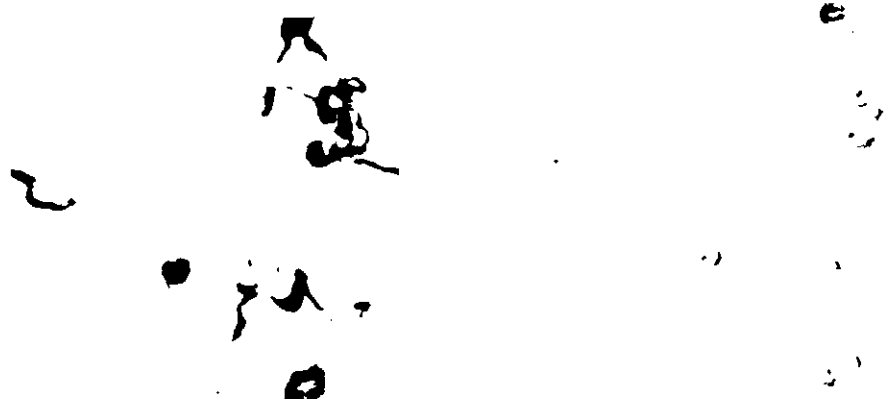


FIGURA 7.2: Masks defining the various clouds at $\rho_{\text{th}} = 4$ (left) and $\rho_{\text{th}} = 16$ (right). The integrals involved in the calculation of the various energies are calculated as sums over the areas defined by the masks.

$$\mathcal{E}_{\text{mag}} \equiv \frac{1}{2} \int B^2 dV. \quad (7.1)$$

In Fig. 7.1 (left) we show the density (contours) and the velocity (arrows) fields at $t = 6.6 \times 10^7$ yr. Similarly, Fig. 7.1 (right) shows the temperature and the magnetic fields. From Fig. 7.1, it is evident that the definition of a “cloud” is somewhat ambiguous, as smaller, denser clouds are hierarchically nested within larger, less dense condensations, as expected for flows in which the local density probability distribution function is independent of the local average density and decays at least exponentially with the fluctuation amplitude (Vázquez-Semadeni 1994). In this paper we adopt a simplistic approach, and define a cloud as a connected set of points whose densities are larger than an arbitrary threshold ρ_{th} .

With this definition, we have developed a numerical algorithm that identifies and labels all clouds, given ρ_{th} , and produces a “mask” file which can be used on all the other fields (Fig. 7.2). This allows us to perform the above integrals inside the exact cloud perimeters

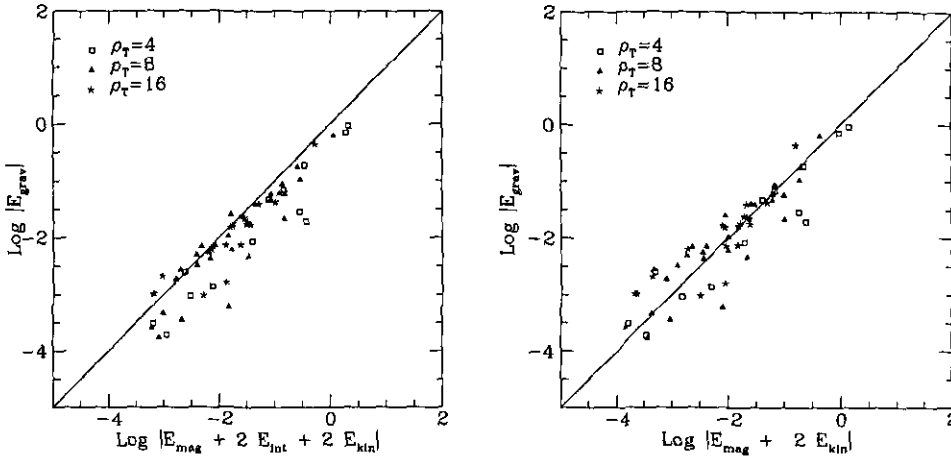


FIGURA 7.3: a) $\log |\mathcal{E}_g|$ vs. $\log(\mathcal{E}_{\text{mag}} + 2\mathcal{E}_{\text{th}} + 2\mathcal{E}_{\text{kin}})$. b) $\log |\mathcal{E}_g|$ vs. $\log(\mathcal{E}_{\text{mag}} + 2\mathcal{E}_{\text{kin}})$

and to evaluate the energies for each cloud. A full “survey” is made by taking several values of ρ_{th} , in order to include a wide range of cloud sizes. This is equivalent to combining observations obtained with several different tracer molecules. Note also that including clouds defined through various values of ρ_{th} does not amount to including the same cloud several times, since “child” clouds may have substantially different average properties than their “parents”. In particular, in the discussion and figures below, we have taken $\rho_{\text{th}} = 4$ (squares), 8 (triangles) and 16 (stars) (in code units).

7.3 Results

In Fig. 7.3a we show a plot of $\log |\mathcal{E}_g|$ vs. $\log(\mathcal{E}_{\text{mag}} + 2\mathcal{E}_{\text{th}} + 2\mathcal{E}_{\text{kin}})$, together with the line $\log |\mathcal{E}_g| = \log(\mathcal{E}_{\text{mag}} + 2\mathcal{E}_{\text{th}} + 2\mathcal{E}_{\text{kin}})$. A clear correlation between the gravitational and the sum of the remaining energies is observed, although with a dispersion of roughly an order of magnitude, similar to that found in observational studies (Myers & Goodman 1988b; Falgarone et al. 1992). Furthermore, it appears that the gravitational energy is systematically too low, and thus, according to this plot, most clouds in the simulation are not gravitationally bound.

However, it is well known (e.g., Shu 1990) that if the pressure is nearly uniform throughout the flow, then the contribution of the internal energy of the cloud is nearly balanced by the external pressure acting on the boundary of the cloud. In the simulation, the typical pressure contrast between clouds and the intercloud medium is ~ 5 , except in regions of star formation. The exact contribution of the external pressure requires an integral over the cloud’s boundary, which will be discussed in a future paper. In this preliminary report, we show in Fig. 7.3b a plot of $\log |\mathcal{E}_g|$ vs. $\log(\mathcal{E}_{\text{mag}} + 2\mathcal{E}_{\text{kin}})$, which corresponds to the case in which the surface pressure term exactly balances $2\mathcal{E}_{\text{th}}$. The actual situation must lie between the limiting cases depicted in Figs. 7.3a and b.

In order to search for possible equipartition among different forms of energy, in Fig. 7.4a we show a plot of $\log(\mathcal{E}_{\text{mag}})$ vs. $\log(2\mathcal{E}_{\text{kin}})$, and in Fig. 7.4b we show a plot of $\log(2\mathcal{E}_{\text{th}})$ vs. $\log(2\mathcal{E}_{\text{kin}})$. A tendency towards equipartition between the turbulent kinetic energy and the magnetic and internal energies is apparent, again with a typical dispersion of roughly

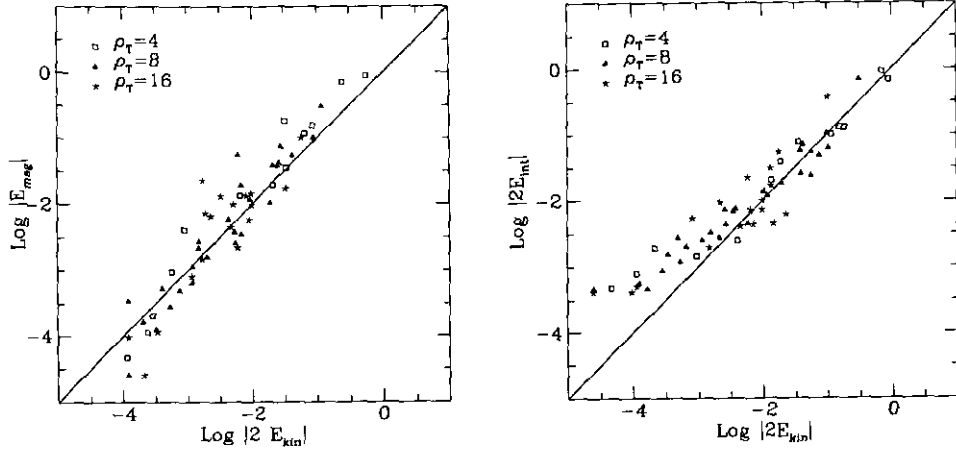


FIGURA 7.4: a) $\log |\mathcal{E}_g|$ vs. $\log(\mathcal{E}_{mag} + 2\mathcal{E}_{th} + 2\mathcal{E}_{kin})$. b) $\log |\mathcal{E}_g|$ vs. $\log(\mathcal{E}_{mag} + 2\mathcal{E}_{kin})$

an order of magnitude. Note that in Fig. 7.4b a deviation from equipartition seen at low values of the energies is probably an artifact of the simulation, because at small scales the velocity is damped by dissipation.

7.4 Conclusions

In this paper we have introduced a simple algorithm for identifying all clouds in numerical simulations of the ISM and presented preliminary statistics over the cloud sample. The gravitational energy appears to be in rough balance with the remaining forms of energy, although with non-negligible dispersion. This result is similar to those obtained from observations (e.g., Larson 1981; Myers & Goodman 1988a,b), and has been taken in those works to be indicative of near-virialization in clouds. However, we emphasize that the surface terms in the virial theorem may have an important, if not decisive, contribution to the overall virial balance of the clouds, as already suggested by the role of the thermal pressure in the data presented here.

The fact that there seems to be a trend for clouds to exhibit balance between gravity and its opposing agents suggests that the flow may indeed have a tendency towards producing nearly-virial clouds, in contradiction with the conjecture in Paper I. However, the relatively small dispersion about this balance may be an artifact of the low contrast in ρ_{th} used here due to numerical difficulties. This selects against small, low-density clouds in which gravity is sub-dominant. This difficulty, plus the contribution of the surface terms, the necessary modifications to the virial theorem in two-dimensions, and the longevity of clouds as a function of their closeness to virial balance, all need to be assessed before a conclusive answer can be given. Work is currently in progress to address these issues.

7.5 Fé de Erratas:

Nótese que el artículo original (Ballesteros-Paredes & Vázquez-Semadeni 1995), tiene dos erratas en la Figura 4: Por un lado, el pie de figura es el mismo que el de la Figura 3. Por

Capítulo 8

Artículo 2

Virial Balance in Turbulent MHD Two Dimensional Numerical Simulations of the ISM

Javier Ballesteros-Paredes and Enrique Vázquez-Semadeni

publicado en

Star Formation, Near and Far.

Eds. S. S. Holt & L. G. Mundy. (New York: AIP Press), p. 81. 1997.

Resumen

Presentamos resultados del análisis virial en simulaciones bidimensionales (2D) completamente no-lineales del MIE. Discutimos el Teorema Virial euleriano en 2D, y describimos resultados preliminares del balance virial de las nubes en las simulaciones. Las nubes están lejos de equilibrio estático, y el teorema virial es dominado por los términos que contienen derivadas temporales, indicando la importancia del flujo a través de las fronteras de la nube y de la redistribución de la masa. Se observa además que el término gravitacional es más importante a mayores escalas, aunque algunas pequeñas nubes son fuertemente autogravitantes. Los términos magnético y cinético escalan linealmente entre sí.

Abstract

We present results from a virial analysis of fully nonlinear two-dimensional (2D) simulations of the ISM. We discuss the Eulerian Virial Theorem in 2D, and describe preliminary results on the virial budget of clouds in the simulations. The clouds are far from a static

equilibrium, and the Virial Theorem is dominated by the time-derivative terms, indicating the importance of flux through the cloud boundaries and mass redistributions. A trend towards greater importance of the gravitational term at larger scales is observed, although a few small clouds are strongly self-gravitating. The magnetic and kinetic terms scale linearly with each other.

8.1 Introduction

Vázquez-Semadeni et al. (1995a, hereafter Paper I) and Passot et. al (1995, hereafter Paper II) have produced a numerical model of the interstellar medium (ISM) including enough physical agents as to render it feasible to perform statistical studies of the clouds formed in the simulations. The simulations include self-gravity, magnetic fields, parameterized cooling and diffuse heating, the Coriolis force, large-scale shear, and localized stellar energy input. In the present work, we discuss the Virial Theorem (VT) as it applies to the simulations, and present preliminary statistical results from a two-dimensional (2D) simulation with a resolution of 800×800 grid points, performed specifically for this analysis. In § 8.2 we discuss the VT, applying the formalism developed by McKee & Zweibel (1992) to the 2D case. In § 8.3 we describe the cloud-identifying algorithm and show preliminary statistical results, and in § 8.4 we present some remarks and discuss future work.

8.2 Virial Theorem in 2D

The VT is obtained by dotting the momentum equation (eq. [1b] in Paper I) with the position vector \mathbf{x} and integrating over volume. McKee & Zweibel (1992) have discussed an Eulerian form of the VT, which is most appropriate for our simulations, since they are performed with an Eulerian code. Because the simulations are 2D (in order to reach a sufficiently large resolution), we must consider the VT in 2D as well. It reads:

$$\frac{1}{2} \frac{d^2 \mathcal{I}_E}{dt^2} = 2 \left(\tau_{\text{kin}} + \tau_{\text{int}} \right) + M - W - E_{\text{cor}} - \frac{1}{2} \frac{d\Phi}{dt} \quad (8.1)$$

where $\tau_{\text{kin}} = 1/2(\int \rho u^2 dV - \oint_X x_i \rho u_i u_j \hat{n}_j dS)$ is the kinetic term, $\tau_{\text{int}} = \int P dV - 1/2 \oint_S P x_i \hat{n}_i dS$ is the thermal term, $M = 1/8\pi \oint_S x_i T_{ij} \hat{n}_j dS$ is the magnetic term, $W = \int x_i \rho g_i dV$ is the gravitational term, $E_{\text{cor}} = 2 \int x_i (\Omega \times \mathbf{u})_i dV$ is the Coriolis term, $\Phi = \oint_S \rho u_i r^2 \hat{n}_i dS$ is the flux of moment of inertia through the surface S , and ρ , \mathbf{u} , P and g_i are the density, velocity, thermal pressure and self-gravitational acceleration, respectively. Because of two-dimensionality, we must replace volumes by areas and surfaces by contours in (8.1). However, we retain the above notation for generality. Since in 2D¹ $\nabla \cdot \mathbf{x} = 2$, in equation (8.1) we note the three following interesting points: *a)* Although magnetic fields are present in the surface term $M = \int_S x_i T_{ij} \hat{n}_j dS$, (where the Maxwell stress tensor is defined as $T_{ij} \equiv 1/4\pi[B_i B_j - 1/2 B^2 \delta_{ij}]$), the “classical” magnetic energy term $E_{\text{mag}} = 1/8\pi \int B^2 dV$ does not enter the virial equation, so it does not provide support

¹Para una discusión más precisa sobre el Teorema virial en 2D, consultese el apéndice §B.

against gravity². b) The internal energy $E_{\text{int}} \equiv \int P dV$ does not contain the 3/2 factor as in 3D. Nevertheless, in 2D this term still coincides with the total internal energy, because there are only two translational degrees of freedom. c) Additionally, it can be shown that the gravitational term $\int x_i \rho g_i dV$ does not coincide with the gravitational energy $E_{\text{grav}} = 1/2 \int \rho \phi dV$ as it does in 3D for isolated clouds. Essentially, this is due to the slower distance dependence of the gravitational potential in 2D.

8.3 Preliminary Statistics

In order to calculate the terms in equation (8.1), we have performed a 2D simulation similar to the one called “Run 28” in Paper II, but with a resolution of 800×800 grid points. In this run we analyze the data shortly after turning off star formation, in order to allow for the largest possible density gradients (see Vázquez-Semadeni, Ballesteros-Paredes & Rodríguez 1997, hereafter Paper III) while still retaining the structure induced by the stellar energy injection. We have developed a numerical algorithm to identify clouds and evaluate within them the various terms entering the VT, as well as their velocity dispersion and mean density. We define a cloud as a connected set of pixels whose densities are larger than an arbitrary threshold ρ_{th} . Previous calculations (Paper III) have shown that the simulations exhibit similar scaling properties as those observed in real interstellar clouds (Larson 1981), except for the density-size scaling relation, supporting the possibility that it may be the result of an observational effect (see also Larson 1981, Kegel 1989, Scalo 1990). With this motivation, we have now performed evaluations of the various terms in the VT. We have the following preliminary results: 1.- Both the second derivative of the moment of inertia and the last term in the equation (8.1) are dominant in the overall virial balance (fig. 8.1a). 2.-Comparing the remaining terms, the turbulent terms are seen to dominate (fig. 8.1b). 3.-The surface terms (which are often neglected under the assumption of vanishing fields outside the clouds) are in general of magnitude comparable to that of the volumetric ones (figs. 8.1c and d). 4.-The gravitational term is most important at large scales (fig. 8.1e). However, there are a few small (low energy content) clouds which have large values of the gravitational term. These may be the best candidates for collapse and star formation. Their scarcity appears consistent with the low efficiency of star formation. 5.-The magnetic term and the sum of the kinetic terms are proportional to each other (fig. 8.1f). This suggests there is equipartition between kinetic and magnetic modes, except for a constant factor, which may be due to the fact that clouds have bulk velocities with respect to the integration volume.

8.4 Final Remarks

The dominance of the time-derivative and kinetic terms indicates the importance of flow through the volume boundaries, contrary to the cases considered by McKee & Zweibel (1992). In order to minimize this effect, it appears necessary to consider Eulerian volumes instantaneously at rest with respect to the center of mass of the clouds. However,

²Para una discusión sobre la contribución magnética al soporte en 2D, consultese el apéndice B.

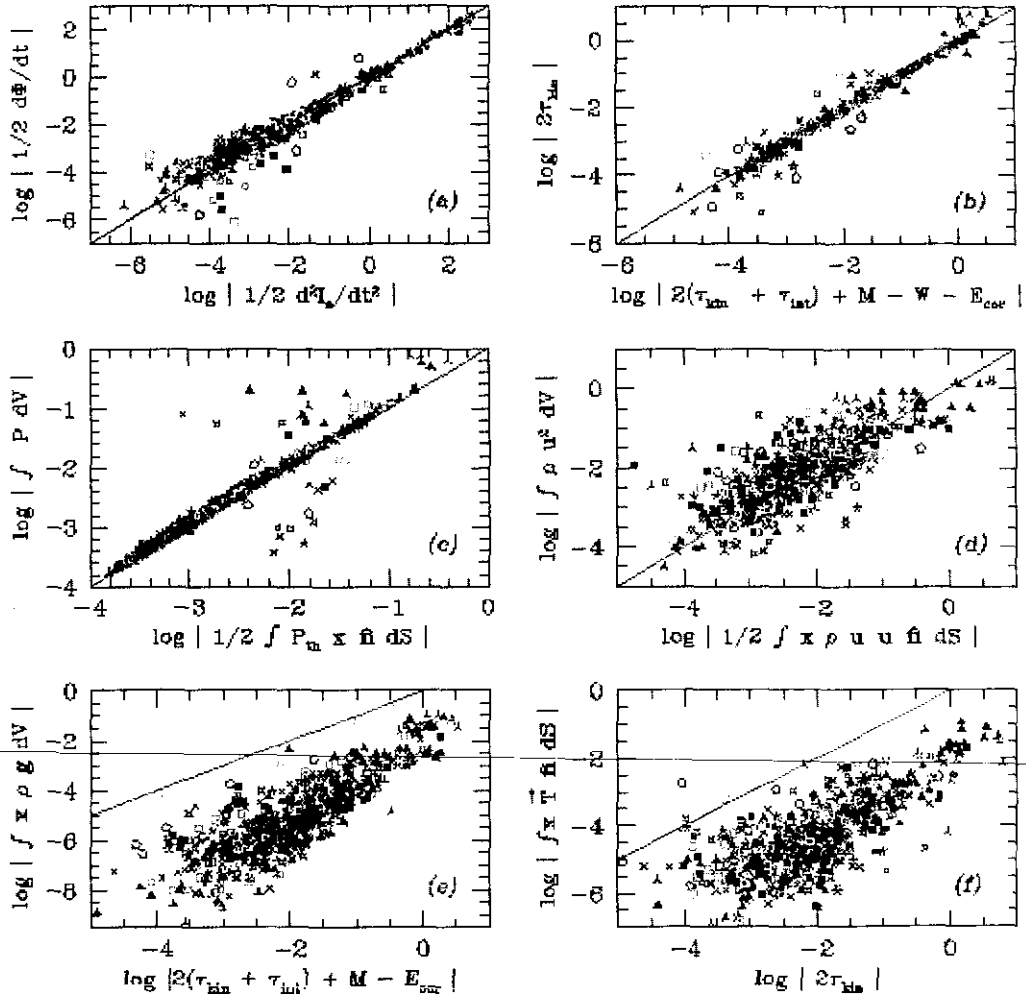


FIGURA 8.1: In all panels, the solid line is the identity. (a) $1/2||d\Phi/dt||$ vs. $1/2||d^2I/dt^2||$. Their near equality shows that the term $1/2d\Phi/dt$ dominates the virial sum, indicating the importance of the variability of the mass flux through the clouds' borders for the total virial balance. (b) Volume-plus-surface kinetic terms vs. the virial sum neglecting the $1/2d\Phi/dt$ term. The near equality of both terms indicates the dominance of the kinetic terms over the remaining ones. This effect may be due to cloud bulk motion and should be eliminated by using an instantaneously-at-rest frame of reference for each cloud. (c) Volume vs. surface terms for internal energy (pressure) and (d) kinetic energy. The surface terms are seen to be comparable to the volume terms in general. The few points with large scatter in (c) are likely to correspond to regions of anomalous pressures due to recent star formation. (e) The gravitational term W vs. the sum of the remaining virial terms. A trend towards greater importance at larger scales is seen. However, a few points at near balance with gravity are seen at all scales. (f) Magnetic term M vs. the sum of the kinetic terms. An almost linear relation is observed. This is consistent with equipartition between kinetic and magnetic modes, if an offset is present, again due to the fact that clouds may have bulk velocities with respect to the integration volume.

preliminary attempts suggest that the flow through the boundaries cannot be eliminated completely, since the clouds are extremely amorphous and change shape rapidly. This work will be reported in a future paper.

Capítulo 9

Las Relaciones de Larson

9.1 Las Relaciones de Larson y Algunas de sus Implicaciones.

Adicionalmente al posible balance energético, el teorema virial ha sido utilizado para explicar las relaciones de escala encontradas observacionalmente por Larson (1981):

$$\begin{aligned}\rho &\propto R^\alpha \\ \delta v &\propto R^\beta.\end{aligned}\tag{9.1}$$

Como se indica en el capítulo 10, los valores más frecuentemente mencionados para α y β son -1 y 0.5 , respectivamente (ver, por ej., Larson 1981; Torrelles et al. 1983; Myers 1983; Falgarone et al. 1986; Myers & Goodman 1988a y b; etc.) Las relaciones de escala (9.1) tienen algunas implicaciones físicas importantes:

1. El valor $\alpha = -1$ tiene la implicación de que la densidad columnar N es constante para un medio de densidad volumétrica constante. En ese caso particular,

$$N = \rho R \propto R^{\alpha+1}.\tag{9.2}$$

de manera que cabe la pregunta ¿sería posible que las nubes interestelares, con tamaños y características que varían en muchos órdenes de magnitud, tuvieran la misma densidad columnar? Como se discute en §10 (ver también Larson 1981; Kegel 1989; Scalo 1990), el resultado de densidad columnar constante puede ser consecuencia del limitado intervalo dinámico de las observaciones, las cuales difícilmente podrían detectar una nube de tamaño pequeño y densidad volumétrica baja (es decir, de densidad columnar pequeña). Existe evidencia observacional (Falgarone et al. 1991) y numérica (Vázquez-Semadeni & Ballesteros-Paredes & Rodríguez 1997), (ver §10) de que la relación densidad promedio-tamaño no es real, sino que es resultado de las limitaciones dinámicas de las observaciones (Scalo 1990).

2. Si se supone equipartición¹ entre la energía gravitacional y la cinética, y algún valor

¹Nótese que frecuentemente se dice “equilibrio virial” en lugar de equipartición (e.g., Fuller & Myers 1992). Sin embargo, como se mencionó en §6.5, equipartición no necesariamente implica equilibrio virial.

particular para alguno de los exponentes α o β , entonces el otro exponente queda determinado (ver, por ejemplo, Shu et al. 1987; Myers & Goodman 1988, Vázquez-Semadeni 1999):

$$\mathcal{E}_{\text{kin}} \sim \mathcal{W} \Rightarrow \delta v^2 \propto \frac{GM}{R} \propto \rho R^2 \propto R^{\alpha+2} \quad (9.3)$$

por lo que, en este caso, $\beta = (\alpha + 2)/2$. En particular, si $\alpha = -1$ entonces $\delta v \propto R^{1/2}$. En otras palabras, $\alpha = -1$ y $\beta = 1/2$ satisfacen simultáneamente la equipartición entre la energía cinética y la gravitacional. Sin embargo, cabe notar que estos valores no son únicos, sino que existe un continuo de valores $\beta = (\alpha + 2)/2$ que satisfacen estas condiciones (Vázquez-Semadeni & Gazol 1995).

3. Un resultado similar se encuentra si se supone equipartición entre la energía magnética y gravitacional, de manera que $\delta v \sim v_A$, donde v_a es la velocidad de Alfvén (Myers & Goodman 1988). En estas condiciones, las nubes típicamente deberían tener una masa cercana a o del orden de la masa crítica M_Φ , definida en §4.3.
4. Existe una escala característica, R_0 , para la cual la dispersión de velocidades es igual al ensanchamiento térmico. Dado que el ensanchamiento térmico depende de la masa de la molécula que se esté observando, esta escala característica varía dependiendo del trazador usado. Sin embargo, para las moléculas más utilizadas, y dentro de las regiones más densas y frías ($T \sim 10$ K), dicha escala es del orden de 0.01 a 0.1 pc.

Es importante mencionar que mientras que el teorema virial se aplica a la evolución de una parcela de fluido (o a una región del espacio en el caso de la versión euleriana), las relaciones de escala, tal como las estableció Larson (Larson 1981), se satisfacen para un conjunto (ensamble) de nubes.

Algunos trabajos se han enfocado a analizar relaciones de escala dentro de una misma región, estudiando la posible variabilidad del ancho no térmico de la línea como función de la distancia al centro (máximo de intensidad) de la región (e.g., Fuller & Myers 1992). Recientemente, Goodman et al. (1998) y Barranco et al. (1998), han encontrado que la relación dispersión de velocidades-tamaño tiene exponente muy pequeño ($\beta \sim 0.1$) en regiones de tamaños ≤ 0.1 pc. Este resultado ha sido interpretado por esos autores en términos de que se ha llegado a la “escala de coherencia” de la turbulencia, es decir, a escalas donde la turbulencia se disipa. Sin embargo, esta interpretación es cuestionable, ya que la disipación de la turbulencia implicaría que el ancho no-térmico tendería a cero, y no a un valor constante conforme el tamaño de la región varía. Este resultado, por el contrario, pudiera ser consecuencia de que los autores calcularon la relación efectuando un promedio sobre isocontornos de intensidad, pudiendo entonces borrar la variabilidad a pequeña escala a lo largo de dicho isocontorno (Ballesteros-Paredes & Vázquez-Semadeni, en preparación).

Por otra parte, se ha encontrado que la relación $\Delta v \sim R$ presenta diferentes exponentes de acuerdo con la región que se analiza. Por ejemplo, regiones de formación estelar masiva tienen exponentes más aplanados (Carr 1983; Caselli & Myers 1995), mientras que regiones

de formación de estrellas de baja masa parecen tener exponentes más parecidos a los valores estándar de $\beta \sim 1/2$ (Torrelles et al. 1983, Myers & Goodman 1988a, b); y regiones HII ultracompactas tienen incluso exponentes β negativos (Xie et al. 1997).

Finalmente, en la mayoría de los estudios observacionales se interpreta que la gran dispersión (de 1 a 2 órdenes de magnitud) en los datos respecto a los valores de balance virial es debido a la incertidumbre en los datos (ver, por ejemplo, Myers & Goodman 1988a,b). Sin embargo, esta dispersión puede ser real, implicando que no existe un verdadero balance virial, como han señalado Scalo (1990) y Vázquez-Semadeni (1988), entre otros.

Otras explicaciones de las relaciones de Larson (9.1) han sido propuestas por diferentes autores, por ejemplo:

- Larson (1981) menciona la posibilidad de que la relación densidad-tamaño pueda ser consecuencia de choques planos, de manera que, en general, la densidad columnar se mantenga razonablemente constante a lo largo de la dirección de propagación del choque. Nótese que esto concuerda con nuestro resultado de que las nubes son formadas por choques o compresiones (§13). Sin embargo, si bien este mecanismo podría explicar la constancia de la densidad columnar para una nube dada, no es claro que todas las compresiones involucren la misma masa y tamaño. Entonces, la relación densidad-tamaño para un conjunto (ensamble) de nubes de diferentes masas, tamaños, etc., no queda claramente explicada.
- Chiéze (1987) propone que un conjunto de nubes al borde de la inestabilidad gravitacional en un ambiente con presión externa debe satisfacer las relaciones de Larson.
- La relación $\Delta v - R^{1/2}$ puede ser consecuencia de que un campo de velocidades dominado por choques tiene un espectro de energías de la forma k^{-2} , siempre y cuando pueda asociarse Δv^2 , el ancho no-térmico de la línea, con u_l^2 , la energía cinética cuadrática media por unidad de masa en modos turbulentos de tamaño menor o igual que una escala l . Para verificar esto de manera cualitativa demostraremos primariamente que para un choque unidimensional, el espectro de energías es del tipo k^{-2} . Representemos entonces al choque por un campo de velocidades de la forma

$$v(x) \propto H(x - x_0)$$

donde $H(x - x_0)$ es la función escalón o de Heaviside. Para encontrar su representación en el espacio de Fourier, notemos que la derivada de esta función está dada por:

$$\frac{dv(x)}{dx} \propto \delta(x - x_0)$$

donde $\delta(x - x_0)$ es la función delta de Dirac. Entonces, la transformada de Fourier (FT) de la derivada espacial del campo de velocidades es una función constante:

$$FT_k(dv/dx) = cte$$

donde k es el número de onda. Como la transformada de Fourier de una derivada espacial es k veces la transformada de la función, entonces

$$FT_k(v) \propto k^{-1}.$$

de manera que el espectro de energías de un choque queda dado por

$$E(k) \propto (FT_k(v))^2 \propto k^{-2} \quad (9.4)$$

Ahora bien, dado un espectro de energías $E(k)$, la energía cinética cuadrática media por unidad de masa contenida en modos de frecuencia mayores a $2\pi/l$ esta dada por:

$$u_l^2 \sim \int_{2\pi/l}^{\infty} E(k) dk.$$

Si $E(k) \propto k^n$, con $n < -1$ entonces

$$u_l^2 \propto \left(\frac{2\pi}{l}\right)^{n+1}.$$

En particular, para $n = -2$ (espectro de choques, ec. [9.4])

$$u_l \propto l^{1/2}. \quad (9.5)$$

Finalmente, el último paso, y a su vez el más incierto, consiste en asociar la “velocidad característica” u_l con $\Delta v(l)$, la dispersión de velocidades observada en una región de tamaño proyectado l en el plano del cielo. En el caso de u_l , ésta es, típicamente, la diferencia de velocidades característica entre puntos separados por una distancia l , obtenida como un promedio sobre todo el espacio, y está relacionada con la función de estructura del sistema (ver, por ej., Vázquez-Semadeni 1999). Por su parte, $\Delta v(l)$ es la dispersión de velocidades característica en el plano del cielo, observada en una región particular, utilizando un trazador dado e integrada a lo largo de la visual. Entonces, en principio, no hay razón para esperar que estas dos cantidades sean iguales, aunque si se supone que el tamaño de la región a lo largo de la línea de visión es comparable a su extensión en el plano del cielo, es de esperar que $\Delta v(l)$ sea, en promedio, similar a u_l .

Existen en la literatura otras explicaciones para las relaciones de escala, por ejemplo, las cascadas de momento angular (Henriksen & Turner 1984), densidad de energía cinética (Ferrini et al. 1983; Fleck 1996), etc., aunque en el presente trabajo no serán consideradas.

9.2 Trabajo Publicado al Respecto

Las simulaciones constituyen un laboratorio ideal para estudiar la presencia y origen de estas relaciones, pues, por un lado, satisfacen la misma física (o al menos, muy cercanamente) que el MI real, y por otro, no se encuentran sujetas a las limitaciones inherentes a las observaciones, como son el tiempo de integración, el ruido instrumental o incertidumbres debidas a los efectos de proyección, etc., aunque por otro lado las simulaciones están limitadas por la resolución máxima que puede alcanzarse y la dimensionalidad, así como los efectos disipativos artificiales, propios de todo código numérico. Sin embargo, con estas limitaciones es posible sugerir cuáles son las bases físicas de dichas relaciones. Así, en el siguiente capítulo (§10) estudiamos las relaciones de Larson y el espectro de masas de las nubes obtenidas en simulaciones numéricas.

Capítulo 10

Artículo 3

A Search for Larson-Type Relations in Numerical Simulations of the ISM. Evidence for Non-Constant Column Densities

Enrique Vázquez-Semadeni, Javier Ballesteros-Paredes and Luis F. Rodríguez

ApJ. **474**, 292 1997

Resumen

Presentamos resultados de un estudio estadístico de nubes en simulaciones numéricas bidimensionales del medio interestelar. Las nubes en las simulaciones presentan un espectro de masas diferencial de la forma $dN(M)/dM \sim M^{-1.44 \pm 0.1}$ y una relación dispersión de velocidades-tamaño de la forma $\Delta v \sim R^{0.41 \pm 0.08}$. Sin embargo, las nubes *no* presentan una clara relación densidad-tamaño. A una densidad promedio dada, las nubes se encuentran dispersas sobre un intervalo de tamaños desde las escalas más pequeñas resueltas hasta la máxima, dada por una recta envolvente tipo de relación de Larson $R_{\max} \sim \rho^{\alpha}$, con $\alpha = -0.81 \pm .15$, aunque no es posible descartar los efectos numéricos como responsables de esta última correlación. Las nubes, adicionalmente, están distribuidas en un intervalo de densidades columnares N de dos órdenes de magnitud, apoyando la sugerencia de que la relación densidad-tamaño pueda ser consecuencia de las limitaciones de los censos. En este caso, la relación $\Delta v-R$ puede ser interpretada como una consecuencia directa de un espectro turbulento de la forma k^{-2} , más que del equilibrio virial de las nubes satisfaciendo una ley $\rho \propto R^{-1}$. El espectro k^{-2} es verificado en las simulaciones y es característico de un

campo de choques. Sin embargo, también discutimos la posibilidad de que las nubes estén en balance entre la autogravedad y la turbulencia, pero con una dispersión de al menos un factor de 10 en la relación $\Delta v - R$, y de 100 en la relación densidad-tamaño., de acuerdo con la relación $\Delta v \sim (NR)^{1/2}$.

Adicionalmente, comparamos estos resultados con datos observacionales. Proponemos un modelo simple que sugiere que recientes resultados, los cuales encuentran densidades columnares aproximadamente constantes para nubes IRAS oscuras, pueden ser artificiales, debidos a un gradiente de temperaturas en las nubes, inducidos por el calentamiento radiativo externo. Como consecuencia, enfatizamos que el brillo superficial de los mapas IRAS no son apropiados para medir densidades columnares.

Abstract

We present results from a statistical study of clouds in two-dimensional numerical simulations of the interstellar medium. The clouds in the simulations exhibit a differential mass spectrum $dN(M)/dM \sim M^{-1.44 \pm 0.1}$ and a velocity dispersion-size relation $\Delta v \sim R^{0.41 \pm 0.08}$. However, the clouds do *not* exhibit a clear density-size relation. At a given mean density, clouds span a range of sizes from the smallest resolved scales up to a maximum given by a Larson-type relation $R_{\max} \sim \rho^\alpha$, with $\alpha = -0.81 \pm .15$, although numerical effects cannot be ruled out as responsible for the latter correlation. The clouds additionally span a range of column densities N of two orders of magnitude, supporting the suggestion that the observational density-size relation may be an artifact of survey limitations. In this case, the $\Delta v - R$ relation can be interpreted as a direct consequence of a k^{-2} turbulent spectrum, rather than of virial equilibrium of clouds satisfying a $\rho \propto R^{-1}$ law. The k^{-2} spectrum is verified in the simulations and is characteristic of a field of shocks. However, we also discuss the possibility that the clouds are in balance between self-gravity and turbulence, but with a scatter of at least a factor of 10 in the $\Delta v - R$ relation, and of 100 in the density-size relation, according to the equilibrium relation $\Delta v \sim (NR)^{1/2}$.

In addition, we compare these results with observational data. We propose a simple model suggesting that recent results which find nearly constant column densities for dark IRAS clouds may be an artifact of a temperature gradient within the clouds induced by external radiative heating. As a consequence, we emphasize that IRAS surface brightness maps are not appropriate for measuring column densities.

10.1 Introduction

Interstellar clouds appear to follow a set of scaling relations first noticed by Larson (1981), and then apparently confirmed (with slight modifications) by a number of other workers. These “Larson’s relations” have the form

$$\rho \sim R^\alpha \quad (10.1)$$

$$\Delta v \sim R^\beta, \quad (10.2)$$

where R is the cloud size, ρ is the gas density, Δv is the velocity dispersion derived from the line widths, and α and β are the constant scaling exponents. Additionally, the clouds

are found to exhibit a mass distribution of the form

$$\frac{dN(M)}{dM} \sim M^n. \quad (10.3)$$

The most commonly quoted values of the exponents are $\alpha \sim -1.15 \pm .15$, $\beta \sim 0.4 \pm .1$, and $n \sim -1.55 \pm .15$ (Larson 1981; Torrelles et al. 1983; Dame et al. 1986; Falgarone & Péault 1987; Myers & Goodman 1988a; Falgarone, Puget & Péault 1992, hereafter FPP; Fuller & Myers 1992; Miesch & Bally 1994; Wood, Myers & Daugherty 1994, hereafter WMD; Caselli & Myers 1995; see also the reviews by Scalo (1985, 1987) and Blitz (1991)). However, significantly discrepant values have also been reported (e.g., Carr 1987; Loren 1989), and the validity of these scaling relations is currently the subject of strong controversy within the community.

The above “standard” values of the exponents for eqs. (10.1) and (10.2) have been interpreted in terms of the virial theorem (e.g., Larson 1981; Myers & Goodman 1988a; Caselli & Myers 1995). For $\alpha = -1$ (which coincidentally implies constant column density), a value $\beta = 0.5$ implies virial balance between self-gravity and the internal velocity dispersion. However, note that for an arbitrary value of the density scaling exponent α , a corresponding virial balance value of β can always be found (Vázquez-Semadeni & Gazol 1995). Thus, the density-size relation (10.1) remains unexplained. In fact, it has been proposed by Scalo (1990) that this relation may be a mere artifact of the dynamic range limitations of the observations, and does not reflect a real property of interstellar clouds. In particular, in the case of molecular line data, the observations are restricted to column densities large enough that the tracer molecule is shielded against photo-dissociating radiation. On the other hand, while the proportionality between line integrated CO intensity and mass surface density has been reliably established for extragalactic observations (Dickman et al. 1986), this relationship is only valid for scales at which calibrations have been possible, i.e., scales larger than a few pc. Furthermore, for clumps within molecular clouds, the structures identified in CO often do not correspond to those identified with higher-density tracers (e.g., Massi & Lizano 1994; J. Scalo, private communication).

In this paper we present the mass spectrum of clouds and search for Larson-type correlations in three two-dimensional numerical simulations of turbulence in the interstellar medium (ISM), one from Passot, Vázquez-Semadeni & Pouquet (1995, hereafter PVP95a), and the other two being variants of the former with respectively larger density contrasts and larger resolution. We have developed a cloud-identifying algorithm which allows us to measure the average density, velocity dispersion and total mass within well-defined (though arbitrary) cloud boundaries in the density fields of the simulations. The cloud sample thus obtained has the advantage over actual observations that no tracer limitations exist in “detecting” the clouds, although, on the other hand, a form of saturation is present due to the relatively small density dynamic range and other numerical limitations of the simulations.

In § 2 we briefly describe the simulations and the cloud-identifying algorithm, and in § 3 we present the resulting statistical cloud properties. In § 4 we analyze the limitations of the simulations, discuss the implications of the absence of a density-size relation, and give a preliminary discussion of the physical mechanisms behind the velocity dispersion-size

relation. We also compare the results with recent corresponding observations, in particular those of WMD. Finally, § 5 summarizes the results.

10.2 Numerical Method

PVP95a presented magneto-hydrodynamical simulations of the ISM incorporating model terms for cooling, diffuse heating and local heating from star formation. The simulations solve the equations for the evolution of the density, velocity, internal energy and magnetic fields in the presence of self-gravity, namely

$$\frac{\partial \rho}{\partial t} + \nabla \cdot (\rho \mathbf{u}) = \mu \nabla^2 \rho, \quad (10.4)$$

$$\frac{\partial \mathbf{u}}{\partial t} + \mathbf{u} \cdot \nabla \mathbf{u} = -\frac{\nabla P}{\rho} - \nu_8 \nabla^8 \mathbf{u} - \left(\frac{J}{M_a}\right)^2 \nabla \phi + \frac{1}{\rho} (\nabla \times \mathbf{B}) \times \mathbf{B} - 2\Omega \times \mathbf{u}, \quad (10.5)$$

$$\frac{\partial e}{\partial t} + \mathbf{u} \cdot \nabla e = -(\gamma - 1)e \nabla \cdot \mathbf{u} + \kappa_T \frac{\nabla^2 e}{\rho} + \Gamma_d + \Gamma_s - \rho \Lambda, \quad (10.6)$$

$$\frac{\partial \mathbf{B}}{\partial t} = \nabla \times (\mathbf{u} \times \mathbf{B}) - \nu_8 \nabla^8 \mathbf{B}, \quad (10.7)$$

$$\nabla^2 \phi = \rho - 1. \quad (10.8)$$

We refer the reader to Vázquez-Semadeni, Passot & Pouquet (1995a) and PVP95a for full details on the simulations. Here we just point out that the simulations from which the data are extracted represent a square section of the ISM along the Galactic plane of size 1 kpc on a side, with a resolution of 512 grid points per dimension. Also, it is important to note that all the evolution equations contain dissipative or diffusive terms which are necessary since the numerical technique used to solve the equations (spectral method) does not produce numerical viscosity, so the dissipation must be included explicitly. The momentum and magnetic field equations contain “hyperviscosity” terms of the form ∇^8 , which confine the viscous effects to the very smallest scales in the simulations (Babiano et al. 1987; McWilliams 1984). However, although globally dissipative, hyperviscosity is not everywhere positive definite (Passot & Pouquet 1988), so standard Laplacian terms are used in the continuity and internal energy equations.

Throughout the paper, densities are expressed in units of 1 cm^{-3} and velocities in units of 11.7 km s^{-1} , the units used in PVP95a. In particular, in the present paper we will use data from the run labeled Run 28 in PVP95a. However, the star-formation scheme used in the simulations of PVP95a assumes that a star is formed wherever the local density exceeds a critical value ρ_{th} . (A “star” in the simulations is a point source of heat.) This naturally imposes an upper limit on the densities reached by the model, since the stellar heating increases the local pressure and causes the gas to expand. Thus, densities above ρ_{th} are very rarely reached. In Run 28, $\rho_{\text{th}} = 30$, limiting the density contrast $\rho_{\text{max}}/\rho_{\text{min}}$ to values ~ 1000 . In order to obtain a somewhat larger dynamic range, we have performed an additional run, called Run 28bis, which is identical to Run 28 up to $t = 6.5 \times 10^7 \text{ yr}$, but afterwards has the star formation turned off. This run ends up collapsing gravitationally at

$t \sim 8.8 \times 10^7$ yr due to the lack of support from stellar energy injection, but intermediate times provide a good framework for study, exhibiting density maxima $\gtrsim 100 \text{ cm}^{-3}$, and density contrasts $\gtrsim 5000$. Finally, a run similar to Run 28bis but at a larger resolution (800×800 , referred to as Run 28.800) was also performed to discuss the effects of dissipation. As an illustration, fig. 10.1 shows a contour plot of the density field of Run 28 at $t = 6.6 \times 10^7$ yr, with the velocity field represented by the arrows. Note that, although the size scales represented by the runs are larger than those studied by most papers concerned with cloud statistics, we expect the results to be applicable, since all terms in the equations solved in the simulations are scale-free, except for the dissipative ones.

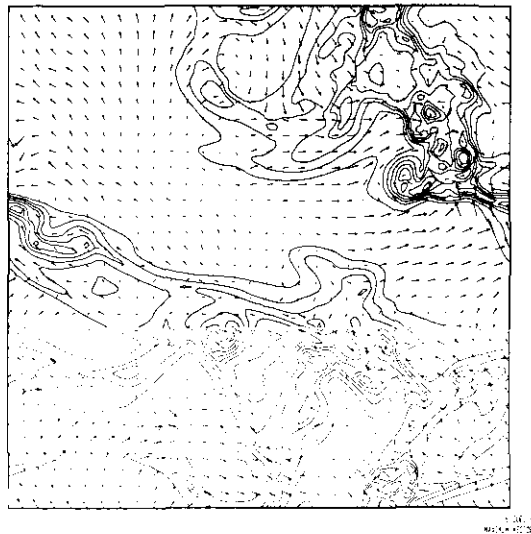


FIGURA 10.1: Density (contours) and velocity (arrows) fields for Run 28 at $t = 6.6 \times 10^7$ yr. The contours are spaced logarithmically, with increments of 0.3125 in $\log \rho$. The minimum density in this plot is 0.04 cm^{-3} , and the maximum density is 40 cm^{-3} .

In order to investigate the statistical properties of the clouds in the simulations, we have developed an automated algorithm which identifies and labels clouds. We define clouds as connected sets of pixels with densities above a user-defined density threshold ρ_{th} . The types of clouds that are identified in this way are thus clearly dependent on the value chosen for ρ_{th} , a somewhat similar situation to performing observations using various density tracers. As an example, figs. 10.2a and 10.2b show the clouds obtained by respectively setting $\rho_{\text{th}} = 4$ and $\rho_{\text{th}} = 16$, at time $t = 6.6 \times 10^7$ yr into the evolution of Run 28.

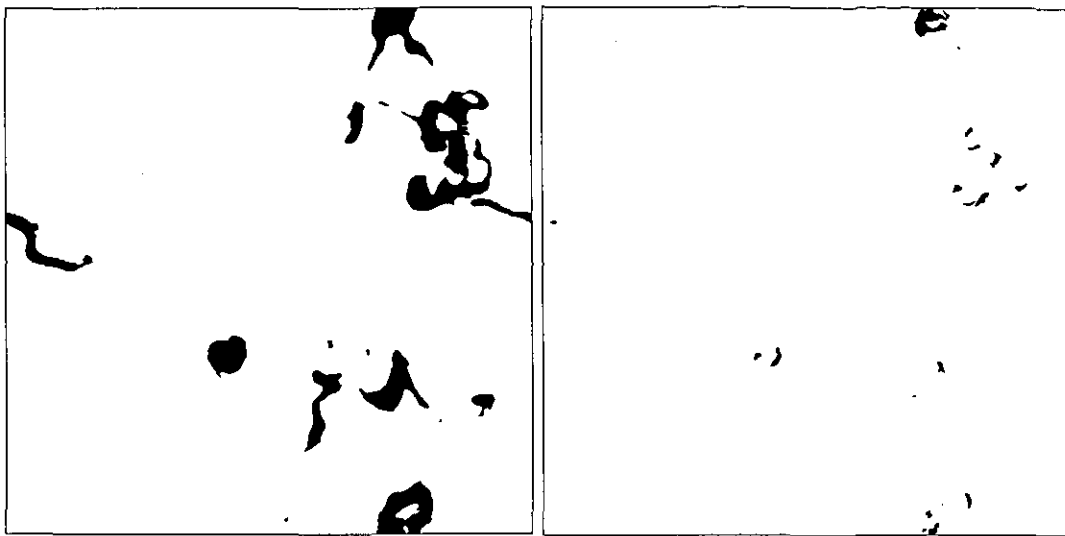


FIGURA 10.2: Regions (“clouds”) with densities larger than an arbitrary threshold ρ_{th} in the density field of Run 28 at $t = 6.6 \times 10^7$ yr. a) $\rho_{\text{th}} = 4$. b) $\rho_{\text{th}} = 16$. Note that small clouds with high densities are nested within larger complexes, but small clouds with low densities can be seen in a) as well.

The extremely irregular shapes of most clouds are noteworthy, and in fact pose a problem in defining the “size” R of a given cloud. For simplicity, here we take the size of a cloud as the square root of the number of pixels it contains. This definition may be somewhat unrealistic if clouds are fractal in such a way that their perimeters are not proportional to the square root of their areas (e.g., Scalo 1990; Falgarone et al. 1991), but for simplicity and similarity to observational work we adopt it here. Also, for convenience, sizes are expressed in pixels in most of the figures below (1 pixel ~ 2 pc).

For each cloud found by the algorithm, it is then a trivial matter to compute the average density, the mass, and the turbulent velocity dispersion, calculated as $\Delta v \equiv \langle (\mathbf{u} - \langle \mathbf{u} \rangle)^2 \rangle^{1/2}$, where \mathbf{u} is the local value of the velocity and $\langle \mathbf{u} \rangle$ is the average over the cloud area. Note that this quantity is not density-weighted.

10.3 Statistical Cloud Properties

We have obtained relatively large samples of clouds by considering values of $\rho_{\text{th}} = 3, 4, 6, 8, 11, 16, 23$, and 29 in Run 28, and $\rho_{\text{th}} = 3, 4, 6, 8, 11, 16, 23, 32, 45, 64$, and 90 in Run 28bis. Clouds obtained with each value of ρ_{th} are indicated with a particular symbol type in the plots discussed below. In what follows, the data from Run 28 will be considered at $t = 6.6 \times 10^7$ yr, and Run 28bis at $t = 7.15 \times 10^7$ yr, unless otherwise noted. The cloud samples for those cases contain 158 and 145 clouds, respectively.

Figures 10.3a and 10.3b show the logarithmic mass distributions of the clouds for Run 28 and Run 28bis, respectively. The masses are expressed in the nondimensional units of the simulations, in which the total mass contained is $4\pi^2$, corresponding to $0.36 \times 10^7 M_\odot$ in real units. The turnover at low masses may be attributed to incompleteness due to the finite resolution. The high-mass sides of the distributions, however, exhibit least-squares slopes

(fitted for $\log M > 0.8$ and shown as the straight lines) which imply indices $n = -1.51$ and -1.43 , respectively (c.f. eq. [10.3]). These values are within the range of values reported in various observational results (e.g., Wood et al. 1994; see also the reviews by Scalo 1985, Blitz 1991, Mundy 1994, and references therein).

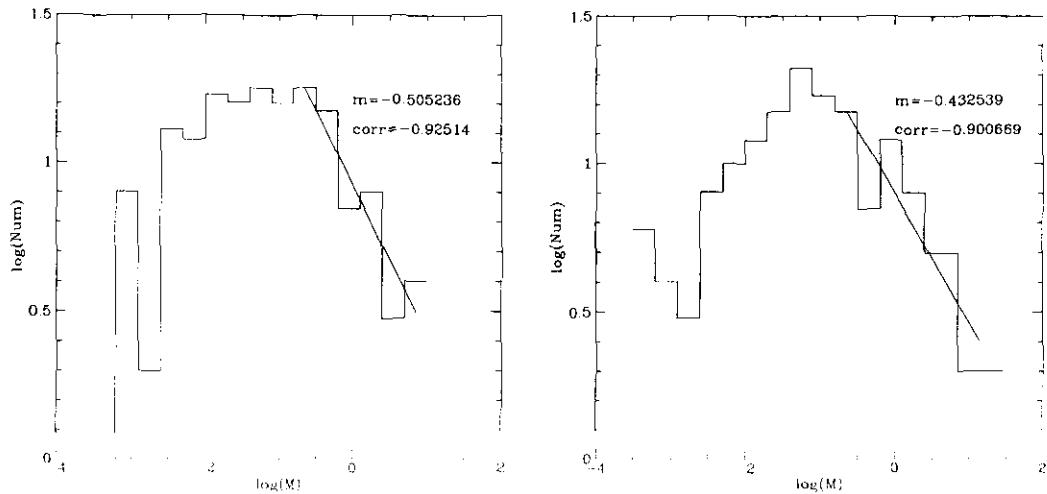


FIGURA 10.3: Logarithmic mass distributions for a) Run 28 at $t = 6.6 \times 10^7$ yr and b) Run 28bis at $t = 7.15 \times 10^7$ yr. The lines show least-squares fits to data bins with $\log M > 0.8$, and have slopes -0.51 in a) and -0.43 in b).

Figures 10.4a and 10.4b show the correlation between velocity dispersion and size for all clouds with sizes $\gtrsim 2$ pixels (1-pixel clouds are excluded as they have no velocity dispersion). Least squares fits to the data give slopes (shown as the solid lines) $\beta \sim 0.37$ and $\beta \sim 0.39$ respectively for Run 28 and Run 28bis, with moderately tight correlation coefficients ~ 0.6 . The large scatter of about one order of magnitude in the correlations should be emphasized. This is comparable to the scatter found for molecular-line data (e.g., FPP). The derived values of $\beta \sim 0.4$ are slightly lower than the most commonly accepted value of 0.5 (dotted lines), but are remarkably close to determinations that include heterogeneous data sets (Larson 1981; FPP; Fuller & Myers 1992).

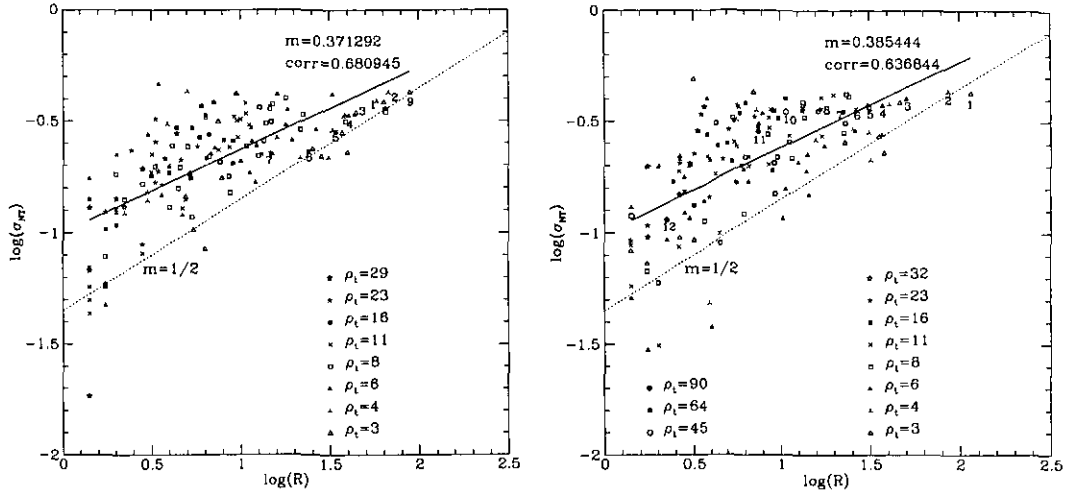


FIGURA 10.4: Velocity dispersion *vs.* size for all clouds in a) Run 28 at $t = 6.6 \times 10^7$ yr and b) Run 28bis at $t = 7.15 \times 10^7$ yr. Clouds obtained with each value of ρ_{th} are shown with a specific symbol as indicated. The solid lines show least-squares fits, with the slopes and correlation coefficients indicated. For reference, a $1/2$ slope is indicated by the dotted lines. The cloud labels in a) and b) are respectively the same as in a) and b) of figs. 10.5a and b.

Figures 10.5a and 10.5b show the average density $\langle \rho \rangle$ *vs.* size for the snapshots of the two runs. Several points should be remarked. First, note that, in general, the average density of the clouds is quite similar to the value of ρ_{th} used to define the cloud, and in fact tends to *increase* with size at each ρ_{th} . This is not surprising, due to the presence of dense “cores” inside the largest clouds at each ρ_{th} , which tend to increase their average density. Second, no clear correlation can be seen in either figure. Instead, at a given ρ_{th} , clouds down to the smallest possible size are seen. These are *small clouds with low densities* and, therefore, low column densities¹ $N = \rho R$. Third, the size of the largest cloud at each ρ_{th} is smaller for larger ρ_{th} . In particular, in both figures the set of largest clouds at each ρ_{th} seems to lie near a $\rho \sim R^{-1}$ law, similar to the standard exponent in Larson’s relation (10.1).

¹Note that the column density defined here refers to a cut through the clouds *on* the plane of the simulations, and has units of cm^{-2} . To obtain a column density with units cm^{-1} , appropriate to our two-dimensional problem, a multiplication by the unit length along the third (z) dimension, perpendicular to the plane of the simulation, should be performed. For simplicity, we omit this constant factor throughout the paper. A similar situation applies to the computation of masses.

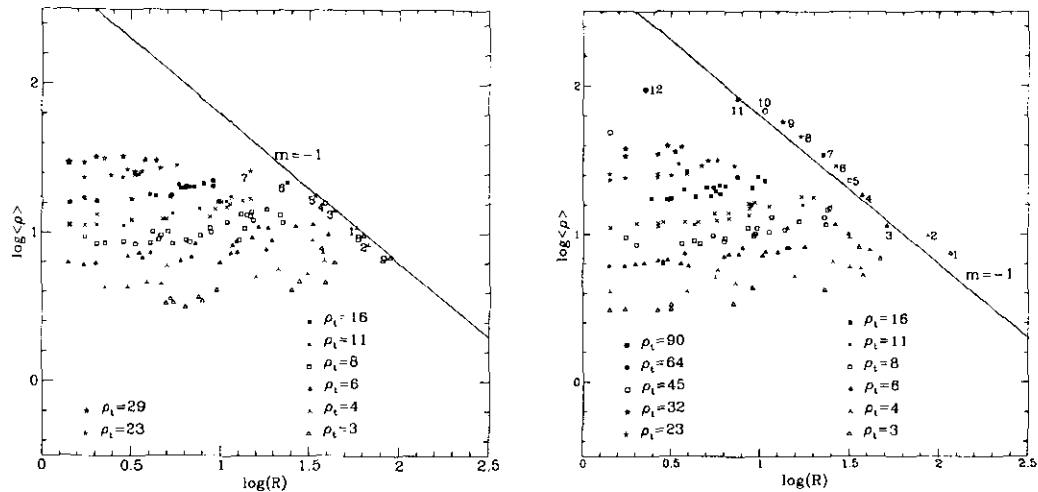


FIGURA 10.5: Average cloud density *vs.* size for all clouds in a) Run 28 at $t = 6.6 \times 10^7$ yr and b) Run 28bis at $t = 7.15 \times 10^7$ yr. The lines show a $\rho \propto R^{-1}$ power law. In both cases, the largest cloud at each ρ_{th} lies near the $\rho \propto R^{-1}$ line, although other times tend to show shallower envelopes (see fig. 10.6). The full ensemble of clouds does not show any trend of $\langle \rho \rangle$ with R . The cloud labels in a) and b) are respectively the same as in a) and b) of figs. 10.4a and b).

In order to test the robustness of the above results, we performed the same analysis at various other times in both runs, namely at $t = 7.8, 9.1, 10.4, 11.7$ and 13.0×10^7 yr in Run 28, and $t = 7.8$ and 8.6×10^7 yr in Run 28bis. The average value of the exponent β of the velocity dispersion-size relation is $\langle \beta \rangle = 0.41 \pm .08$, with typical correlation coefficients ~ 0.6 . For the mass spectrum, an average exponent $\langle n \rangle = -1.44 \pm .1$ is found. The errors are the standard deviations of the set of values found for all times. These results confirm the fact that the simulations show correlations consistent with the observations in both cases.

Regarding the density, in all cases small clouds with low densities exist, the plots (not shown) being qualitatively similar to figs. 10.5a and 10.5b, and the full ensemble of clouds not exhibiting any correlation with size. The largest clouds at each ρ_{th} , on the other hand, continue to exhibit a near power-law relation with size, with average exponent $\langle \alpha \rangle = -0.81 \pm .16$. This is smaller than the slopes found in figs. 10.5a and 10.5b, which coincidentally seem to have some of the steepest slopes in the distribution. This is illustrated in fig. 10.6, which shows density *vs.* size for the largest cloud at each value of ρ_{th} at all times considered above for the two runs. In this figure, clouds obtained with a given value of ρ_{th} at any one time in either run are shown with the same symbol and joined by a dotted line. The resulting curves have been displaced by increments of 0.2 in $\log \langle \rho \rangle$ for clarity. For reference, the solid line shows a $\langle \rho \rangle \propto R^{-1}$ power law. The three uppermost curves in the figure correspond to Run 28bis and, because of the larger density dynamic range of this run, exhibit power-law behavior over a larger range of scales, while those for Run 28 saturate at $\rho \sim 30$. For this reason, only clouds with $\log R > 1$ for Run 28bis, and with $\log R > 1.5$ for Run 28 were considered in computing $\langle \alpha \rangle$. The implications of these

results are discussed in 10.4.2 For convenience, in what follows we drop the brackets when referring to the average density of clouds.

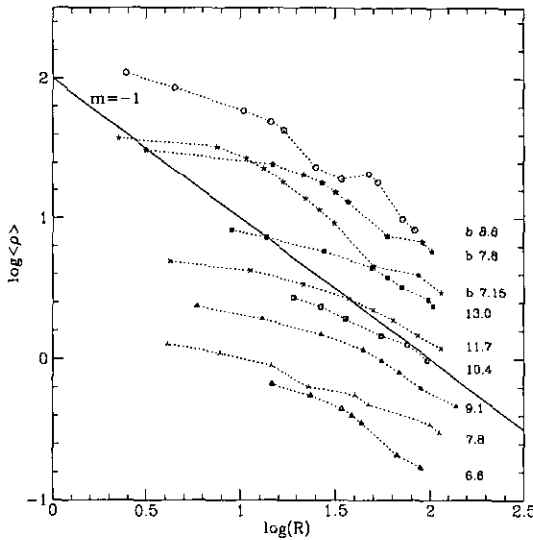


FIGURA 10.6: Average density *vs.* size for the largest cloud at each value of ρ_{th} at six different times in Run 28 (bottom curves) and three times in Run 18bis (top curves, labeled “b”). Each point denotes the largest cloud at one value of ρ_{th} . Different values of ρ_{th} for the same time in the simulation are joined by dotted lines and indicated with the same symbol. The various curves are displaced by increments of 0.2 in $\log \rho$ for clarity. The numbers next to each curve show the time into the evolution of the run to which it corresponds, in units of 10^7 yr. Note that time $t = 6.6 \times 10^7$ yr for Run 28 and time $t = 7.15 \times 10^7$ yr for Run 28bis have some of the steepest slopes. The straight line shows a $\rho \propto R^{-1}$ power law. The average slope for all times is -0.81 , with a standard deviation of 0.16 . Because of the “compression” at high densities due to various numerical effects, only clouds with $\log R > 1$ (Run 28bis) or $\log R > 1.5$ (Run 28bis) were considered in the calculation of the average slope (see text).

Finally, it should be pointed out that, although clouds with low column densities exist in the simulations, most of the mass still resides in the largest clouds, since the distribution of cloud sizes at a given mean density appears to be roughly uniform. However, this is possibly an effect of the absence of supernovae in the simulations, since the “expanding HII regions” included do not have enough power to disrupt the largest gravitationally bound complexes.

10.4 Discussion

10.4.1 Applicability and limitations of the results

The results presented in § 10.3 have important implications, provided that the simulations are indeed representative of ISM dynamics. That this is likely to be the case, in spite of their two-dimensionality, is suggested by the fact that the simulated ISM reproduces both the velocity dispersion-size relation and the mass spectrum of the clouds (c.f. § 10.3), as well as other physical properties of the ISM, such as the mean density of giant cloud complexes (PVP95a), the cloud and intercloud magnetic field strengths (PVP95a), the rate of formation of massive stars (Vázquez-Semadeni et al. 1995b), etc. However, one

important possible criticism due to the two-dimensionality, is that a $\rho \sim R^{-1}$ scaling relation in three dimensions might translate into a $\rho \sim R^0$ relation in two dimensions, just because of the elimination of one dimension. This could be at the origin of the near constancy of $\langle \rho \rangle$ observed at every value of ρ_{th} . Closer examination shows that this argument is invalid. Even though the clouds seem to have nearly constant densities at each value of ρ_{th} , this only reflects the fact that, due to our cloud-identifying algorithm, small, dense clouds are not seen at small ρ_{th} , since they are “hidden” within the larger, low density ones. But obviously the density is not constant in the simulations, invalidating the possibility of an R^0 dependence of the density.

Another important source of concern is that a significant fraction of the clouds in the samples have sizes of only a few pixels, and their properties are thus likely to be affected by viscosity and diffusion. Thus, it is important to quantify the extent to which the results of the previous section might be influenced by these terms. In particular, the question arises as to whether the existence of low-column density, small clouds might be an artifact of the dissipative terms.

Concerning viscosity, owing to the hyperviscosity scheme with a ∇^8 operator, its effects on the velocity field are confined to wavenumbers k in the range $k_{\text{max}}/2 \lesssim k \leq k_{\text{max}}$ with $k_{\text{max}} = 255$ for Runs 28 and 28bis, as can be seen from the spectrum in fig. 10.10 (see §10.4.2). The same applies to the dissipative term in the magnetic equation (see fig. 5 of PVP95a). Naively, one would then expect the effects of viscosity to be present at scales up to twice the smallest scale of the simulation, i.e., from one to two pixels. Actually, the correspondence between scale ranges in real and Fourier spaces is not as sharp, and one can expect “leakage” up to possibly 4 pixels. Visual inspection of the velocity field confirms that shocks are spread over typically 4 pixels. Nevertheless, note that viscosity is not effective if the velocity gradients are not large, and thus the 4-pixel estimate is an upper limit to the sizes affected by viscosity. It is worth pointing out that in PVP95a the range of influence of viscosity was estimated at ~ 5 pixels. However, this was an over-conservative estimate not based on a detailed analysis of shock widths, and the 4-pixel figure given here should be considered as a slightly more precise estimate based on the above considerations.

In order to correct for viscosity effects, clouds with sizes up to 4 pixels in size are excluded from the “corrected” plots shown in the Appendix. Note that, since clouds have in general elongated shapes and sizes are computed as the square root of the number of pixels, the possibility exists that clouds with computed sizes larger than 4 pixels will still be 4 pixels or less across one particular direction. However, we believe this effect may be roughly compensated by the fact that the 4-pixel estimate is an upper limit, and thus we retain all clouds with sizes larger than this.

Of greater concern are the possible effects of mass diffusion, since the standard Laplacian diffusive operator used in the continuity equation causes diffusion to be important over a larger range of scales than the hyperviscosity. Indeed, the characteristic diffusion time τ_{dif} can be shorter than the turbulent crossing time τ_{nl} for clouds smaller than about 16 pixels (see Appendix), and diffusion may dominate over turbulent advection for those clouds. In particular, it is possible that the small, low-density clouds reported in the previous section might be a numerical artifact of the diffusion, which tends to reduce density

peaks and spread the clouds out, or, conversely, to prevent clouds from reaching higher densities and smaller sizes than they do in the simulations.

Note, however, that the effect of mass diffusion is exclusively to damp density gradients originated by the turbulent velocity field, and so diffusion is incapable of forming clouds by itself; instead, it only modifies the properties of clouds formed by turbulence or other processes (gravity or the various instabilities discussed in PVP95a). We can thus obtain a crude estimate of the size and maximum density a cloud would have in the absence of diffusion by integrating the diffusion equation backwards in time for initial conditions corresponding to the clouds in the simulation, over the length of a nonlinear time τ_{nl} . This correction overestimates the effects of diffusion, since it neglects the advection term entirely, and the nonlinear time is computed using the turbulent velocity associated to the size of the cloud, as given by the turbulent spectrum in fig. 10.10. However, it is actually turbulent scales larger than a cloud's size which are most likely to form it (Elmegreen 1993; Vázquez-Semadeni et al. 1995b). In particular, in the simulations at least, clouds often form at the interfaces of expanding shells from previous star formation events, which may have velocities of several kilometers per second, rather than the significantly smaller velocities ($\lesssim 1 \text{ km s}^{-1}$) indicated by the spectrum, which is a globally averaged quantity. Nevertheless, for robustness, we will use the worst-case correction. The details of this calculation are given in the Appendix. There it is shown that the central density of a cloud varies by factors of 3–5 in the worst cases under the influence of diffusion. Using this “correction” factor and assuming the clouds move along lines of constant mass in the density-size plot, one can produce a “corrected” such diagram, shown in fig. 10.16 in the Appendix for Run 28bis. ~~There it can be seen that, although clouds are indeed brought slightly closer to a correlation, at the lowest average densities cloud sizes still vary by factors of about 100, maintaining the conclusions from §10.3.~~

As a further test, we have also produced a preliminary higher-resolution run, labeled Run 28.800, similar to Run 28bis, but at a resolution of 800×800 pixels, the largest that we can perform in the CRAY YMP of DGSCA, UNAM. The density field for this run is shown in fig. 10.7. In order to produce this run, the data from Run 28 at $t = 6.5 \times 10^7 \text{ yr}$ were interpolated to produce initial conditions for the 800×800 simulation, and then evolved for another $0.65 \times 10^7 \text{ yr}$, enough to develop the additional small scale structure corresponding to the larger resolution. Incidentally, it is worth noting that, even though Run 28.800 has a resolution only $\sim 60\%$ larger than Runs 28 and 28bis, the computational effort it requires is roughly 5 times larger in CPU run time. Fig. 10.8 shows the resulting density-size raw plot for this run, including cloud sizes down to 1 pixel. In the Appendix, fig. 10.17 shows the corresponding plot incorporating the corrections described above, namely elimination of clouds with sizes ≤ 4 pixels, and the correction for diffusion. In order to maximize the available dynamic range, in the figures in the Appendix we have used values of the density threshold as low as $\rho_{\text{th}} = 0.5$. For Run 28.800, it is seen that the clouds with the lowest average densities span a range of roughly a factor of 200 in sizes after the corrections, while the raw data exhibit a range of a factor ~ 500 .



FIGURA 10.7: Logarithmic grayscale image of the density field of run 28.800 at time $t = 7.15 \times 10^7$ yr. This run is similar to run 28bis, except that it has larger resolution (800×800), and that star formation is turned off at time $t = 6.9 \times 10^7$ yr. The density extrema are $\rho_{\max} = 129$, and $\rho_{\min} = 3.4 \times 10^{-2}$.

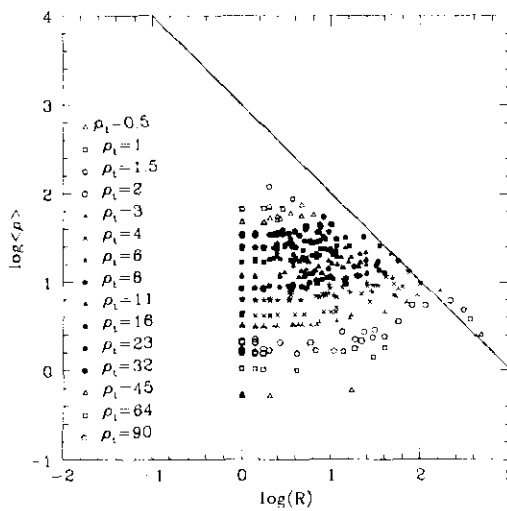


FIGURA 10.8: Mean density-size plot, equivalent to figs. 10.5a and b, but for the high-resolution Run 28.800. A large range of sizes, in this case spanning over two and a half orders of magnitude, is again seen at the lowest values of the average cloud density.

In summary, the discussions from this section suggest that the existence of small clouds with low densities described in §10.3 is a true consequence of the dynamics and not an artifact of the dissipative terms used to stabilize the equations.

10.4.2 Implications of the results

Density, size and equilibrium

With the above considerations in mind, we then have a number of direct implications. First, as already stated above, the absence of a density-size relation implies non-constant column densities for the clouds. Specifically, cloud column densities vary by over two orders of magnitude in the simulations. Additionally, the result that clouds with sizes down to the smallest scales exist at all values of the mean density implies that the observed density-size relation may indeed be a product of the limited dynamic range of typical surveys. Under these conditions, the derived column densities could appear to show variation over a modest range only, while the observed sizes might span a range larger than three orders of magnitude, thus creating an apparent correlation. Observational effects as a possible origin of the density-size relation were first suggested by Larson (1981) himself, and later discussed in more detail by Scalo (1990). Another reason for the appearance of a spurious density-size relation may be a selection effect introduced by the tendency of observational work to focus primarily on global intensity maxima of the maps, therefore possibly missing weaker, local maxima, a bias that only recently has started to be avoided (e.g., FPP).

The Larson-type relation defined by the largest clouds, with a scaling exponent $\alpha \sim -0.8 \pm .16$ is particularly interesting. The immediate question that arises is whether this relation is physical, or is induced by numerical constraints. On the physical side, a first consideration is that, if the clouds are hierarchically nested (smaller, denser clouds are part of larger, less-dense ones), then mass conservation implies $-\alpha < 3$ in three dimensions. In our two-dimensional case, this limit becomes $-\alpha < 2$. This is a physical limit which in the simulations is pushed closer to the observed relation because of the two-dimensionality.

Another physical issue is whether the large clouds which follow a density-size scaling law are virialized, so that the standard scenario in which Larson's relations hold for virialized clouds would apply to the largest clouds. However, examining cloud virialization in our simulations turns out not to be a straightforward task (§10.4.2). Here, we just check whether the standard $\Delta v - R$ relation is also satisfied in the large clouds. To this end, some clouds in figs. 10.4 and 10.5 have been labeled with numbers so that they can be identified from one figure to another. Interestingly, for Run 28 at $t = 6.6 \times 10^7$ yr (case *a* in the figures), the largest clouds, which are very close to the constant-column density line $\rho \sim R^{-1}$, shown as the straight line in fig. 10.5a, are also very close to the line $\Delta v \sim R^{1/2}$ in fig. 10.4a, suggesting balance between gravity and turbulence for this set of clouds. However, this is not the case for the clouds in Run 28bis at $t = 7.15 \times 10^7$ yr (case *b* in the figures). In this case, although the clouds again show a slope very close to -1 (fig. 10.5b), it can be seen from fig. 10.4b that they all have comparable velocity dispersions. We conclude that even clouds with a $\rho \propto R^{-1}$ density dependence are not necessarily in equilibrium between turbulence and self-gravity. Possibly, magnetic support is more important for the latter set of clouds, as in the results of Myers & Goodman (1988).

An interesting question is whether the various clouds along the large column density "envelope" of the distribution in the density-size relation are essentially the same cloud seen at various different thresholds ρ_{th} , or else they are truly different clouds. In fact, the

answer is that they are neither. This is exemplified in fig. 10.9, which shows a few selected branches of the cloud hierarchy for Run 28bis. One branch off the largest cloud includes all the clouds along the envelope, but both the largest and second largest clouds are seen to also have other branches to daughter clouds off the envelope (dotted lines). The same is true of clouds lying immediately below the envelope (dashed lines), which seem to define a second envelope of similar slope (see fig. 10.5).

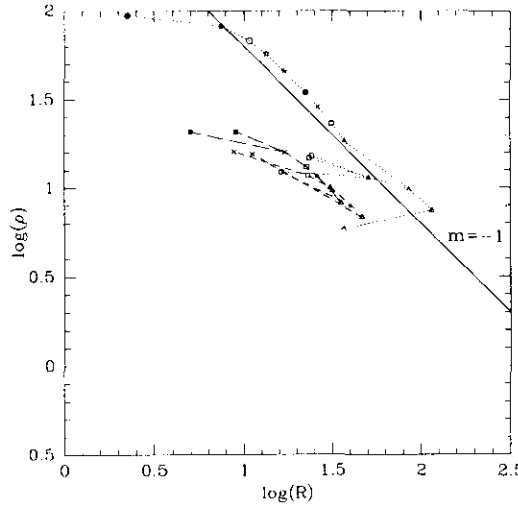


FIGURA 10.9: “Familiy tree” of a few selected clouds from fig. 10.5b. The largest cloud is seen to branch off to both clouds defining a Larson-type relation as well as to clouds away from it (dotted lines). A similar branching pattern is observed for clouds of lower column densities (dashed lines).

On the numerical side, the mass diffusion term in the continuity equation may tend to reduce the column density of clouds defined through the threshold density-criterion we use here, since the diffusion widens and smooths clouds, whose outer parts may then be left out of the domain defined by ρ_{th} . This effect, plus the plain limitations imposed by the resolution, clearly prevent the formation of very small clouds with very large column densities, causing shallower slopes of the high-column density envelope. In fact, while the average slope we obtain implies smaller column densities for smaller clouds, it has been pointed out by Scalo (1985, sect. III.A) that it is obvious from inspection of Lynds’ dark cloud catalog that smaller clouds are darker. Indeed, in our case, the correction discussed in 10.4.2 and in the Appendix tends to bring this envelope towards steeper slopes. In summary, the specific slopes defined by the largest clouds in the $\log \rho$ - $\log R$ plot cannot be unambiguously attributed to real physical effects. High-resolution, three-dimensional simulations are needed to resolve this issue. Unfortunately, the largest simulations of supersonic compressible turbulence known to us (e.g., Porter et al. 1994, using 512^3 grid points), are purely hydrodynamic and do not contain many essential ingredients of ISM dynamics, such as the magnetic field, self-gravity, and stellar (i.e., small-scale, compressible) forcing. Thus, the necessary calculations are still a few years in the future.

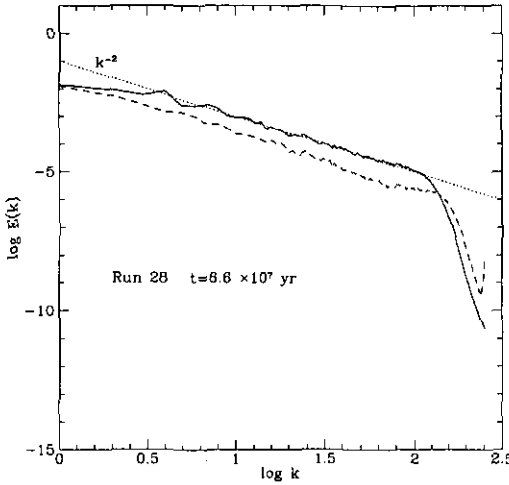


FIGURA 10.10: Turbulent energy spectra for Run 28 at $t = 6.6 \times 10^7$ yr. *Solid line*: incompressible component of the spectrum. *Dashed line*: compressible component. The straight line shows a k^{-2} power law, characteristic of shocks, which implies an $R^{-1/2}$ dependence of the velocity dispersion.

In any case, regardless of what the specific slope of the envelope turns out to be upon removal of numerical effects, our results suggest that the notion of a density-size scaling relation should probably be replaced by that of an “allowed” region in ρ - R space. Whether the high-column density boundary is truly a power law, the value of its corresponding index, and the physical mechanisms responsible for it, are issues that remain to be determined by high resolution 3D simulations.

Velocity dispersion-size relation and turbulence

Since the density-size relation is not verified for the clouds in the simulations, yet the dispersion-size relation is, the standard argument explaining the Δv - R relation, namely virial equilibrium in clouds satisfying $\rho \propto R^{-1}$, cannot be invoked. This implication is independent of the dimensionality of the simulations, as it only relies on the non-existence of a density-size relation, and not on particular values of the scaling exponents. That is, the two-dimensionality would, at most, change the exponent in the virial equilibrium relation between Δv and ρ , but not destroy the correlation altogether. Since in the simulations no density-size relation exists, a unique virial equilibrium relation between Δv and ρ does not exist either (although see § 10.4.2). Note, however, that a Jeans-type analysis incorporating a “turbulent pressure” (Chandrasekhar 1951; Scalo & Struck-Marcell 1984; Bonazola 1987; Elmegreen 1991; Vázquez-Semadeni & Gazol 1995) such that $\nabla P_{\text{turb}} = (\Delta v)^2 \nabla \rho$ gives

$$\Delta v \sim R \rho^{1/2}, \quad (10.9)$$

for clouds of size R equal to their Jeans length. Since the latter is independent of dimensionality, relation (10.9) holds also independently of dimensionality. Thus, the same scaling laws as in 3D are expected for two-dimensional clouds in balance between self-gravity

and turbulence. This is consistent with a crude estimate of virial balance in which one equates the gravitational energy W to the turbulent kinetic energy K . For simple cloud geometries and uniform densities and turbulent velocity dispersions, in 3D one obtains $GM^2/R \sim M(\Delta v)^2$. Taking $M \propto \rho R^3$ gives the usual result $(\Delta v)^2 \propto \rho R^2$. In 2D, on the other hand, $M \propto \rho R^2$, but the gravitational energy becomes $W \sim GM^2$, thus preserving the result $(\Delta v)^2 \propto \rho R^2$. However, such a simplified treatment may not be applicable, since in 2D logarithmic corrections appear, and also the gravitational term in the virial theorem may differ from the gravitational energy. A detailed analysis of this problem is in progress. Thus, the instability analysis is provisionally a more reliable indicator of the equilibrium relation expected in 2D.

In the absence of a density-size relation, a plausible origin of the velocity dispersion-size relation is the statistical properties of the turbulence itself. Indeed, an index $\beta = 1/2$ is expected for turbulence characterized by an energy spectrum $E(k) \propto k^m$ with spectral index $m = -2$ (e.g., Bonazola 1987; Vázquez-Semadeni & Gazol 1995; Padoan 1995; Fleck 1996), where k is the wavenumber associated with scale $R = 2\pi/k$. Such a spectral index is the signature of a field of random shocks (see Passot et al. 1988 and references therein). Figure 10.10 shows the spectra for the incompressible (solid line) and irrotational (dashed line) parts of the velocity fields of fig. 10.1. For comparison, the straight dotted line shows a k^{-2} power law. It is clearly seen that the spectrum of the incompressible component is remarkably well described by this slope. The irrotational, or compressible, component exhibits somewhat stronger fluctuations (most likely due to the fact that the “stars” in the simulations inject purely compressible energy), but is still very close on the average. The 20% discrepancy with the index $\beta \sim 0.4$ found in the simulations may be due to the fact that in the simulations there exists an upper bound to the turbulent velocity dispersion (of order a few km s^{-1}) that can be imparted to the medium by the stellar heating, since in the model they only heat the gas to $\sim 10^4$ K. This introduces a “truncation” on the $\Delta v-R$ relation, which flattens the resulting slope, as can be seen in figs. 10.4a and 10.4b.

An alternative interpretation

At this point, one important alternative must be pointed out. The large scatter in the velocity dispersion-size relation would be consistent with the clouds *not* having constant column densities, even if they were in equilibrium between turbulence and self-gravity. Indeed, in equilibrium, the scatter of about one order of magnitude in the velocity dispersion would imply a scatter of roughly two orders of magnitude in the column density, as can be seen from the equilibrium relation

$$\Delta v \sim (NR)^{1/2}. \quad (10.10)$$

which is equivalent to relation (10.9). Thus, our results can also be interpreted in the sense that all clouds tend to be virialized, although with a scatter of at least two orders of magnitude in the column density. Preliminary results on the energy budget of a smaller cloud sample in Run 28 (Ballesteros-Paredes & VS 1995) suggest that the sum of the kinetic and magnetic energies is within one order of magnitude of the gravitational energy,

although surface terms were not considered there. Also, the total gravitational and the turbulent kinetic energies per unit mass in the simulations are almost in equipartition, as shown in fig. 10.11

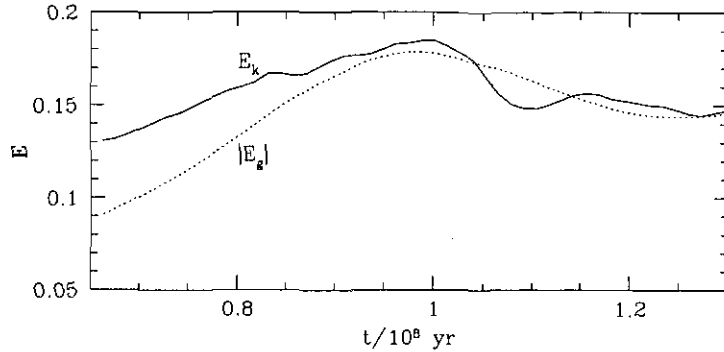


FIGURA 10.11: Evolution of the total turbulent kinetic (*solid line*) and the gravitational (*dotted line*) energies per unit mass in code units for run 28 over the last half of its evolution. The two energies are very close to equipartition at all times.

In this alternative interpretation, a density-size correlation may still be present, but missed by the simulations because the scatter is larger than the column density dynamic range in the simulations (and in most observational studies). This scenario would leave the origin of the putative density-size relation unexplained, although it may still be possible that the $\Delta v - R$ relation is originated by the turbulent energy spectrum, and that the $\rho - R$ relation is the consequence of virial equilibrium. Although this scenario cannot be ruled out with certainty until significantly higher-resolution simulations are performed, it seems unlikely, because in the simulations, clouds with sizes down to the smallest resolved scale are often found even at the lowest values of ρ_{th} , thus not giving any indication of the presence of a density-size relation. Instead, clouds of similar average densities often span the whole range of scales accessible to them. Also, the global balance between the turbulent and gravitational energies is mostly just a consequence of the presence of a self-regulated cycle of gravitational contraction, star formation, energy injection to the medium and dispersal, and again gravitational contraction, as discussed in Vázquez-Semadeni et al. (1995a), so that near global balance between turbulence and self-gravity is maintained at all times.

Finally, note that here we have not discussed other mechanisms that have been suggested in the literature as responsible for the $\Delta v - R$ relation, such as inverse cascades of angular momentum, (Henriksen & Turner 1984), critical thermal pressure equilibria (Chièze 1987) or the contribution from the magnetic support (Shu 1987; Myers & Goodman 1988a; Mouschovias & Psaltis 1995; Gammie & Ostriker 1986). We will address the role of these processes in the simulations in future work.

10.4.3 Comparison with observations

The lack of correlation between cloud density and size in the simulations appears to be in contradiction with the correlations found in most observational results (Larson 1981;

Torrelles et al. 1983; Dame et al. 1986; Falgarone & Péault 1987; Myers 1990; Wood et al. 1994). However, as discussed in § 10.4.2, we interpret the discrepancy as an effect of the limited column density dynamic range of the observations or of selection effects introduced by focusing exclusively on global intensity maxima in the maps. There are some examples of observations that have intended to avoid these problems (Carr 1987; Loren 1989; FPP). The first two authors have focused on clumps within a single molecular cloud with extensive star formation, thus better sampling the non-gravitationally-bound turbulent transients. The work of FPP was specifically tailored towards studying low-brightness regions in molecular clouds. In both Loren (1989) and FPP, column densities spanning over one and a half orders of magnitude are found.

On the other hand, WMD have recently concluded from an analysis of 60 μm and 100 μm IRAS maps, that column densities of dark clouds cluster typically at $N(\text{H}_2) \simeq 4 \times 10^{21} \text{ cm}^{-2}$ (corresponding to a typical 100 μm opacity of $\tau_{100} \simeq 200 \mu\text{Nepers}$), while claiming that the dynamic range of the data would have allowed detection of any significant variations. The discrepancy between these results and those of the present paper seemingly cannot be explained in terms of the limited column density dynamic range of their observations.

In actuality, we believe that the results of WMD may be spurious and attributed to a combination of their selection criteria and the following effect. At 60 μm and 100 μm , one is observing “warm” dust that could be coming from the “edges” of molecular clouds. If this “warm” dust is being heated by the visible photons from the galactic stellar radiation field, it is expected that the depth of the “warm” region will be of order of a few Nepers in the visible. This will lead to apparent constant optical depths when determined from observations of the “warm” dust.

Detailed radiative transfer models have been presented by Bernard et al. 1992, whom have already warned against using 100 μm surface brightness as a tracer of dust column density. In what follows, we present a simpler model that allows us to give first-order estimates of the scaling of the intensities in the IRAS 60 and 100 μm bands and the *apparent* dust opacity as a function of the true dust opacity through the cloud.

Similarly to Jarret et al. 1989 and WMD, we assume that the ratio of visible to 100 μm absorption efficiency is $(Q_V/Q_{100}) = 2.0 \times 10^4$. It is important to emphasize that the 100 μm opacity considered in this ratio is being produced by small dust particles that become heated to relatively large temperatures and that are responsible for the observed 100- and 60 μm emission. The absorption efficiency ratio that includes all the dust at 100 μm is about a factor of 10 smaller (Chini et al. 1986). Furthermore, in the range of wavelengths between 60 and 100 μm , the absorption efficiency scales approximately as ν^{-1} . Using this functional dependence, we can write a crude approximation for the dust temperature as

$$T_{\text{DUST}} = (T_{\text{cr}}^5 + T_{\text{RAD}}^5 e^{-\tau_V})^{1/5},$$

where T_{cr} and T_{RAD} are pseudotemperatures that parameterize the heatings due to cosmic rays and radiation, respectively. (Although this approximation is not valid at all wavelengths, we have checked that using slightly different functional dependences does not significantly alter our results.) We assume that cosmic ray heating is constant for any

point in the cloud. Specifically, $T_{\text{cr}} = 10$ K is the temperature that the dust has if heated only by cosmic rays, and T_{RAD} is the temperature that the dust would have if heated only by the stellar radiation field (at the edge of the cloud, where no absorption is present). Also, τ_V is the opacity in the visible, that increases as we get deeper into the cloud. In this simple model $T_{\text{DUST}} \simeq T_{\text{RAD}}$ at the edge of the cloud and it tends to T_{cr} for the inner regions of the cloud (fig. 10.12). The intensities at $60 \mu\text{m}$ and $100 \mu\text{m}$, I_{60} and I_{100} , can be calculated for clouds with different values of τ_V , as shown in fig. 10.13. This calculation is made assuming that $Q_{100}/Q_{60} = 60\mu/100\mu$. From this figure it is evident that for clouds exceeding a few Nepers in τ_V , I_{60} and I_{100} do not continue growing with τ_V . An apparent dust temperature, $T_{60/100}$ can be derived from I_{60} and I_{100} and the far-infrared opacities are then obtained. In fig. 10.14, we plot the $100 \mu\text{m}$ opacity derived in this manner as a function of the cloud's τ_V for different values of T_{rad} . The apparent $100 \mu\text{m}$ opacity "saturates" at values in the order of 70 to 100 μNepers . Considering that along a line of sight one expects to intersect the front and the back edges of a cloud, the typical $100 \mu\text{m}$ opacities of $\tau_{100} \simeq 200\mu\text{Nepers}$ appear to be explained as a result of this effect. The few clouds with much larger values of τ_{100} (up to $\tau_{100} \sim 10^4$) reported by WMD are regions of strong star formation activity, which may heat the clouds from the inside, raising τ_{100} . The presence of this effect is also consistent with the limb brightening observed in some clouds in the far-infrared by Snell et al. 1989 and WMD, and predicted by the models of Bernard et al. 1992. Note that this effect continues to be applicable even if the clouds are clumpy, since it should hold at the edges of any density peaks, large or small, as long as they have a large enough column density. However, note also that this "saturation" effect in the determination of the apparent τ_{100} will occur only if reasonably high temperatures ($T_{\text{DUST}} \gtrsim 20$ K) are present at the cloud's surface. In any case, for lower dust temperatures the emission at 60 and $100 \mu\text{m}$ is very weak and undetectable in practice. One consequence of this effect is that in order to fully sample the dust from dark clouds one requires observations at longer wavelengths that will trace the predominant cooler dust component. We intend to verify this effect by comparing column densities obtained with different indicators in future work.

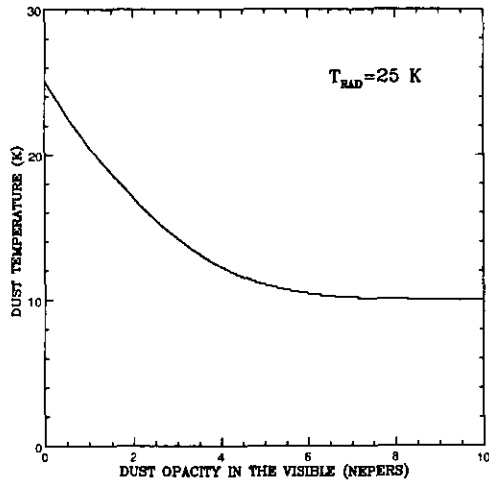


FIGURA 10.12: Dust temperature, T_{DUST} , as a function of dust opacity in the visible for $T_{RAD} = 25$ K. Near the edge of the cloud (left side) T_{DUST} tends to T_{RAD} , while toward the inner regions of the cloud (right side) heating by radiation becomes negligible and T_{DUST} tends to the value provided by cosmic ray heating (10 K in our model).

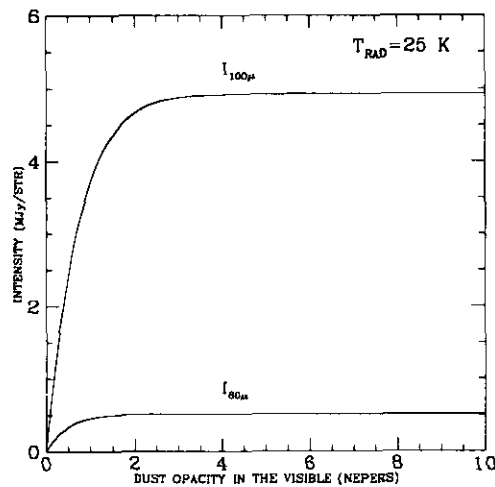


FIGURA 10.13: Intensity of cloud emission at $100\ \mu\text{m}$ and $60\ \mu\text{m}$ as a function of dust opacity in the visible, for $T_{RAD} = 25$ K. Note that the growth of the intensity “saturates” above a few Nepers of dust opacity in the visible. The reason for this effect is that beyond a few Nepers of dust opacity in the visible there is no significant radiation heating and the dust becomes too cold to emit significantly at $100\ \mu\text{m}$ and $60\ \mu\text{m}$.

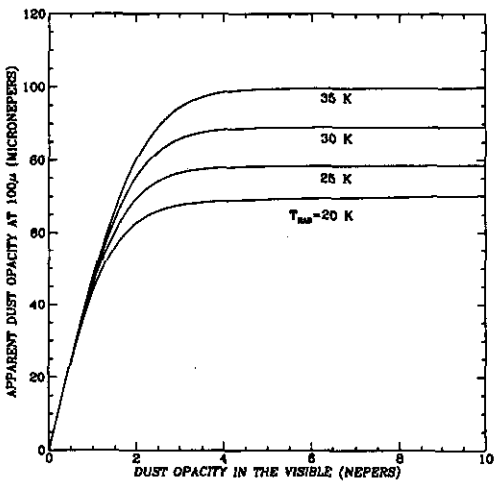


FIGURA 10.14: Apparent warm dust opacity at $100 \mu\text{m}$ (derived from the intensities at $100 \mu\text{m}$ and $60 \mu\text{m}$), as a function of dust opacity in the visible for different values of T_{RAD} . Note the “constancy” in the apparent dust opacity at $100 \mu\text{m}$ once the cloud exceeds a few Nepers in dust opacity in the visible, practically independently of T_{RAD} .

The effect discussed above may clearly impose an upper bound to the column densities derived by WMD. Furthermore, concerning their selection criteria, it should be noticed that WMD define core, cloud and cloud complex in terms of ranges of extinction. This directly selects against identification of low-column density structures. In fact, in their maps, small, low-extinction clouds are readily seen, but not classified as such precisely because of their low extinctions. Thus, the column densities of the cores studied by WMD are bound from above due to the “saturation” effect of the cloud edges, and from below by their very definition of a core, rendering their derived column density constancy open to question.

10.5 Summary and Conclusions

In this paper we have searched for Larson-type (1981) correlations and cloud mass spectrum slopes in the clouds generated in numerical simulations of the ISM, one from PVP95a, a similar one with a larger density dynamic range, and another with higher resolution. We define a cloud as a connected set of pixels in the density field with values larger than an arbitrary threshold ρ_{th} . From the results at various different times in the two simulations, we find that the mass spectrum has the form $dN/dM \propto M^{-1.44 \pm .1}$, and the velocity dispersion is related to the cloud size by $\Delta v \propto R^{0.41 \pm .08}$, where the errors are the standard deviations in the set of values including all the various times. The dispersion-size relation exhibits a scatter of about an order of magnitude, comparable to the scatter observed in real clouds.

The simulated clouds do not exhibit a density-size relation, but instead, at all mean densities, clouds of sizes down to the smallest resolved scales are commonly found. This

result implies that the clouds do not have constant column densities, but instead exhibit a range of roughly two orders of magnitude, thus providing strong support to the possibility that the observationally-derived density-size relation is an artifact of the limited dynamic range employed by observational surveys, and of the criteria used for selecting the clouds, as first noticed by Larson (1981), and then strongly argued for by Scalo (1990). Our results suggest that low-column density clouds do exist in the ISM, but are systematically missed by most observations. In the simulations, low-column density clouds are turbulent transients, as in the suggestion by Magnani et al. (1993). Observational work that has used complete cloud samples (e.g., Loren 1989), or specifically looked at structures in the low brightness regions of molecular clouds (FPP), has indeed found a reported column density variability of over one and a half orders of magnitude, and masses well below the virial mass, by factors up to two orders of magnitude. However, note that in our simulations most of the mass resides in the largest clouds at each mean density, since there are comparable numbers of small and large clouds.

The set of largest clouds at every threshold ρ_{th} exhibits a density-size relation $\rho \sim R^\alpha$, with $\alpha = -0.8 \pm .15$. These clouds appear to be close to balance between turbulence and self-gravity on occasions, but not in general. On the other hand, pure mass conservation, which gives an upper limit $-\alpha < 2$ for the two-dimensional case, together with numerical limitations of the simulations, cannot be ruled out as the sole causes responsible for this result. In any case, regardless of what the specific slope of the envelope turns out to be upon removal of numerical effects, our results suggest that the notion of a density-size scaling relation should probably be replaced by that of an “allowed” region in ρ - R space. Whether the high-column density boundary is truly a power law, the value of its corresponding index, and the physical mechanism responsible for it, are issues that remain to be determined by high resolution 3D simulations.

The result that the Δv - R relation is verified in the simulations but the ρ - R relation is not, supports the interpretation that the former relation is a direct consequence of the statistical properties of the turbulence, since a turbulent energy spectrum of the form $E(k) \sim k^{-2}$, as observed in the simulations, implies an $R^{1/2}$ scaling for the velocity dispersion. However, we discussed the possibility that a density-size relation does exist, although with a scatter larger than the column density dynamic range spanned by the clouds in the simulations. Such a scatter would be consistent with balance between turbulence and self-gravity, with a scatter of one order of magnitude in the velocity dispersion, according to relation (10.10). In this case, the origin of the ρ - R relation would remain unknown, and the turbulent origin of the Δv - R relation would have not as strong a support. This possibility cannot be ruled out without very high resolution simulations in order to add at least another order of magnitude to the column density dynamic range. However, the simulations do not give any indication that this may be the case, since cloud sizes down to the smallest resolved scales are found even at the lowest values of ρ_{th} . Besides, the column density dynamic range in the simulations is already larger than that of most observational surveys.

We also discussed the recent results of WMD, who have argued in favor of a surprisingly constant column density (to within a factor of a few) in a large sample of cores studied

through IRAS 60 and 100 μm maps, while claiming a very large dynamic range in their observational method. We argued that this result may be spurious, by presenting a model in which the warm “skin” of clouds and cores, which is likely to always have visual extinctions of order unity, puts an upper bound to the column densities measured by WMD. From below, WMD’s own selection criteria eliminate low-column density clouds, thus mimicking a nearly uniform column density.

Finally, we remark that in this paper we have limited the discussion to the trends of the density and velocity dispersion with size, omitting any discussion of the role of the magnetic field, which is clearly important for the dynamics of the simulations (PVP95a). A detailed account of the energy budget in the simulations including the magnetic energy density, as well as surface terms is under way.

Acknowledgments

We gratefully acknowledge fruitful discussions with A. Raga, J. Cantó, S. Lizano and T. Passot, as well as helpful comments and criticisms from J. Scalo. An anonymous referee emphasized the importance of the effects of dissipation and diffusion. Runs 28bis and 28.800 were performed on the Cray YMP 4/64 of DGSCA, UNAM. This work has received partial financial support from UNAM/CRAY grant SC-002395 and UNAM/DGAPA grant IN105295. J. B.-P. acknowledges financial support from a UNAM DGAPA fellowship.

10.6 Appendix

In this appendix² we make an order of magnitude estimate of the effect of the numerical diffusion term in the continuity equation. Consider the continuity equation, eq. (10.4):

$$\frac{\partial \rho}{\partial t} + \nabla \cdot (\rho \mathbf{u}) = \mu \nabla^2 \rho. \quad (10.11)$$

In order to estimate the effects of diffusion, we consider the extreme case when the advection term can be neglected, so that the mass equation becomes the standard diffusion equation:

$$\frac{\partial \rho}{\partial t} = \mu \nabla^2 \rho. \quad (10.12)$$

For simplicity, we consider a one-dimensional (axisymmetric) problem, whose solution is (see, e.g., Habermann 1987):

$$\rho(x, t) = \frac{1}{2\pi} \int_{-\infty}^{+\infty} f(x') \sqrt{\frac{\pi}{\mu t}} \exp\left(-\frac{(x-x')^2}{4\mu t}\right) dx', \quad (10.13)$$

where $f(x')$ is the initial density distribution, which we assume to be a Gaussian, $f(x') = \rho_0 \exp(-x'^2/2\sigma^2)$. In what follows, we will identify the width σ of the Gaussian with the size of the cloud of interest. Equation (10.13) then becomes:

$$\rho(x, t) = \rho_0 \left(\frac{1}{t/t_0 + 1} \right)^{1/2} \exp\left(-\frac{x^2/2\sigma^2}{t/t_0 + 1}\right), \quad (10.14)$$

²En el artículo original (ApJ 474, 292) existen un par de errores tipográficos en las ecuaciones (10.16) y (10.17), las cuales han sido corregidos en la presente versión. Adicionalmente, en el capítulo siguiente se comenta la existencia de este par de erratas.

where

$$\left(\frac{t_0}{t_{\text{code}}}\right) = \frac{\sigma^2}{2\mu} = 9.41 \times 10^{-3} \left(\frac{\sigma}{\text{pixels}}\right)^2. \quad (10.15)$$

is the characteristic diffusion time in units of the code, $t_{\text{code}} = 1.3 \times 10^7$ yr, and the second equality follows from using the value $\mu = 0.008$ (see PVP95a) (note that the size of the integration box is 2π in the code units). This value of t_0 can be made independent of the resolution of the simulation by choosing μ such that $\mu k_{\max}^2 = \text{cst}$, where k_{\max} is the maximum Fourier wave number in the simulation, equal to $1/2$ of the resolution.

Now consider the turbulent crossing (or nonlinear) time for scale σ :

$$\tau_{\text{NL}} \sim \sigma/u_l,$$

where u_l is the turbulent speed associated to the scale l . Note that we are allowing for the possibility that clouds of size σ are generated by turbulent streams of different, typically larger, size l (see §10.4.1). This velocity can be estimated from the turbulent energy spectrum $E(k)$ as:

$$\frac{1}{2}u_l^2 = \int_{2\pi/l}^{\infty} E(k) dk,$$

that is, u_l is the root mean square energy per unit mass in scales smaller than l . Using $E(k) = 0.1k^{-2}$, as indicated by fig. 10.10, one obtains:

$$\left(\frac{\tau_{\text{NL}}}{t_{\text{code}}}\right) = 14.05 \left(\frac{l/\text{pixels}}{n_{\text{res}}/\text{pixels}}\right)^{1/2}, \quad (10.16)$$

where n_{res} is the number of pixels (i.e., the resolution) per spatial dimension of the simulation. From equations (10.15) and (10.16), we can now compare the diffusion and nonlinear times, in order to determine the scale at which they are equal. Assuming that $l = m\sigma$, we obtain:

$$\left(\frac{l_{\text{eq}}}{\text{pixels}}\right) = \frac{16.33}{m^{1/3}}, \quad (10.17)$$

and thus, clouds with sizes lower than ~ 16 pixels are dominated by the numerical mass-diffusion. Therefore, it is important to assess the effect of mass diffusion in the results of §10.3. To do this, we take the extreme position that for time durations $\Delta t \leq \tau_{\text{NL}}$, a Gaussian cloud is affected exclusively by diffusion, and compute the fractional variation of its central density over τ_{NL} . In fig. 10.15 we show the evolution of $\rho(0, t)/\rho_0$ given by equation (10.14) over τ_{NL} for a cloud of size $\sigma = 4$ pixels. Note that this is a worst-case estimate, since on the one hand, in the plots below we have discarded clouds with sizes ≤ 4 pixels in order to avoid viscosity effects (see §10.4.1), which is most affected by diffusion, while, on the other hand, we have taken $m = 1$.

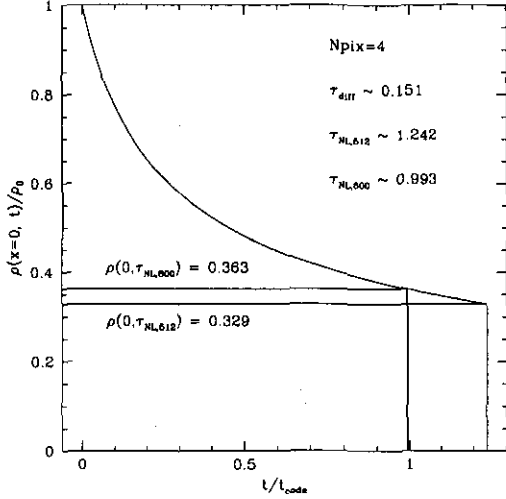


FIGURA 10.15: Fractional change of the central density $\rho(0, t)/\rho_0$ of a cloud of size 4 pixels. The fractional change shown here is an upper bound to the corrections applied to the simulated data, since we have considered a cloud with size smaller than the minimum cloud size retained, and $m = 1$ in eq. (10.17).

As we can see from fig. 10.15, the density decreases by a factor $\lesssim 5$. Typically, thus, we can expect our density data to change by factors smaller than half an order of magnitude.

Using the above results, we can produce a “corrected” density-size plot with the estimated “true” densities ρ_{corr} calculated as:

$$\rho_{\text{corr}} \sim \rho_{\text{data}} (1 + \tau_{\text{NL}}/t_0)^{1/2}. \quad (10.18)$$

where ρ_{data} are the raw cloud mean densities as produced by the simulations, and the “true” sizes are obtained assuming mass conservation:

$$R_{\text{corr}} \sim \frac{R_{\text{data}}}{(1 + \tau_{\text{NL}}/t_0)^{1/4}}. \quad (10.19)$$

The “corrected” density-size plots are shown in figs. 10.16 and 10.17 for Run 28bis and the high-resolution Run 28.800, respectively. We see that, although slightly pushed closer to a correlation in the case of Run 28 bis, the general trend of these plots still supports the main conclusion from §10.3, namely that clouds of sizes down to the resolution are seen at all mean densities.

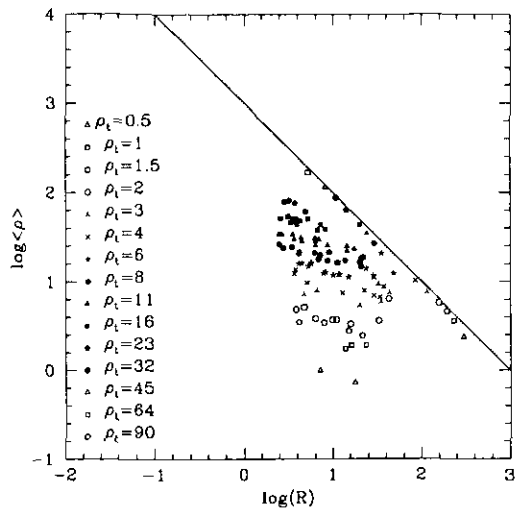


FIGURA 10.16: “Corrected” density-size plot for Run 28bis using the estimates for the ‘true’ density and size of the clouds given by equations (10.18) and (10.19). Note that a range of roughly two orders of magnitude in size remains for the lowest mean density clouds.

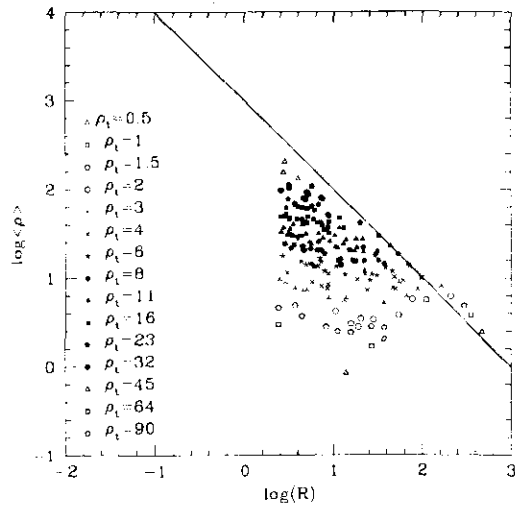


FIGURA 10.17: Same as figure 10.16, but for Run 28.800. Here, the sizes of the lowest-density clouds vary by nearly 2.5 orders of magnitude. Note that, although only clouds with sizes larger than 4 pixels are retained, the smallest clouds in this figure have sizes smaller than that because of the size ‘correction’, eq. (10.19).

Capítulo 11

Dimensión Fractal y Autosimilaridad de las Nubes Interestelares

Recientemente, han aparecido en la literatura sugerencias de que las nubes interestelares tienen una estructura fractal (e.g., Fagarone et al. 1990, 1991; Elmegreen & Falgarone 1996; MacLow & Ossenkopf 1999), e incluso multifractal (Chappel & Scalo 1999). El nombre “fractal” fue introducido por Mandelbrot (1975) para definir conjuntos matemáticos o geométricos cuya dimensión no es entera, sino fraccionaria¹.

La dimensión de un objeto cuantifica cómo cambia el área o volumen de un objeto, según cambia su extensión lineal (tamaño). Por ejemplo, en el caso en que una curva puede aproximarse por N segmentos de línea recta de tamaño r , la longitud de dicha curva es $L(r) = Nr$. En el caso de los fractales, conforme N tiende a infinito, la longitud L diverge. Sin embargo, existe un exponente crítico $D_H > 1$ tal que el producto Nr^{D_H} es finito, de manera que para exponentes mayores que D_H , el producto tiende a cero, y para exponentes menores que D_H el producto diverge. Este exponente crítico se llama dimensión de Hausdorff. Nótese además que para una curva suave, $D_H = 1$. Otro ejemplo es el caso de una figura geométrica regular, como es el caso de un círculo, donde el área va como su radio al cuadrado, mientras que si la figura es fractal, el área aumenta como una potencia fraccionaria del radio. Este exponente constituye la *dimensión fractal* del objeto.

Mientras que, para los fractales matemáticos, la autosimilaridad (es decir, la capacidad de presentar la misma estructura a diferentes resoluciones) se da sobre un número infinito de escalas, para los objetos físicos con características fractales la autosimilaridad se da tan sólo en un intervalo limitado de escalas. En particular, el intervalo de escalas para las nubes interestelares es de unos 4 órdenes de magnitud, desde ~ 0.01 hasta 100 pc (ver, e.g., Combes 1999).

Para objetos bidimensionales, una manera conveniente de calcular la dimensión fractal es calcular los valores del perímetro y del área usando sucesivamente diferentes resoluciones para el mismo objeto, y construir la relación entre el perímetro p y el área A . Así, la

¹ Actualmente, se reconoce que existen fractales con dimensión entera. Estrictamente hablando, un objeto es fractal si su dimensión es diferente de 0.5. Sin embargo, no es el interés del presente trabajo entrar en este tipo de discusión.

dimensión fractal d queda definida mediante la relación

$$p \propto A^{d/2} \quad (11.1)$$

Haciendo uso de esta definición, Falgarone et al. (1991) estudian un conjunto de observaciones de nubes moleculares², encontrando que la dimensión fractal³ d es ~ 1.36 , valor similar al reportado por Bazell & Desert (1988) usando isocontornos de emisión en 100μ , o por Vogelaar & Wakker (1994) utilizando emisión de H I.

A fin de cuantificar la dimensión fractal de las nubes en las simulaciones numéricas, en la Fig. 11.1 graficamos el perímetro vs. el área de el mismo conjunto de nubes utilizado para cuantificar los valores de los términos del teorema virial en las secciones anteriores. El perímetro es calculado contando todos aquellos píxeles que hacen contacto con el medio exterior, mientras que el área es calculada contando todos los píxeles que constituyen la nube. De esta gráfica notamos que para las nubes más grandes se cumple la relación

$$p \propto A^{0.7} \quad (11.2)$$

de manera que la dimensión fractal de las nubes en las simulaciones es $d \sim 1.4$ (ec. [11.1]). Por otra parte, dado que las simulaciones tienen resolución finita, para las nubes más pequeñas (unos cuantos píxeles) el número de píxeles que constituyen la nube se acerca al número de píxeles que son frontera de ésta (especialmente en nubes filamentarias), de manera que éstas nubes caen sobre la recta $y = x$. Por último, es importante mencionar que existe un conjunto de nubes medianas, las cuales tienen una dimensión fractal del orden de la unidad (conjunto de puntos con pendiente ~ 0.5 en la Fig. 11.1, con áreas entre 10 y 100 píxeles, aproximadamente). Para este conjunto de puntos, el área aumenta de manera cuadrática con el tamaño, posiblemente debido al efecto de la difusión de masa, que suaviza las estructuras de tamaños hasta ~ 15 píxeles (Ballesteros-Paredes et al. 1997. §10).

²Nótese que si bien las nubes son objetos tridimensionales, las imágenes obtenidas en diferentes frecuencias son, por construcción, 2D.

³Es importante hacer recalcar que en este cálculo está implícito el hecho de que la dimensión fractal es la misma para todas las nubes, de manera que medir la dimensión fractal para una nube dada con diferentes resoluciones es equivalente a medir la dimensión fractal para muchas nubes, usando la misma resolución.

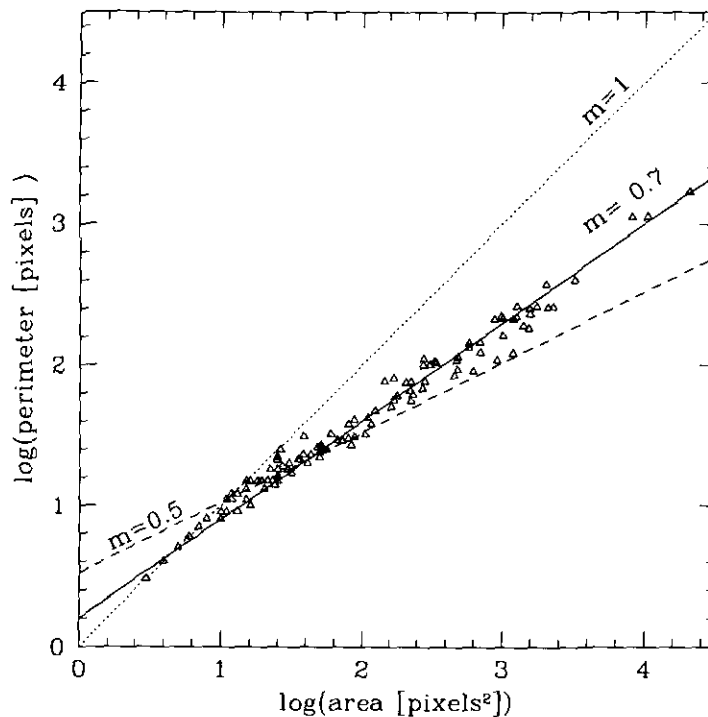


FIGURA 11.1: Perímetro vs. área (en unidades logarítmicas) para un conjunto de nubes en las simulaciones numéricas. Nótese la existencia de tres regímenes diferentes: para las nubes más pequeñas (≤ 20 pixeles), el perímetro y el área son iguales, ya que el número de puntos que constituyen el área de la nube también constituyen la frontera de éstas. Para las nubes de escalas intermedias (entre 20 y 100 pixeles), la pendiente puede aproximarse a 0.5, sugiriendo que la dimensión fractal es 1, o bien, que el área de la nube varía de manera cuadrática con la escala lineal. Sin embargo, para las nubes más grandes (≥ 100 pixeles), cuyas escalas son considerablemente mayores a la resolución, la dimensión fractal es aproximadamente 1.4, como se obtiene para las nubes interestelares.

Antes de finalizar el presente capítulo debemos mencionar que, si bien las simulaciones son 2D, las nubes observadas son la proyección 2D de objetos tridimensionales. Por lo tanto, aunque este resultado podría sugerir que las simulaciones exhiben valores razonables de la dimensión fractal, no es claro que la fractalidad de objetos estrictamente bidimensionales deba coincidir con la de objetos tridimensionales proyectados en un plano. Además, es importante mencionar que este resultado podría ser debido al método de medición utilizado, y no tanto a una característica relacionada con los procesos físicos en las nubes interestelares (Scalo, comunicación privada). Será necesario más trabajo antes de poder estimar la relevancia de este resultado.

Parte III

Formación de Nubes

Capítulo 12

Presentación

En los capítulos anteriores hemos visto cómo el medio interestelar, de estar bien representado por las simulaciones numéricas, constituye un fluido altamente dinámico y turbulento, donde las estructuras se encuentran lejos de un posible balance virial o de equilibrio hidrostático. Esto sugiere que los procesos físicos involucrados afectan de manera continua a las nubes, haciendo que exista un flujo de masa, momento y energía entre las nubes y su medio circundante. De hecho, en estas condiciones, las nubes mismas constituyen las fluctuaciones de densidad inducidas por la turbulencia.

Con ésto en mente, nos propusimos entender el comportamiento de las estructuras de densidad y su relación con el campo de velocidades en todas las escalas, encontrando que los movimientos coherentes a cierta escala son capaces de formar estructuras en escalas menores, e incluso de desatar colapso gravitacional en regiones gravitacionalmente estables de acuerdo al criterio lineal.

De esta manera, en los capítulos subsecuentes se estudiarán las simulaciones bajo el enfoque de la formación de nubes. En el capítulo 13 discutimos las posibles implicaciones de la turbulencia en la formación y deformación de las estructuras. Dado que este modelo parece tener implicaciones sobre las escalas de tiempo para la formación de estructuras, en el capítulo 14 introducimos el problema de la aparente incompatibilidad entre la edad estimada para nubes moleculares, del orden de varias veces 10^7 años, y la de su población estelar, del orden de 10^6 años (el problema post-T Tauri enunciado por Herbig 1978), mientras que en el capítulo 15 damos una posible solución a este problema desde la perspectiva de las nubes formadas por flujos turbulentos convergentes en escalas de tiempo cortas (unos cuántos millones de años).

Capítulo 13

Artículo 4

Clouds as turbulent density fluctuations. Implications for pressure confinement and spectral line data interpretation

Javier Ballesteros-Paredes, Enrique Vázquez-Semadeni and John Scalo

ApJ. **515**, 286. 1999

Resumen

Examinamos la idea de que las nubes difusas de HI y las nubes moleculares gigantes, junto con su subestructura, se forman como fluctuaciones de densidad inducidas por la turbulencia interestelar a gran escala. Hacemos ésto mediante la investigación detallada de la topología de los campos de velocidad, densidad y magnético dentro y en las fronteras de las nubes en simulaciones bidimensionales de alta resolución del medio interestelar, las cuales incluyen autogravedad, campos magnéticos, calentamiento y enfriamiento parametrizado y un modelo simple de formación estelar. Encontramos que el campo de velocidad es continuo a través de las fronteras de las nubes para un conjunto jerárquico de nubes de tamaños progresivamente menores. Encontramos que las fronteras de las nubes, definidas mediante un criterio de densidad umbral, son arbitrarias, sin correspondencia con alguna frontera real, tal como una discontinuidad en la densidad. Los saltos abruptos de velocidad coinciden con los máximos de densidad, indicando que las nubes son formadas por flujos de gas en colisión. Esta conclusión también está fundamentada por el hecho de que los términos cinéticos superficial y volumétrico del Teorema Virial culeriano para un conjunto de nubes son comparables en general, así como por la topología del campo magnético, el cual exhibe dobleces e inversiones donde las corrientes de gas chocan. Sin embargo, no se observa ninguna tendencia a que las estructuras de densidad estén alineadas con el campo magnético. Observamos también movimientos sub- y super-alfvénicos dentro de las nubes.

A la luz de estos resultados, argumentamos que el equilibrio de presión térmica es irrelevante para confinar a las nubes en un medio turbulento, pues los movimientos iniciales pueden distorsionar o romper las nubes, a menos de que éstas estén ligadas gravitacionalmente. Tampoco confinamiento por presión turbulenta parece relevante, pues la turbulencia contiene movimientos a gran escala que necesariamente distorsionarían las fronteras lagrangianas de las nubes o, equivalentemente, causarían un flujo a través de las fronteras eulerianas.

Discutimos la compatibilidad del presente escenario con datos observacionales. Encontramos que los histogramas de velocidad pesados por masa son consistentes con perfiles de línea observacionales cuya resolución espacial y espectral es comparable, presentando anchos de línea y subestructura espectral similar. Un análisis de las regiones que contribuyen a cada intervalo de velocidad indica que las características espectrales de estos histogramas no provienen de núcleos aislados. Por el contrario, provienen de regiones extendidas a lo largo de la nube, los cuales frecuentemente tienen vectores de velocidad completamente diferentes.

Finalmente, argumentamos que el escenario presentado aquí también puede ser aplicable a escalas menores y densidades mayores (nubes moleculares y su subestructura, al menos hasta $n \sim 10^3\text{--}10^5 \text{ cm}^{-3}$), y sugerimos que las configuraciones en equilibrio cuasi-hidrostático no pueden ser producto de fluctuaciones turbulentas a menos de que el comportamiento termodinámico del flujo se vuelva aproximadamente adiabático. Demostramos, usando tasas de enfriamiento apropiadas, que ésto no ocurre excepto en regiones muy pequeñas ($\lesssim 10^{-2} \text{ pc}$) o hasta que se alcancen densidades protoestelares.

Abstract

We examine the idea that diffuse HI and giant molecular clouds and their substructure form as density fluctuations induced by large scale interstellar turbulence. We do this by closely investigating the topology of the velocity, density and magnetic fields within and at the boundaries of the clouds emerging in high-resolution two-dimensional simulations of the ISM including self-gravity, magnetic fields, parameterized heating and cooling and a simple model for star formation. We find that the velocity field is continuous across cloud boundaries for a hierarchy of clouds of progressively smaller sizes. Cloud boundaries defined by a density-threshold criterion are found to be quite arbitrary, with no correspondence to any actual physical boundary, such as a density discontinuity. Abrupt velocity jumps are coincident with the density maxima, indicating that the clouds are formed by colliding gas streams. This conclusion is also supported by the fact that the volume and surface kinetic terms in the Eulerian Virial Theorem for a cloud ensemble are comparable in general, and by the topology of the magnetic field, which exhibits bends and reversals where the gas streams collide. However, no unique trend of alignment between density and magnetic features is observed. Both sub- and super-Alfvénic motions are observed within the clouds.

In the light of these results, we argue that thermal pressure equilibrium is irrelevant for cloud confinement in a turbulent medium, since inertial motions can still distort or disrupt a cloud, unless it is strongly gravitationally bound. Turbulent pressure confinement appears

self-defeating, because turbulence contains large-scale motions which necessarily distort Lagrangian cloud boundaries, or equivalently cause flux through Eulerian boundaries.

We then discuss the compatibility of the present scenario with observational data. We find that density-weighted velocity histograms are consistent with observational line profiles of comparable spatial and velocity resolution, exhibiting similar FWHMs and similar multi-component structure. An analysis of the regions contributing to each velocity interval indicates that the histogram “features” do not come from isolated “clumps”, but rather from extended regions throughout a cloud, which often have very different total velocity vectors.

Finally, we argue that the scenario presented here may be also applicable to small scales with larger densities (molecular clouds and their substructure, up to at least $n \sim 10^3\text{--}10^5 \text{ cm}^{-3}$), and conjecture that quasi-hydrostatic configurations cannot be produced from turbulent fluctuations unless the thermodynamic behavior of the flow becomes nearly adiabatic. We demonstrate, using appropriate cooling rates, that this will not occur except for very small regions ($\lesssim 10^{-2} \text{ pc}$) or until protostellar densities are reached for collapse.

13.1 Introduction

Theoretical models of interstellar clouds and clumps most frequently assume static or stationary configurations, the clouds being either confined by the external pressure (Maloney 1988; Bertoldi & McKee 1992), or in “virial equilibrium” between their self-gravity and some form of internal energy, be it thermal (e.g., Chieze 1987), micro-turbulent (e.g., Chandrasekhar 1951; Bonazola et al. 1987; Leorat et al. 1990; Vázquez-Semadeni & Gazol 1995) or magnetic (e.g., Shu et al. 1987; Mouschovias 1987, Myers & Goodman 1988b), forming out of instabilities or coagulation of smaller clouds (see Elmegreen 1993a for a review). Nevertheless, the interstellar medium (ISM) is well known to be highly violent (e.g., McCray & Snow 1979), and recently it has become increasingly accepted that it is turbulent throughout (e.g., Scalo 1987; see also the volume “Interstellar Turbulence” [Franco & Carramiñana 1998]). In such a medium, clouds may naturally form as turbulent density fluctuations as well.

Within this dynamic, turbulent framework, it is important to reconsider a number of the standard assumptions of those models. This is most adequately done in the context of detailed inspections of the topology of the various fields in numerical simulations of turbulence in the ISM (Passot, Vázquez-Semadeni & Pouquet 1995), in which clouds are observed to form and evolve, and a Virial Theorem (VT) analysis of such data.

The VT is a very useful tool for describing the balance between all the physical agents in molecular clouds. Customarily, the VT is considered in a Lagrangian frame, i.e., a frame moving with the flow. However, there are circumstances when one would prefer to use an Eulerian description. For example, a Lagrangian description is clearly not well suited for describing the propagation of a wave, in which the fluid does not move along with the perturbation, while in the case of an isolated object a Lagrangian description fits most naturally (see also Vázquez-Semadeni, Passot & Pouquet 1996, hereafter VSPP96). In the interstellar case, if significant mass exchange occurs between a cloud and its surroundings,

such as an accreting cloud, an Eulerian description (fixed in space) may be preferable since a Lagrangian boundary would undergo severe distortions. Parker (1969) derived an Eulerian form of the Virial Theorem (EVT) in tensor form, but he explicitly neglected the mass flux through the surface of the cloud. More recently, McKee & Zweibel (1992) (hereafter MZ92) have written all the terms entering the EVT:

$$\frac{1}{2} \dot{I}_E = 2 \left(\mathcal{E}_{\text{th}} + \mathcal{E}_{\text{kin}} - \mathcal{T}_{\text{th}} - \mathcal{T}_{\text{kin}} \right) + \mathcal{M} + \mathcal{W} - \frac{1}{2} \frac{d\Phi}{dt}, \quad (13.1)$$

where $I_E \equiv \int_V \rho r^2 dV$ is the moment of inertia of the cloud, $\mathcal{E}_{\text{th}} \equiv 3/2 \int_V P_{\text{th}} dV$ is the thermal energy, with P_{th} being the thermal pressure; $\mathcal{E}_{\text{kin}} \equiv 1/2 \int_V \rho u^2 dV$ is the kinetic energy, $\mathcal{T}_{\text{th}} \equiv 1/2 \oint_S (x_i P_{\text{th}}) \hat{n}_i dS$ is the surface thermal term, $\mathcal{T}_{\text{kin}} \equiv 1/2 \oint_S (x_i \rho u_i u_j) \hat{n}_j dS$ is the surface kinetic term, $\mathcal{M} \equiv 1/8\pi \int_V B^2 dV + \int_S x_i T_{ij} \hat{n}_j dS$ is the magnetic term, with T_{ij} the Maxwell stress tensor, $\mathcal{W} \equiv \int_V \rho x_i g_i dV$ is the gravitational term and $\Phi \equiv \oint_S \rho x^2 u_i \hat{n}_i dS$ is the flux of moment of inertia through the surface of the cloud. Sums over repeated indices are assumed unless otherwise stated.

Frequently, the surface terms are neglected altogether, especially in observational work (Larson 1981; Torrelles et al. 1983; Myers & Goodman 1988a; Fuller & Myers 1992), although it is also a common practice in theoretical studies, as a consequence of assuming isolated clouds (e.g., Chandrasekhar 1953; Parker 1969; Parker 1979). The most notable exception is the thermal pressure surface term \mathcal{T}_{th} , which is frequently invoked for “pressure confinement” (e.g. McCrea 1957; Keto & Myers 1986; Maloney 1988; Bertoldi & McKee 1992; McLaughlin & Pudritz 1996; Yonemura et al. 1997). By analogy, McKee & Zweibel (1992) have considered the possibility of turbulent pressure confinement by means of the term \mathcal{T}_{kin} . However, in the present paper we will argue that both kinds of pressure confinement require idealized conditions that are not likely to be realized in the actual ISM. If the interstellar medium (ISM) is globally turbulent, the velocity field is in general locally nonzero, and thermal pressure balance may be irrelevant, since a cloud can still undergo deformation due to the inertial motions, which will induce a nonzero RHS via the kinetic terms \mathcal{E}_{kin} , \mathcal{T}_{kin} , and $d\Phi/dt$.

Concerning turbulent pressure confinement, its feasibility requires the underlying assumption that the turbulence be microscopic, so that it can be considered isotropic compared to the scale of the cloud. However, turbulence is inherently a multi-scale phenomenon, and is expected to contain excitation at scales comparable or even larger to that of the cloud. It is in this context that the clouds may be considered as density fluctuations produced by larger-scale compressive turbulent motions (e.g., Hunter 1979; Larson 1981; Hunter & Fleck 1982; Hunter et al. 1986; Elmegreen 1993b; Vázquez-Semadeni, Passot & Pouquet 1995, hereafter VSPP95). Such clouds are then turbulent fluctuations, and can either rebound, fragment or collapse depending on the compressive energy available, the cooling ability of the flow, the topology of the velocity and magnetic fields, the production of internal turbulent motions and a number of instability mechanisms (e.g., Elmegreen & Elmegreen 1978; Vishniac 1983, 1994; Hunter et al. 1986; Tohline, et al. 1987; Stevens et al. 1992; Elmegreen 1993b; VPP96; Kornreich & Scalo 1998). On observational grounds,

Gómez de Castro et al. (1997) have similarly suggested that high-latitude molecular clouds may originate at the collision sites of infalling HI high-velocity streams.

Note that in this scenario, clouds and clumps need not be in a static or quasi-static equilibrium at any time. Moreover, the fact that clouds and clumps are observed to be internally turbulent suggests that the turbulence has not been completely dissipated inside. In fact, Kornreich & Scalo (1998) showed that shocks running obliquely through a density gradient will produce further internal turbulence. This also underscores the importance of the question of the degree to which clouds have “sharp” boundaries, since shock-cloud simulations for clouds with sharp boundaries only produce vorticity in a surface shear layer (e.g. Klein et al. 1995), not internal motions.

The plan of the paper is as follows. We start in §13.2 by discussing the role of the kinetic terms in the VT and the implications for pressure confinement. Then, after briefly describing the numerical simulations (§13.3), we proceed to a description of our results (§ 13.4), starting with a discussion of the density, velocity and magnetic features that arise, and their spatial correlations (§13.4.1). Then we present an evaluation of the surface and volume kinetic terms in the VT, suggesting that their similarity may be the result of both types of terms measuring the same phenomenon (§ 13.4.2). The super- or sub-Alfvénic character of the motions is discussed in §13.4.3. In § 13.5 we present several comparisons with known observational data, such as line profiles observed in cloud complexes (§13.5.1), the topology of the magnetic field (§ 13.5.2), and the lifetimes of the clouds (§ 13.5.3). In § 13.6 we then discuss several consequences and possible caveats, like whether the scenario proposed here can be applicable to smaller, denser scales, the unlikelihood of forming quasistatic clumps in a turbulent medium, and the effect of the dimensionality of our simulations. Finally, we give a summary and some conclusions in §13.7.

It is interesting to note that the present paper may be regarded as theoretical justification for the suggestion made over 45 years ago by Chandrasekhar & Münch 1952 that an alternative to the picture that visualizes the interstellar medium as consisting of a distribution of discrete clouds might be necessary.

13.2 Kinetic Terms in the Eulerian Virial Theorem

As is well known (e.g., Parker 1979; McKee & Zweibel 1992), the EVT can be obtained from the conservative form of the momentum equation,

$$\frac{\partial(\rho u_i)}{\partial t} + \frac{\partial(\rho u_i u_j)}{\partial x_j} = \sum_k F_k \quad (13.2)$$

(where F_k generically represents the various force densities involved in the problem) by dotting it with the position vector \mathbf{x} and integrating over a volume V fixed in space. We remind the reader that the full Virial Theorem, eq. (13.1), holds always because it is a direct consequence of the momentum equation, although this does not necessarily imply that the system is in equilibrium or, in particular, that the linewidth of an interstellar cloud is directly related to its mass and radius (Maloney 1988). A detailed analysis of the VT in our simulations will be presented elsewhere (Ballesteros-Paredes et al. 1999).

In the present paper we focus on the relative importance of the surface and volumetric kinetic terms, and their role in shaping the clouds. It can be easily checked that, in the EVT (eq. [13.1]), the kinetic energy \mathcal{E}_{kin} , the kinetic surface term \mathcal{T}_{kin} , and the time-derivative terms \dot{I}_E and $d\Phi/dt$, originate from the LHS in the momentum equation (eq. [13.2]). While the meaning of the kinetic energy term \mathcal{E}_{kin} is obvious, the kinetic surface term \mathcal{T}_{kin} has two possible interpretations. One is as half the flux of the instantaneous rate of change of the moment of inertia $\rho x_i u_i$ through the cloud's surface. Alternatively, it can be interpreted as the sum of the ram pressure plus the kinetic stresses, both evaluated at the surface of the cloud:

$$\oint_S x_i \rho u_i u_j \hat{n}_j dS = \oint_S x_i \rho u^2 \hat{n}_i dS + \oint_S x_i \rho u_i u_j \hat{n}_j dS, \quad (13.3)$$

where $i \neq j$ in the last surface integral. The first term on the RHS of eq. (13.3) is analogous to the thermal pressure surface term. The second term, on the other hand, reflects the fact that the turbulent motions are not isotropic, giving off-diagonal contributions to the total pressure tensor $\Pi_{ij} = P_{\text{th}} \delta_{ij} + \rho u_i u_j$ (Landau & Lifshitz 1987). This exhibits in a clear way the difference between the isotropic nature of the thermal pressure and the anisotropic nature of the “turbulent” pressure.

Another important difference between the thermal and “turbulent” pressures lies in the fact that the latter is in general expected to involve motions of scales comparable to that of the cloud, as mentioned in §13.1. But since the velocity field carries mass with it, such large-scale motions necessarily imply a mass flux across fixed, Eulerian cloud boundaries. Conversely, in a Lagrangian description, such turbulent motions should lead to severe distortions of the Lagrangian cloud boundary, possibly giving it a fractal character (e.g., Scalo 1990; Falgarone et al. 1991).

The exception to the scenario depicted above is the case of strongly self-gravitating clumps in (magneto-) hydrostatic equilibrium, from which the gas cannot escape once it has been captured (“decouples” from the intercloud medium). In this case, the cloud should be bound by an accretion shock and, although strictly speaking there is flux across the shock, the accreted material is not mixed far beyond the shock into the cloud’s “body”. However, it seems to us that the question as to whether such quasi-hydrostatic configurations can actually be produced in a turbulent ISM remains open, as discussed in § 13.6.1.

13.3 Numerical Simulations

In the following sections, we discuss the topology of the density, velocity and magnetic fields in 2D numerical simulations of the ISM based on the model of Passot, Vázquez-Semadeni & Pouquet (1995) (hereafter PVP95), which represents 1 kpc² of the ISM on the Galactic plane, centered at the solar Galactocentric distance. We refer the reader to that paper for the equations and parameters of the model, which includes self-gravity, magnetic fields, parameterized cooling and diffuse heating, the Coriolis force, large-scale shear, and parameterized localized stellar energy input due to ionization heating. The parameterized cooling is as in Chiang & Bregman (1988), who fitted piecewise power laws to the standard

cooling calculations of Dalgarno & McCray (1972) and Raymond et al. (1976), and are appropriate for atomic and ionized gas. As discussed in VPP96, the cooling and diffuse heating timescales are much shorter than the dynamical timescales, implying that the flow is always very near thermal equilibrium (except in the vicinity of star formation sites). Setting up the thermal equilibrium condition, one can find the equilibrium pressure as a function of the density, which behaves as a piecewise power law $P \propto \rho^{\gamma_{\text{eff}}}$. We refer to this as a *piecewise barotropic behavior*. We should emphasize here that, although in previous papers (e.g. VPP96) we have referred to such barotropic behavior as “polytropic”, we have now chosen to abandon such nomenclature in order to avoid any possible confusion with polytropic hydrostatic spheres. Indeed, the simulations are highly dynamic, and the clouds within them are not in hydrostatic equilibrium, in sharp contrast with equilibrium models of polytropic gas spheres (e.g., Chandrasekhar 1939; Turner 1994; McLaughlin & Pudritz 1996; for further discussion, see Vázquez-Semadeni et al. 1998). We refer to γ_{eff} as the “barotropic exponent”.

It has been shown by VSPP95 that, for the heating and cooling functions used there, the thermal equilibrium values of the temperature and pressure can be expressed as functions of the density in the range $100 \text{ K} < T < 10^5 \text{ K}$ for non star-forming regions. Therefore, γ_{eff} can also be expressed as a piecewise constant over the corresponding density range. For the fiducial values adopted in the model (PVP95), γ_{eff} takes the values (VPP96)

$$\gamma_{\text{eff}} = \begin{cases} 0.25 & 1.57 < \rho \quad (100 < T < 2000) \\ 0. & 0.39 < \rho \leq 1.57 \quad (2000 \leq T < 8000) \\ 0.48 & 3.15 \times 10^{-3} < \rho \leq 0.39 \quad (8000 \leq T < 10^5) \end{cases} \quad (13.4)$$

where densities are in units of cm^{-3} and temperatures in Kelvins.

In eq. (13.4), equilibrium temperature ranges equivalent to the specified density ranges are indicated in parentheses. In the simulations, stellar ionization heating is modeled by means of a local heating source which is turned on if the density exceeds a critical value $\rho_{\text{th}} = 30\langle\rho\rangle$, where the brackets denote an average over the whole volume of the simulation. Note that temperatures over a few $\times 10^4 \text{ K}$ are never reached in the simulations, because supernovae are not included, since these require non-trivial modifications to the code (Gazol-Patiño & Passot 1999). The maximum densities reached in the simulations are $\sim 100 \text{ cm}^{-3}$, with $T \sim 100 \text{ K}$.

The simulations we use are refinements of the PVP95 model at a higher resolution (800×800 grid points), presented in Vázquez-Semadeni, Ballesteros-Paredes, & Rodríguez (1997). The stellar energy injection maintains the turbulence in the medium, promoting further cloud formation. Nevertheless, we turn off star formation shortly before the time at which the data are analyzed, in order to allow for the largest possible density gradients, since otherwise the stellar heating prevents the density from reaching values significantly larger than ρ_{th} , by causing the neighboring gas to re-expand. The various physical quantities are in units of $\rho_0 = 1 \text{ cm}^{-3}$, $u_0 = 11.7 \text{ km s}^{-1}$, $T_0 = 10^4 \text{ K}$ and $B_0 = 5\mu\text{G}$ (see PVP95).

We have developed a cloud-finding numerical algorithm in physical space (as opposed to the position-velocity space of observational data) for the density data from the simulations

(Ballesteros-Paredes & Vázquez-Semadeni 1995). A cloud is defined as a connected set of points (pixels) whose densities are larger than a given threshold ρ_{th} . The clouds obtained through this procedure are clearly quite arbitrary, since as ρ_{th} is increased the boundary of the cloud simply moves “inwards”. However, eventually an increase in ρ_{th} will lead to a more qualitative change in which a given cloud splits into two or more “children”, in a similar manner to the “structure trees” used by Houllahan & Scalo 1992. This procedure is in a sense analogous to performing observations using different tracers sensitive to different density ranges. Alternative cloud identification algorithms based on locating density maxima (e.g., Williams et al. 1994) were not investigated, but we do not expect that such procedures would affect the qualitative nature of our results, which, as will be seen, appear to follow quite generally from the physics of the problem.

Given the above algorithm for defining the clouds, the kinetic terms entering the VT are then evaluated numerically for each cloud, having previously subtracted its bulk mass-averaged velocity, defined as

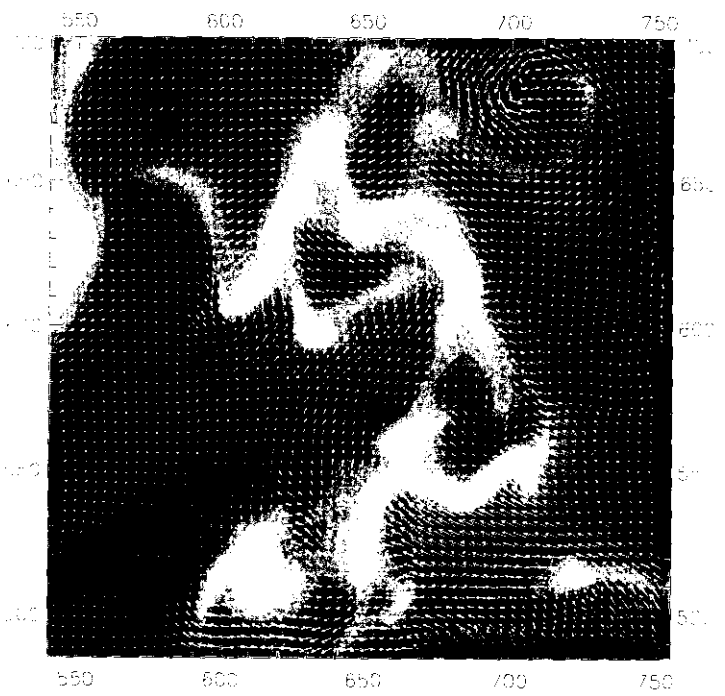
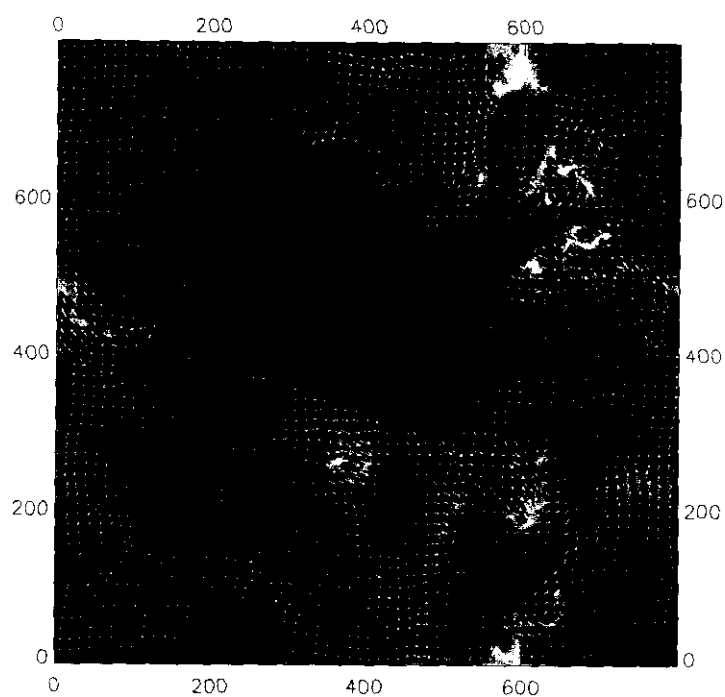
$$\langle u_i \rangle_{\text{mass}} \equiv \frac{\int_V \rho u_i dV}{\int_V \rho dV}, \quad (13.5)$$

in order to measure only the contribution associated to the fluctuations. We refer to this as measuring the velocities in the “cloud frame”.

13.4 Results and Discussion

13.4.1 Density and velocity field topology

In figs. 13.1a, b and c we show three hierarchical levels of the density field (gray scale), with the corresponding velocity fields (arrows). In fig. 13.1c we further denote super- and sub-Alfvénic velocities with black and white arrows, respectively (see § 13.4.3), where the Alfvén speed is defined as $v_a^2 = B^2/\rho$ in the code’s units.



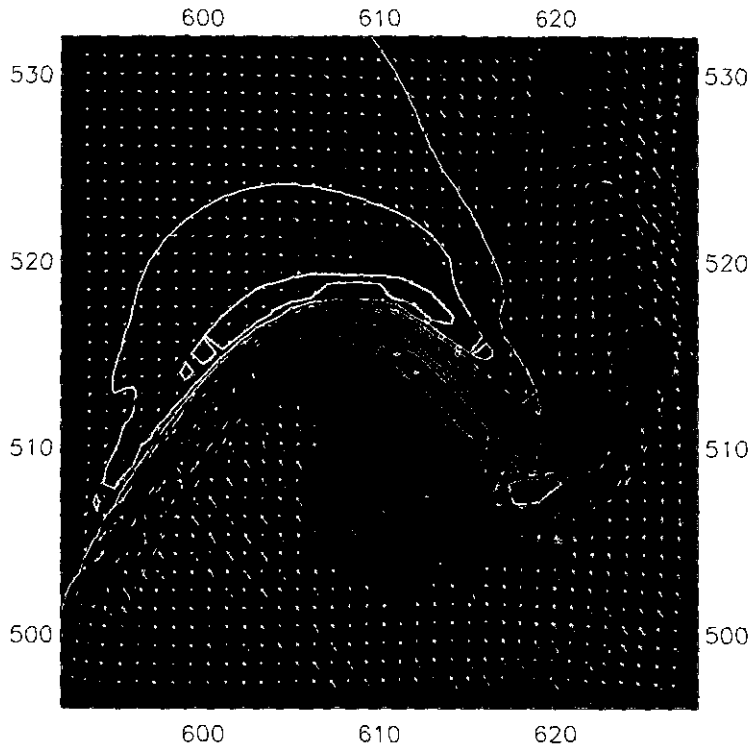


FIGURA 13.1: Three hierarchical levels of clouds in the simulation, showing the logarithmic density scale with shades of gray, and the velocity field with arrows. Pixel numbers are indicated by the grids. a) The whole simulation field field, 800 pixels on a side, corresponding to 1 kpc. The gray scale shows structures with $\rho \geq \rho_{\text{th}} = 1.5 \text{ cm}^{-3}$. b) Magnification of the complex that appears when setting $\rho_{\text{th}} = 4$ in the upper right quadrant of fig. 1a. c) Magnification of the cloud that appears when setting $\rho_{\text{th}} = 8$ in the lower left region of fig. 1b. Black arrows indicate super-Alfvénic velocities in the frame moving with the cloud, and white arrows indicate sub-Alfvénic velocities. The contours give the magnetic field strength B . Thicker contours indicate larger B -values. The maximum density value is 55 cm^{-3} . The velocities in a and b are shown in the simulation frame, while in c they are in the cloud frame.

Figure 13.1a shows a snapshot of the simulation at $t = 7.2 \times 10^7 \text{ yr}$. The density field ranges from ~ 0.01 to $\sim 100 \text{ cm}^{-3}$. Figs. 13.1b and c show two subsequent hierarchical levels of clouds, obtained at $\rho_{\text{th}} = 4$ and 8, respectively. The sizes of the boxes shown in the three panels are 800, 215 and 45 pixels per side (1 pixel = 1.25 pc). We refer to the cloud in fig. 13.1b as the “parent” cloud, and to that in fig. 13.1c as the “child” cloud. Note that only fig. 13.1c shows the velocity field in the cloud frame.

Inspecting the plotted density and velocity fields, we observe that the fluid velocity at the cloud boundaries is in general continuous, at any level of the hierarchy. Sharp changes in the velocity field (shocks¹) are in general oblique and tend to occur mostly at the centermost parts of the clouds, where the highly filamentary density field exhibits “ridges”. This indicates that the density features are produced by colliding streams, a fact that can be seen more accurately in figs. 13.2a, b and c. These show cuts, along the x - (at $y = 514$, fig. 13.2a) and y - (at $x = 602$ and $x = 614$, figs. b and c respectively) axes,

¹In the simulations, shocks are sharp gradients extending over 3 to 5 pixels, due to the action of viscosity (Vázquez-Semadeni, Ballesteros-Paredes & Rodríguez 1997)

of the density ρ (solid line), and the x - and y -components of the velocity, u_x (dotted line) and u_y (long dashed line) for a region containing the clouds of figs. 13.1b and c. The axes in these plots indicate pixel number. For added clarity, we show in fig. 13.3 the lines along which these cuts are taken.

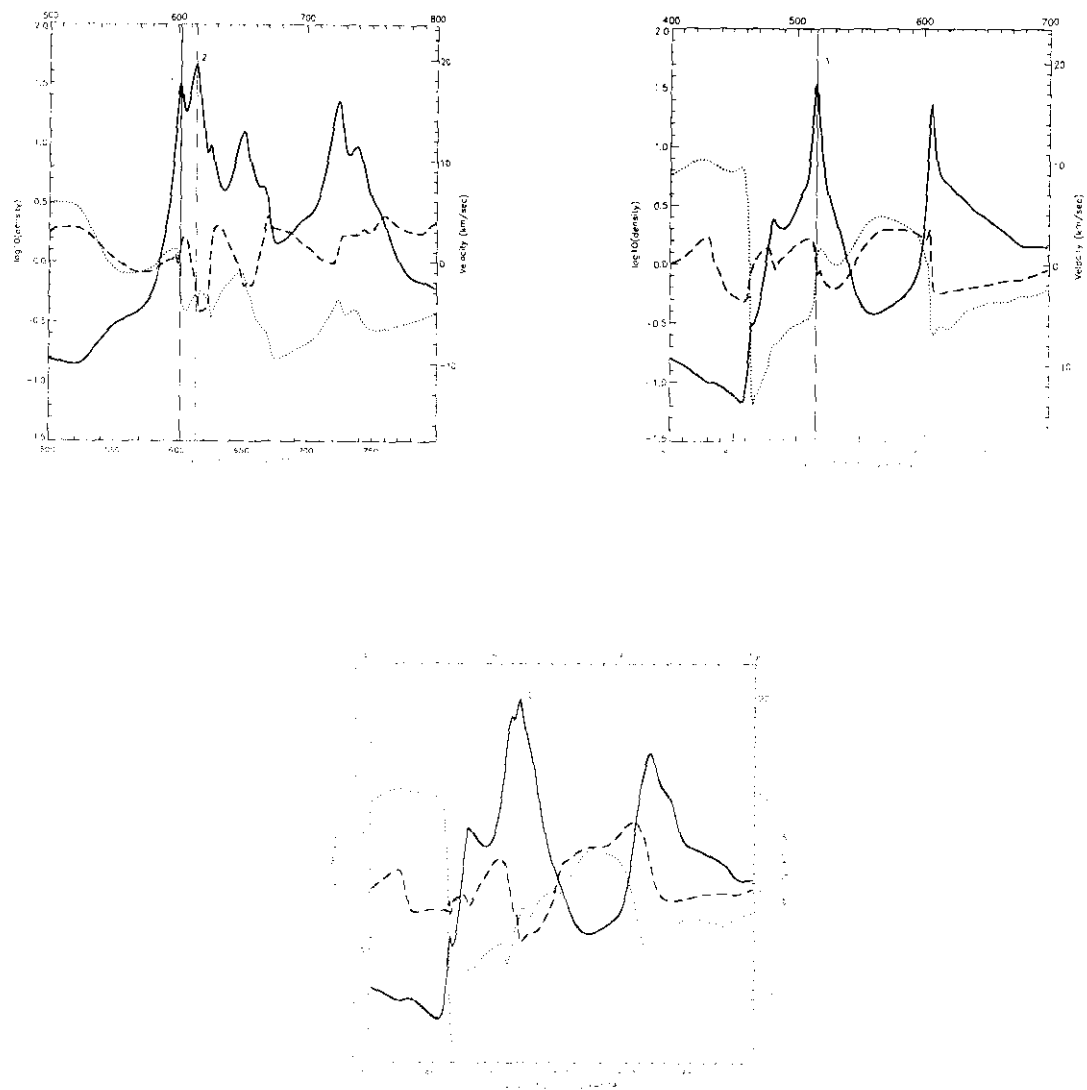


FIGURA 13.2: Cuts passing through the cloud shown in fig. 13.1c, (as indicated by the lines in fig. 13.3), showing the log of the density (solid line), and the x - (dotted line) and y - (dashed line) components of the velocity. a) Cut along x at $y = 514$. b) Cut along y at $x = 602$. c) Cut along y at $x = 614$. In a), two peaks are indicated. Peak 1 is seen to correspond to an x -shock (abrupt negative gradient) in a) and to a y -shock in b). Peak 2 is almost imperceptible in u_x , but is seen to correspond to a y -shock in c). Also, note the “plateau” in u_x extending 50 pixels to the right of peak 1, with average negative values, although with further substructure. Note that the scale is larger than in fig. 13.1c, in order to give a broader view of the velocity components.

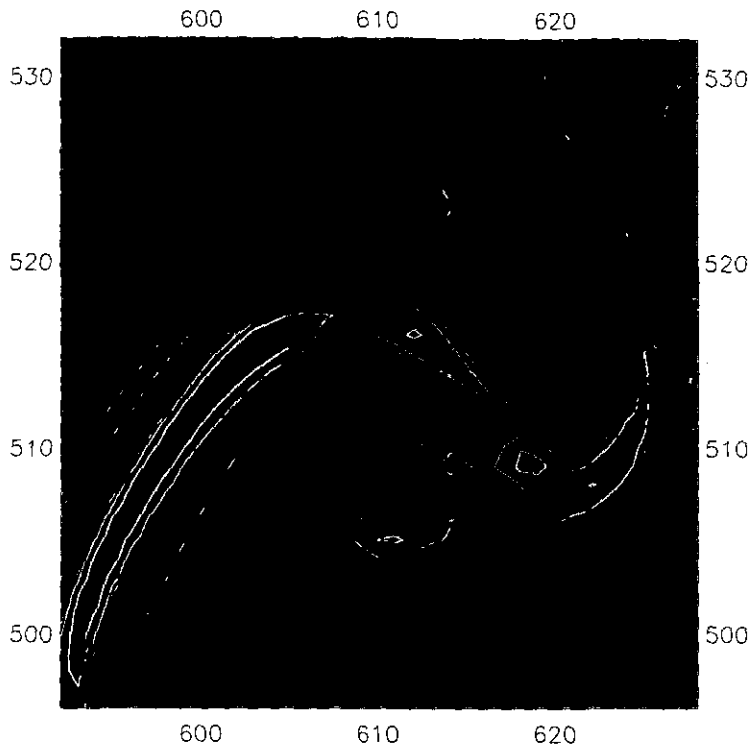


FIGURA 13.3: The same cloud as in fig. 13.1c, but with superimposed velocity divergence contours. Density maxima are seen to correspond to maximum negative values of the divergence. Also indicated are the lines along which the cuts of fig. 13.2 are taken.

The central parts (3-5 pixels) of the density peaks are seen to correspond in general to large negative longitudinal gradients $\partial u_i / \partial x_i$ (no sum over i) of the velocity, i.e., shocks. However, the clouds (i.e., large density values) extend beyond the shocks for many more pixels, where the velocity component exhibits plateaus with superimposed small-scale structure. These plateaus are indicative of the approaching streams (extended inward motions). As an example, consider the peaks labeled “1” and “2” in fig. 13.2a. Peak 1 corresponds to a shock at $x = 602$, and is flanked by an expansion wave ($\partial u_x / \partial x > 0$) on the left, and by a plateau with $u_x < 0$ on the right, although the plateau itself contains substructure. This peak also corresponds to a shock along the y -direction (fig. 13.2b). Interestingly, peak “2” in fig. 13.2a does not seem to correspond to a shock along the x -direction, but in fig. 13.2c it can be seen that it is caused by a shock in the y -direction. In order to further illustrate this point, in fig. 13.3 we show the same cloud as in fig. 13.1c, but showing the density field as a gray-scale image and the divergence $\partial u_i / \partial x_i$ of the velocity field with contours. Local density maxima clearly coincide with local (negative) minima of the divergence.

It is worth noting that in figs. 13.2a, b and c, larger-scale density features are also seen to correspond to large-scale negative gradients of the velocity field, although with much substructure. See, for example, the large cloud complex (multiple density peak) extending from $580 \lesssim x \lesssim 780$ in fig. 13.2a. The very largest-scale inward flows are probably of gravitational rather than turbulent origin (e.g., Vázquez-Semadeni & Pouquet

1998), since, for example, the upper right quadrant of the simulation has a mean density of 1.7 cm^{-3} , implying an effective Jeans length (taking into account the effective polytropic exponent, as in eq. (15) of VPP96) of 0.42 times the length of the box. Thus, the region is Jeans unstable. Besides, the simulations do not include supernovae which could induce turbulent motions at the largest scales. However, note that in the real ISM both sources of motion are likely to occur.

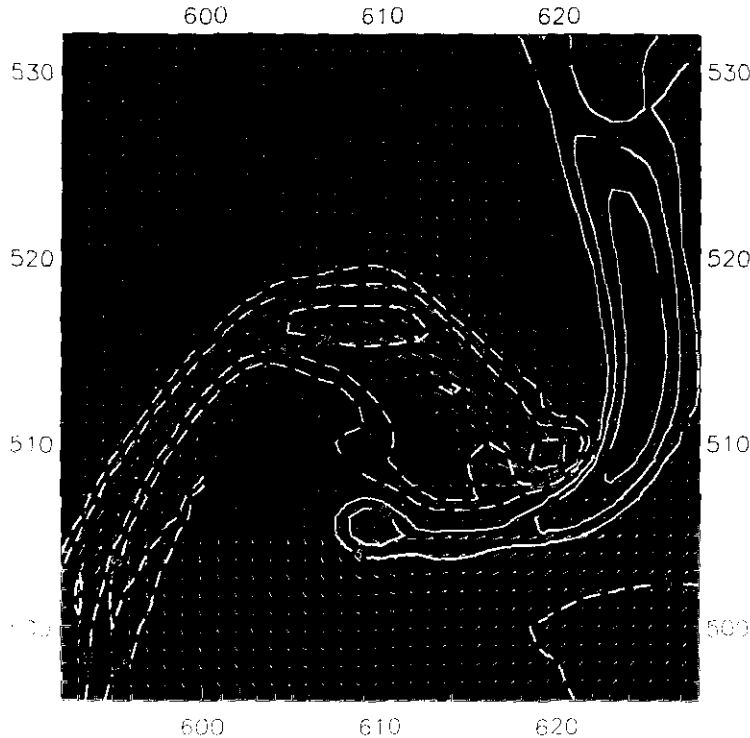


FIGURA 13.4: Same cloud as in fig. 13.1c, but with superimposed vorticity contours. There is a significant correlation between the density (and therefore the divergence) and the vorticity fields. We interpret this as a result of the generally oblique nature of the stream collisions. Solid (dashed) contours indicate positive (negative) vorticity. Also shown are the magnetic field vectors (arrows). Note the correlation between density and magnetic field bendings and the field reversal along the central ridge of the cloud. Note also the general alignment of the field with the density, although at many places the field crosses the cloud's "boundary" perpendicularly (e.g., at the concave region below the left filament).

There also appears to be a certain amount of spatial correlation between density and vorticity features. In figure 13.4 we show the vorticity field (contours) superposed onto the density field (gray-scale) for the cloud of fig. 13.1c. In this case, the correlation between local maxima of the density field and maxima (or minima) of the vorticity field is not as tight, the critical points of the vorticity being shifted by a few pixels with respect to the density peaks. Nevertheless, there is still a clear correspondence between vorticity and density features. This correlation can be understood because, as mentioned above, the stream collisions are in general oblique. It is possible then that the detailed structure inside the clouds consists of shocks and tangential discontinuities. Moreover, the shocks are generally curved and are encountering density variations in the pre-shock gas, so vorticity

production is expected behind them (Hayes 1957; Passot & Pouquet 1988; Kornreich & Scalo 1998).

The continuity of the velocity field through the cloud boundaries has an interesting subjective implication. The definition of a cloud by a density threshold is actually seen to be rather arbitrary, since the clouds do not have sharp physical boundaries. Thus, as long as the change in the density threshold does not imply a “splitting” of a cloud into its offspring, it only amounts to considering the same cloud out to different distances from the maximum, but without there being any clear “edge” to the cloud (In the Appendix we rule out the possibility that this might be a numerical artifact of the mass diffusion term used in the continuity equation [see eq. (3) in Vázquez-Semadeni, Ballesteros-Paredes & Rodríguez 1997].) In § 13.6.3 we discuss the consistency of this result with observational data.

13.4.2 Virial surface terms and pressure confinement

The velocity fields observed in the simulations indicate a strong flux of the relevant dynamical quantities through the cloud boundaries at all scales. To quantify this, in fig. 13.5 we show a plot of the kinetic energy \mathcal{E}_{kin} vs. the kinetic surface term \mathcal{T}_{kin} for the parent complex shown in fig. 13.1a and all its daughter clouds resulting from setting $\rho_{\text{th}} = 4, 8, 11$ and 16 , and with areas larger than 300 square pixels. The latter requirement is imposed in order to avoid including clouds so small that they are strongly influenced by viscous and diffusive numerical effects. The clouds shown in figs. 13.1b and c are represented with a different symbol in fig. 13.5 for identification. Note that both kinds of virial terms are computed in the cloud frame.

It is seen that in general the surface kinetic virial term is of the same order of magnitude as the volume term, i.e., the kinetic energy contained in the cloud’s volume. This means that both terms are of similar importance in shaping and supporting the clouds. At a more detailed level, this seems to be a reflection of the continuity of the velocity field. The flow is entering the clouds, and shocking at their innermost regions. Thus, the two terms refer to essentially the same process, only measuring it at different places (one over the cloud’s volume, the other at the cloud’s boundary but weighted by the distance to the center of mass), explaining their similar values. This is analogous to the well known property of the surface and volume thermal pressure terms, that if the pressure is constant the two terms cancel.

It is important to remark that the similarity between these two terms does not imply that the cloud is “confined” by turbulent pressure, in the sense that this is not a static configuration. First, the two terms do not cancel each other exactly, leaving a net contribution available for shaping the cloud (the contribution $\mathcal{E}_{\text{kin}} - \mathcal{T}_{\text{kin}}$ to d^2I/dt^2). Second, it is important to note that the points in fig. 13.5 lie sometimes above and sometimes below the line $\mathcal{E}_{\text{kin}} = \mathcal{T}_{\text{kin}}$, indicating that for some clouds the contribution to d^2I/dt^2 is positive, and negative for others. This implies that the kinetic terms sometimes provide net “support” and sometimes cause net compression, although in general the clouds are expected to suffer distortions that cannot be classified as either one of the above. Thus, the clouds

are evolving with time, continuously changing their volume and shape, since they are the density fluctuations produced by the turbulence².

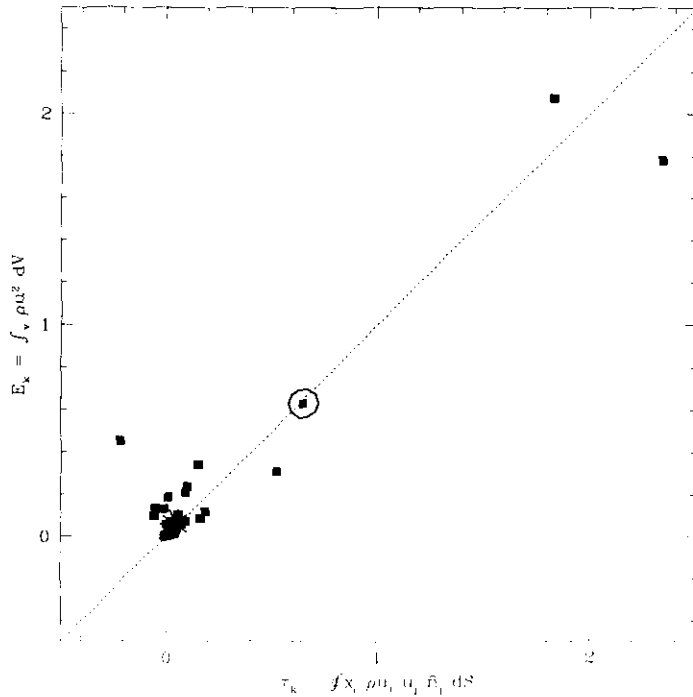


FIGURA 13.5: Kinetic energy \mathcal{E}_{kin} vs. the kinetic surface term T_{kin} for all clouds with areas larger than 300 pixels in the whole field. The complex of fig. 13.1b is shown by a circle, and the cloud in fig. 13.1c is shown by the star. Note the similarity of the two terms for most of the clouds, indicating that both contribute in similar amounts to the clouds' virial balance.

The thermal pressure, as discussed in VSPP95, shows little spatial variation (except near star formation sites where it is much larger) because $0 \leq \gamma_{\text{eff}} < 1$ in general for the temperature range spanned by the simulations. In particular, $\gamma_{\text{eff}} = 0$ implies an isobaric medium. Note that $\gamma_{\text{eff}} < 1$ is in agreement with the elementary fact that in the ISM denser regions are colder in that temperature range (Myers 1978). In other words, the near constancy of the pressure in this temperature range is a consequence of thermal balance (giving $\gamma_{\text{eff}} < 1$) in a medium whose density is determined by the turbulent motions. However, this near "pressure equilibrium" has no effect in confining the clouds, which are in a state of constant change. As stated in VSPP95, the pressure is *slaved* to the density field, which in turn is determined by the velocity field.

²See the accompanying video to VSPP95 for a non-magnetic example. An mpeg video of a fully MHD simulation from PVP95, among others, can be seen at <http://www.astroscu.unam.mx/turbulence/movies.html>

13.4.3 Super- and sub-Alfvénic motions and magnetic field topology

Another point worth discussing is the sub- or super-Alfvénic character of the velocity, since it has been traditionally argued that the motions in molecular clouds are supersonic but sub-Alfvénic (e.g., Shu et al. 1987), although more recently it has been claimed by Padoan & Nordlund (1999) that this may not be so, but rather that motions may generally be super-Alfvénic. Since in our simulations clouds form out of the general ISM, they represent a good test to see which of these conditions develop, rather than using some pre-determined assumption about the sub- or super-Alfvénic character of the problem (e.g., Mouschovias 1987; Lizano & Shu 1989). In fig. 13.1c the black and white arrows respectively denote super- and sub-Alfvénic velocities in the cloud frame. It is seen that *inside the cloud there are both sub- and super-Alfvénic velocities*. Since the velocity field does not show large magnitude fluctuations at the transition sites, this can only be understood in terms of a change in the Alfvén speed v_a . To see this, in fig. 13.1c contours of the magnitude B of the magnetic field are shown as well. The contours span the range from 4 to 10 μG , in intervals of 1.5 μG . Thicker lines indicate progressively larger values of B . The velocity is seen to be sub-Alfvénic everywhere outside the cloud. Inside the cloud, it is super-Alfvénic in the lower region of the cloud. In the upper region, the velocity is sub-Alfvénic due to a combination of large B -values and low densities. Looking down towards the center, another super-Alfvénic region is seen, due mainly to the increase in the density, which reaches $\rho = 55 \text{ cm}^{-3}$ at the peak. However, at the peak, the velocity becomes sub-Alfvénic again, this time due to a sharp decrease in the velocity magnitude itself – sort of a “stagnation point” at the density peak. These variations are thus due again to the collisions between the magnetized gas streams, which push the field and cause magnetic shocks and field-reversals where the fluid shocks occur, and in general produce a rather chaotic flow. One such reversal is seen to occur on the filament extending out of the cloud towards the lower left corner of fig. 13.1c. This is seen on the contours as a decrease in the field’s intensity towards the central ridge of the filament. Figure 13.4, which shows the magnetic field vectors on top of the density (gray scale) and the vorticity (contours), shows this phenomenon more clearly.

Note that this trans-Alfvénic character of the motions may explain why the density peaks are “fat” compared to the stream-collision sites: the information of the presence of the collision is often able to travel upstream of the flow. Furthermore, since the collisions are generally oblique, it is likely that magnetosonic waves propagating perpendicular to the collision surface may overtake the perpendicular component of the oblique fluid motion, even if the total fluid velocity is super-Alfvénic. In contrast, it is well known that in Burgers turbulence, where no pressure is available, the density structures are as thin as allowed by viscosity exclusively (see, e.g., Chappel & Scalo 1998).

The advection of the magnetic field described above is contrary to the usual assumption that the field controls the fluid motions, forcing the gas to flow along the field lines. Nevertheless, it is noteworthy that the field strengths developed by the simulations in both the intercloud medium and in the clouds are not unrealistic. The typical low values of the field occur at the intercloud medium, and are $\sim 1 \mu\text{G}$, while the largest values occur in the densest regions, with values $\sim 25 \mu\text{G}$. Nevertheless, the field is quite intermittent, and

does not follow a unique scaling with the density (PVP95), exhibiting significant variations within the cloud of fig. 13.1c. Moreover, even under near-equipartition conditions between kinetic and magnetic energy, the velocity field should be expected to exert as much of an influence on the magnetic field as viceversa. In § 13.5.2 we discuss the degree to which this field topology is consistent with observations.

13.5 Comparison with observations.

The scenario presented here differs significantly from the standard view in which clouds and clumps have well defined boundaries (density discontinuities) which separate them from a much more tenuous, warmer medium, as in simulations of cloud collisions (e.g., Scalo & Pumphrey 1983; Klein et al. 1995; Miniati et al. 1997) and models of cloud confinement (e.g., Bertoldi & McKee 1992), quasi-static contraction (e.g., Lizano & Shu 1989) and stability (e.g., Ebbert 1955; Bonnor 1956; McLaughlin & Pudritz 1996). On the other hand, Scalo 1990 has suggested that such a standard model may be an over-idealization stemming from the low resolutions and column density ranges of early studies, and proposed instead a much more complex scenario in which clouds do not have a well-defined identity. Our results support this view, and in fact such poorly-defined identity is reflected in the arbitrariness of cloud- and clump-finding algorithms (e.g., Williams et al. 1994; Vázquez-Semadeni, Ballesteros-Paredes & Rodríguez 1997). It is necessary, however, to test whether the scenario proposed here is consistent with different observations.

13.5.1 Comparison between observed spectral-line maps and mass-weighted velocity histograms

The colliding streams we have described as responsible for cloud formation should manifest themselves as multiple peaks in density-weighted velocity histograms of one velocity component, the equivalent in our simulations of the optically thin line profiles in observational spectral line maps. Although frequently Gaussian or other smooth curves are used to fit such lines, conferring the idea that the lines are uni-modal and correspond to well-defined, isolated entities, in actuality the profiles generally exhibit multiple peaks (for recent examples, see, e.g., Falgarone et al. 1994) which are in fact normally interpreted as “clumps” (e.g., Williams, Blitz & Stark 1995, hereafter WBS95).

For comparison with observational profiles, we show in fig. 13.6 the density-weighted histogram of the x -component of the velocity (u_x) for the “parent” cloud showed in fig. 13.1b. As usual, this histogram has been obtained using the local speeds in the cloud frame. This histogram may be compared with the ^{13}CO line profile for the Rosette Molecular Cloud (RMC) shown in fig. 4 of WBS95³. This cloud is in many aspects comparable to the cloud of fig. 13.1b: while the RMC’s dimensions (as deduced from fig. 17 in WBS95) are $\sim 90 \times 70$ pc, the cloud in fig. 13.1b is $\sim 250 \times 120$ pc. Furthermore, the cloud in fig.

³Although fig. 4 in WBS95 shows ^{12}CO spectra, which are optically thick, there is little, if any, qualitative difference with the optically thin ^{13}CO spectra shown in fig. 5 of that paper

13.1b has a mean density of $\sim 10 \text{ cm}^{-3}$, while the gas sampled in the spectrum of fig. 4 of WBS95 has a mean density $\sim 15 \text{ cm}^{-3}$.

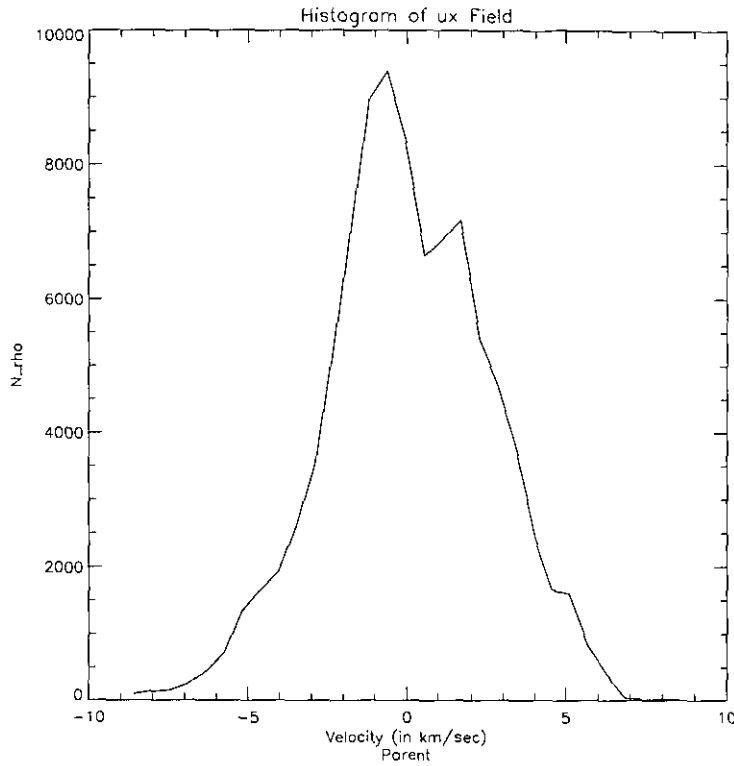


FIGURA 13.6: Density-weighted velocity histograms for the parent cloud (fig. 13.1b). Note the FWHM $\sim 5\text{-}7 \text{ km s}^{-1}$, and the multi-component structure.

Comparing the histograms for both of these clouds, we note several points in common. First, both sets of data have FWHMs of roughly 6 km s^{-1} when only the main features are considered. Second, both sets exhibit high-velocity bumps, at several km s^{-1} from the centroid. Finally, and probably most importantly, the “main” features are seen to contain substructure in both sets of plots. However, while such features have been traditionally interpreted as “clumps”, in our simulations they originate from extended regions within the cloud.

In order to explain this phenomenon, we show in fig. 13.7 a different representation of the parent cloud (fig. 13.1b). The isocontours denote the density field, the arrows show the velocity field in the frame of the cloud, and the various tones of gray represent zones with nearly the same x -component of the velocity u_x . The velocities range from less than -8 km s^{-1} to more than 8 km s^{-1} . Each tone of gray indicates a velocity interval of 2 km s^{-1} . Several issues are then observed. First, we note that the various peaks in the histogram of fig. 13.6 contain contributions from extended and separate regions in space. Second, local density peaks often encompass several velocity intervals, in a similar fashion to the situation for the entire cloud, suggesting a kind of self-similarity. Note then that the relative height in the histogram depends mainly in the mass fraction of the gas with

the corresponding value of u_x , since every velocity interval appears to sample a wide range of densities. Third, a given feature (peak) in the histogram may have contributions from regions with very different total velocity vectors, which only happen to have a similar x -component. The above results suggest that the identification of “clumps” as features in velocity space is risky at best, and possibly erroneous, as already pointed out by Adler & Roberts (1992)

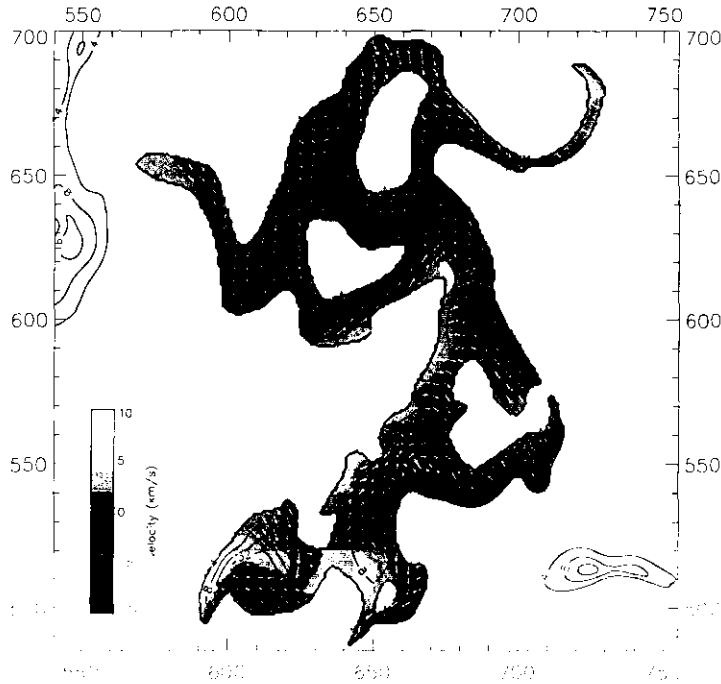


FIGURA 13.7: Same cloud as in fig. 13.1b, but indicating the magnitude of the local x -component of the velocity (gray-scale), in order to identify the origin of the x -velocity features appearing in the histogram of fig. 13.6. The velocity ranges are indicated in the sidebar. The arrows and contours indicate the velocity and the density fields, respectively. Three points are noticed. 1. The contribution to any given velocity interval originates from extended regions throughout the cloud. 2. Regions contributing to a given velocity interval contain zones of significantly different densities. 3. Regions with the same x -component of the velocity can have completely different total velocity vectors.

Note that these results may seem contradictory with observations of smaller molecular clouds which appear to have a single narrow velocity component (e.g., Lada et al. 1997). However, again this may be a problem of insufficient spectral resolution. Recent work by Falgarone et al. (1998) shows spectral maps with angular and spectral resolution of ~ 0.01 pc and $\sim 0.025 \text{ km s}^{-1}$ respectively, in which substantial spatial and spectral structure appears. Furthermore, even with high-density tracers, which are normally thought to select “isolated” features, multi-component spectral structure is often observed (e.g., Pratap et al. 1997). At very high spatial and spectral resolutions, such components can sometimes be separately identified (e.g., Girart et al. 1997), although line-of-sight confusion is in general unavoidable and should always produce spectral substructure.

A final word concerning the velocity field is in order. As pointed out in § 13.4.1, significant vorticity is found within the clouds.⁴ Observationally, this may be detected as velocity gradients along the cloud's projected area on the sky, which indeed have been observed (e.g., Arquilla & Goldsmith 1986; Goodman et al. 1993). Furthermore, Miville-Deschéne et al. (1998) have recently reported possible indirect evidence for vorticity in clouds, based on the filamentary shapes of regions with large velocity differences and comparison with nearly incompressible simulations, although the analogy with the incompressible case is not confirmed in a similar study of velocity statistics in clouds with vigorous internal star formation (Miesch et al. 1999). In any case, velocity gradients that may reflect vorticity are clearly seen in many regions.

13.5.2 Magnetic Field: alignment, advection and field reversals

Concerning the magnetic field topology, the field reversals and bendings mentioned in § 13.4.3 might seem contrary to the widely accepted fact that the magnetic field lines projected on the plane of the sky, as obtained in polarization analyses (see e.g., Goodman et al. 1990), are relatively smooth over the area of the clouds. However, on closer inspection of the field topology in our simulations, there is no contradiction. As can be seen in fig. 13.4, the magnetic field bendings are correlated with bendings of the density features, so that, along elongated density features, the field appears rather smooth. Besides, the projection along the line of sight can make the field lines appear smoother than they are (Ballesteros-Paredes & VS 1999), and also field reversals may go unnoticed in polarization studies not accompanied by corresponding Zeeman measurements that determine the direction of the field.⁵ On the other hand, evidence that the interaction of a shock with dense molecular gas is producing a reversal in the line-of-sight field component in the Orion/Eridanus region has been recently reported (Heiles 1997).

Note also that it is by now well established that the field lines do not in general show a unique direction of alignment with the density features (Goodman et al. 1992). In our simulations this is also true. Although in particular for the case shown in fig. 13.4 the field lines are mostly parallel to the density features, in other cases they are perpendicular (see, e.g., the concave region at coordinates $x \sim 605$ and $y \sim 510$ in fig. 13.4).

13.5.3 Lifetimes of turbulent clouds

An important consideration is whether the turbulent-fluctuation nature of the clouds proposed here gives cloud lifetimes consistent with current estimates. First of all, we should point out that clouds are not necessarily completely disrupted by the turbulence. Frequently they are simply sheared, split, merged with others, or they can just re-expand into the general medium if they are not very strongly self-gravitating, again indicating that the medium is not in precise pressure balance (see the videos mentioned above).

In any case, a conventional estimate for a typical "lifetime" can be given by $\tau = l/\Delta v$, where l is a characteristic size of the cloud and Δv its internal velocity dispersion. As an

⁴Note that "vorticity" here does not necessarily imply solid body rotation.

⁵We thank Carl Heiles for pointing out this possibility.

example, we calculate this for the “daughter” cloud of fig. 13.1c. We find $\Delta v = 2.3 \text{ km s}^{-1}$, and $l \sim 30 \text{ pixels} = 37.5 \text{ pc}$. Thus, $\tau \sim 1.6 \times 10^7 \text{ yr}$. This value is consistent with various estimates of GMC lifetimes of order a few $\times 10^7 \text{ yr}$ (Bash et al. 1977; Blitz & Shu 1980; Larson 1981; Blitz 1994).

Note that cloud lifetime estimates of a few 10^8 yr have also been suggested (e.g., Kwan & Valdés 1987), but these are based mostly on coagulation models which require long times to build up GMCs out of small clouds, and which include the build-up time in the total lifetime estimate. Moreover, those models were particularly motivated by the need to explain the presence of molecular clouds in the Galactic interarm region (Solomon et al. 1985), in terms of a cloud lifetime longer than the arm crossing time, neglecting the possibility that interarm clouds may form there. Such models are probably inconsistent with the present turbulent view of the ISM.

13.6 Discussion

13.6.1 Applicability to molecular gas and the role of γ_{eff}

The analyses from the previous sections have been performed on simulations which have reasonably realistic cooling functions and a diffuse heating which decays with increasing density (mimicking self-shielding) (PVP95). As seen from eq. (13.4), such heating and cooling rates imply effective barotropic exponents typically smaller than 1. These heating and cooling rates are most appropriate for diffuse HI structures, which may be very large (up to $\sim 1 \text{ kpc}$, although small-scale structure must exist there as well). The question then arises as to whether the dynamical scenario we have proposed here is applicable to molecular clouds (MCs) and their substructure (with sizes ~ 10 to $\lesssim 0.1 \text{ pc}$). Although the ultimate test for this problem will require new numerical simulations, which will be presented elsewhere, we can discuss the issue to a certain extent here, based on recent results on the role of γ_{eff} (Tohline et al. 1987; VPP96; Passot & Vázquez-Semadeni 1998), which is a measure of the thermal characteristics of the flow.

The main difference between the parameters of the simulations presented here and some other set, more appropriate for MCs, is the effective barotropic exponent of the flow. (Note that the only scale-dependent quantities in our simulations are the heating and cooling rates. All other quantities are scale-free.) While in general in our simulations $0 \leq \gamma_{\text{eff}} < 0.5$ (c.f. § 13.3), it is possible that in molecular gas $\gamma_{\text{eff}} \gtrsim 1$ (Myers 1978). Actually, the situation at densities $\gtrsim 10^3 \text{ cm}^{-3}$ is rather uncertain, with γ_{eff} possibly being ~ 1 between 10^3 and a few $\times 10^4 \text{ cm}^{-3}$ because of the importance of collisional deexcitation and radiative trapping in CO lines, and either larger or smaller than unity at larger densities depending on the presence of embedded stellar sources and other factors (Scalo et al. 1998).

In any case, we can discuss the expected effect of the gas having $\gamma_{\text{eff}} \gtrsim 1$ on the nature of the density fluctuations arising in the flow. It has recently been shown by Passot & Vázquez-Semadeni (1998) that at larger γ_{eff} the density peaks are spatially more extended and of smaller amplitude, while the density minima are very deep. At small γ_{eff}

($0 \leq \gamma_{\text{eff}} < 1$), the situation is reversed, the peaks being very concentrated and large, while the minima are not as deep. This is because the sound speed c scales with the density as $\rho^{(\gamma_{\text{eff}}-1)/2}$, causing the peaks to re-expand faster at larger γ_{eff} . At $\gamma_{\text{eff}} = 1$ a critical case occurs, the fluctuations of $\ln \rho$ being symmetrical with respect to the mean. VPP96 have calculated the density jump for shocks in a barotropic fluid parameterized by γ_{eff} . Thus, if γ_{eff} is larger at MC densities than in our simulations, we can expect the density peaks to be wider and less pronounced. But we do not expect the general scenario of clumps being formed by turbulent compressions to change significantly. The colliding streams, if supersonic (or super-magnetosonic), create non-stationary shock-bounded slabs, which simply re-expand after the compression subsides (if not made self-gravitating by the compression—see below) on timescales which depend on γ_{eff} . If the compressions are subsonic no shocks form, but, for sufficiently small γ_{eff} and/or cloud masses close to their Jeans mass, collapse may still be induced by the compressions (Tohline et al. 1987).

13.6.2 Can hydrostatic structures form within turbulent clouds?

One crucial issue, however, is whether the compressed slabs can become self-gravitating upon the compression, and, if so, whether a quasi-hydrostatic configuration can be formed. The former problem has been addressed by a number of authors (Hunter 1979; Hunter & Fleck 1982; Tohline et al. 1987; Vishniac 1983, 1994; Elmegreen 1993b; VPP96). Two main issues are at play here. One is the total gravitational (\mathcal{E}_g) and internal (\mathcal{E}_{th}) energies of the cloud (for the purpose of this discussion the “internal” energy can be generalized to include all forms of energy that provide support for the cloud against gravity). The other is the *rate* at which each energy increases upon compression. If $|\mathcal{E}_g| > \mathcal{E}_{\text{th}}$, the cloud is gravitationally unstable, and collapses upon a perturbation. This is essentially an integral version of the Jeans criterion (e.g., Bonazola et al. 1987). However, for three-dimensional collapse, it is well-known that, if $\gamma_{\text{eff}} > \gamma_{\text{cr}} \equiv 4/3$, then the collapse will ultimately be halted, since \mathcal{E}_{th} increases faster than $|\mathcal{E}_g|$. The corresponding values of γ_{cr} for 2- and 1-dimensional collapse are respectively 1 and 0 (VPP96).

Conversely, if a cloud is initially stable according to Jeans ($\mathcal{E}_{\text{th}} \geq |\mathcal{E}_g|$), it may be rendered unstable upon compression. Tohline et al. (1987) have calculated the required Mach number of a 3-dimensional compression as a function of γ_{eff} for this to occur, provided that $\gamma_{\text{eff}} < 4/3$ (for $0 < \gamma_{\text{eff}} < 1$ they found that the required Mach number is independent of the cloud’s mass). Two- and one-dimensional compressions require $\gamma_{\text{eff}} < 1$ and $\gamma_{\text{eff}} < 0$, respectively (VPP96). The issue is then the following. In order for an initially stable cloud to be pushed over the internal energy “barrier” (Tohline et al. 1987) by a strong enough turbulent compression, it is necessary that $\gamma_{\text{eff}} < \gamma_t$, where γ_t is the critical γ for $|\mathcal{E}_g|$ to increase faster than \mathcal{E}_{th} upon the turbulent compression. From there on, gravitational collapse takes over. Since in general turbulent compressions are expected to be less than three-dimensional, then generally we expect $\gamma_t \leq \gamma_g$, where γ_g is the critical γ for gravitational collapse.⁶ Then, $\gamma_{\text{eff}} < \gamma_t \leq \gamma_g$. Thus, we conclude that, if collapse

⁶Here we are allowing for the possibility of gravitational collapse to occur faster in one direction than in the other two, as is the case of cosmological “pancakes”.

was triggered by a turbulent compression, it cannot later be halted by the internal energy, unless γ_{eff} changes in the process. The latter may happen in the late stages of collapse, if the dynamical timescales become shorter than the radiative cooling timescales, causing γ_{eff} to approach the actual heat capacity ratio of the gas γ , rather than the value derived from the condition of thermal equilibrium (see, e.g., PVP95).

We should insist here that the effects of all forms of support, such as the magnetic pressure and turbulent support, can in principle be included in γ_{eff} . On the other hand, this is a very simplistic description, since in general γ_{eff} may be a function of the density, and the anisotropic nature of magnetic support may not be well described by a simple barotropic exponent. In any case, this discussion illustrates our main point: *quasi-hydrostatic configurations cannot be produced out of turbulent fluctuations, unless the flow becomes closer to adiabatic than to isothermal during the collapse.* Fluctuations either rebound or collapse. However, at small γ_{eff} , the rebound time is long (VPP96; Passot & Vázquez-Semadeni 1998).

We can examine more quantitatively the conditions under which adiabatic compression or collapse would occur if thermal pressure provides the main support mechanism for a clump, by comparing the cooling timescale $\tau_{\text{cool}} = nkT/\Lambda$ (Λ = cooling rate in units of $\text{erg cm}^{-3}\text{s}^{-1}$) to the compression time $\tau_{\text{comp}} \equiv L/v$ and the collapse time $\tau_{\text{coll}} \equiv (G\rho)^{-1/2}$. For the cooling rate we distinguish two density regimes. For $10^3 \lesssim n \lesssim 10^4 \text{ cm}^{-3}$ the cooling is dominated by CO line cooling. We adopt a rough approximation for the CO cooling rate (see references in Scalo et al. 1998) as $\Lambda \sim 10^{-20}n_3T^2$, where $n_3 = n/10^3\text{cm}^{-3}$ and we have assumed that collisional deexcitation yields a linear (rather than quadratic) density dependence at these densities. We recognize that this is a crude representation of the molecular cooling rate, but it suffices for our order of magnitude estimates. At larger densities the cooling will be dominated by gas-grain collisions (if there are no embedded protostellar sources), with a rate $2 \times 10^{-33}n_5^2T^{1/2}(T - T_{\text{gr}})$, where T_{gr} is the grain temperature and the coefficient depends somewhat on the adopted grain parameters. We assume $T - T_{\text{gr}} \approx T$ for our order of magnitude estimates.

For compressions, we find that the condition for adiabatic evolution ($\tau_{\text{comp}} < \tau_{\text{cool}}$) yields a critical length scale $L_{\text{pc}} = L/1\text{pc}$

$$L_{\text{pc}} < \begin{cases} 4 \times 10^{-3}M/T_{10}^{1/2} & \text{CO cooling} \\ 7 \times 10^{-4}M/n_5 & \text{gas-grain cooling,} \end{cases}$$

where M is the Mach number of the compression, $T_{10} = T/10\text{K}$, and $n_5 = n/10^5\text{cm}^{-3}$. For any reasonable Mach number adiabatic compression is only possible for tiny regions of size $\lesssim 10^{-2} \text{ pc}$.

If a (non-adiabatic) compression results in collapse, the condition for adiabatic collapse is $\tau_{\text{coll}} < \tau_{\text{cool}}$. At densities $10^3 \lesssim n \lesssim 10^4$, the adopted CO cooling rate results in the condition $n_3 > 2.1 \times 10^3T_{10}^2$. But at such large densities the cooling will be controlled by gas-grain collisions, not molecular line cooling. Using the gas-grain cooling rate, the condition for adiabatic collapse is found to be $n_5 < 1.2 \times 10^{-3}T_{10}^{-1}$. But at such small densities molecular line cooling would dominate and be non-adiabatic. Thus for collapse induced by compression, adiabatic evolution will never occur until the collapsing entity is

so dense that it becomes opaque to its own infrared radiation, which only occurs at very large (protostellar) densities.

Other possible sources of pressure are Alfvén waves and the small-scale modes of the turbulence. McKee & Zweibel (1995) have recently estimated the barotropic exponent for Alfvén-wave pressure for a variety of situations, finding it to equal 1/2 for hydrostatic configurations, 3/2 for dynamic cases with uniform density or in which the waves are isotropic, and up to 2 for shocks. The latter two values are larger than the critical value of 4/3 for halting a collapse, implying that Alfvén-wave pressure might be capable of stopping a collapse triggered by a turbulent fluctuation. However, again we insist on the need for a *change* in γ_{eff} in order to stop an ongoing collapse. If γ_{eff} starts too large, the collapse cannot be initiated (unless the system is globally gravitationally unstable to begin with) and the fluctuation will only rebound. One can think that, given the wide range of values for γ_{eff} found by McKee & Zweibel (1995) under various circumstances, a change in γ_{eff} in the right direction may occur, but this appears as a highly special situation.

Moreover, indirect evidence that magnetic pressure in the fully developed turbulent case does not provide a large increase in the total γ_{eff} of the flow follows from the results of Scalo et al. (1998). In that paper, the same simulations reported here are shown to have a density probability distribution characteristic of a $\gamma_{\text{eff}} < 1$ case (namely, a power-law tail at large densities; cf. Passot & Vázquez-Semadeni 1998), even though the simulations include a uniform plus turbulent magnetic field and the Coriolis force. Clearly, the role of the magnetic field in the turbulent regime still requires more investigation.

Concerning the support by the small-scale modes of the turbulence, Vázquez-Semadeni, Cantó & Lizano (1998) have found, for collapsing clouds, that the corresponding γ_{eff} ranges between 3/2 and 2, depending on the rate at which the collapse proceeds. Again these values of γ_{eff} appear large enough to stop the collapse, but the same problem arises as to how to change γ_{eff} during the collapse. Furthermore, in this case one might expect the turbulence to dissipate as the collapse proceeds, because the velocity gradients must increase as the spatial scales decrease. Recent results by Ostriker et al. (1998) and Mac Low (1998) suggest that the dissipation time is smaller than the free-fall time, implying that indeed turbulence without replenishment of energy is not an effective source of support for a cloud.

In summary, we conclude that none of the sources of pressure discussed above appears as a clear-cut mechanism for stopping the collapse. This problem will be investigated in detail elsewhere.

Is there any observational evidence for a dynamical rather than quasistatic state of clumps? A preliminary answer appears affirmative. Indeed, Girart et al. 1997 have recently reported on a system which may be interpreted as a collision of streams in L723. Furthermore, Tafalla et al. 1998 have reported a core with inward motions that do not correspond to classical gravitational infall models. A detailed comparison of these data with our scenario will be presented elsewhere.

13.6.3 Do molecular clouds have sharp boundaries?

The generalization of our results, in particular the gradual density gradients in the simulated clouds, to molecular clouds might be thought to be questionable because of the different form of the cooling function in molecular gas. However our results do not depend on the absolute value of the cooling function, as long as the cooling time is small compared to the dynamical time (which should also be valid in the molecular case), but only on the functional temperature and density dependence of the cooling function, which enters the effective barotropic index. In fact the value of γ_{eff} for molecular gas is similar to that used in the present calculations (see De Jong et al. 1980, Scalo et al. 1998), and so we see no physical reason why the shallow density falloffs found here should not apply to molecular regions. However there is a slight “hardening” of the equation of state in the molecular case that occurs at densities above about 10^3 cm^{-3} , as γ_{eff} approaches unity due to the importance of collisional deexcitation and radiative trapping (Scalo et al. 1998; this feature can also be seen in the figures in De Jong et al. 1980), but this in fact may be expected to cause the density peaks to have even shallower gradients and lower maxima (given the same rms Mach number), as observed by Passot & Vázquez-Semadeni (1998).

Note that our result of the non-existence of sharp cloud density boundaries need not be in conflict with observations suggesting that molecular clouds have sharp edges (Blitz 1991), since in this case the observed boundaries may just reflect a transition from molecular to atomic gas, without a discontinuity in the gas mass density (e.g., Goldsmith 1987, Blitz 1991). But besides this molecular-atomic transition effect, the impression of a sharp boundary often mentioned appears to be subjective, and may be simply due to the fact that the sensitivity was not sufficient to map a sufficiently large region. In fact, in most cases of ^{13}CO maps which cover large areas (i.e. contain large numbers of pixels) at good sensitivity, we do not see the claimed evidence for sharp or regular boundaries. Examples are Zimmermann and Ungerechts (1990) for the nearby L1497 cloud; Kramer and Winnewisser (1991) for L1495, a high-column density bound cloud with an embedded cluster in Taurus; and Heithausen et al. (1993) for several high-latitude clouds. Notice that these regions span a range of conditions (e.g. from essentially non-gravitating to strongly self-gravitating). Also, infrared studies do not show sharp boundaries for the molecular clouds (Alvés et al. 1998). Similar sensitivity effects may occur in HI (e.g., Verschuur 1991).

What is needed is maps that are sensitive to all the gas. Eventually this question can be settled by comparisons of submillimeter maps (which include all the mass, not just molecular) with, say ^{13}CO or C^{18}O maps. Comparison of IRAS 100- μ column density images (Chappel & Scalo 1998) with ^{13}CO images, while generally agreeing on the positions of density enhancements, indicate that the IRAS “clouds” are often more diffuse than the molecular images (e.g. some Taurus subregions, R CrA, ρ Oph filaments), supporting our claim that our results can be generalized to molecular clouds. However the IRAS column density images are uncertain because of their bias against very cold dust and the assumption of a single temperature along a line of sight used in calculating column densities from intensities and color temperature, so we consider the IRAS results as inconclusive.

On the other hand, we will need to include CO cooling in order to substantiate our

claim that the types of results we find here should apply to dense molecular clouds as well as the atomic clouds directly modeled in our simulations.

The question of degree to which cloud boundaries are more-or-less discontinuous also has serious theoretical implications for other problems. For example, if cloud boundaries are relatively “soft”, then shocks propagating through the density gradient can efficiently generate internal turbulence and perhaps even account for the supersonic internal line-widths (Kornreich & Scalo 1998), but if the boundaries are “hard”, one might expect the initial vorticity to be confined to a narrow surface layer (e.g. Klein et al. 1995).

13.6.4 Effect of dimensionality

In this paper we have used two-dimensional simulations because of the larger resolution they allow compared to the 3D case. This higher resolution is essential for the type of multi-scale analyses performed here. However, an important question concerns whether our results will remain valid when extended from two dimensions to three. Because our simulations are of “turbulence”, one might think there could be a large difference, as seen for incompressible turbulence, where one finds an inverse cascade of energy to larger scales and an end state of two counter-rotating vortices in two dimensions, instead of the direct cascade to smaller scales and resulting much-less ordered equilibrium state. However it is a common misconception in the astrophysical literature that such huge differences in behavior depending on dimension might occur in compressible turbulence. In fact there is no reason to expect such a difference. For incompressible turbulence the different behaviors are almost entirely due to the different numbers of quadratic conserved quantities in two (enstrophy and kinetic energy) and three (kinetic energy alone) dimensions. In contrast, in compressible turbulence, there is no Galilean-invariant quadratic conserved variable (momentum density is a quadratic invariant, but not Galilean invariant); the total energy is conserved, but is partitioned between the kinetic and internal energy, and the latter is not quadratic in the variables⁷. Thus there should be no difference in 2D *vs.* 3D flows analogous to the incompressible differences. However there still may be important differences stemming from other causes. For example, in 2D, effects like vortex stretching, magnetic flux tube formation and the dynamo are not present. In addition, there may be instabilities whose behavior is somewhat different in 2 rather than 3 dimensions (e.g. Kelvin-Helmholtz). However we do not see how such differences could significantly alter our conclusions, since they are based essentially on the fact that turbulent density fluctuations arise from negative values of the velocity divergence, a fact which follows from the continuity equation, and is independent of the number of dimensions. Besides, enlargement of the dimensionality only results in even more complex spatial behavior (e.g. see the 3D simulations of shock-cloud interactions by Stone & Norman 1992).

⁷After some time, we have learned that there can be inverse cascades with cubic nonlinearities, and what would be important is just the number of invariants (T. Passot, private communication).

13.7 Summary and conclusions

In this paper we have conducted a close examination of the topology of the density, velocity and magnetic fields that result in our 2D simulations of the ISM at the kpc scale, in particular within the clouds that emerge as the turbulent density fluctuations in that medium. We found that, in general, the cloud boundaries are rather arbitrary, being defined only by a density threshold criterion, but not by a physical boundary, such as a density or velocity discontinuity. The same arbitrariness is likely to be present in clouds defined by the tracer used to observe them, since a cloud may seem to “end” where the tracer density falls below a threshold density necessary to excite the transition, but this need not correspond to any abrupt drop in the *mass* density.

We furthermore considered a hierarchy of clouds in the simulations, by using a sequence of three progressively larger density thresholds for defining them. For clouds at all levels of this hierarchy, the velocity field in the simulations is continuous across the clouds’ “boundaries”, indicating that the clouds are formed by colliding gas streams (Hunter et al. 1986; Elmegreen 1993b; VSPP95), with the density increasing towards the collision site. The density enhancements need not be confined exclusively to the collision site as in Burgers flows, because the velocities involved are typically trans-Alfvénic, meaning that the information on the collision can often propagate upstream (see also Pouquet et al. 1991). Furthermore, since the collisions are generally oblique, it is likely that magnetosonic waves propagating perpendicular to the collision surface may overtake the oblique fluid motion, even if the total fluid velocity is super-Alfvénic. This scenario is in sharp contrast with static models in which the clouds are immersed in an intercloud medium of lower density but higher temperature, and confined by pressure balance between the two “phases” (e.g., Bertoldi & McKee 1992; McKee & Zweibel 1992; McLaughlin & Pudritz 1996). In our simulations, which employ standard cooling functions, both “phases” exist, but the transition between them is smooth, and the situation, rather than being static, is highly dynamic.

To further characterize the role of the flux across the clouds’ boundaries, we considered the surface (\mathcal{T}_{kin}) and volume (\mathcal{E}_{kin}) kinetic terms in the virial theorem for the whole ensemble of clouds at one temporal snapshot in the simulation. It was found that both terms are typically of the same order of magnitude, indicating that the surface terms contribute an amount comparable to the total kinetic energy of the clouds to their overall virial balance. This was interpreted as a signature of the fact that, when the clouds are formed by stream collisions, the same flow is responsible for both the total kinetic energy contained within the clouds and for the flux across its boundaries.

We discussed the differences between the thermal and turbulent pressures, emphasizing the fact that while the former is microscopic and isotropic, the latter may involve macroscopic scales, comparable or even larger than the clouds’ sizes, and is in general anisotropic, as indicated by its off-diagonal contribution to the total pressure tensor Π_{ij} . We thus concluded that turbulent pressure confinement is a contradictory concept, because it involves motions at large scales which by definition cause a change in the clouds’ boundaries. In turn, we argued that thermal pressure equilibrium in a non-static medium is irrelevant,

because inertial motions may still distort or disrupt a cloud, even under thermal pressure balance with its surroundings.

Additionally, we studied the magnetic field topology and strength in the clouds in the simulations, and their implication on whether the motions are super- or sub-Alfvénic, finding both super- and sub-Alfvénic motions within the clouds, supporting the suggestion that the field is highly intermittent (Padoan & Nordlund 1999). We noticed that the field is significantly distorted and advected by the flow, in agreement with the result that the flow within the clouds is trans-Alfvénic. The field tends to be correlated with the density features, although without a unique mode of alignment (PVP95). This causes the field to look relatively smooth along density features, in agreement with most polarization studies (Goodman et al. 1990), but at the same time being bent where the density filaments are bent as well.

A crucial question is whether the scenario depicted in this paper is consistent with observational data. We addressed this problem at the level of density-weighted velocity histograms, which can be compared to observational spectral line profiles from real clouds of similar characteristics to those in the simulations. Although there are limitations to this comparison, our velocity histograms are encouragingly similar to the observational line profiles, both exhibiting comparable FWHMs ($\sim 6 \text{ km s}^{-1}$) and high-velocity isolated features, and both containing not completely resolved substructure, indicating multiple components. We emphasized that while this substructure is usually interpreted as isolated “clumps”, in our simulations it originates from different regions of the clouds, which may correspond to different “streams” and in general have one similar component of the velocity but very different total velocity vectors, as found also by Adler & Toberts 1992. We also mentioned observational evidence for field reversals in shocks (Heiles 1997), and noted that the topology of the magnetic field seen in the simulations is consistent with observations (Goodman et al. 1992).

Finally, we discussed at considerable length the possibility that the scenario of clouds as turbulent density fluctuations may apply to molecular clouds and their substructure (clumps and cores). Essentially, only the adopted cooling and heating functions in our simulations distinguish them from a case more appropriate to molecular clouds, which are believed to behave in a nearly isothermal manner. Based on recent results on the effect of the effective thermal behavior (Tohline et al. 1987; VPP96; Passot & Vázquez-Semadeni 1998), parameterized by the effective barotropic exponent γ_{eff} , we conjectured that only the shape (height and width) of the density fluctuations is expected to change, but not the general character of the inflowing streams characteristic of their turbulent nature. We also suggested that quasi-hydrostatic configurations cannot be produced from turbulent compressions, and that density fluctuations must either collapse or rebound, unless the effective thermal behavior changes during the collapse, becoming closer to adiabatic ($\gamma_{\text{eff}} \geq 4/3$). However, for small γ_{eff} , the rebound times can be quite long. We suggested, considering appropriate cooling rates and the contributions from magnetic and small-scale turbulent support, that adiabatic evolution, and hence quasistatic configurations, are unlikely to occur either during compressions or during compression-induced collapse.

In summary, we conclude this paper by stating that the results presented here are

not in contradiction, but rather quite consistent, with observational data. They seem to be, however, discrepant with the standard interpretation of those data in terms of sharply-bounded clouds in pressure equilibrium with their surroundings, and with the identification of velocity features in spectral-line data with isolated “clumps”. It is interesting that our results give theoretical support to the suggestion made long ago by Chandrasekhar & Münch (1952) that the interstellar medium may not best be visualized as a system of *discrete* clouds. However, the “cloud model” is difficult to displace because, as they say, “...a tendency to argue in circles can be noted in the literature, in that confirmation for the *picture* of interstellar matter as occurring in the form of discrete clouds is sought in the data analyzed”.

Acknowledgements

We thank Alyssa Goodman, Thierry Passot and Jonathan Williams for carefully reading early versions of the manuscript and providing us with detailed comments. We also thank Paola D’Alessio, Carl Heiles, Susana Lizano and Luis Rodríguez for useful discussions, and Bárbara Pichardo for helpful IDL procedures. We acknowledge the hospitality of the Star Formation Group at the Harvard-Smithsonian CfA. The simulations were performed on the Cray Y-MP/4-64 of DGSCA, UNAM. This work has received partial support from grants UNAM/DGAPA IN105295 and UNAM/CRAY SC-008397 to E.V.-S. and a UNAM/DGAPA fellowship to J.B.-P.

13.8 Appendix A

In this Appendix we check the possibility that the width of the clouds in the simulations might be due to a numerical artifact. Indeed, the simulations solve the continuity equation as (see, e.g., Vázquez-Semadeni, Ballesteros-Paredes & Rodríguez 1997):

$$\frac{\partial \rho}{\partial t} + \nabla \cdot (\rho \mathbf{u}) = \mu \nabla^2 \rho, \quad (13.6)$$

where the right-hand side is a mass diffusion term, included only for numerical reasons, so that the code can handle shocks. This term has the effect of spreading out density peaks. Thus the possibility exists that the clouds in the simulations are actually thin shock-bounded slabs, artificially widened by the mass diffusion. In order to test for this possibility, we compare the characteristic dynamical and diffusion times in the vicinity of shocks. If the dynamical time is shorter, then diffusion does not have time to spread out the shock, and the width is real, caused by dynamical agents, rather than the artificial mass diffusion term.

The effects of mass diffusion have already been discussed in the Appendix of Vázquez-Semadeni, Ballesteros-Paredes & Rodríguez 1997.⁸⁹ There it was shown that the charac-

⁸Note that in that paper a couple of typographical errors appear. In eq. (15), the quotient on the right-hand side should be raised to the power 1/2, and in eq. (16), the term in the denominator on the RHS should be $m^{1/3}$, not $m^{1/2}$.

⁹La nota de pie de página anterior se aplica a la versión publicada del artículo Vázquez-Semadeni et al. 1997 (ApJ 474, 292). En la presente tesis dichas correcciones ya han sido incorporadas.

teristic timescale for diffusion, in code units, is

$$\frac{t_{\text{diff}}}{t_0} = 9.41 \times 10^{-3} \left(\frac{\sigma}{1\text{pix}} \right)^2, \quad (13.7)$$

where $t_0 = 1.3 \times 10^7$ yr is the code time unit, and σ is the size scale of interest. Mass diffusion is most important when density peaks are large (i.e., of large amplitude) and thin. As mentioned in the text, the shock width in the code is typically of a few pixels, and we thus take $\sigma = 5$ pix. Then, the diffusion timescale is $t_{\text{diff}} = 0.23$ code time units. On the other hand, the dynamical timescale is

$$\frac{t_{\text{dyn}}}{t_0} = 7.9 \times 10^{-3} \left(\frac{\sigma/\text{pix}}{\delta v} \right). \quad (13.8)$$

The typical velocity difference across shocks is $\delta v \sim 0.5$ in code units (i.e., $\sim 6 \text{ km s}^{-1}$), giving $t_{\text{dyn}} = 7.9 \times 10^{-2}$ in code units. Thus, the dynamical time is roughly 3 times shorter than the diffusion time. Of course, lower velocity differences will imply longer dynamical times, but then these velocities become sub-magnetosonic and do not cause shocks in the first place, implying that the density peaks will have much larger widths as well, augmenting the diffusion time as well. We conclude that the width of the density peaks is in general not due to the artificial mass diffusion.

Capítulo 14

Introducción al Problema Post-T Tauri

Las estrellas T Tauri fueron identificadas originalmente por sus intensas líneas de emisión y variaciones irregulares en su brillo, además de estar asociadas con gas molecular. En la actualidad se entiende genéricamente por estrella T Tauri a una estrella de baja masa ($M \leq 2M_{\odot}$) que aún no llega a la secuencia principal, independientemente de si se le encuentra asociada a alguna nebulosidad, o de si tiene líneas de emisión intensas. A las que presentan emisión intensa se les denomina estrellas T Tauri Clásicas (CTTS), mientras que a las que tienen emisión débil se les denomina estrellas T Tauri débiles (WTTS).

Las edades estimadas para nubes moleculares son del orden de varias veces 10^7 años (Blitz & Shu 1980), de manera que, suponiendo que las nubes moleculares forman estrellas a lo largo de toda su vida, es de esperar que las regiones de formación estelar tengan estrellas con edades similares a las edades de las nubes donde se formaron. Sin embargo, Herbig (1978) mostró que había una falta de estrellas con edades¹ mayores a ~ 3 millones de años en la región de Taurus-Auriga². Incluso, argumenta Herbig (1978), si la formación estelar es muy intermitente, uno esperaría un cociente de *al menos* una estrella post-T Tauri³ (PTTS) por cada estrella T Tauri (TTs) en regiones de formación estelar suficientemente

¹ La determinación de las edades para estrellas T Tauri involucra los siguientes pasos (Hartmann 1998): a) Medición de los cocientes de las intensidades de las líneas fotosféricas de absorción, a fin de determinar el tipo espectral y por ende la temperatura efectiva; b) Corrección por extinción de los flujos observados, a fin de determinar la luminosidad si se conoce la distancia a la estrella. c) ubicación en el diagrama HR. y d) utilización de trazas evolutivas (ver Fig. 15.1a del §15). Es importante notar que, para estrellas más tardías que del tipo M, la determinación de edades usando la intensidad de la línea de Litio Li I $\lambda 6707$ Å o la tasa de rotación es difícil, ya que estos discriminadores sólo ponen una cota superior a la edad, pero no permiten determinarla con precisión (Briceño, comunicación privada).

² El argumento de Herbig (1978) es como sigue: si un objeto pasa una fracción p de su vida (con p entre 0 y 1) en un estadio dado, entonces es de esperar que, al levantar un censo, se encuentren $(1-p)/p$ objetos en fases diferentes a la fase en cuestión. Por ejemplo, para comparar cuántas estrellas post-T Tauri entre 3 y 10 millones de años debe haber, respecto a las estrellas T Tauri con menos de 3 millones de años, concluiríamos que debería haber 7 estrellas post-T Tauri por cada 3 estrellas T Tauri.

³ Una definición clara de estrella post-T Tauri no existe. Sin embargo, dado que las estrellas de secuencia principal (edades de 10^8 años) no poseen líneas de emisión intensas, se espera que las estrellas post-T Tauri tengan valores de intensidad intermedios (Herbig 1978).

grandes.

A la fecha han sido realizados varios intentos por identificar esta supuestamente “numerosa” población de estrellas post-T Tauri. Por ejemplo, Jones & Herbig (1979) estudiaron los movimientos propios de 250 estrellas débiles en la dirección de Tauro, encontrando que solamente la cuarta parte de éstas tienen la misma dispersión de velocidades ($\sim 2 \text{ km s}^{-1}$) que el gas molecular en Tauro y las 75 estrellas T Tauri previamente conocidas en esta región. Es decir, por cada 4 estrellas T Tauri conocidas, los autores solamente encontraron una estrella sin características T Tauri que compartía el movimiento global de la población en esta zona. Similarmente, Hartmann et al. (1991) encontraron un cociente de 1 estrella de ~ 10 millones de años por cada 10 estrellas T Tauri.

Los intentos por identificar la población de estrellas post-T Tauri “perdida” involucran censos en rayos X (RX) (ver por ejemplo, Feigelson et al. 1987; Walter et al. 1988 y referencias ahí citadas). En particular, Walter et al. (1988), usando datos del satélite Einstein determinaron la existencia de 44 estrellas con edades de entre 1 y 40 millones de años en la región de Taurus-Auriga. Sin embargo, Hartmann et al. (1991) mostraron que estas estrellas no poseen litio, de manera que sus edades debían ser mayores a 30 millones de años, y sugirieron que dichas estrellas debían ser de campo, con intensidad considerable en RX. Más aún, Hartmann et al. (1991) mostraron que *al menos* algunas deben estar asociadas con el grupo Cassiopea-Taurus, y no propiamente con la nube de Tauro.

Por otra parte, con la ayuda del ROSAT All-Sky Survey (RASS), Neuhäuser et al. (1995) y Wichmann et al. (1996) sugirieron haber encontrado la población de PTTS. Sin embargo, esta población tiene una distribución espacial muy extendida, y no centralmente condensada en dirección de Tauro, como sería de esperar si hubiese una tasa de formación estelar continua (más no necesariamente constante) durante unos 10^7 millones de años. Adicionalmente, la determinación de edades dada por los autores que usan mediciones en RX presenta algunos problemas, como mencionan Briceño et al. (1997):

- 1. Emisión de RX.** La emisión en RX decrece poco en escalas de tiempo de entre 10^6 y 10^8 años en estrellas G y K; éstas constituyen una gran fracción de las fuentes detectadas por ROSAT. En otras palabras, los censos en RX no solamente son sensibles a las estrellas pre-secuencia principal (PMS), sino también a estrellas jóvenes de secuencia principal. Resultados obtenidos con EXOSAT y con el Einstein Extended Medium Sensitivity Survey (Tagliaferri et al. 1994; Favata et al. 1993) han sugerido que la mayoría de las fuentes estelares en esos censos son estrellas con edades comparables a las de las Pléyades (10^8 años). Sterzik et al. (1994) sugirieron que RASS puede estar detectando una población de estrellas de campo mucho más viejas que las TTS y que no están relacionadas físicamente con su lugar de nacimiento.

Para ilustrar el problema, en la Fig. 14.1 presentamos una gráfica del “cociente de dureza” HR1 vs. HR2 en RX, donde

$$\text{HR1} \equiv \frac{h + m - s}{h + m + s};$$

$$\text{HR2} \equiv \frac{h - m}{h + m}, \quad (14.1)$$

son los índices de dureza, y h , m , y s son las emisiones en RX en las bandas dura (0.9-2 keV), media (0.5-0.9 keV) y suave (0.1-0.4 keV) respectivamente. Tomando datos obtenidos por Gagné et al. (1995), Briceño et al. (1997) han encontrado que estrellas como las Pléyades (puntos en la Fig. 14.1), con edades de $\sim 10^8$ años, presentan cocientes de dureza similares a los de las WTTs, con valores de $-0.15 \leq \text{HR1} \leq 1$ y $-0.3 \leq \text{HR2} \leq 0.5$ (recuadro en la Fig. 14.1). De esta gráfica parece ser que el cociente de dureza no es un buen discriminador de edad.

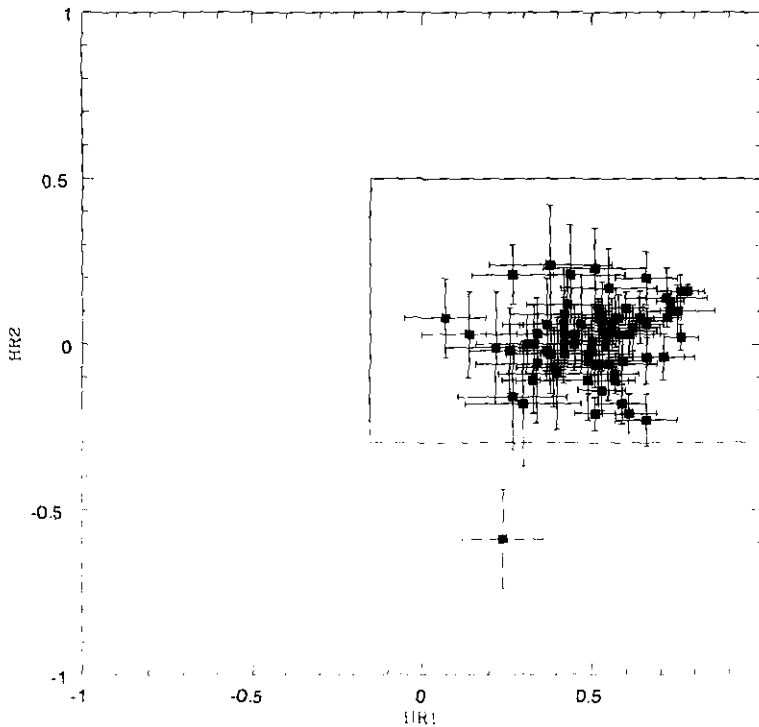


FIGURA 14.1: Cocientes de dureza en RX para las Pléyades. Nótese que prácticamente todas las Pléyades tienen cocientes de dureza similares a los de las WTTs, como se denota por la caja. (Tomada de Briceño et al. 1997, cortesía de Cesar Briceño).

2. **El Problema del Litio.** El ancho equivalente de la línea de absorción Li I $\lambda 6707 \text{ \AA}$ ha sido usado como un indicador de juventud para estrellas tardías con envolventes convectivas. El litio tiene una temperatura de fusión relativamente baja, $\sim 2 \times 10^6 \text{ K}$, de manera que es fácilmente destruido mediante reacciones termo nucleares en el interior estelar. Aquellas estrellas que tienen envolventes convectivas pueden transportar el litio de la superficie a las regiones interiores y destruirlo. Sin embargo, mientras que las estrellas M presentan una falta de Li considerable durante sus estados pre-secuencia principal (varios 10^7 años), las estrellas G y K tempranas limitan la convección a las capas externas, lo cual les permite llegar a la secuencia principal

con una considerable fracción del Li con el que se formaron, como en el caso de las estrellas G y K en las Pléyades (ver, p.ej., Soderblom et al. 1993).

Por lo anterior, al igual que la emisión de RX, la intensidad de la línea de absorción de Li I λ 6707 Å usada para identificar objetos PMS tampoco decae sustancialmente con la edad para estrellas G y K, que por otra parte constituyen una gran fracción de las fuentes RASS. Para ilustrar este problema, en la figura 14.2 presentamos una gráfica de ancho equivalente (W_λ) contra temperatura efectiva para las estrellas WTTS (símbolos rellenos) y para las Pléyades (símbolos vacíos). De esta figura es claro que el ancho equivalente para estrellas G y K-tempranas es mayor a 0.1 tanto para las Pléyades como para las WTTS, de manera que el suponer que la condición $W(Li) > 0.1$ Å es indicadora de estrellas T Tauri como lo hacen Neuhäuser et al. (1995), Wichmann et al. (1996) y Sterzik et al. (1995), es claramente riesgoso.

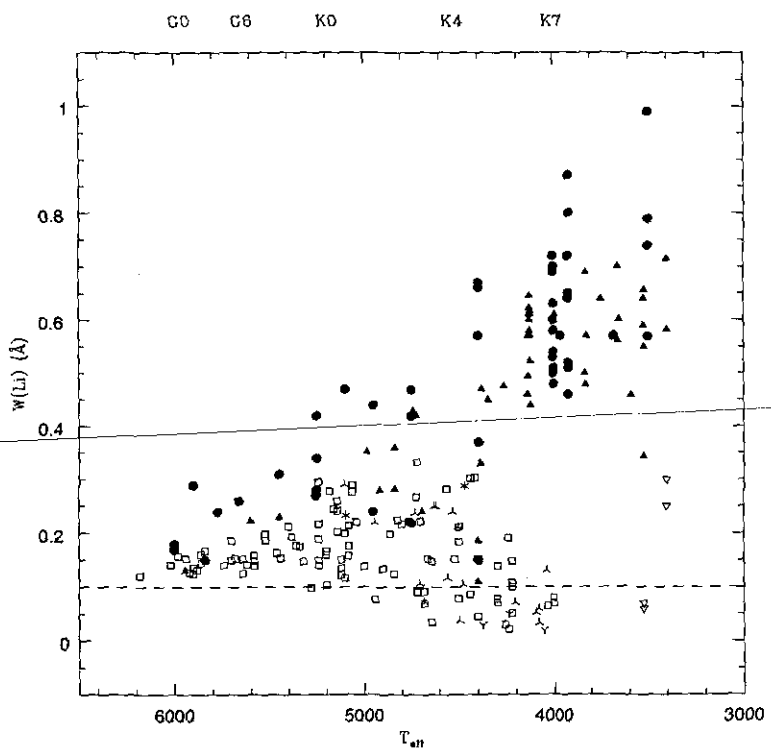


FIGURA 14.2: Ancho equivalente de la línea Li I λ 6707 Å $W(Li)$ vs. temperatura efectiva T_{eff} de la estrella (eje inferior) o tipo espectral (eje superior). Los círculos y triángulos rellenos representan datos para TTS tomados de Basri et al. (1991) y de Martín et al. (1994), respectivamente. Los círculos vacíos y los asteriscos representan datos para las Pléyades, tomados de Soderblom et al. (1993) y López et al. (1994), respectivamente. Los símbolos invertidos representan límites inferiores para las Pléyades, y la línea horizontal representa el límite de detección de 100 mÅ usada por Neuhäuser (1995), Wichmann et al. (1996) y Sterzik et al. (1995) para identificar las fuentes RASS como candidatos TTS. (Tomada de Briceño et al. (1997), cortesía de Cesar Briceño).

Además, las primeras mediciones de ancho equivalente de Li I λ 6707 Å presentan problemas: el ancho equivalente medido para las estrellas RASS ha sido determinado usando una resolución espectral mucho menor que la resolución con la que se deter-

minó el ancho equivalente de Li I para las Pléyades: las medidas para las Pléyades fueron obtenidas con resoluciones espectrales de $\sim 0.15 - 0.25 \text{ \AA}$ (Soderblom et al. 1993; López et al. 1994), mientras que las resoluciones espectrales usadas para las WTTS en RASS son del orden de ~ 4.3 y $\sim 8 \text{ \AA}$ (Alcalá et al. 1995). Con estas resoluciones, las líneas vecinas de Fe I (λ 6703, 6705, 6710 y 6713 \AA) pueden estar mezcladas con la línea de litio λ 6708 \AA , aumentando artificialmente su ancho equivalente⁴ (Briceño et al. 1997).

3. **Emisión H α y Magnitudes Visuales:** Análogamente a las discusiones anteriores, tanto la distribución de magnitudes visuales como la emisión H α esperada para estrellas G y K tempranas con edades de 10^8 años es comparable con las magnitudes visuales y la emisión H α para las WTTS (Briceño et al. 1997).
4. **Velocidades Radiales:** Del total de fuentes RASS, solamente 15 de ellas tienen velocidades radiales medidas (Neuhäuser et al. 1995). La dispersión de velocidades oscila entre 8 y 15 km s^{-1} , valores considerablemente mayores a la dispersión de velocidades de las TTS y del gas en Tauro ($\sim 2 \text{ km s}^{-1}$). Más aún, la dispersión de velocidades para estrellas de secuencia principal de disco con edades de 10^8 años cerca del plano Galáctico es de $\sim 10 \text{ km s}^{-1}$ (Wielen 1977). Así, aunque hubiese algunas estrellas PMS en la muestra de fuentes RASS, la edad del grueso de estas estrellas, obtenida a partir de la dispersión de velocidades, sería mucho mayor (Briceño et al. 1997).

Un comentario adicional mencionado por Briceño et al. (1997) es que si, como sostiene el grupo de RASS, todas estas fuentes fuesen en efecto las estrellas post-T Tauri perdidas, entonces cabría la pregunta ¿dónde se encuentra la población de estrellas con edades de entre 10^7 y 10^8 años que debería existir en caso de una tasa de formación razonablemente continua?

Una técnica que presenta menos ambigüedad es la búsqueda de estrellas post-T Tauri de tipo espectral M, ya que tales estrellas deben ser mucho más numerosas, estar bien localizadas en el diagrama HR por encima de la secuencia principal, y el litio puede ser usado como un criterio de selección más efectivo para éstas si sus edades son menores a ~ 12 millones de años. En este sentido, Briceño et al. (1999) realizaron un estudio moderadamente profundo de campo ancho en el óptico y en RX en la región de Taurus-Auriga, buscando la presencia de estrellas tipo M con edades de ~ 10 millones de años, sin encontrar evidencia de éstas y reforzando el argumento de que la mayoría de las fuentes RASS no son las estrellas PTTS.

⁴ Recientemente, Zickgraf et al. (1999) realizaron un estudio donde intentaron corregir los anchos equivalentes por posible contaminación de las líneas de Fe I mencionadas. En este estudio, los autores reportan ocho estrellas K y una estrella M con absorción de litio, en una muestra de 35 estrellas. Sin embargo, esta tampoco parece ser la población de estrellas post-T Tauri con entre 3 y 10 millones de años por dos razones: primeramente, porque Zickgraf et. al (1999) reportan edades que oscilan entre 10 y 30 millones de años. Adicionalmente, de su Fig. 5 tan solo dos de las estrellas K con emisión de litio tienen anchos equivalentes de litio mayores al ancho equivalente de las Pléyades (César Briceño, comunicación personal).

Ahora bien, si en realidad no existen PTTS en la región de Taurus-Auriga, ¿cómo es posible que nubes con edades de 10^7 años hayan formado estrellas tan sólo en los últimos ~ 3 millones de años?

Una alternativa para resolver el problema fue propuesta por Palla & Galli (1997), quienes sugirieron que la aparente falta de estrellas T Tauri viejas puede deberse a que la formación estelar no es instantánea. Basándose en el modelo clásico de formación de estrellas de baja masa (ver Shu et al. 1987 y referencias ahí citadas), proponen que una vez que la nube molecular se ha formado, es necesario esperar entre 10 y 12 millones de años para que se deshaga de su exceso de campo magnético mediante difusión ambipolar, y las regiones más densas puedan realmente formar estrellas. Sin embargo, este esquema presenta dos problemas básicos: por un lado, el tiempo de difusión ambipolar depende fuertemente del estado de ionización de la nube (Myers & Khersonsky 1995), de manera que un retraso de 10 – 12 millones de años para toda la región de Tauro parece poco probable, sobre todo si se toma en cuenta que los valores de extinción hacia la región de Tauro oscilan entre $A_v \sim 1$ y 5 magnitudes, lo cual implicaría estados de ionización considerablemente distintos en diferentes regiones de la nube. Por otro lado, si consideramos que Tauro tiene una extensión de $l \sim 20$ pc, y el gas molecular presenta una dispersión de velocidades de $\delta v \sim 2 \text{ km s}^{-1}$, entonces la edad dinámica de Tauro es del orden de $\tau = l/\delta v \sim 10$ millones de años. La pregunta entonces es, ¿cómo es posible que la formación estelar en la nube se sincronice dentro de un lapso de tan sólo 3×10^6 años si la edad dinámica de la región es de 10^7 años? Además, otro problema con este escenario es que el esquema de formación estelar mediante el cual núcleos (*cores*) cuasiestáticos se forman en un medio interestelar turbulento ha sido cuestionado recientemente (§13, Ballesteros-Paredes et al. 1999a).

En el trabajo que se presenta a continuación (§15, Ballesteros-Paredes et al. 1999b), adoptamos una posición similar a la de Palla y Galli (1997) en el sentido de proponer que Tauro no ha tenido tiempo de formar estrellas post-T Tauri. Sin embargo, el mecanismo propuesto es completamente diferente, y se basa en el escenario de que las nubes son fluctuaciones turbulentas descrito en §13. Es posible entonces que el complejo de Tauro se haya formado recientemente, apenas hace unos 3×10^6 años, bajo la acción de este campo turbulento de manera coherente a lo largo de toda su extensión. En otras palabras, es el campo de velocidades el encargado de acarrear masa para formar estructuras. En este esquema, la colisión de corrientes turbulentas a mayor escala que el tamaño de Tauro, con velocidades características mayores que la dispersión de velocidades interna de la nube de Tauro, es capaz de apilar este material en unos cuantos millones de años, sincronizando entonces la formación estelar en regiones que estarían causalmente desconectadas, si se juzgase únicamente por la dispersión de velocidades *interna* de la nube. Para esto, se hace uso tanto de simulaciones numéricas del MI como de observaciones de gas molecular y de gas atómico hacia la región de Tauro.

Capítulo 15

Artículo 5

Turbulent Flow-Driven Molecular Cloud Formation: A Solution to the Post-T Tauri Problem?

Javier Ballesteros-Paredes Lee Hartmann, and Enrique Vázquez-Semadeni

ApJ, 527, 10 de diciembre de 1999

Resumen

Sugerimos que las nubes moleculares pueden ser formadas en escalas de tiempo cortas mediante la compresión de flujos a gran escala en el medio interestelar. En particular, argumentamos que el complejo de Taurus-Auriga, con filamentos de $10\text{-}20 \text{ pc} \times 2\text{-}5 \text{ pc}$, puede haber sido formado por flujos de H I en $\lesssim 3$ millones de años, explicando la ausencia de estrellas post-T Tauri con edades de $\gtrsim 3$ millones de años en la región. Observaciones con la línea de 21 cm de los "halos" alrededor del gas molecular de Tauro muestran muchas características (perfils anchos y asimétricos, desplazamientos en velocidad de H I respecto al ^{12}CO) predichas por nuestras simulaciones MHD, en la cuales las corrientes de H I a gran escala chocan para producir estructuras densas y filamentarias. Esta evolución rápida es posible porque los flujos de H I que producen y rompen la nube tienen velocidades mucho mayores ($5\text{-}10 \text{ km s}^{-1}$) que el gas molecular que resulta de la colisión de dichos flujos. Las simulaciones sugieren que tales flujos pueden ocurrir debido a la turbulencia global del MIE sin la necesidad de un mecanismo disparador, como el caso de una explosión de supernova.

Abstract

We suggest that molecular clouds can be formed on short time scales by compressions from large scale streams in the interstellar medium (ISM). In particular, we argue that in the Taurus-Auriga complex, with filaments of $10\text{-}20 \text{ pc} \times 2\text{-}5 \text{ pc}$, must have been formed by H I flows in $\lesssim 3 \text{ Myr}$, explaining the absence of post-T Tauri stars in the region with ages $\gtrsim 3 \text{ Myr}$. Observations in the 21 cm line of the H I “halos” around the Taurus molecular gas show many features (broad asymmetric profiles, velocity shifts of H I relative to ^{12}CO) predicted by our MHD numerical simulations, in which large-scale H I streams collide to produce dense filamentary structures. This rapid evolution is possible because the H I flows producing and disrupting the cloud have much higher velocities ($5\text{-}10 \text{ km s}^{-1}$) than present in the molecular gas resulting from the colliding flows. The simulations suggest that such flows can occur from the global ISM turbulence without requiring a single triggering event such as a SN explosion.

15.1 Introduction

It has been recognized for many years that the nearest star-forming regions exhibit little evidence for stars of ages $\gtrsim 5 \text{ Myr}$, even though one would expect that such “post-T Tauri stars” (PTTSs) should be more numerous than the $\sim 1 \text{ Myr}$ -old T Tauri stars. More than a decade ago, Herbig, Vrba, & Rydgren (1986) stated that “it is a source of some unease that this large population of PTTSs has not yet been identified.” Since that time, a variety of techniques have been used to search for PTTSs, including proper motion surveys, fainter objective prism plates, and CCD photometric selection. As outlined in §2, none of these techniques has yielded evidence for PTTSs in any significant numbers.

The lack of PTTSs, combined with the presence of newly-formed stars in all substantial nearby molecular clouds, is most simply explained if molecular clouds like Taurus come together, form stars, and disperse in a few Myr. However, this simple picture causes difficulties for current theories of star formation. Since Taurus has a spatial extent of 20 pc, but the molecular gas has a velocity dispersion of only about 2 km s^{-1} , it is difficult to understand how such widely separated regions produced stars almost simultaneously, i.e., how star formation is “triggered” throughout the cloud on a scale shorter than the crossing (or dynamical) timescale. In principle, a single powerful event like a supernova explosion might trigger star formation in a molecular cloud over short timescales, but there is no obvious candidate for this triggering source in the case of Taurus (Elmegreen 1993a).

In addition, Taurus is supposed to be the archetype for the “standard” picture of isolated, low-mass star formation, in which magnetically subcritical cloud cores collapse to form stars only after ambipolar diffusion has removed excess magnetic flux on timescales of order 5–10 Myr (Shu, Adams, & Lizano 1987; Mouschovias 1991, and references therein). If protostellar cloud cores are highly subcritical, the long ambipolar diffusion timescale makes it difficult to understand star formation events lasting only a few Myr. A long diffusion time also is difficult to reconcile with statistics of cloud cores (Lee & Myers).

Palla & Galli (1997) argued that the ambipolar diffusion timescale simply introduces an

age offset. In this picture, the molecular cloud cores which produced the present-day Taurus stars started contracting, say, 11-12 Myr ago, so that the cores have become supercritical and started collapsing only over the last 1-2 Myr. However, there is no unique ambipolar diffusion timescale; it depends upon the ionization fraction, which in turn depends upon precise conditions of shielding (Myers & Khersonsky 1995), and on how subcritical the cloud core is initially. Thus it is difficult to understand how ambipolar diffusion does not introduce a spread of at least several Myr into the onset of star formation. Moreover, as pointed out by Fiedler & Mouschovias (1993), Nakano (1998), and Hartmann (1998), strongly subcritical clouds must be confined by external pressure to prevent disruption by expansion. The possibility of producing a steady external pressure in the generally turbulent environment of molecular clouds has been questioned recently by Ballesteros-Paredes, Vázquez-Semadeni, & Scalo (1998), who suggest that the turbulent motions are not steady, and can disrupt as well as compress clouds. Given these problems and the evidence of the stellar population, it appears likely that ambipolar diffusion is not a major constraint on the timescale of star formation in Taurus, as argued by Nakano (1998) on general grounds, and as proposed many years ago by Shu, Adams, & Lizano (1987) for much denser regions.

Even if the ambipolar diffusion timescale is not relevant, there still remains the problem of triggering star formation in Taurus. This is possible in a dynamical scheme, where large-scale turbulent streams collide, collecting the material they are advecting and creating density fluctuations (Hunter 1979; Hunter & Fleck 1982; Hunter et al. 1986; Tohline et al. 1988; Elmegreen 1993b; Vázquez-Semadeni, Passot & Pouquet 1995a; Ballesteros-Paredes et al. 1999a; see also Vázquez-Semadeni et al. 1999). In this picture the formation of molecular clouds cannot be considered separately from the formation of their parent diffuse H I clouds. If molecular gas clouds like Taurus are "assembled" by the convergence of higher-velocity neutral hydrogen flows, one might explain the nearly-simultaneous star formation over larger distance scales without invoking a single triggering event, like a SN explosion.

In this paper we consider the dynamical, kinematic and spatial relationship between the neutral hydrogen and molecular gas in the Taurus region. Our analysis is based on H I and ^{12}CO observations, showing that in many places there is H I, which appears to be dynamically correlated with the molecular gas, but with substantial velocity offsets and larger velocity dispersions. The dynamical timescales for the clouds are then given by the scale of the clouds divided by the velocity dispersion of the external H I, contrary to the assumption that the internal velocity dispersion is the relevant quantity. We further show that these results are qualitatively consistent with MHD simulations of the ISM, suggesting that the molecular clouds like Taurus can be rapidly assembled, eliminating the need to find PTTSs in the present molecular gas complex.

In §15.2 we review the observations leading to the post T-Tauri problem. In §15.3 we explore the dynamical relationship between H I and CO gas in the Taurus region, while in §15.4 we show simulations of the ISM dynamics that we use to interpret the observations in §15.5.1. Finally, we point out limitations of our simulations in §15.5.2, and summarize our conclusions in §15.6.

15.2 Historical Context: The post-T Tauri problem

Analyses of molecular cloud lifetimes have rarely included constraints from their stellar populations; yet the ages of the stars produced by these clouds provide uniquely detailed constraints on cloud ages that are not obtainable in any other way (e.g., Hartmann et al. 1991; Feigelson 1996). Because of the importance of the stellar population ages, it is worth reviewing the situation in some detail, especially given some of the conflicting literature on the subject. We focus on the Taurus-Auriga molecular cloud complex, where the most detailed observational efforts have been made.

To illustrate the problem, Figure 1 a shows the HR diagram for stars in the Taurus-Auriga molecular cloud region, with stellar luminosities and effective temperatures taken from Kenyon & Hartmann (1995). The great majority of the stars have ages near 1 Myr; approximately half are younger than this, while only a few stars have ages greater than 3 Myr (see Fig 1 b).

The group of stars near the 100 Myr isochrone (i.e., near the zero-age main sequence) were discovered through early *Einstein* X-ray surveys (Walter et al. 1988, and references therein). These stars were originally suggested by Walter et al. (1988) as members of the missing PTTs population. However, there is a striking gap in the HR diagram; there are very few stars filling in the age range between ~ 5 and 50 Myr. This gap makes it very unlikely that a single, reasonably continuous star formation event is responsible for both the near-ZAMS stars and the young T Tauri stars. Furthermore, with such large ages it is difficult to connect these stars with the present Taurus molecular cloud. Walter et al. (1988) found ages for these stars ~ 30 Myr at a modest velocity dispersion of 2 km s^{-1} , typical of Taurus molecular gas. These stars can have traveled 60 pc from their birth-sites during their lifetimes, 3 times the diameter of the Taurus molecular complex.

The apparent coordination of star formation on relatively short timescales in Taurus (and other regions) has led to several efforts to identify hypothetical older stars that might be present but missed in previous objective prism surveys dependent upon strong H α emission. Herbig, Vrba, & Rydgren (1986) obtained objective prism data covering the Ca II H and K emission lines, which are present in much older stars. Indeed, Herbig et al. (1986) identified several outlying members of the Hyades in their survey (see also Hartmann, Soderblom, & Stauffer 1987), but failed to identify any older PTTs. Hartmann et al. (1991) and Gomez et al. (1992) used proper-motion surveys to try to select members of Taurus without regard to emission line properties; again, no substantially older stars were found.

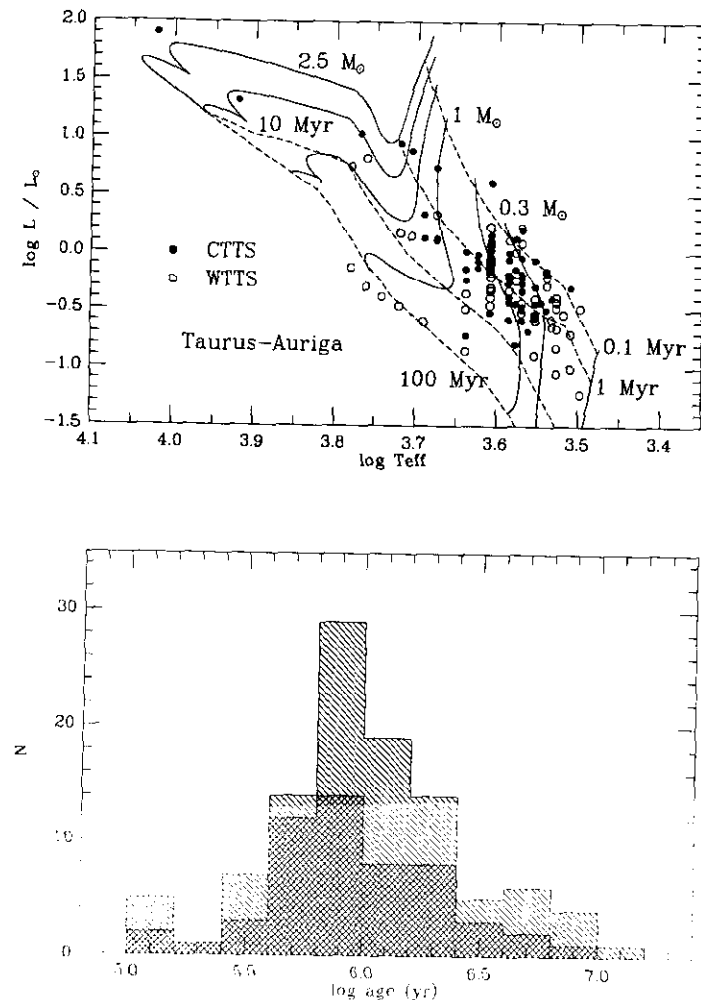


FIGURA 15.1: a) HR Diagram for stars in the Taurus-Auriga molecular cloud region, with evolutionary tracks from D'Antona & Mazzitelli (1994). Filled circles denote the Classical T Tauri Stars (CTTS). Open circles denote the Weak T Tauri Stars (WTTS). The great majority of stars have ages of ~ 1 Myr, and only a few stars have ages greater than ~ 3 Myr. The group of stars near the ~ 100 Myr isochrone were discovered with Einstein X-ray observations (Walter et al. 1988); X-ray detected sources in the region are generally older than 10 Myr (Briceño et al. 1997), and are likely to be field stars. b) Age histogram for the stars in fig 1a. The single line denotes the classical T-Tauri stars, and the crossed lines, the weak T-Tauri stars. Note that the great majority of stars is between 1 and 3 Myr.

It has been suggested that recent X-ray surveys (e.g., Walter et al. 1988; Neuhäuser et al. 1995; Wichmann et al. 1996) have discovered the missing PTTSSs. However, the ages of the typical G and early K stars in these samples are uncertain, because neither X-ray activity nor Li depletion clearly discriminate between 1 Myr-old T Tauri stars and 100 Myr-old stars. It seems likely that most of these objects are 30-100 Myr-old stars, given their numbers and properties (Briceño et al. 1997a). More recent measurements of Li depletion (Martín & Magazzu 1998) and limits on the M star component of the G-K ROSAT survey population (Briceño et al. 1997b; Briceño et al. 1999) support the idea

that most of the dispersed X-ray population is much older than 10 Myr. Indeed, it is difficult to explain the spatial distributions of these stars if they are much younger. The dispersed X-ray sources are spread fairly uniformly over large distances (up to 70 pc in projected distance from the center of Taurus); it would be very difficult to move stars from the present molecular regions this far at typical velocity dispersions of $\sim 2 \text{ km s}^{-1}$ in anything less than about 30 Myr. Instead, it seems much more likely that these stars are mostly ~ 50 Myr-old objects that formed in a variety of individual regions whose molecular gas has by now dispersed (Fiegeelson 1996). Whatever the exact age of the Einstein- and ROSAT-discovered young stars, they do not seem to represent the “missing” stars in Taurus of ages 3-10 Myr.

Another approach has been to consider whether the ages of the Taurus stars have been systematically underestimated. For example, the evolutionary tracks of Swenson et al. (1994) give ages for Taurus stars that would be several times larger than those of D’Antona & Mazzitelli (1994), which were used in Figure 15.1. However, as pointed out by Stauffer et al. (1995), if one modifies the calibrations of evolutionary tracks so that the calculations match the zero-age main sequence, most of the age discrepancy between those works disappears. Another possibility was raised by Hartmann & Kenyon (1990), who suggested that the effects of accretion might produce spurious age estimates, but more recent investigations (Hartmann, Cassen, & Kenyon 1997; Siess, Forestini, & Bertout 1997) indicate that T Tauri accretion has little effect, making the stars appear slightly older, not younger. One may also note (Mizuno et al. 1995) that most of the pre-main sequence stars in Taurus lie within 1-2 pc of dense molecular gas; at a velocity of $1-2 \text{ km s}^{-1}$, this suggests that these stars have not been dispersing for more than 1-2 Myr from their natal material, in agreement with the conventional HR diagram ages.

Thus, all the Taurus observational constraints are consistent with a picture in which the molecular gas comes together and forms stars in $\lesssim 3$ Myr, so that few stars of ages 3-10 Myr are expected. The widely-distributed X-ray sources mostly represent stars that, though relatively young, are generally substantially older than 10 Myr, and it is likely that their natal molecular clouds no longer exist.

A general absence of PTTSs implies not only that clouds form stars rapidly, but that star-formation timescales are also relatively short. Since Taurus is still forming stars, its ultimate dispersal time is not known. However, studies of other regions such as Cha I and IC 348 (Lawson et al. 1996; Herbig 1998) provide relatively little evidence for large populations of PTTSs, especially when older ROSAT sources are eliminated and mass-dependent biases are eliminated.¹ From the absence of known molecular cloud regions containing 10 Myr-old stars, it appears that the molecular gas may also disperse in a few Myr, a timescale consistent with the cluster survey results of Leisawitz, Bash, & Thaddeus (1989). In this picture many molecular clouds will not have substantial populations of PTTSs.

¹ Age estimates for cluster stars generally depend systematically on stellar mass, probably due to birth-line errors (i.e., uncertainty in the initial positions of protostars in the HR diagram; Hillenbrand 1997; Hartmann 1999.)

15.3 Atomic and molecular gas: Maps and velocity-position diagrams

The Taurus clouds are well-suited for understanding gas dynamics as well as the stellar population. The Taurus Molecular Cloud (TMC) is one of the most well-studied molecular clouds in the sky, with extensive H I and CO maps; it is one of the nearest clouds and lies well below the Galactic plane, making it easier to isolate the H I associated with the CO cloud from the general material in the Galactic plane. Finally, the morphology and kinematics of TMC suggests a close relationship between the molecular and atomic gas (see PhD thesis and series of papers by Andersson (1993), and references therein).

In the following discussion we make use of both H I and ^{12}CO data. The 21 cm line data were taken from the Atlas of Galactic Neutral Hydrogen (Hartmann & Burton 1997) obtained with the 25 m Leiden/Dwingeloo telescope, while the ^{12}CO molecular data have been taken from Ungerechts & Thaddeus (1987), obtained with the Columbia millimeter-wave telescope. Details of the observations and analysis may be found in the original papers. Here we note that both data sets have 0.5 degree spatial resolution, which facilitates comparison. The velocity resolution of the H I data is 1.03 km s^{-1} , slightly lower than that of the CO data, 0.65 km s^{-1} . To overlap the ^{12}CO and atomic maps, we transformed the molecular data set (originally in (RA,DEC)) to Galactic coordinates (l, b) by triangulating and re-sampling the transformed data in a half degree resolution grid. We present both sets of data extending from 140 to 201 degrees in Galactic longitude, and from -44 to $+17$ in Galactic latitude (note that the original ^{12}CO data does not cover the whole range. We add zeros in the external region, in order to match the H I and ^{12}CO data at large scales).

Figure 15.2 shows a velocity-integrated map in ^{12}CO (isocontours) and H I (gray-scale) for the velocity range where the CO data has been obtained ($-20.33 \text{ km s}^{-1} \leq v_{\text{LSR}} \leq 29.1 \text{ km s}^{-1}$). The straight lines indicate the loci of the cuts along which the velocity-position diagrams shown in Figure 15.3 are made. Assuming an optically thin medium, the H I intensity (in K km s^{-1}) can be considered as proportional to the column density with a conversion factor of $1.8 \times 10^{18} \text{ cm}^{-2}$. The gray scale range in Figure 15.2 corresponds to a column density range from $\sim 2.5 \times 10^{20} \text{ cm}^{-2}$ (darker pixels), to a few times 10^{21} cm^{-2} (white pixels). A column density of 10^{21} cm^{-2} , corresponding to $A_V \sim 0.5$, is generally taken to be roughly the minimum column density needed for sufficient shielding of the UV radiation field to produce CO (e.g., Elmegreen 1993a).

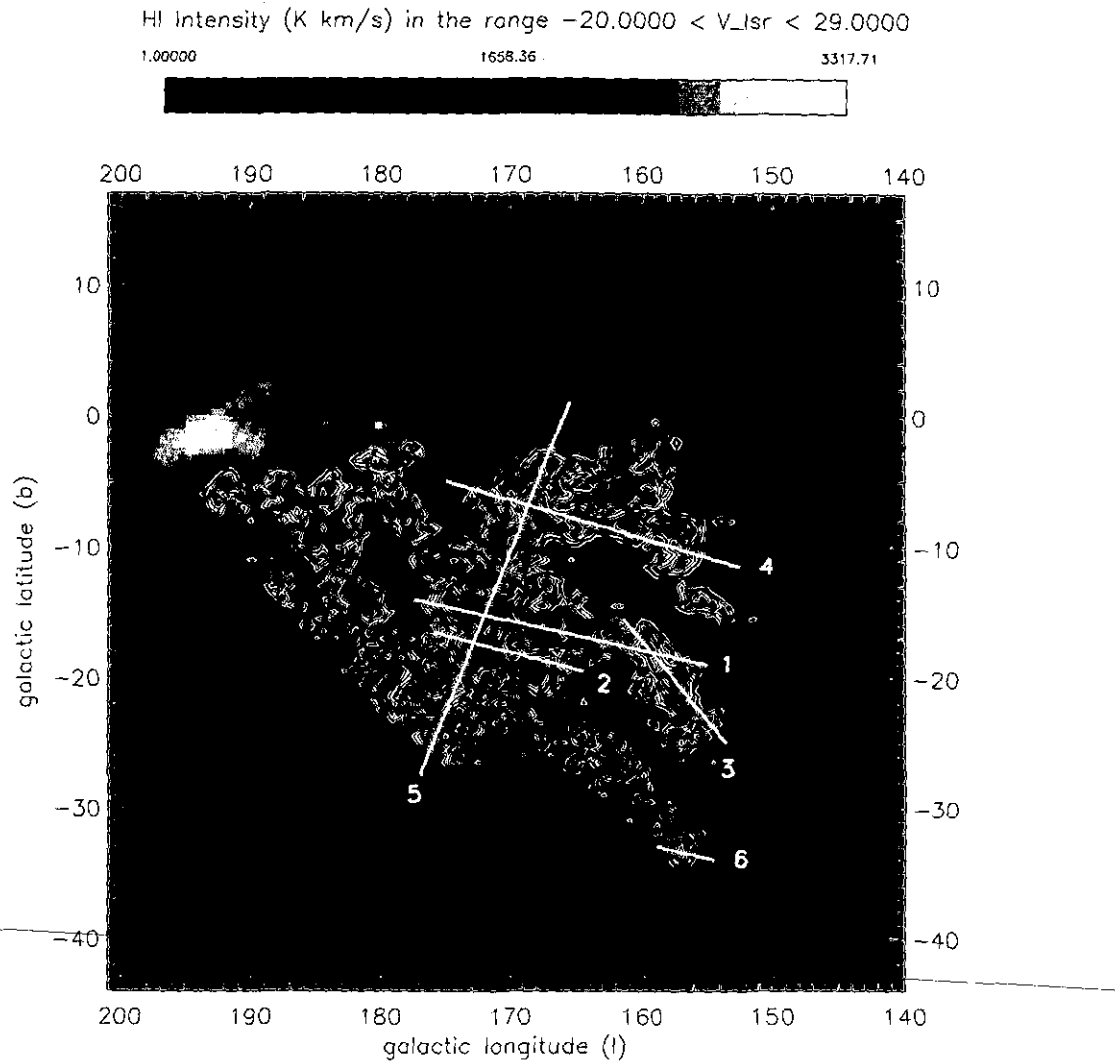
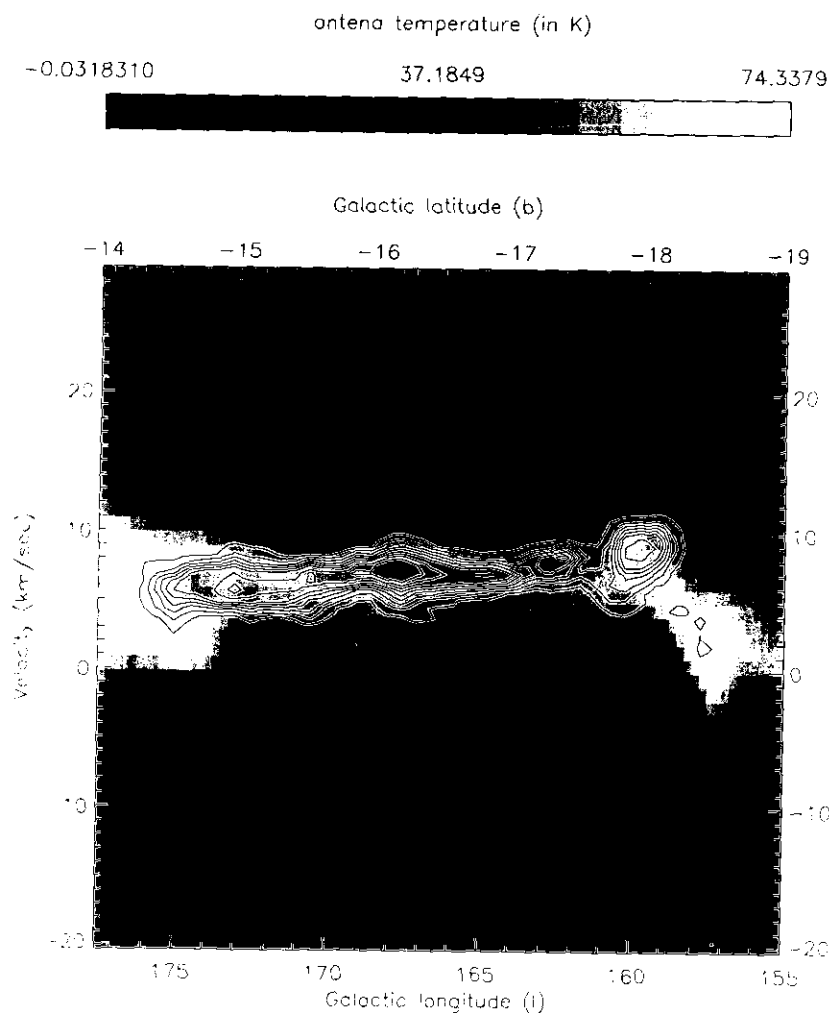
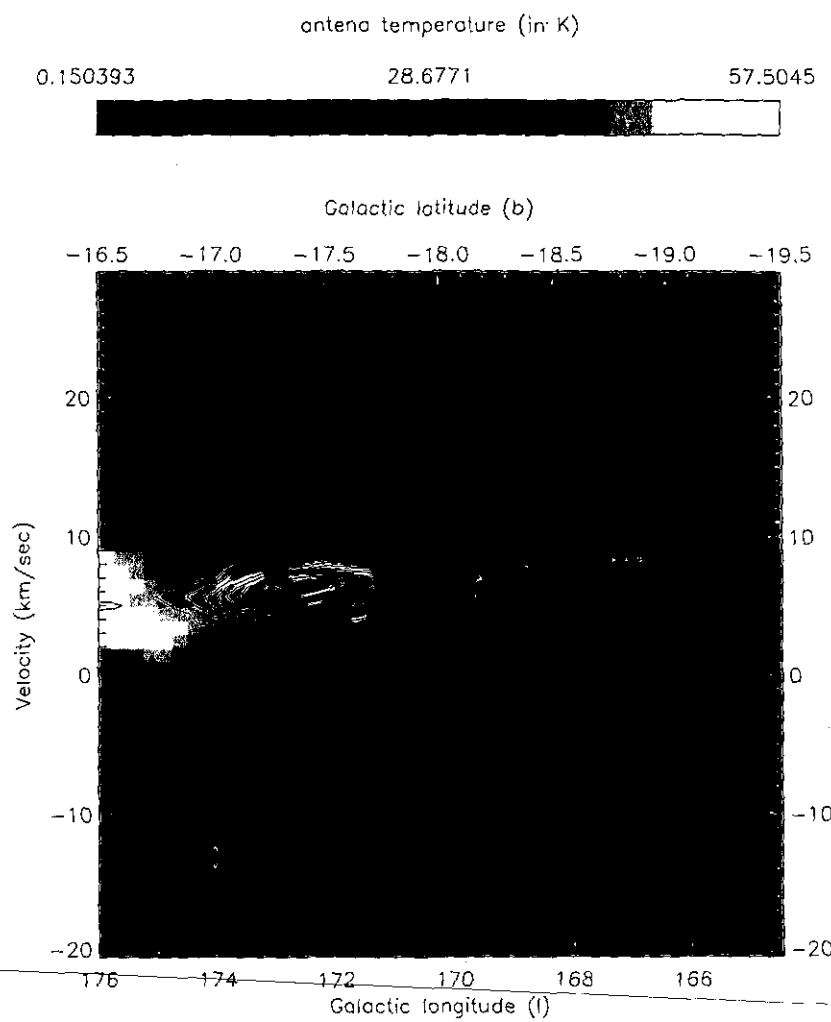


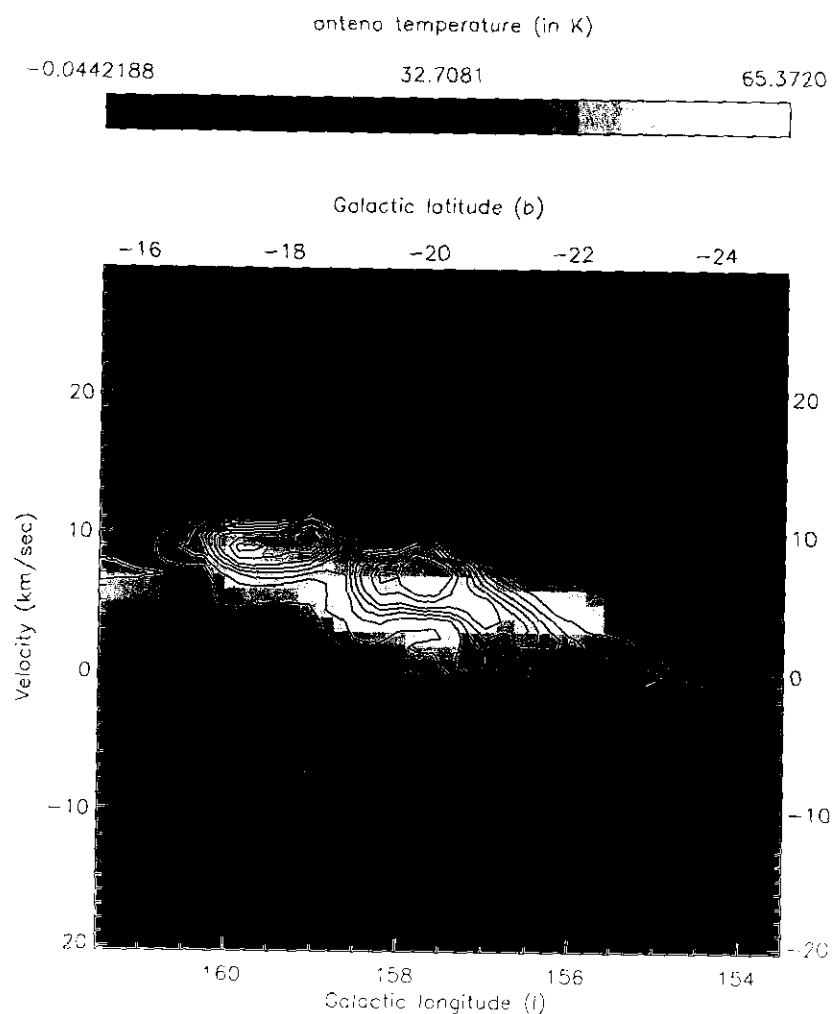
FIGURA 15.2: Velocity integrated (from -20.3 to 29.08 km s^{-1}) large-scale map of antenna temperature for CO (contours, from Ungerechts & Thaddeus 1987) and HI (grayscale, from Hartmann & Burton 1997) data through Taurus, in units of K km s^{-1} . Contours: 2, 4, 8, 16, 32, 64. The grey scale is indicated on the top. The white lines denote the places where the velocity-position diagrams have been made.

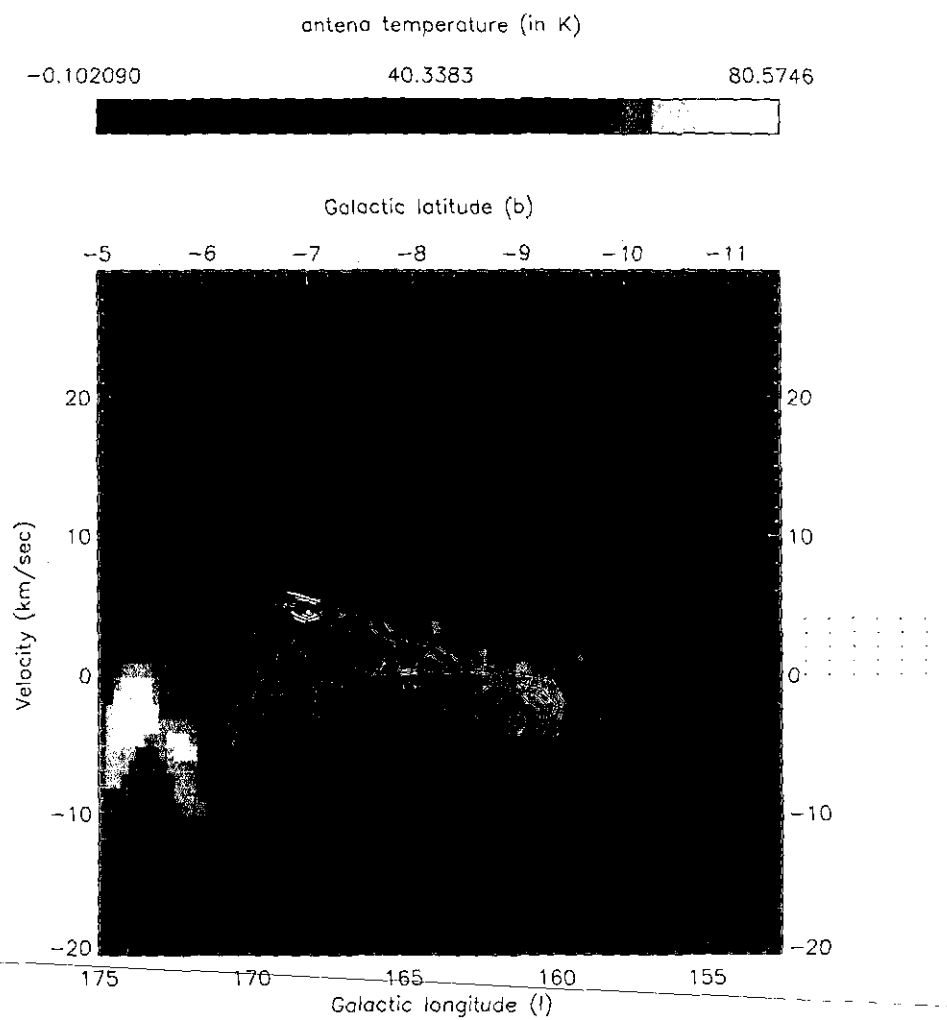
In Figure 15.3 we present a set of six velocity-position diagrams for both the H I and ^{12}CO emission. The first two panels (cuts 1 and 2 in Fig. 15.2) are the velocity-position diagrams for the region that formally is known as TMC, in which ^{13}CO has been detected (see e.g. Kleiner & Dickman 1984; Mizuno et al. 1995; etc.). Figure 15.3 c (cut 3) corresponds to the region associated with Perseus Arm, and shows a strong velocity gradient, from $\sim 8\text{-}10 \text{ km s}^{-1}$ to $\sim -2 \text{ km s}^{-1}$. Figure 15.3 d (cut 4) corresponds to the northernmost region mapped by Ungerechts & Thaddeus (1987). In Figure 15.3 e (cut 5) we present a velocity-position diagram that covers a large region, going from high southern latitudes to close to the Galactic plane. Finally, in Figure 15.3 f (cut 6) we

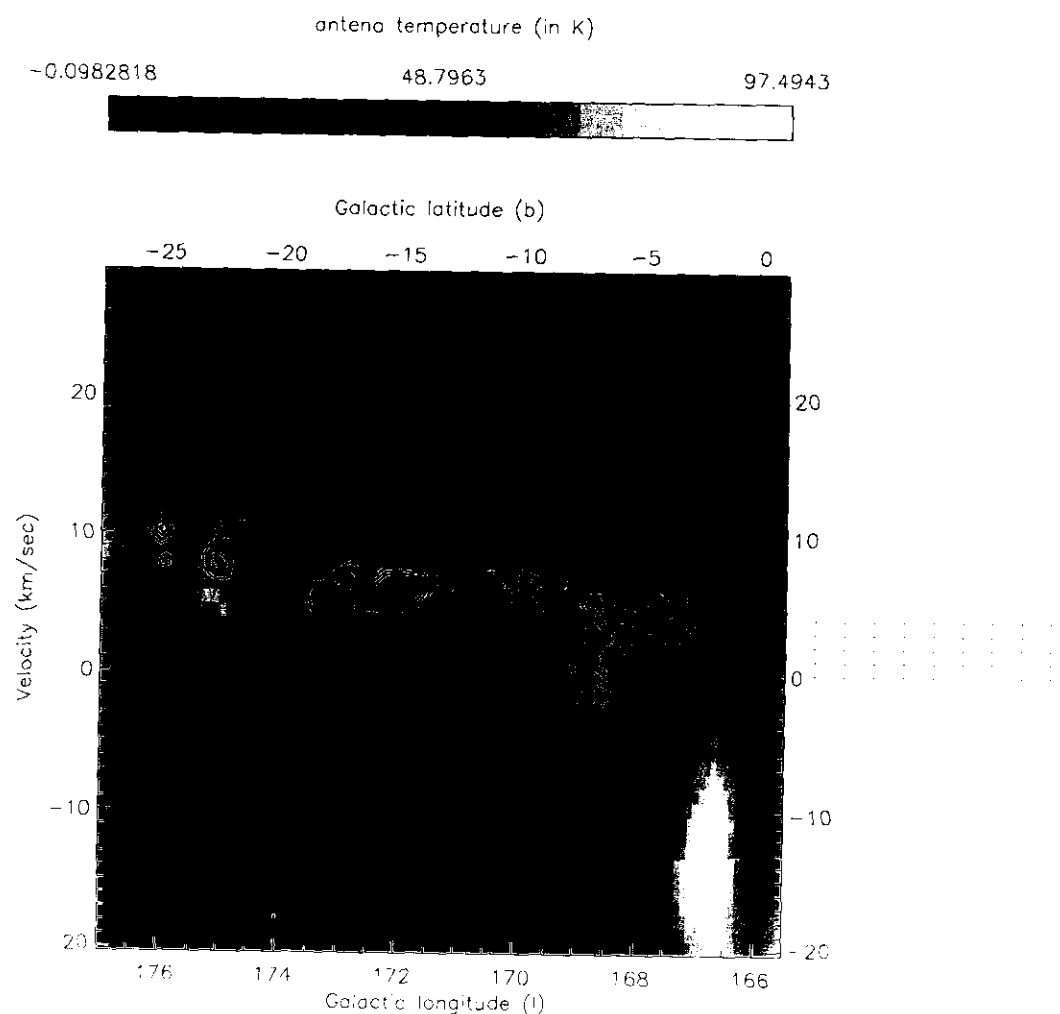
show the velocity-position diagram for the nearby cloud L1457. In particular, note from Figure 15.3d and e that at low Galactic latitudes the H I exhibits a large velocity spread due to the detection of material at a wide range of distances in the Galactic plane. However, once one moves out of the plane a sufficient distance ($b < -10^\circ$), the H I velocity width becomes substantially smaller. The H I velocity peak is generally fairly close to, although not identical with, the ^{12}CO peak. This reflects the fact that the ^{12}CO and H I emission are spatially and kinematically related, suggesting that they are produced as part of a single dynamical complex (see, e.g., Blitz & Thaddeus 1980).











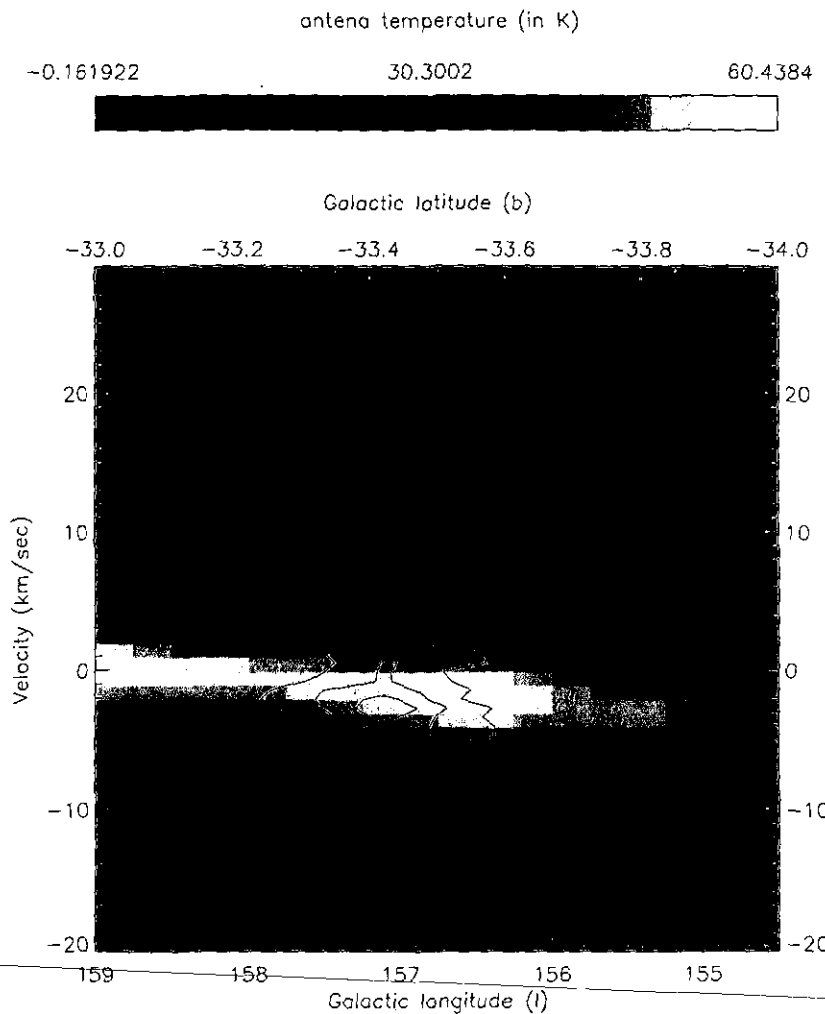


FIGURA 15.3: Velocity-Position diagrams at the positions showed in fig. 15.2. Grey scale denotes the HI emission, and contours denote the ^{12}CO emission. The y -axis denotes the velocity in km s^{-1} ; the upper x -axis denotes the Galactic latitude, and the lower x -axis denotes the Galactic longitude, both in degrees. Note the following general characteristics: a) wherever there is ^{12}CO , HI is also found, with an approximate column density similar to that required by shielding. b) the converse is not true: not all HI in this velocity system is associated with molecular gas. c) at the same spatial position, the HI emission often does not peak at the same velocity than the ^{12}CO ; frequently there is a shift of a few km s^{-1} between the two species. d) the velocity widths in the HI spectra are larger than the ^{12}CO spectra by a factor of roughly 3 or more. e) both the ^{12}CO and HI line profiles are asymmetric, as indicated by the variation of gray-scale and contours.

From Figure 15.3 the following features can be noted. First, wherever there is a ^{12}CO feature, H I is also found, with an approximate column density similar to that required by shielding (see above). Second, the converse is not true: not all H I in this velocity system is associated with molecular gas. Third, at a given spatial position, the H I emission often does not peak at the same velocity than the ^{12}CO ; frequently there is an offset of a few km s^{-1} between the two species. Fourth, velocity widths in the H I spectra are larger than the ^{12}CO spectra by a factor of roughly 3 or more. Fifth, both the ^{12}CO and H I line profiles are asymmetric, as indicated by the variation of gray-scale and contours in

Figure 15.3a-f. These characteristics have been noticed previously in other regions (see e.g., Blitz & Thaddeus 1980; Magnani et al. 1985; Elmegreen & Elmegreen 1987), and we shall focus on these properties when comparing with numerical simulations in the next section.

15.4 Numerical Simulations

15.4.1 The Model

To interpret the significance of the observed features of the atomic and molecular gas enumerated at the end of §15.3, we turn to numerical simulations of the interstellar medium by Passot, Vázquez-Semadeni, & Pouquet (1995 = PVP95a). These two-dimensional simulations represent the behavior of one square kiloparsec of the ISM centered at the solar galactocentric distance. The simulations solve the MHD equations, including self-gravity, parameterized cooling and diffuse heating, the Coriolis force, large-scale shear, and parameterized localized stellar energy input due to ionization heating. The parameterized cooling is as in Chiang & Bregman 1988, who fitted piecewise power laws to the standard cooling calculations of Dalgarno & McCray (1972) and Raymond et al. (1976, see Vázquez-Semadeni, Passot, & Pouquet 1996 = VPP96 for details). As discussed in VPP96, the cooling and diffuse heating time scales are in general much shorter than the dynamical time scales, implying that the flow is always in thermal equilibrium, except in the vicinity of star formation sites. We refer to the reader to VPP96 for further details in the equations and the model itself, and to the video accompanying PVP95a, which gives an animated view of the dynamics of the ISM and shows the transient character of the clouds².

Because the present MHD simulations do not include chemistry, we adopt a picture in which molecular clouds are the “tips of the icebergs” of the density features in the simulations. We define a ‘molecular’ cloud as a connected set of pixels with density above some density threshold ρ_{th} . The selection of this density threshold is arbitrary, but it must be a compromise between realistic values for molecular clouds and the limitations of the simulations. Because the densest and smallest structures in the simulations reach values $\rho \sim 50 - 100 \text{ cm}^{-3}$, we select a density threshold of 35 cm^{-3} , unless otherwise stated. For comparison, typical mean densities in molecular clouds start at roughly 20 cm^{-3} (e.g., Blitz 1987). In particular, an average value of 15 cm^{-3} is reported for the Rosette Molecular cloud (Williams et al. 1995).

For the analysis here, we use a run presented in Vázquez-Semadeni, Ballesteros-Paredes, & Rodríguez (1997) called run 28.800, which has a resolution of 800×800 pixels. In order to mimic as much as possible the conditions in Taurus, we turn off the star formation at $t = 68.9 \text{ Myr}$ (5.3 code units). This allows us to maximize the density contrasts, and to avoid the heating from massive stars, which are not present in Taurus. Then, we follow the time evolution of a relatively small cloud, which is localized far away from the big cloud complexes formed in the simulations.

²See also <http://www.astroscu.unam.mx/turbulence/movies.html>

The subregion of the simulation analyzed here has a mean density of $\langle n \rangle > 11 \text{ cm}^{-3}$, which corresponds to a mean column density of $\langle N \rangle > 3 \times 10^{21} \text{ cm}^{-3}$. This value is large enough to envision enough shielding to UV radiation to form molecular hydrogen (see e.g. Franco & Cox 1986).

15.4.2 Results

In Figure 15.4 we show a time-sequence of a subsection of the whole simulation box, starting 7.02 Myr after the time in which we turn off the star formation. The grey scale indicates the density field, ranging from 0.31 to 56.6 cm^{-3} in the field, and arrows denote the velocity field in a reference frame moving with the cloud's center of mass. The snapshots are separated by $\Delta t = 0.39 \text{ Myr}$ (0.03 time code units). The black isocontour is the region where the density values are higher than 35 cm^{-3} . Note that the cloud is located where the velocity field converges, as required by the continuity equation. Also, one observes rapid growth (within less than 2 Myr) of a “cloud” above our density threshold, which approximately 20 pc in length (each pixel unit is 1.25 pc), comparable to the length of the main Taurus clouds.

To show that the density features observed in the simulations are produced by the confluence of external large-scale streams³ rather than other way around (e.g., the velocities being the consequence of, say, gravitational collapse of the cloud), we calculate the time evolution of both characteristic lengths and energies for the density features in Fig. 15.4. We select a connected set of pixels with densities equal or higher than the half value of the maximum density at each timestep to calculate properties for the “cloud”, a choice motivated by the fact that the maximum density in the box is changing substantially during the simulation (from ~ 16 to $\sim 60 \text{ cm}^{-3}$).

In Fig. 15.5 we display the evolution of two different characteristic lengths: a) l_x , the maximum x -length of the cloud (solid line); and b) l_J , the Jeans length (dotted line) calculated as

$$l_J = \left[\frac{\gamma_{\text{eff}} \pi c_i^2}{G \rho_0^{2-\gamma_{\text{eff}}}} \right]^{1/2}, \quad (15.1)$$

where γ_{eff} is the effective polytropic index in the simulations resulting from equilibrium between the heating and cooling rates, c_i is the isothermal speed of sound, and ρ_0 is the mean density of the cloud (see VPP96 for details). The values of these lengths are denoted on the left-hand side y -axis. We also display the evolution of three different energies: a) the absolute value of the gravitational energy $E_{\text{grav}} = -1/2 \int \rho \phi dV$ (long-dashed line), where ρ is the density and ϕ is the gravitational potential; b) the kinetic energy in the frame of the cloud $E_{\text{kin}} = 1/2 \int_V \rho (\mathbf{u} - \mathbf{u}_{\text{mass}})^2 dV$ (dot-short-dashed line), where \mathbf{u} is the velocity field and \mathbf{u}_{mass} is the mass-weighted average velocity of the cloud; and c) the magnetic energy $E_{\text{mag}} = 1/8\pi \int_V B^2 dV$ (dot-long-dashed line), where B is the magnetic field strength. Note that in all the previous integrals, the volume element is $dV = dx dy$, because of the two-dimensional character of the simulations and thus all the energies considered here are

³By large-scale streams we refer to random motions whose scales are comparable with the scales of the observed structures.

strictly per unit length in the z -direction. The values of the energies are denoted in the left-hand side of the y -axis. The x -axis runs from $t = 0$, the time at which we turned off the star-formation in the simulations, to 15.2 Myrs after.

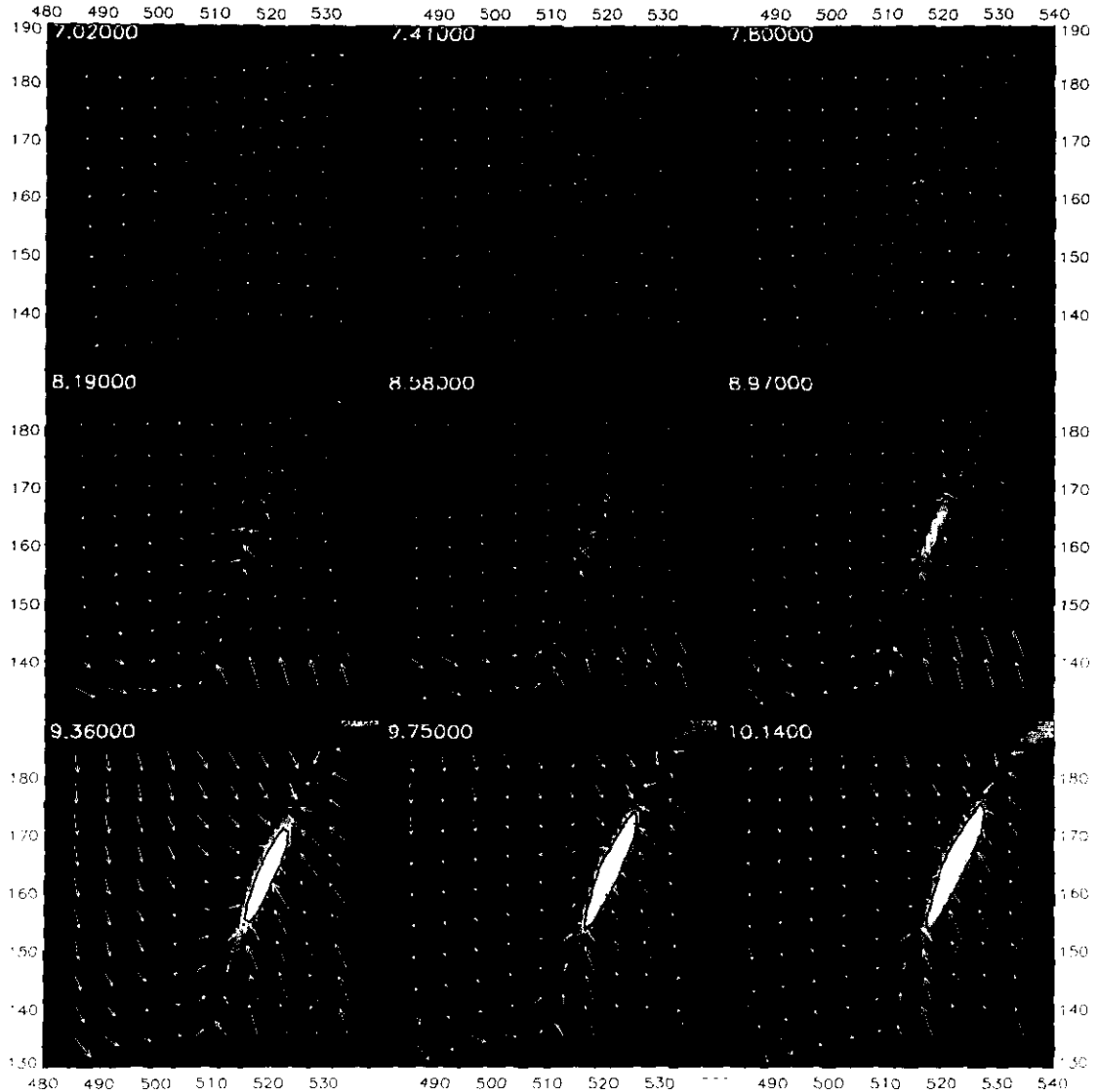


FIGURA 15.4: Time sequence of a small region of the simulation. We show the density field (grey scale), ranging from $\rho < 0.31 \text{ cm}^{-3}$ (darker) to $\rho > 56 \text{ cm}^{-3}$. The label in the upper left corner in each panel is the age in Myr after turning-off the star formation in the simulation. Note that material with $n > 35 \text{ cm}^{-3}$ (the “molecular cloud”) is formed in few Myr by the large-scale compression.

At $t = 0$ the Jeans length (dotted line) is initially larger than the x -length l_x (solid line) (the difference was larger at earlier times). This comparison suggests that, at least in this direction, the density structure is not formed by gravitational collapse. We have calculated also the Jeans-length for the whole subregion (not showed here), and find that it is again larger than the length of the subregion size. These results suggest that, even if

the region does ‘feel’ the action of the gravity at all times, it is Jeans stable initially, and that the velocity field is mostly the result of the global dynamics of the turbulent flow, not the central gravitational action. Note that, as a result of the global flow, the (2D) “filament” that first appears merges with another structure at $t \sim 7.5$ Myr (see Fig. 15.4). This results in the jump in properties seen in Fig. 15.4, except for l_J , which depends on intensive quantities: the mean temperature and mean density. Independent of this merging, at this time $l_J \sim l_x$, suggesting that now the growth of the cloud is mainly determined by the gravitational field. Note that the time of 7.5 Myr from the turn off of star formation to the equality of l_J and l_x is rather arbitrary. On the other hand, what we consider the time for formation of the “molecular cloud” is the roughly 2 Myr it takes from the time at which “molecular” gas first appears to the time at which the cloud reaches a size comparable to that of Taurus.

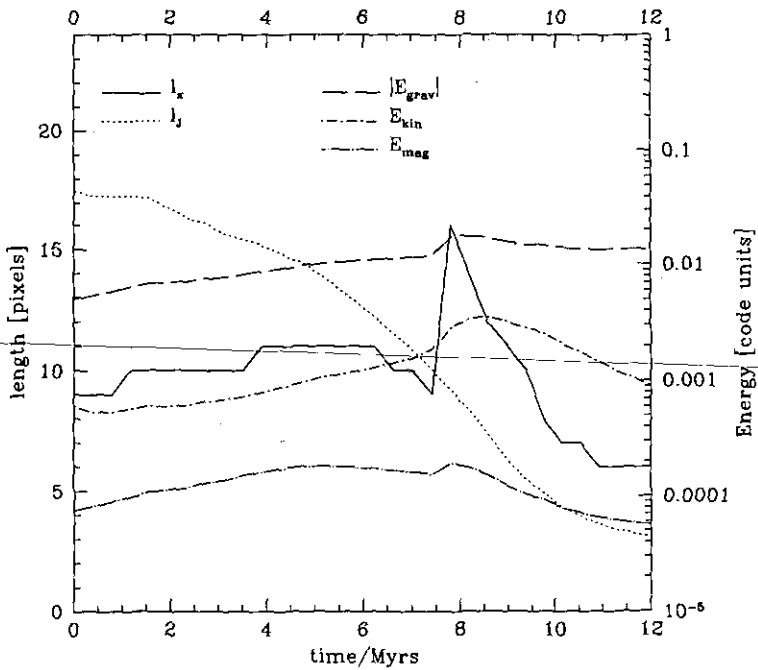


FIGURA 15.5: Time-evolution of the characteristic lengths (left-hand side of the y -axis), and energies (right-hand side of the y -axis) for the region defined as a connected set of pixels with density equal or higher than $1/2$ value of the density maxima at each timestep. Solid line, l_x , the maximum length in the x -direction; dotted-line, l_J . Long-dashed line, absolute value of the gravitational energy; dot-short-dashed line, kinetic energy in the frame of the cloud, and dot-long-dashed line, magnetic energy. Note that initially the cloud is Jeans-stable, but after some time, it becomes Jeans-unstable. Also, note that the magnetic energy is two orders of magnitude lower than the gravitational energy, suggesting that there is no magnetic-flux problem, i.e., the cloud is supercritical. The strong jump in the extensive quantities at $t \sim 8$ Myr. is due to the merging of the filament with another density feature, as can be seen in Fig. 15.4.

Concerning the time evolution of the energies, it can be seen that the absolute value of the gravitational energy (long-dashed line) is higher than the magnetic energy (dot-

long-dashed line) by at least two orders of magnitude. This indicates that the cloud is supercritical by a large margin. Furthermore, it can also be seen that the kinetic energy can not be an agent to stop the collapse: besides being smaller than $|E_{\text{grav}}|$, the velocity field is convergent, implying that it is not working against gravity.

Finally, we want to stress that the region called the “molecular cloud” (black isocontour at $\rho_{\text{th}} = 35 \text{ cm}^{-3}$ in Figure 15.4) appears at roughly the same time in which the region has similar physical and Jeans lengths, i.e., $l_x \sim l_J$, indicating that the value selected of 35 cm^{-3} is reasonably indicative of the time at which the cloud becomes self-gravitating.

As a corollary of the fact that the velocity field is not due to the gravitational potential of the cloud, self-gravitating clouds like that shown in Figure 15.4 can therefore be produced by the turbulent velocity field, out of an initially stable medium. How fast these “molecular clouds” can be produced by the general turbulence must depend on how much mass the streams are carrying, how strong the compression is, the rate of cooling of the compressed (shocked) region, the geometry of the compression, etc. For example, the diffuse structure that it is present when we turned off the star formation spends $\sim 7 \text{ Myr}$ to become self gravitant. Nevertheless, Figure 15.4 shows that in the simulations, self-gravitating structures of 10-20 pc can be coherently formed within a few Myr by this mechanism. Since the densities and velocities in the simulations are realistic, this is a plausible mechanism for molecular cloud formation in the ISM.

15.4.3 Comparison with Observations

In order to test how the simulations compare with observations, we construct “spectra” for both the densest regions ($\rho \geq \rho_{\text{th}}$, which we call “molecular cloud”) and for the low-density regions ($\rho < \rho_{\text{th}}$, which we call “atomic clouds”). Those spectra are constructed as the mass-weighted velocity (x -component) histograms, mimicking the emission of an optically thin line observed from the left hand side of the box, with a spatial resolution of 1.25 pc (1 pixel), and an ideal telescope. With this approximation, we are implying that the observed ^{12}CO and H I line profiles are good representations of the (mass-weighted) line of sight-velocity field. Also, we are assuming that the ^{12}CO and H I emission do not coexist, which is not necessarily true.

With those spectra (mass-weighted velocity histograms) it is possible to construct a velocity-position diagram, and compare it with those in Fig 15.3. Figure 15.6 is the corresponding velocity-position diagram for the cloud and its surrounding medium shown in the bottom right pannel of Figure 15.4. We emphasize several points of similarity between this synthetic position-velocity diagram and the observations (see figure 15.3). First, the synthetic CO emission is always located within a region of strong synthetic H I emission; second, there are regions where synthetic H I emission is present, but where synthetic ^{12}CO emission is not; third, the maximum of the high-density emission does not necessarily coincide with maximum of the low-density emission; fourth, the velocity dispersion is higher for the synthetic H I emission than from the synthetic ^{12}CO emission, and the velocity dispersions of both the low- and in the high-density gas “emission” have similar line-widths to those of the observational data. Fifth, both the ^{12}CO and H I line profiles are asymmetric.

Finally, as in the case of Taurus, the filament is almost coherent in velocity dispersion, i.e., it has approximately the same velocity dispersion throughout its full extension, with values $\sim 2 \text{ km s}^{-1}$ along 10-20 parsecs. We will discuss this in §15.5.1.

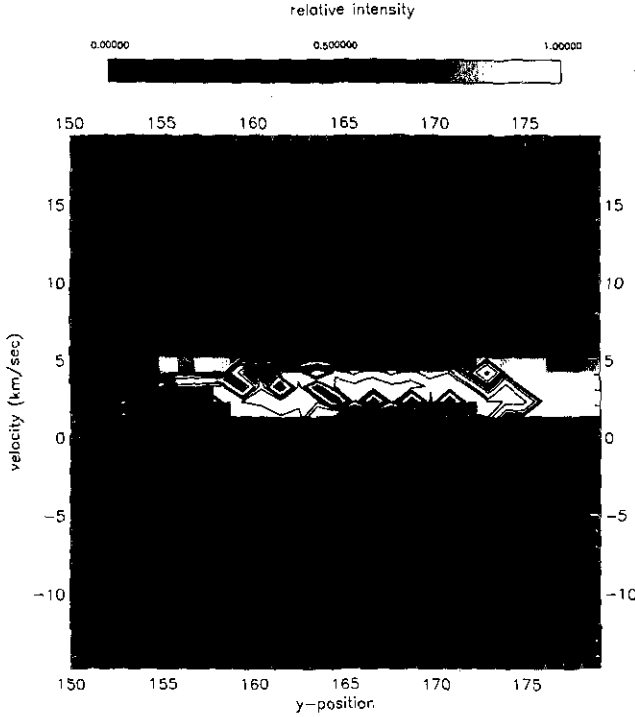


FIGURA 15.6: Synthetic Velocity-Position diagram for the cloud in panel 15.4i. As in fig. 15.3, grey scale denotes the “HI emission”, and contours denotes the “emission” coming from the “molecular cloud”. Note that the same characteristics observed in the observational position-velocity diagrams are reproduced also here.

15.5 Discussion

15.5.1 Evidence for Turbulent Compressions

It is frequently assumed that the ISM is permeated by small-scale non-thermal motions that maintain clouds in a stationary state. Collapse is prevented by those motions, and the role of the external “intercloud” medium is only as an agent for (thermal) pressure confinement and as a shielding for the UV radiation. However, the external medium also exerts a dynamical influence on the cloud, compressing and/or disrupting it (Hunter 1979; Hunter & Fleck 1982; Hunter et al. 1986; Tohline et al. 1988; VPP96; Ballesteros-Paredes et al. 1999a). In this sense, the fragmented appearance of clouds and the existence of multiple velocity components observed at high velocity resolution suggest that the cloud’s internal velocity field possesses a disordered or turbulent component at scales comparable with the scales of the clouds. If molecular clouds are embedded in an intercloud medium of atomic hydrogen (see Andersson 1993 and references therein), and if the intercloud medium is highly turbulent (see e.g. Braun 1999), it is plausible that molecular clouds and their

surrounding gas are in a dynamical state.

Based on refinements of the ISM simulations by PVP95a, Ballesteros-Paredes et al. 1999a consider the turbulent pressure at cloud "boundaries". They show that this boundary pressure is generally anisotropic, which distorts the cloud because the energy involved is generally comparable to the internal cloud kinetic energy. In their picture, turbulent motions are not only responsible for cloud support, as is widely accepted: they may also be responsible, through the large-scale modes of the external turbulence, for shaping and compressing the cloud, possibly even initiating collapse.

In §15.3 we have shown that line-profiles are asymmetric and show important substructure, features that have been increasingly noticed in high spectral and spatial resolution observations (e.g., Falgarone et al. 1998). These features have been proposed as indicative of large-scale turbulent motions, which may be shaping, distorting and disrupting the cloud (Ballesteros-Paredes et al. 1999a).

According to the scenario presented here, the features of the observational data, which are also reproduced in the simulations, may be interpreted as follows. First, because collisions between H I streams produce the higher density gas (and for reasons of shielding), there should always be H I spatially correlated with molecular gas. Second, the larger velocity dispersion of the H I gas is interpreted as a consequence of its larger spatial extension, and of the compression (shocks) and consequent kinetic energy dissipation that occur when the H I streams collide to form the cloud. Finally, because it is the convergence of macro-turbulent H I streams that produce the high-density material, the H I line profiles should be asymmetric and frequently shifted in velocity with respect to the molecular gas⁴.

Thus, the breadth and asymmetry of the H I line profiles indicate a macroscopically-turbulent medium in which clouds exchange mass, momentum and energy with their surroundings. Note that the picture outlined here does not require a coherent or single triggering event in which atomic gas pushes molecular gas together as in a SN explosion. Our scenario is more general, reflecting statistical fluctuations resulting from the combined effects of differing sites.

Recognition of these features is not new. The correspondence between H I and CO in position-velocity diagrams has already been noted by several authors (e.g. Blitz & Thaddeus 1980; Elmegreen & Elmegreen 1987; see also Blitz 1987; and references therein). Andersson (1993 and references therein), who observed the spatial transition between molecular and atomic gas in 62 edges in 14 clouds, found all five observational features that we described at the end of §15.3 and §15.4.3. Moriarty-Schieven, Andersson & Wannier (1997) suggested that there is morphological evidence that nearby clouds (L 1457, see cut 6 in Figs. 15.2 and 15.3 f) have suffered compressions at scales similar to the scales of the cloud. These authors proposed an unobserved SN explosion as a possible mechanism of

⁴Note that in a laminar 2-stream collision producing a shock-bounded slab, the optically thin line-profile from the 'external' medium must be a double-peaked line, at velocities $-v$ and $+v$, where $2v$ is the velocity difference between the streams. On the other hand, the line-profile from the compressed region must be a single-peak line at zero velocity. Nevertheless, in a turbulent medium, which adds strong fluctuations on top of the laminar velocity and density structure, the double-peak might become a single, broader line profile enveloping the narrower line that comes from the compressed region.

producing this morphology. However, the observed morphology is hard to reconcile with a single point source of compression, while it is fully consistent with our scenario. Furthermore, the existence of multi-peak, asymmetric line-profiles at all scales (for larger scales, see e.g., Mizuno et al. 1995; for smaller scales, see e.g., Falgarone et al. 1998) strongly suggests the multi-scale nature of the turbulent motions (Ballesteros-Paredes et al. 1999a). Finally, the velocity-dispersion coherence along large structures have already seen before both in low-mass clouds (Taurus, Mizuno et al. 1995) as well as in high mass clouds (W51, Carpenter & Sanders 1998).

15.5.2 Limitations of the Model

One of the most important limitations of these simulations is that the cooling laws and the available resolution limit the simulations to densities $\lesssim 100 \text{ cm}^{-3}$, so that the evolution of higher-density (10^2 or more) structures cannot be followed. This is important, because molecular gas probably cannot be formed sufficiently rapidly within our density range. Characteristic H_2 formation rate on grains are of the order of $\tau^{-1} \sim nR$, where n is the density of atomic hydrogen and R , the rate coefficient, has typical values of the order of $3 \times 10^{-17} \text{ cm}^3 \text{ seg}^{-1}$ (Jura 1975). Then, the typical H_2 formation timescales are given by

$$\left(\frac{\tau_{H_2}}{\text{yr}} \right) \sim 10^6 \left(\frac{n}{10^3 \text{cm}^{-3}} \right)^{-1}. \quad (15.2)$$

Thus, at our threshold density of 35 cm^{-3} , the H_2 formation timescale is 30 Myr, uncomfortably long.

The low values of the density reached in the simulations' clouds are consequence of the spatial resolution and the mass diffusion, which smooths the strong density gradients (see e.g., Vázquez-Semadeni, Ballesteros-Paredes & Rodríguez 1997). Nevertheless, we envisage that the clouds simulated here would really collapse to structures of much higher density in even shorter times (for example, at $n \sim 100 \text{ cm}^{-3}$, the free-fall time is approximately 3 Myr), given the strength of the external flows, if we were to use higher spatial resolution. In this way our "molecular gas" above the threshold density merely indicates the approximate location and velocity of the higher-density material that would be formed within it. In the real interstellar gas, there is no barrier to compressing gas in the cloud to typical Taurus densities of the order of 10^3 cm^{-3} so that the molecular gas could be produced as rapidly as the dynamical compression occurs.

On the other hand, regions that we identify with molecular gas are not really isothermal in the simulations, but this is not a reason for concern, since we are not dealing with the internal structure of these clouds, which are at the limit of the resolution anyway.

Another limitation of the simulations is that they are two-dimensional calculations that assume no variation of properties perpendicular to the Galactic plane. While colliding streams in two dimensions produce filaments, in three dimensions they may produce sheets. Nevertheless, the most probable situation is one in which the colliding streams are oblique, such that the compressed region becomes a filament again. Also, inhomogeneities in the physical properties of the streams (density, temperature, etc.) and a set of instabilities that

are produced when streams are colliding may destroy the possible appearance of the sheet. Furthermore, the structure in 3D simulations is still strongly filamentary (see e.g., Ostriker et al. 1999; Padoan & Nordlund 1999; Mac Low 1999; Pichardo et al. 1999). Ballesteros-Paredes et al. 1999a discuss other possible differences of 2D and 3D simulations.

Thirdly, the energy input into the ISM is assumed to be from high mass star formation, which seems to be of little relevance to low-mass star forming regions like Taurus. However, the only role of the energy input in the present situation is to produce large-scale flows and turbulence which in turn produce the “molecular cloud”; since the predicted motions agree quite well with the H I data, our approach is justified. Moreover, since the stellar energy input is turned off to follow cloud formation, disruption by local high-mass stars is not an issue.

It should be emphasized that while we are considering the simulations with a view toward understanding the Taurus region, we are not attempting to model the complex in detail, because turbulent flows exhibit a chaotic behavior, i.e., the time histories of arbitrarily close initial conditions diverge exponentially and end up completely different (e.g. Lessieur 1990). Instead, they are expected to reproduce the dynamical relationship between H I flows and molecular gas only in a statistical sense

15.6 Summary

In this paper we have used H I and ^{12}CO data to show that the dynamical features observed through Taurus can be interpreted as large-scale compressions of the atomic gas producing the molecular gas in timescales of few Myr. Also, we followed the evolution of a small piece of a two dimensional numerical MHD simulation to show how large-scale turbulence is able to induce the formation of Taurus-sized regions within a few Myr, while making them self gravitating in the process.

With this picture in mind, we suggest that the Taurus molecular cloud may have formed quite recently (~ 3 Myr ago). This would solve the post T-Tauri problem, suggesting that the very few stars with ages between 5 and 10 Myr in the region might be field stars. We also suggest that the general large-scale interstellar turbulence (in H I) is the mechanism responsible for triggering coherent collapse in regions that apparently are dynamically disconnected.

In this paper we have only considered the timescale of cloud formation, not the timescale of disruption or dissipation. Even with a rapid formation time, if clouds live for 10 Myr or more, at least some complexes should have PTTSs. Thus, our investigation only addresses one-half of the more general post-T Tauri problem. We intend to explore the rate of cloud disruption and dissipation in a future contribution.

Acknowledgements

The simulations were performed on the Cray Y-MP/4-64 of DGSCA, UNAM. This work has received partial support from grants UNAM/DGAPA IN105295 and UNAM/CRAY SC-008397 to E.V.-S. and a UNAM/DGAPA fellowship to J.B.-P. Á

Capítulo 16

Conclusiones

La presente tesis ha tenido por objeto el estudio de las propiedades físicas y estadísticas de las nubes en simulaciones numéricas del medio interestelar producidas por Vázquez-Semadeni et al. (1995a; 1996), Passot et al. (1995), y Vázquez-Semadeni, Ballesteros-Paredes, & Rodríguez (1997). Estas propiedades son el balance energético, el cálculo detallado del Teorema Virial en su forma euleriana, las relaciones de escala (relaciones de Larson, espectro de masas, y la dimensión fractal), y los mecanismos de formación de nubes en un régimen turbulento. En dichas simulaciones las nubes se forman de manera espontánea, es decir, no se imponen condiciones *ad hoc* para simular las nubes. Debido a que las funciones de enfriamiento y calentamiento consideradas no implican la existencia de una inestabilidad térmica, las nubes de las simulaciones pueden tener su origen solamente en la turbulencia o en la inestabilidad gravitacional. Por ello, se implementó un algoritmo capaz de identificar a las nubes como conjuntos conexos de puntos con densidades por encima de un umbral predeterminado.

A lo largo del presente trabajo dos elementos han estado presentes. Por un lado, la importancia de la turbulencia interestelar como un fenómeno multiescala, ya que en la literatura astronómica usualmente la turbulencia ha sido descrita como un fenómeno exclusivamente a pequeña escala. Por otra parte, hemos intentado hacer una continua comparación entre los resultados obtenidos con las simulaciones numéricas y las observaciones reportadas en la literatura.

De esta manera, hicimos primeramente un resumen de los modelos más importantes del medio interestelar global, así como de los mecanismos de formación de nubes. Posteriormente hicimos un análisis crítico del Teorema Virial en su forma lagrangiana, mencionando los resultados más comúnmente citados y recalando las fuertes hipótesis tanto geométricas como físicas involucradas, así como la posible relevancia de estos análisis en los mecanismos de formación estelar. Hemos también discutido el teorema virial euleriano, el cual ha sido poco estudiado y, creemos, ha sido tratado erróneamente en la literatura (McKee & Zweibel 1992). Bajo la óptica de esta versión euleriana, hemos dado una evaluación de los términos involucrados para las nubes en simulaciones numéricas, en particular, en el caso de un medio turbulento. Los resultados más importantes al respecto han sido que, si bien las nubes generadas están en una aproximada equipartición de energías, no están

en equilibrio virial. Por el contrario, los términos que involucran derivadas temporales son los dominantes, cuantificando la impresión visual que se obtiene de observar la evolución temporal de las simulaciones: que el medio interestelar es un medio dinámico, en el cual las estructuras de densidad (nubes) se forman, deforman, transforman y destruyen de manera continua.

Así mismo, hemos estudiado las relaciones de escala para las nubes formadas en las simulaciones. En particular, se discutieron las relaciones de Larson, el espectro de masas, y la dimensión fractal. Hemos encontrado que para las nubes en estas simulaciones, la relación dispersión de velocidades vs. tamaño obtenida observacionalmente por Larson (1981) se confirma, aunque con una fuerte dispersión. También se confirma el espectro de masas observado, así como la dimensión fractal (ver Falgarone et al. 1991; Blitz 1993). Sin embargo, la relación densidad promedio vs. tamaño (Larson 1981) no se confirma, ya que es posible encontrar siempre estructuras pequeñas de baja densidad promedio. Atribuimos su no detección a que podrían pasar desapercibidas observacionalmente dadas las limitaciones de sensitividad de los censos observacionales.

En las simulaciones, las estructuras de densidad a escalas medianas y pequeñas son producidas por la advección (transporte) de masa del campo (compresible) turbulento, y por lo tanto, son en general transitorias. Las nubes más grandes (complejas) se forman por inestabilidad gravitacional, ayudada por el enfriamiento. De esta manera, las nubes pueden estar afectadas no solo por su turbulencia interna, como tradicionalmente ha sido sugerido, sino también por la turbulencia global, a todas las escalas, del medio interestelar. Estos movimientos turbulentos son capaces, en principio, de formar, deformar, inducir el colapso gravitacional o bien romper las nubes. En particular, encontramos que para un gas efectivamente barotrópico (i.e., $P \propto \rho^{\gamma_{\text{eff}}}$), el colapso-gravitacional desatado por la turbulencia no puede ser detenido a menos que el índice barotrópico γ_{eff} cambie durante el proceso, lo cual puede ocurrir solamente hasta que se alcancen densidades protoestelares, si se considera únicamente la contribución térmica a la presión. Este resultado sugiere que es difícil formar núcleos quasi-hidrostáticos dentro de un medio turbulento.

Así mismo, encontramos que el campo magnético puede ser significativamente deformado por el campo de velocidades, produciendo dobleces de las líneas de campo, y que aparentemente no existe una restricción muy severa a los movimientos en el interior de las nubes, ya que las velocidades pueden ser sub- o supersónicas, y sub- o superalfvénicas.

Una pregunta importante es que “si el medio interestelar es demasiado turbulento, entonces podría no haber tiempo suficiente para formar estrellas” (L. F. Rodríguez, comunicación privada). En efecto, el paradigma de la formación estelar (en particular, de estrellas de baja masa) es que este proceso es lento (e.g., Shu, Adams & Lizano 1987). Sin embargo, existe en la literatura un problema relacionado con las escalas de tiempo de la formación de estrellas de baja masa (el problema post-T Tauri): la región de Tauro, una de las nubes moleculares más cercanas al Sol, aparentemente no posee estrellas con edades mayores a 3 millones de años. Cabe entonces la posibilidad de que las nubes interestelares (o al menos Tauro) se formen en escalas de tiempo de ese orden, significativamente menores que las escalas consideradas tradicionalmente (algunas veces 10^7 años), mediante la confluencia de flujos turbulentos a gran escala. De esta manera, el proceso de formación

estelar puede ser de 3 a 10 veces más rápido que lo que señala el paradigma. Con esta idea, usando datos de H I y ^{12}CO , tomados de Hartmann & Burton (1997) y de Ungerechts & Thaddeus (1987) respectivamente, estudiamos el campo de velocidades hacia la región de Tauro, encontrando que las características observacionales (distribución del gas en el espacio posición-velocidad) son consistentes con el esquema de rápida formación de estructuras mediante la convergencia de flujos turbulentos a gran escala presente en las simulaciones, dando una posible solución al problema post-T Tauri.

Los resultados de la presente tesis tienen una serie de derivaciones e implicaciones que será necesario evaluar en trabajos posteriores. La primera es si nuestros resultados se aplican al régimen de nubes moleculares, de escalas de tamaño menores y densidades mayores que las que hemos considerado, y en donde la auto-gravedad podría mantener la identidad de las regiones más densas (núcleos) durante escalas de tiempo mayores, implicando entonces los núcleos densos estarían cerca del estado de equilibrio virial. Así mismo, en caso de existir estos núcleos quasi-estáticos, será importante estudiar en detalle la contribución de la presión magnética turbulenta a su soporte.

La segunda implicación está relacionada con la escala de tiempo de vida de las nubes: tradicionalmente se ha considerado que, dado que la tasa de formación estelar es muy baja, las nubes no están en colapso generalizado. Esto sugiere que, si las nubes son longevas, entonces deben estar sostenidas contra su propia gravedad mediante algún mecanismo de soporte. Dos mecanismos han sido propuestos para ésto: la inyección continua de energía y momento debida a la formación estelar (Norman & Silk 1980), y la posible existencia de campos magnéticos intensos, capaces de reducir la disipación de la turbulencia e impidiendo el colapso gravitacional¹ (Arons & Max 1975).

Sin embargo, existen sugerencias tanto observacionales como teóricas de que las nubes no son tan longevas. Del lado observacional, se ha encontrado que la formación estelar se da en escalas de tiempo cortas, del orden de un millón de años, tanto en regiones de alta masa (Hillenbrand 1997) como en regiones de baja masa (Hartmann et al. 1991). Del lado teórico, simulaciones numéricas en un régimen isotérmico y densidades del orden de 10^3 cm^{-3} indican que la turbulencia se disipa en escalas de tiempo comparables con el tiempo de caída libre de la nube (Ostriker et al. 1999; Mac Low 1999; Padoan & Nordlund 1999).

Una posible solución que compaginaría tanto la baja eficiencia de formación estelar como escalas cortas de formación de nubes y estrellas cortas podría estar dada por el mecanismo de formación de nubes propuesto en el presente trabajo: si las nubes se forman por la confluencia de flujos (en general oblicuos) de las escalas externas a la nube, existe la posibilidad de que la componente tangencial de la velocidad sea capaz de desgarrar a la nube en tiempos menores que el de caída libre. De esta manera el mecanismo de formación de estructuras será, a su vez, el responsable (al menos parcialmente) de la destrucción de éstas.

Es importante mencionar que esta sugerencia parece ir en contra del resultado de Léorat et al. (1990) de que el forzamiento turbulento en las escalas mayores a la longitud de Jeans no es capaz de inhibir el colapso en las escalas menores. Sin embargo, estos autores de

¹Nótese, sin embargo, que esta segunda propuesta no necesariamente evita el colapso gravitacional (Gazol & Passot 1999)

hecho prueban solamente que a fin de asegurar que no hay colapso, uno debe forzar a escalas pequeñas, pero no excluye la posibilidad de que el forzamiento a gran escala puede tener el doble efecto de producir algunas estructuras densas y romper otras. De hecho, planeamos probar nuestra sugerencia considerando la geometría particular de una colisión oblicua, a fin de incluir el efecto simultáneo de los modos compresibles e incompresibles. De esta manera, el mismo mecanismo responsable de la formación de nubes puede ser el responsable de su destrucción.

Así, con la idea de estudiar los mecanismos de formación de las nubes moleculares, sus tiempos de vida, los mecanismos de destrucción de éstas, así como la formación de estructuras más densas, hemos planeado realizar a futuro nuevas simulaciones numéricas, donde se consideren simultáneamente todos los agentes físicos mencionados previamente de manera autoconsistente, en escalas de entre 0.05 y 50 pc, y continuar en ellas el tipo de análisis que se ha realizado en esta tesis. Esperamos así determinar si el medio interestelar es verdaderamente autosimilar en un amplio intervalo de escalas, y en caso afirmativo, cuándo la autosimilaridad acaba por efectos de disipación y gravedad, para finalmente formar estrellas.

Capítulo 17

Conclusions

The present thesis has focused on the study of the physical and statistical properties of clouds in numerical simulations of the interstellar medium produced by Vázquez-Semadeni et al. (1995a; 1996), Passot et al. (1995), and Vázquez-Semadeni, Ballesteros-Paredes, & Rodríguez (1997). These properties are the energy budget, the detailed calculation of the Virial Theorem in its Eulerian form, scaling relationships (Larson relations, mass spectrum and fractal dimension), and the cloud formation mechanisms in the turbulent regime. In those simulations, the clouds are formed spontaneously, i.e., no *ad hoc* conditions are imposed to simulate the clouds. Because the cooling and heating functions considered in the simulations do not imply the existence of a thermal instability, the clouds in the simulations can be produced only by the turbulence or by gravitational instability. Then, we implemented an algorithm able to identify the clouds as connected sets of pixels with densities higher than a predetermined threshold.

Throughout the present work two fundamental ideas have been present. First, the importance of interstellar turbulence as a multiscale phenomenon, contrary to the frequent assumption that the turbulence is a small scale phenomenon. Second, we have continually tried to make comparisons between the results from the numerical simulations and the observational data from the literature.

Thus, we first made a brief summary of the most important models of the interstellar medium, as well as the cloud formation mechanisms. Afterwards, we did a critical analysis of the Virial Theorem in its Lagrangian form, mentioning the most frequently used results and stressing the strong geometric and physical hypothesis involved, and the possible relevance of those analysis on star formation mechanisms. We also discussed the Eulerian Virial Theorem (VT), which has been less frequently considered and, we believe, has been treated questionably in the literature (McKee & Zweibel 1992). Under the scope of the Eulerian version, we have evaluated all the terms involved in the VT for clouds in numerical simulations of the turbulent ISM. The most important results are that, even though the clouds are in an approximate energy equipartition, they are not in virial equilibrium. Instead, the dominant terms are those involving time derivatives, quantifying the visual impression from the observation of the temporal evolution of the simulations that the interstellar medium is very dynamic, in which the density structures are formed, deformed,

transformed and destroyed continuously.

We then studied the scaling relations for the clouds formed in the simulations. In particular, we discussed the Larson relations, the mass spectrum and the fractal dimension. We found that the velocity dispersion-size relation encountered observationally by Larson (1981) is confirmed, but with very large scatter. The observed mass spectrum and the fractal dimension are reproduced (see Falgarone et al. 1991; Blitz 1993). However, the mean density-size relationship (Larson 1981) is not confirmed; instead, it is always possible to find small structures with low mean density. These are difficult to detect due to the sensitivity limitations of the observational surveys.

In the simulations, the density structures at small and intermediate scales are produced by the mass advection of turbulent and compressible field, and thus, they are transient in general. The largest clouds (complexes) are formed by gravitational instability, with the help of the cooling. Therefore, clouds can be affected not only by their own internal turbulence, as traditionally has been suggested, but also by the global turbulence, at all scales, of the interstellar medium. These movements are able, in principle, to form, deform, induce gravitational collapse, or even disrupt the clouds. In particular, we found that, for an effective barotropic gas (i.e., $P \propto \rho^{\gamma_{\text{eff}}}$), the gravitational collapse triggered by turbulence cannot be stopped unless the barotropic index γ_{eff} changes in the process. This only occurs until protostellar densities are reached, if only the thermal contribution to the pressure is considered. This result suggest that it is difficult to form quasi-hydrostatic cores in the turbulent medium.

Also, we found that the magnetic field can be deformed significantly by the velocity field, producing reversals of the field lines, and that apparently there is not a severe restriction to the movements inside the clouds, because the velocities are trans-Alfvénic in general.

An important question is that "if the interstellar medium is very turbulent, then there may not be enough time to form stars" (L. F. Rodríguez, private communication). In fact, the paradigm of the star formation (in particular, of low mass stars), is that this process is slow (e.g., Shu, Adams & Lizano 1987). In fact, there exists in the literature a problem related with the timescales of low-mass star formation (the so-called "post-T Tauri problem"): the Taurus molecular cloud, one of the clouds nearest to the Sun, apparently does not contain stars with ages larger than 3 million years. This apparent paradox may be resolved if interstellar clouds (or at least Taurus) are formed by the confluence of large-scale turbulent streams in timescales of that order, which are significantly lower than the timescales most frequently considered (a few times 10^7 years). In this way, the process of star formation can be 3 to 10 times faster than previously thought. To test this scenario we studied the velocity field through the Taurus region, using H I and ^{12}CO data (from Hartmann & Burton (1997) and Ungerechts & Thaddeus (1987) respectively). We found that the gas' distribution in position-velocity space is consistent with the scheme of rapid cloud formation by the confluence of large-scale turbulent streams suggested by the simulations, thus offering a possible solution to the post-T Tauri problem.

The results of the present Thesis have a number of implications, which we will evaluate in future work. The first one is whether our results extend to the molecular cloud regime, which involves smaller sizes and higher densities, and in which self-gravity can mantain

the identity of the densest regions (cores) over longer timescales, so that the cores can be closer to virial equilibrium. Also, if such quasi-static cores do form in the simulations, it will be important to study in detail the contribution of the magnetic turbulent pressure to their support.

The second implication is related with the lifetimes of clouds. It has been traditionally considered that the low star formation rate in clouds is a sign that they are not in a generalized collapse, and are thus long-lived. This implies that they have to be supported against their self-gravity through some mechanism. Two mechanisms have been proposed for this: the continuous energy and momentum injection from stars (Norman & Silk 1980), and the possible existence of strong magnetic fields which could reduce the dissipation of turbulence, and help supporting the cloud against collapse¹ (Arons & Max 1975).

However, there are both observational and theoretical suggestions that the clouds are not so long-lived. From the observational point of view, it has been found that star formation can occur in short time scales, of the order of a million years, both in high and low mass regions (Hillenbrand 1997; Hartmann et al. 1991). From the theoretical point of view, numerical simulations in the isothermal regime, with densities of the order of 10^3 cm^{-3} show that the turbulence is dissipated in time scales comparable to the free-fall time (Ostriker et al. 1999; Mac Low 1999; Padoan & Nordlund 1999).

A possible solution that may reconcile the low-efficiency of star formation and the short cloud lifetimes and star formation time scales could be offered by the same cloud formation mechanism proposed in the present work: if clouds are formed by the confluence of large-scale streams (in general oblique), the tangential component of the velocity field may be able to disrupt the cloud in timescales shorter than the free-fall time. In this way, the cloud formation mechanism itself is responsible (at least partially) of the cloud's disruption.

It is worth mentioning that this suggestion seems to disagree with the result of Léorat et al. (1990) that turbulent forcing at scales larger than the Jeans length is not able to prevent collapse of the lower scales. However, those authors actually prove only that in order to insure that there is no collapse, one must force at small scales, but do not rule out the possibility that large-scale forcing may have the dual effect of both producing some denser structures while disrupting others. We plan to then test our suggestion considering the specific geometry of the oblique collision, in order to include the simultaneous effect of the compressive and shearing modes. In this way, the same mechanism responsible for the formation of clouds may be responsible for their destruction.

Then, with the idea of studying the formation of molecular clouds, their lifetimes, their destruction mechanisms, as well as the formation even denser structures (cores), we plan to perform new numerical simulations, considering all the relevant processes in a consistent way, at scales between 0.05 and 50 pc, and continuing in them the kind of analyses performed in the present thesis. We hope to determine in this way whether the interstellar medium is actually self-similar in a wide range of scales, and, if so, when the self-similarity is broken by dissipation or gravity effects, to finally form stars.

¹Note, however, that this second proposal does not necessarily avoids the gravitational collapse (Gazol & Passot 1999)

Apéndice A

Término Gravitacional en el Teorema Virial

En el presente apéndice se muestra cómo el término gravitacional del teorema virial,

$$\mathcal{W} \equiv \int x_i \rho \frac{\partial \phi}{\partial x_i} \quad (\text{A.1})$$

puede reescribirse como la energía gravitacional

$$\mathcal{E}_g \equiv -1/2 \int_V \rho \phi dV. \quad (\text{A.2})$$

Decidimos incluir la presente demostración porque es diferente a las demostraciones comúnmente dadas en los libros de texto (e.g.. Shu 1992), donde se utilizan argumentos de simetría de las variables de integración. La hipótesis fundamental es que las integrales de superficie que involucren ϕ , ρ o sus derivadas, pueden hacerse cero al integrar sobre una superficie en infinito. En lo que sigue, haremos uso de la notación

$$\partial_i \equiv \frac{\partial}{\partial x_i} \quad (\text{A.3})$$

y de la ecuación de Poisson:

$$\nabla^2 \phi = \partial_{jj} 4\pi G \rho \quad (\text{A.4})$$

Tomando entonces el término gravitacional (A.1), y usando la ecuación de Poisson (A.4):

$$\begin{aligned} \mathcal{W} &\equiv \int x_i \rho \partial_i \phi dV = \frac{1}{4\pi G} \int (\partial_{jj} \phi) x_i \partial_i \phi dV = \\ &= \frac{1}{4\pi G} \left\{ \int \partial_j (\partial_j (\phi x_i) \partial_i \phi) - \int (\partial_j \phi) \partial_j (x_i \partial_i \phi) dV \right\} \end{aligned} \quad (\text{A.5})$$

La primera es la integral de una divergencia, la cual puede convertirse en una integral de superficie y evaluarse como cero. De la segunda obtenemos:

$$\begin{aligned}\mathcal{W} &= -\frac{1}{4\pi G} \int (\partial_j \phi) \left[x_i \partial_{ij} \phi + \partial_i \phi \delta_{ij} \right] dV = \\ &= \frac{1}{4\pi G} \int \phi \left[\partial_j (x_i \partial_{ij} \phi + \partial_j \phi) \right] dV - \frac{1}{4\pi G} \int \partial_j \left[\phi (x_i \partial_{ij} \phi + \partial_i \phi \delta_{ij}) \right] dV \quad (A.6)\end{aligned}$$

En esta ocasión, es la segunda integral la que puede convertirse en una integral de superficie y ser eliminada, quedando

$$\begin{aligned}\mathcal{W} &= \frac{1}{4\pi G} \int \phi \left[\partial_{jj} \phi + x_i \partial_{ijj} \phi + \partial_{ij} \phi \delta_{ij} \right] dV = \\ &= \frac{1}{4\pi G} \int \left[2\phi \partial_{jj} \phi + \phi x_i \partial_{ijj} \phi \right] dV = \\ &= 2 \int \rho \phi dV + \frac{1}{4\pi G} \int \left[\partial_i (\phi x_i \partial_{jj} \phi) - \partial_{jj} \phi \partial_i (\phi x_i) \right] dV = \\ &= 2 \int \rho \phi dV - \frac{1}{4\pi G} \int \left[3\phi \partial_{jj} \phi + x_i \partial_i \phi \partial_{jj} \phi \right] dV = \quad (A.7)\end{aligned}$$

de manera que se obtiene

$$\mathcal{W} = - \int \rho \phi dV - \int x_i \rho \partial_i \phi dV \quad (A.8)$$

El primer término del lado derecho es la energía gravitacional. El segundo término es precisamente \mathcal{W} . Pasándolo sumando del lado izquierdo y dividiendo por dos se obtiene:

$$\mathcal{W} = -\frac{1}{2} \int \rho \phi dV \quad (A.9)$$

qed.

Apéndice B

Teorema Virial en 2D

El presente apéndice es relevante para el cálculo de los términos del Teorema Virial en el capítulo 8.

Dado que las simulaciones estudiadas son bidimensionales, es necesario verificar de qué manera esta geometría afecta a los términos del Teorema Virial. Por definición de 2D,

$$\begin{aligned}\alpha(x, y, z) &= \alpha(x, y) \\ A_z(x, y, z) &= 0\end{aligned}\tag{B.1}$$

para todo escalar α , excepto z , y todo vector A . El considerar que la variación en z de la componente z de un vector es no-nulo, pero constante es lo que se conoce como 2.5D, es decir:

$$A_z(x, y, z) = A_0\tag{B.2}$$

donde A_0 depende únicamente de x , y y no necesariamente es cero.

La definición de 2D adoptada es equivalente a suponer que el plano x, y se extiende a infinito, de manera que los elementos de volumen $dV = dx dy dz$ se vuelven infinitos. Sin embargo, es posible definir un nuevo elemento de volumen por unidad de longitud en z , $dV' \equiv dV/dz = dx dy$. Como la cantidad dz aparece en todos los términos de la ec. (6.4), entonces es posible cancelarla, de manera que las integrales de volumen se pueden calcular como integrales sobre una superficie en el plano x, y . Por otra parte, hacemos notar también que aún en 2D.

$$\nabla \cdot \mathbf{x} = \frac{\partial x_i}{\partial x_i} = 3\tag{B.3}$$

Adicionalmente, el término de presión térmica y el término magnético en el teorema virial en 2D adoptan formas diferentes que en 3D. Consideremos estos casos.

B.1 Término de Presión Térmica

Consideremos primero el término de presión térmica:

$$\int_V x_i \frac{\partial P}{\partial x_i} dV = \int_V \frac{\partial(x_i P)}{\partial x_i} dV - \int_V P \frac{\partial x_i}{\partial x_i} dV \quad (\text{B.4})$$

Como se mencionó previamente, todos los elementos de volumen contienen dz , de manera que podemos considerar el elemento de volumen por unidad de longitud en z , $dV' = dx dy$. Desarrollando los términos del lado derecho de esta ecuación,

$$\begin{aligned} \int_{V'} x_i \frac{\partial P}{\partial x_i} dV' &= \int_{V'} \left(\frac{\partial(xP)}{\partial x} + \frac{\partial(yP)}{\partial y} + \frac{\partial(zP)}{\partial z} \right) dV' - 3 \int_{V'} P dV' = \\ &= \int_{V'} \left(\frac{\partial(xP)}{\partial x} + \frac{\partial(yP)}{\partial y} \right) dV' + \int_{V'} \frac{\partial(zP)}{\partial z} dV' - 3 \int_{V'} P dV' = \\ &= \int_{V'} \left(\frac{\partial(xP)}{\partial x} + \frac{\partial(yP)}{\partial y} \right) dV' + \int_{V'} P dV' - 3 \int_{V'} P dV' \end{aligned} \quad (\text{B.5})$$

Hasta aquí hemos considerado que $\nabla \cdot \mathbf{x} = 3$. Ahora bien, sumando los últimos dos términos de (B.5) obtenemos:

$$\int_{V'} x_i \frac{\partial P}{\partial x_i} dV' = \int_{V'} \left(\frac{\partial(xP)}{\partial x} + \frac{\partial(yP)}{\partial y} \right) dV' - 2 \int_{V'} P dV' \quad (\text{B.6})$$

que es equivalente a haber convertido la integral de volumen en integral de superficie, y considerar $\nabla \cdot \mathbf{x} = 2$. Por esta razón, en el artículo *Virial Balance in Turbulent MHD Two Dimensional Numerical Simulations of the ISM* (§8) se utiliza $\nabla \cdot \mathbf{x} = 2$, y se toma la integral de superficie como integral de contorno en x, y .

B.2 Término Magnético

Consideremos ahora el término magnético.

$$\begin{aligned} \int x_i \frac{\partial T_{ij}}{\partial x_j} dV &= \int \frac{\partial(x_i T_{ij})}{\partial x_j} dV - \int T_{ij} \frac{\partial x_i}{\partial x_j} dV = \\ &= \int \frac{\partial(x_i T_{ij})}{\partial x_j} dV - \int T_{ii} dV \end{aligned} \quad (\text{B.7})$$

donde $T_{ii} = -B^2/2$ es la traza del tensor de esfuerzos electromagnéticos.

Dado que

$$\begin{aligned} x_i T_{ij} &= \frac{x_i}{4\pi} \left\{ B_i B_j - \frac{1}{2} B^2 \delta_{ij} \right\} = \\ &= \frac{1}{4\pi} \left\{ x B_x B_x - \frac{1}{2} x B^2 + y B_y B_x \right\} \hat{i} + \\ &\quad + \frac{1}{4\pi} \left\{ x B_x B_y + y B_y B_y - \frac{1}{2} y B^2 \right\} \hat{j} - \frac{1}{8\pi} z B^2 \hat{k}, \end{aligned} \quad (\text{B.8})$$

donde

$$B^2 = B_x B_x + B_y B_y, \quad (\text{B.9})$$

entonces

$$\begin{aligned} 4\pi \frac{\partial(x_i T_{ij})}{\partial x_j} - T_{ii} &= \frac{\partial}{\partial x} \left\{ x B_x B_x - \frac{1}{2} x B_x^2 + y B_y B_x \right\} + \\ &\quad \frac{\partial}{\partial y} \left\{ x B_x B_y + y B_y B_y - \frac{1}{2} y B_y^2 \right\} + \\ &\quad + \frac{\partial}{\partial z} \left\{ -\frac{1}{2} z B_z^2 \right\} + \frac{1}{2} B^2 \end{aligned} \quad (\text{B.10})$$

y como el último renglón se cancela idénticamente, el término magnético del Teorema Virial en 2D es:

$$\begin{aligned} \int \frac{\partial(x_i T_{ij})}{\partial x_j} - T_{ii} dV &= \frac{1}{4\pi} \int \frac{\partial}{\partial x} \left\{ x B_x B_x - \frac{1}{2} x B_x^2 + y B_y B_x \right\} dV + \\ &\quad \frac{1}{4\pi} \int \frac{\partial}{\partial y} \left\{ x B_x B_y + y B_y B_y - \frac{1}{2} y B_y^2 \right\} dV. \end{aligned} \quad (\text{B.11})$$

Como se menciona en el capítulo 8, el resultado de considerar T_{ij} dado por (4.4) con $i, j = x, y, z$, es equivalente a considerar que la energía magnética

$$\mathcal{E}_{\text{mag}} \equiv \frac{1}{8\pi} \int B^2 dV \quad (\text{B.12})$$

no contribuye al balance virial en 2D y suponer que a T_{ij} solamente contribuyen las componentes x y y del campo magnético.

Bibliografía

- [1] Adler, D. S. & Roberts, W. W. Jr. 1992, ApJ, 384, 95
- [2] Alves, J., Lada, C., & Lada, E. 1999, ApJ, 515, 265
- [3] Andersson, B-G. 1993. *PhD Thesis. University of Gothenburg, Gothenburg. Sweden*
- [4] Arons, J., & Max, C. E. 1975, ApJL, 196, 77
- [5] Arquilla, R., & Goldsmith, P. F. 1986, ApJ, 303, 356
- [6] Asseo, E., Cesarsky, C. J., Lachièze-Rey, M., & Peillat, R. 1978, ApJL, 225, L21
- [7] Asseo, E., Cesarsky, C. J., Lachièze-Rey, M., & Peillat, R. 1980, ApJ, 237, 752
- [8] Babiano, A., Basdevant, C., Legras, B., & Sadourny, R. 1987, J. Fluid Mech., 183, 379
- [9] Ballesteros-Paredes, J., Hartmann, L., & Vázquez-Semadeni, E., 1999. ApJ, 527. En prensa (10 de diciembre de 1999)
- [10] Ballesteros-Paredes, J. & Vázquez-Semadeni, E., 1995, en *Fifth Mex-Tex Meeting in Astrophysics. Gaseous Nebulae and Star Formation*, eds. M. Peña, & S. Kurtz, Rev. Mex. Astron. Astrof. Ser. Conf. 3, 105
- [11] Ballesteros-Paredes, J. & Vázquez-Semadeni, E., 1997, en *Star Formation, Near and Far*, eds. S. S. Holt & L. G. Mundy. (New York: AIP Press), p. 81
- [12] Ballesteros-Paredes, J., Vázquez-Semadeni, E. C., Gazol, A., and Passot, T. 1999, en preparación.
- [13] Ballesteros-Paredes, J., Vázquez-Semadeni, E., & Scalo, J. 1999, ApJ, 515, 286. (BVS99)
- [14] Bash, F. N., Green, N., & Peters, W. L., III. 1977, ApJ, 217, 464
- [15] Bernard, J. P., Boulanger, F., Desert, F. X., & Puget, J. L. 1992, A & A, 263, 258
- [16] Bertoldi, F. & McKee, C. F. 1992, ApJ 395, 140
- [17] Blaauw, A. 1952. Bull. Astron. Inst Netherlands, 11, 459
- [18] Blitz, L. 1987, in *Physical Processes in Interstellar clouds*, eds. G. E. Morfill, & Scholer, M. (Dordrecht: D. Reidel Publishing Company), p. 35
- [19] Blitz, L. 1991, en *The Physics of Star Formation and Early Stellar Evolution*, ed. C. Lada and N. Kylafis (Dordrecht: Kluwer), p. 3.
- [20] Blitz, L. 1994, en *The Cold Universe*, ed. T. Montmerle, C. J. Lada, I. F. Mirabel, & J. Tran Than Van (Gif-sur-Yvette: Frontiers), p. 99.
- [21] Blitz, L., & Shu, F. H. 1980, ApJ, 238, 148
- [22] Blitz & Thaddeus, P. 1980, ApJ 241, 676
- [23] Bonazzola, S., Falgarone, E., Heyvaerts, J., Péault, M., & Puget, J. L. 1987, A & A 172, 293
- [24] Bonnor, W. B. 1956, ApJ 116, 351
- [25] Bowyer, S., Lieu R., Sidher, S.D., Lampton, M., & Knude, J. 1995, Nature 375, 212
- [26] Braun, R. 1999, en *Interstellar Turbulence*. Eds. Franco, J. & Carramiñana, A. (Cambridge: University Press), pp 12
- [27] Burton, W. B., Gordon, M. A., Bania, T. M., & Lockman, F. J. 1975, ApJ, 202, 30
- [28] Briceño, C., Hartmann, L. W., Stauffer, J. R., Gagné, M., Stern, R. A., & Caillault, J. P. 1997a, A J, 113, 740
- [29] Briceño, C., Hartmann, L. W., Stauffer, J. R., Martín, E. 1997b, A J, 115, 2074
- [30] Briceño, C., Calvet, N., Kenyon, S., & Hartmann, L. 1999, ApJ, accepted
- [31] Carpenter, J. M., & Sanders, D. B. 1998, A J, 116, 1856
- [32] Carr, J. S. 1987, ApJ, 323, 170
- [33] Caselli, P. & Myers, P. C. 1995, ApJ, 446, 665
- [34] Cernicharo, J. 1991, en *The Physics of Star Formation and Early Stellar Evolution*, eds. C.J. Lada & N.D. Kylafis (Dordrecht: Kluwer), p. 287
- [35] Chandrasekhar, S. 1939. *An Introduction to the Study of Stellar Structure* (Chicago: The University of Chicago Press)
- [36] Chandrasekhar, S. 1951, Proc. R. Soc. London, 210, 26

- [37] Chandrasekhar, S. & Fermi, E. 1953. *ApJ* 118, 116
- [38] Chandrasekhar, S. & Munch, G. 1952, *ApJ*, 115, 103
- [39] Chappell, D., & Scalo, J. 1999, *ApJ*, in press.
- [40] Chiang, W. H. & Bregman, J. N. 1988. *ApJ* 328, 427
- [41] Chièze, J. P. 1987, *A & A*, 171, 225
- [42] Chini, R., Krugel, E., & Kreysa, E. 1986, *A & A*, 167, 315
- [43] Cordes, J. 1999. en *Interstellar Turbulence*. Eds. Franco, J. & Carramiñana, A. (Cambridge: University Press), p. 33
- [44] Combes, F. 1999., en *The Chaotic Universe. World Scientific Advanced Series in Astrophysics and Cosmology*, ed. V. Gurzadyan, Li-Zhi Fang y Remo Rufini, en prensa
- [45] Cox, D. 1995. *Nature* 375, 185
- [46] Crovisier, J. 1978. *A A*, 70, 43
- [47] Dalgarno A. & McCray, R. A. 1972. *ARA& A* 10, 375
- [48] Dame, T., Elmegreen, B. G., Cohen, R., Thaddeus, P. 1986, *ApJ*, 305, 892
- [49] De Jong, T.; Boland, W., & Dalgarno, A. 1980. *A& A* 91, 68
- [50] D'Antona, F., & Mazzitelli, I. 1994, *ApJS*, 90, 467
- [51] Dickman, R. L. 1985, en *Protostars and Planets II*, eds. D. C. Black & M. S. Matthews (Tucson: Univ. of Arizona Press), 150
- [52] Dickman, R. L., Snell, R. L., & Schloerb, F. P. 1986, *ApJ*, 309, 326
- [53] Ebbert, R. 1955. *Z. Astrophys.* 37, 222
- [54] Elmegreen, B. G. 1991, *ApJ*, 378, 139
- [55] Elmegreen, 1993a, en *Protostars and Planets III*, eds. E. H. Levy & J. I. Lunine. (Tucson: Univ. of Arizona Press), p. 97.
- [56] Elmegreen, 1993b. *ApJL*, 419, L29
- [57] Elmegreen, B.G. 1996. en *Unsolved Problems of the Milky Way*, ed. L. Blitz y P. Teuben. Kluwer Academic Publishers, p. 551
- [58] Elmegreen, B. G. & Elmegreen D. 1987. *ApJ*, 320, 182
- [59] Elmegreen, D. M. & Elmegreen, B. G. 1978. *ApJ* 220, 1051
- [60] Estalella, R., & Anglada, G. 1996. *Introducción a la Física del Medio Interestelar*. Departament d'Astronomia i Meteorologia, Universitat de Barcelona
- [61] Falgarone, E. 1989, en *IAU Colloquium 120, Structure adn Dynamics of the Interstellar Medium*, eds. G. Tenorio-Tagle, M. Moles & J. Melnick (Berlin: Springer), 68
- [62] Falgarone, E., Lis, D.C., Phillips, T. G., Pouquet, A., Porter, D. H. & Woodward, P. R. 1994. *ApJ* 436, 728
- [63] Falgarone, E. Panis, J.-F., Heithausen, A., Péault, M., Stutzki, J., J.-L. Puget, & Bensch, F. 1998. *A& A* 331, 669.
- [64] Falgarone, E., & Péault, M. 1987, en *Physical Processes in Interstellar Clouds*, eds. G. Morfill, & M. Scholer (dordrecht: Reidel), 59
- [65] Falgarone, E., Phillips, T. G., & Walker, C. K. 1991, *ApJ*, 378, 186
- [66] Falgarone, E., Puget, J.-L., & Péault, M. 1992, *A&A*, 257, 715
- [67] Feigelson, E.D., 1996, *ApJ*, 468, 306
- [68] Ferrini, F., Marchesopni, F., & vulpiani, A. 1983. *Ap & SS*, 96, 83.
- [69] Field, Goldsmith & Habing. 1969. *ApJL*, 155, L149
- [70] Fielder, R. A., & Mouschovias, T. Ch. 1993. *ApJ*, 415, 680
- [71] Fleck, R. C. 1981, *ApJL*, 246, 151
- [72] Fleck, R. C. 1992, *ApJ*, 401, 146
- [73] Fleck, R. C. 1996, *ApJ*, 458, 739
- [74] Franco, J. J., 1983. *ApJ*, 264, 508
- [75] Franco, J. & Carramiñana, A. 1999, *Interstellar Turbulence*. (Cambridge: University Press), in press.
- [76] Franco, J. J., & Cox, D. P. 1986. *PASP*, 98, 1076
- [77] Fuller, G. A., & Myers, P. C. 1992, *ApJ*, 384, 523
- [78] Gammie, C. & Ostriker, E. 1996. *ApJ*, 466, 814
- [79] Gazol, A., & Passot, T. 1999a, *ApJ*, 518, 748
- [80] Gazol, A., & Passot, T. 1999b, en preparación
- [81] Girart, J. M. Estalella, R., Anglada, G., Torrelles, J. M., Ho, P. T. P. & Rodríguez, L. F. 1997. *ApJ* 489, 734
- [82] Goldsmith P. F. 1987, en *Interstellar Processes*, eds. D. J. Hollenbach & H. A. Thronson. (Dordrecht: Reidel), p. 51.

- [83] Gómez, M., Jones, B.F., Hartmann, L., Kenyon, S.J., Stauffer, J.R., Hewett, R., & Reid, I.N. 1992, AJ, 104, 762
- [84] Gómez de Castro, A. I., Pudritz, R. E. & Bastien, P. 1997, ApJ 476, 717.
- [85] Goodman, A. A., Barranco, J. A., Wilner, D. J., & Heyer, M. H. 1998, ApJ 504, 223
- [86] Goodman, A. A., Bastien, P. Menard, F & Myers, P. C. 1990, ApJ 359, 363
- [87] Goodman A. A., Benson, P. J., Fuller, G. A. & Myers, P. C. 1993, ApJ, 406, 528
- [88] Goodman, A. A., Jones, T., Lada, E. A. & Myers, P. C. 1992, ApJ 399, 108
- [89] Habermann, R. 1987, *Elementary Applied Partial Differential Equations with Fourier Series and Boundary Value Problems* (New Jersey: Prentice Hall)
- [90] Hartmann, D., & Burton, W. B. 1997, *Atlas of Galactic Neutral Hydrogen*. Cambridge University Press.
- [91] Hartmann, L., 1998, *Accretion Processes in Star Formation*, Cambridge University Press, p. 33
- [92] Hartmann, L., 1999, New Astronomy Rev., 43, 1
- [93] Hartmann, L., Cassen, P., & Kenyon, S.J. 1997, ApJ, 475, 770
- [94] Hartmann, L.W., Jones, B.F., Stauffer, J.R., & Kenyon, S.J., 1991, A J, 101, 1050
- [95] Hartmann, L., & Kenyon, S.J. 1990, ApJ, 349, 190
- [96] Hartmann, L., Soderblom, D.R., & Stauffer, J.R. 1987, A J, 93, 907
- [97] Hartmann, L., & Stauffer, J. R. 1989, A J, 97, 873
- [98] Hayes, W. D. 1957, J. Fluid Mech. 2, 595
- [99] Heiles, C. 1997, ApJS, 111, 245
- [100] Heithausen, A., Stacy, J.G., de Vries, H.W., Mebold, U., and Thaddeus, P. 1993, A & A 268, 275
- [101] Henriksen, R., & Turner, B. 1984, ApJ, 287, 200
- [102] Herbig, G.H. 1978, en *Problems of Physics and Evolution of the Universe*, ed. L.V. Mirzoyan. (Yerevan: Publ. House of Armenian Academy of Sciences). p. 171
- [103] Herbig, G.H. 1998, ApJ, 497, 736
- [104] Herbig, G.H., Vrba, F.J., & Rydgren A.E., 1986, A J, 91, 575
- [105] Hillenbrand, L.H. 1997, AJ, 113, 1733
- [106] Houlahan, P. & Scalo, J. 1992, ApJ 393, 172
- [107] Huang, S. S. 1950, ApJ, 112, 399
- [108] Hunter, J. H. Jr. 1979, ApJ, 233, 946
- [109] Hunter, J. H., Jr. & Fleck, R. C. 1982, ApJ, 256, 505
- [110] Hunter, J. H. Jr., Sandford, M. T. II, Whitaker, R. W. & Klein, R. I. 1986, ApJ, 305, 309
- [111] Jarrett, T. H., Dickman, R. L., & Herbst, W. 1989, ApJ, 345, 881
- [112] Jeans, J. H. 1902, Phil. Trans. Roy. Soc. London, A199, 1.
- [113] Jones, B.F., & Herbig, G. H. 1979, A J, 84, 1872
- [114] Jura, M. 1975, ApJ, 197, 575
- [115] Kaplan, S. A. 1954, Astr. J. USSR, 31, 137
- [116] Kegel, W. H. 1989, Astron. & Astrophys, 225, 517.
- [117] Kenyon, S.J., & Hartmann, L. 1995, ApJS, 101, 117
- [118] Keto, E. R. & Myers, P. C. 1986, ApJ 304, 466
- [119] Klein, R. I., McKee, C. F., & Woods, D. T. 1995, en *The Physics of the Interstellar Medium and Intergalactic Medium*, eds. A. Ferrara, C. F. McKee, C. Heiles, & P. Shapiro (San Francisco: Astronomical Society of the Pacific), p. 366.
- [120] Kleiner, S. C., & Dickman, R., L. 1984, ApJ, 286, 255.
- [121] Kornreich, P. & Scalo, J. 1999, ApJ, in press.
- [122] Kurtz, S.E., Cesaroni, R., Churchwell, E., Hofner, P., & Walmsley, C.M. 1999, en *Protostars & Planets IV*, eds. V. Mannings, A. Boss, & S. Russell.. (Tucson, Univ. of Arizona Press) in press.
- [123] Kwan, J., 1979, ApJ, 229, 567
- [124] Kwan, J., & Valdés, F. 1987, ApJ, 315, 92
- [125] Lada, E. A., Evans, N. J., II, & Falgarone, E. 1997, ApJ, 488, 286
- [126] Landau, L. D. & Lifshitz, E. M. 1987, *Fluid Mechanics*, 2nd ed. (New York: Pergamon)
- [127] Larson R. B. 1981, MNRAS, 194, 809
- [128] Lawson, W.A., Feigelson, E.D., & Huenmoerder, D.P. 1996, MNRAS, 280, 1071
- [129] Lee, C. W. & Myers, P. C. ApJS, 123, 233

- [130] Leisawitz, D., Bash, F. N., & Thaddeus P. 1989. *ApJS*, 70, 731
- [131] Léorat, J., Passot, T., & Pouquet, A. 1990. *M.N.R.A.S.* 243, 293
- [132] Lesieur, M. 1990. *Turbulence in Fluids. Stochastic and Numerical Modeling*. Kluwer Academic Publishers.
- [133] Lizano, S. & Shu, F. H. 1989. *ApJ* 342, 834
- [134] Loren, R. B. 1989, *ApJ*, 338, 902
- [135] Mac Low, M.-M.. 1999. *ApJ*, 524, in press
- [136] Mac Low, M., Klessen, R. S., Burkert, A., & Smith, M. D. 1998. *Phys. Rev. Lett.*, 80, 2754
- [137] Magnani, L., Blitz, L., & Mundy, L. 1985. *ApJ*, 295, 402
- [138] Magnani, L., LaRosa, T. N., & Shore, S. N. 1993, *ApJ* 402, 226
- [139] Maloney, P. 1988. *ApJ* 334, 761
- [140] Martin & Magazzu 1998. ASP Conf. Ser. 154, *The Tenth Cambridge Workshop on Cool Stars, Stellar Systems and the Sun*. Eds R. A. Donahue and J. A. Bookbinder, p. 1742
- [141] Mast, J.W., & Goldstein, S.J., 1970. *ApJ*, 159, 319
- [142] Massi, M. & Lizano, S. 1994, *A & A*, 287, 581
- [143] Mc Cray, R. & Snow, T. P. Jr. 1979. *ARA& A* 17, 213
- [144] McCrea, W. H. 1957. *MNRAS* 194, 809
- [145] McKee C.F., & Ostriker, J.P. 1977. *ApJ*, 218, 148
- [146] McKee C.F., Zweibel, E.G., Goodman, A.A., & Heiles, C. en *Protostars and Planets III*, eds. E. H. Levy & J. I. Lunine. (Tucson: Univ. of Arizona Press), p. 327
- [147] McKee C. F. & Zweibel, E., 1992. *ApJ* 399, 551 (MZ92)
- [148] McKee, C.F., & Zweibel, E.G. 1995, *ApJ*, 440, 686
- [149] McLaughlin, D. E. & Pudritz, R. E. 1996. *ApJ* 469, 194
- [150] McWilliams, J. 1984, *J. Fluid Mech.*, 146, 21
- [151] Mestel, L., & Spitzer , L. Jr. 1956. *MNRAS*, 116, 503
- [152] Miesch, M. S., & Bally, J. 1994, *ApJ*, 429, 645
- [153] Miesch, M., Scalo, J., and Bally, J. 1999, *ApJ*, submitted
- [154] Miniati, F., Jones, T. W., Ferrara, A., & Ryu, D. 1997, *ApJ*, 491, 216
- [155] Miville-Deschénes, M.-A., Joncas, G., & Falgarone, E. 1998, en *Interstellar Turbulence*, eds. J. Franco and A. Carramiñana, (Cambridge: University Press) in press.
- [156] Mizuno, A., Onishi, T., Yonekura, Y., Nagahama, T., Ogawa, H. & Fukui, Y. 1995. *ApJ*, 445, L161
- [157] Moriarty-Schieven, G. H., Andersson, B-G., & Wannier, P. G. 1997. *ApJ*, 475, 642
- [158] Mouschovias 1987, en *Physical Processes in Interstellar Clouds*, ed. G.E. Morfill, M. Scholer (Dordrecht: Reidel), p. 453.
- [159] Mouschovias, T. Ch. 1991, en *The Physics of Star Formation and Early Stellar Evolution*, eds. C.J. Lada & N.D. Kylafis (Dordrecht: Kluwer) pp. 61, 449
- [160] Mouschovias, , T. C., & Psaltis, D. 1995, *ApJL*, 444, L105
- [161] Mundy, L. G. 1994, en *Clouds, Cores, and Low Mass Stars*, eds. D. P. Clemens, & R. Barvainis (San Francisco: ASP), 35
- [162] Myers, P. C. 1978. *ApJ*, 225, 380
- [163] Myers, P. C. 1983. *ApJ*, 270, 105
- [164] Myers, P. C. 1990, en *Molecular Astrophysics*, ed. T. W. Hartquist (Cambridge: University Press), 328
- [165] Myers, P. C., & Goodman, A. A. 1988a. *ApJL* 326, L27
- [166] Myers, P. C., & Goodman, A. A. 1988b. *ApJ* 329, 392
- [167] Myers, P. C. & Khersonsky 1995. *ApJ* 442, 186
- [168] Nakano, T. 1998. *ApJ*, 494, 587
- [169] Neuhäuser, R., Sterzik, M. F., Torres, G., & Martín E. L. 1995. *A A*, 299, L13
- [170] Norman, C. A., & Ferrara, A. 1996. *ApJ*, 467, 280
- [171] Norman & Silk 1980. *ApJ*, 238, 158
- [172] Ostriker, E. C., Gammie, C. F., & Stone, J. M. 1999. *ApJ*, 513, 259
- [173] Padoan, P. 1995, *MNRAS*, 277, 377
- [174] Padoan, P., & Nordlund, A. 1999. *ApJ*, in press
- [175] Palla, F., & Galli, D. 1997, *ApJ*, 476, L35
- [176] Parker, E. N. 1966. *ApJ*, 145, 811
- [177] Parker, E. N. 1969. *Space Science Reviews* 9, 651

- [178] Parker, E. N., 1979. *Cosmical Magnetic Fields. Their Origin and Their Activity* (Oxford: University Press).
- [179] Passot, T. & Pouquet, A. 1987. J. Fluid Mech. 181, 441
- [180] Passot, T., & Pouquet, A., J. 198X. Comp. Phys. 75, 300
- [181] Passot, T., Pouquet, A. & Woodward P., 1988, A&A, 197, 228.
- [182] Passot, T., & Vázquez-Semadeni, E. 1998, Phys. Rev. E., in press.
- [183] Passot, T., Vázquez-Semadeni, E. & Pouquet, A. 1995. ApJ 455, 536 (PVP95)
- [184] Péault, M., Falgarone E., & Puget, J.L. 1986. A A, 157, 139
- [185] Pichardo, B., Vázquez-Semadeni, E., Gazol-Patiño, A., Passot, T., & Ballesteros-Paredes, J. 1999. ApJ, en prensa
- [186] Plume, R. Jaffe, D.T., Evans II, N. Martin-Pintado, J. Gómez-González, J. ApJ, 476, 730
- [187] Porter, D. H., Pouquet, A., & Woodward, P. R. 1994, Phys. Fluids, 6, 2133
- [188] Pouquet, A., Passot, T. & Léorat, J. 1991, in Fragmentation of Molecular Clouds and Star Formation, ed. E. Falgarone, F. Boulanger & G. Duvert (Dordrecht: Kluwer), p. 101.
- [189] Pratap, P., Dickens, J. E., Snell, R. L., Miralles, M. P., Bergin, E. A., Irvine, W. M., & Schloerb, F. P. 1997, ApJ, 486, 862
- [190] Pumphrey, W. A., Scalo, J. 1983. ApJ 269, 531
- [191] Raymond, Cox & Smith 1970. ApJ 204, 290
- [192] Rosen, A., Bregman, J. N., & Norman, M. L. 1993, ApJ, 413, 137
- [193] Rosen, A., & Bregman, J. N. 1995, ApJ, 440, 634
- [194] Rosolowsky, E. W., Goodman, A. A., Wilner, D. J., & Williams, J. P. 1999. ApJ, en prensa
- [195] Santillán, A., 1999. *PhD. Thesis*. Universidad Nacional Autónoma de México. México.
- [196] Scalo, J. M. 1985, en *Protostars and Planets II*, ed. D. C. Black & M. S. Matthews (Tucson: Univ. of Arizona Press), 201
- [197] Scalo, J. M. 1987, en *Interstellar Processes*, ed. D. J. Hollenbach & H. A. Thronson (Dordrecht: Reidel), 349
- [198] Scalo, J. 1990, en *Physical Processes in Fragmentation and Star Formation*, eds. R. Capuzzo-Dolcetta, C. Chiosi, & A. Di Fazio (Dordrecht:Kluwer), 151
- [199] Scalo, J. M., & Struck-Marcell, C. 1984, ApJ, 276, 60
- [200] Schroeder, M. 1996. *Fractals, Chaos, Power Laws. Minutes from an Infinite Paradise*. W. H. Freeman Company.
- [201] Scoville, , N. Z., & Solomon, P. M. 1975. ApJL, 199, L105
- [202] Scalo, J., Vázquez-Semadeni, E., Chappel, D., & Passot, T. 1998. ApJ, 504, 835
- [203] Snell, R. L., Heyer, M. H., & Schloerb, F. P. 1989, ApJ, 337, 738
- [204] Siess, L., Forestini, M., & Bertout, C. 1997, A A, 326, 1001
- [205] Shu, F. 1987, en *Star Formation in Galaxies*, ed. C. Persson (Washington: NASA Office of Space Science and Applications), 743
- [206] Shu, F., 1990, Gas Dynamics (Mill Valley: University Science Books)
- [207] Shu, F.H., Adams, F.C., & Lizano, S. 1987, ARA & A, 25, 23
- [208] Solomon, P.M. Rivolo, A.R., Barret, J.W., & Yahil, A. 1987. ApJ, 319, 730
- [209] Solomon, P. M., Sanders, D.B. & Rivolo, A.R. 1985, ApJ, 292, L19
- [210] Spitzer, L. 1956. ApJ, 124, 20
- [211] Spitzer, L. 1978. *Physical Processes in the Interstellar Medium*. (Princeton University, New Observatory, Princeton, N.)
- [212] Stauffer, J.R., Hartmann, L.W., & Barrado y Navascués, D. 1995, ApJ, 454, 910
- [213] Stevens, I. R., Blondin, J. M., & Pollock, A. M. T. 1992. ApJ 386, 265
- [214] Stone, J. M. & Norman, M. L. 1992, ApJ, 390, L17
- [215] Swenson, F.J., Faulkner, J., Rogers, F.J., & Iglesias, C.A. 1994, ApJ, 425, 286
- [216] Tafalla, M., Mardones, D., Myers, P. C., Caselli, P., Bachiller, R., & Benson, P. J. 1998, ApJ, 504, 900
- [217] Tohline, J. E., Bodenheimer, P. H., & Christodoulou, D. M. 1987. ApJ, 322, 787
- [218] Torrelles, J. M., Rodríguez, L. F., Cantó, J., Carral, P., Marcaide, J., Moran, J. M., & Ho, P. T. P. 1983. ApJ 274, 214

- [219] Tufte, S., Reynolds, R., & Haffner, M. 1999, en *Interstellar Turbulence*, eds. J. Franco, J. & A. Carramiñana (Cambridge: University Press), p. 27
- [220] Turner, B.E. 1994. ApJ, 420, 661.
- [221] Ungerechts, H. & Thaddeus, P., 1987. ApJS, 63, 64
- [222] Vázquez-Semadeni, E. 1994, ApJ, 423, 681
- [223] Vázquez-Semadeni, E. 1999, en *The Chaotic Universe*, eds. V. Gurzadyan and L. Bertone, en prensa
- [224] Vázquez-Semadeni, E. Ballesteros-Paredes, J., & Rodríguez, L. F. 1997. ApJ 474, 292 (VBR97)
- [225] Vázquez-Semadeni, E., Cantó, J. & Lizano, S. 1998. ApJ 492, 596
- [226] Vázquez-Semadeni, E. & Gazol, A. 1995. A&A 303, 204
- [227] Vázquez-Semadeni, E., Ostriker, E., Passot, T., Gammie, C. & Stone, J. 1999, en *Protostars and Planets IV*, eds. V. Mannings, A. Boss, S. Russell (Tucson: Univ. Of Arizona Press).
- [228] Vázquez-Semadeni, E. & Passot, T. 1998, en *Interstellar Turbulence*, eds. J. Franco, J. & A. Carramiñana (Cambridge: University Press), p. 223
- [229] Vázquez-Semadeni, Passot & Pouquet, 1995. ApJ 441, 702
- [230] Vázquez-Semadeni, E., Passot, T., & Pouquet, A. 1995b, en *Fifth Mex-Tex Meeting in Astrophysics. Gaseous Nebulae and Star Formation*, ed. M. Peña, & S. Kurtz, Rev. Mex. Astron. Astrof. Ser. Conf. 3, 61
- [231] Vázquez-Semadeni, E., Passot, T. & Pouquet, A. 1996. ApJ 473, 881
- [232] Verschuur, G. L. 1991, Ap&SS, 185, 305
- [233] Vishniac E. T. 1983. ApJ 274, 152
- [234] Vishniac E. T. 1994. ApJ 428, 186
- [235] von Weizsäcker, C.F. 1943. Zs. F. Ap., 22, 319
- [236] Walter, F.M., Brown, A., Mathieu, R.D., Myers, P.C., & Vrba, F.V., 1988, A J, 96, 297
- [237] Wichmann, R., Krautter, J., Schmitt, J.H.M.M., Neuhäuser, R., Alcalá, J.M., Zinnecker, H., Wagner, R.M., Mundt, R., & Sterzik, M.F., 1996, A A, en prensa
- [238] Williams, J. P., de Geus, E. J., & Blitz, L. 1994, ApJ, 428, 693
- [239] Williams, J. P., Blitz, L. & Stark, A. 1995. ApJ 451, 252.
- [240] Wright, M.C.H., Warner, P.J., & Baldwin, J. E. MNRAS, 155, 337
- [241] Wood, D. O. S., Myers, P. C., & Daugherty, D. 1994, ApJS, 95, 457
- [242] Yonekura, Y., Dobashi, K., Mizuno, A., Ogawa, H., & Fukui, Y. 1997, ApJS 110, 21
- [243] Zickgraf, F.-J., Alcalá, J. M., Krautter, J., Sterzik, M.F. Appenzeller, I., Motch, C., & Pakull, M.W., 1998. A A, 339, 457.
- [244] Zimmermann, T. & Ungerechts, H. 1990. A & A 238, 337
- [245] Zuckerman B., & Evans, N.J. 1974. ApJL, 192, 149.